ENHANCEMENTS IN ANALYSIS OF BEAM-LIKE STRUCTURES USING ASYMPTOTIC METHODS

A Dissertation
Presented to
The Academic Faculty

By

Mohit Gupta

In Partial Fulfillment
of the Requirements for the Degree
Doctor of Philosophy in the
School of Aerospace Engineering

Georgia Institute of Technology

May 2019

ENHANCEMENTS IN ANALYSIS OF BEAM-LIKE STRUCTURES USING ASYMPTOTIC METHODS

Approved by:

Prof. Dewey H. Hodges
School of Aerospace Engineering
Georgia Institute of Technology

Prof. Julian J. Rimoli
School of Aerospace Engineering
Georgia Institute of Technology

Prof. George A. Kardomateas
School of Aerospace Engineering
Georgia Institute of Technology

Prof. Massimo Ruzzene
School of Aerospace Engineering
Georgia Institute of Technology

Prof. Donald W. White
School of Aerospace Engineering
Georgia Institute of Technology

Date Approved: March 25, 2018

Don’t measure if you can estimate, and you won’t need to estimate if you can calculate

– *Frugal Engineer*

To the two most important women in my life,

my mother, Navita Gupta and my fiancee, Aarohi Shah

ACKNOWLEDGEMENTS

It has been a journey that I will remember for my entire life. I would like to thank Dr. Dewey H. Hodges and the department of aerospace engineering at Georgia Tech. for providing me a chance to research and earn my graduate degrees. I am grateful to Prof. Hodges for having me around every day, for the incessant encouragement, for supporting and guiding in my endeavors. I am also thankful to the United States Army for funding my education throughout the grad school.

I would like to acknowledge the efforts of my committee members, Profs. Julian J. Rimoli, Massimo Ruzzene, George A. Kardomateas, and Donald W. White for their valuable feedback which helped me take on the challenges towards my dissertation.

I would also like to express my gratitude to the efforts of my senior academic brothers Profs. Dineshkumar Harursampath, Carlos Cesnik, and Wenbin Yu for their support and help in gathering the resources needed to gain an in-depth understanding of the various concepts involved. I sincerely thank Drs. Anurag Rajagopal, Ravi Kovvali and Jimmy Ho for helping me throughout the course of my Ph.D. either by answering my silly questions or finding time to engage in intense discussions on VAM. I have enjoyed every meeting with them before or after their graduation.

I learned a lot in the interesting discussions during COSMOS meetings with Profs. Abowd, Starner, Vogel, Filler, Conte, and all the graduate students who form that brilliant group. I got a chance to work with Prof. Abowd on thin-film microphones and I am grateful to him for the opportunity. I enjoyed interacting with my professors with whom I took amazing courses, Profs. Costello, Ramachandran, Rubinoff, Liu, Rimoli, Xia and Zhou.

I am indebted to all my colleagues at Georgia Tech., Korak, Nivedita, Darshan, Hanif, Etienne with whom I have spent considerable amount of time, while working. We shared ideas, concepts, interesting applications and at times, personal concerns. I enjoyed playing the challenging game of squash with Dr. Hodges, Dr. Di Leo and Korak. I will never forget

all the time I enjoyed with my friends, Harshit, Chetan, Arman, Donald, Ankit, Saurabh, Luca, Matheus, Hernan, Amir, Julie, Manan, Sushant, Umesh, Dushhyanth, Manish, and all others with whom I have enjoyed a dinner, a trip or celebration. I deeply apologize if I forgot to mention names. They are all skillful individuals whom I admire and I believe that they have a future full of greatness and appreciation.

My special thanks goes to my parents and my brother who have always been very supportive. They have been the real foundation behind this work while staying very far from me. I enjoyed visiting them and traveling with them whenever they visited me in the United States. If someone admires me for the qualities that I have, they are all derived from them.

Lastly, I would like to acknowledge the efforts of my fiancee, Aarohi Shah who is a friend, a colleague, and my life partner. She has always been very supportive of my work and my endeavors. Her affection and respect kept me motivated to keep going and put the best of my efforts towards the dissertation.

In short, at Georgia Tech., I was surrounded by many highly experienced and intellectually sound individuals that they made my stay in Aerospace Engineering, a wonderful experience and worth to ponder upon.

TABLE OF CONTENTS

LIST OF TABLES

LIST OF FIGURES

SUMMARY

Engineering design of aerospace structures requires a detailed structural analysis. Due to the immense and well-known benefits of composite materials over conventional structural materials, they constitute a large and rapidly growing industry, necessitating holistic modeling tools. Industries resort to the use of standardized 3-D Finite Element Methods (FEM) for this purpose. While 3-D FEM is versatile and well-established for successfully simulating complex structural problems, but the FEM tools invariably are extremely slow, expensive to maintain and computationally intensive.

As a complement to conventional FEA, state-of-the-art Variational Asymptotic Method (VAM) is being employed which is very fast, provides rigorous physics based material models for composites while ensuring efficiency and accuracy. In the present work, some major issues with use of VAM-based framework for solving thin-walled structures have been identified and fixed. Further, the overall framework has been facilitated with analysis of piezoelectric materials, analysis involving structural damping and a method to obtain, store and visualize time-histories of 3D stresses, strains and displacements. Finally, a method to use dimensional reduction techniques for solving beam-like structures involving complex and intricate 3-D geometries is demonstrated. Thus, the present work expands the scope of VAM-based beam theory and provides extensive validation for implemented techniques against commercially available 3-D FEM tools.

Part 1

Introduction

CHAPTER I

INTRODUCTION

Structural analysis is a study which explains the behavior of a component or a combination of those, under a given set of conditions. It is a key step in the overall engineering design of components. Knowingly or not, people have been using the concepts of structural analysis throughout history. This fact is evident largely by the presence of ancient monuments, bridges, and even the tools that were used to make them. It is believed that ancient engineers would have some kind of empirical rules, procedures, tests, and information from previous experiences that helped them complete tasks, which today are components of structural analysis. Sir Isaac Newton laid out the fundamentals of structural analysis in the 17^{th} century and we have seen tremendous progress in this field over the last 150 years.

To perform structural analysis, one must determine information such as structural loads, geometry, boundary conditions, and material properties. The results of such an analysis typically include stresses and displacements. This information is then compared to the criteria of failure. Advanced structural analysis may examine dynamic response, stability, and non-linear behavior. There are multiple ways to perform the analysis and each method is based on three fundamental relations: equilibrium equations, constitutive law, and compatibility equations. The present work deals with the structural analysis of beam-like structures in aerial vehicles, such as rotor blades and aircraft wings. These structures are typically designed with a gentle out-of-plane curvature and pre-twist. During the flight,

they undergo large displacements and rotations, making it important to employ a geometrically non-linear analysis for design.

1.1 Background and Motivation

Over the past few decades, composite materials have revolutionized the field of aerospace structural engineering due to their effective reduction in weight for the desired stiffness properties, directional nature facilitating tailorability and their excellent fatigue behavior. The American Composite Manufacturer's Association (ACMA) projects that the market size of composite materials in the field of aerospace engineering would be approximately \$15B by 2021, after seeing a compounded annual growth rate of almost 10%, the largest for any industry. With the introduction of composite materials, however, aircraft structures have become very complex in their design. Among those, beam-like structures such as rotor blades and aircraft wings can be solved using conventional beam theories or by techniques in elasticity. Although conventional beam theories are fast, the results are seldom satisfactory. Consequently, because of the complex designs and the use of composite materials, the analysis is thought to be best carried out using 3-D Finite Element Method (FEM). FEM is a numerical method for solving partial differential equations generated by the same theories of mechanics. 3-D FEM facilitates high-fidelity modeling of complex geometries with accurate and reliable results.

However, there are some obvious drawbacks: invariably all FEA tools are computationally expensive as compared to beam modeling tools, often by two to three orders of magnitude. For example, a single simulation to analyze a composite aircraft wing could typically take a few weeks, even on state-of-the-art computer systems. To make matters worse, FEA results frequently disagree with results from lab experiments and flight tests. This stems from irrelevant and unnecessary assumptions inherent in the models, usually obtained by generalizing legacy models for metallic structures. The annual licenses for commercial available 3-D FEA tools are too expensive for medium/small-scale manufacturers, who do

not use the software throughout the year and also need to install and maintain high-end workstations or clusters to run such software. Another aspect often overlooked is how labor-intensive even the modeling process can become for complex layups and geometries. With the motivation to develop a fast and user-friendly, computationally efficient method for analysis of complex beam-like aerospace structures, Variational Asymptotic Method (VAM) was employed for the first time almost 30 years back by Hodges et al. Building on Berdichevsky's work n the 1970s, a beam theory to perform structural analysis was developed which is termed as Nonlinear Composite Beam Theory. With the application of this theory, computational time is reduced by multiple orders of magnitude. One may argue that the 1990s were actually the times to focus on developing tools which were fast because the computers were slow, bulky and expensive. The advent of clever ways of manufacturing integrated circuits has led to a significant reduction in the cost of computation since then. With the developments in computer architecture, there has been a reduction in the size of electronic components as well. This is an interpretation of Moore's law, which assented that the cost of computing would decrease as we go forward in time. The empirical data which is the basis of this law, now shows that the Moore's law is more or less dead. This is also confirmed by researchers at MIT and Intel. Thus, we can no longer count on computers getting faster and cheaper. Consequently, developing and using tools based on reduced-dimensional modeling remains a priority, as they are fast, accurate, reliable as well as computationally efficient.

But how did we really get to the development of a comprehensive Nonlinear Composite Beam Theory? First the need for a beam theory to solve such complex problems is established to save computational costs and user labor. Indeed, almost any beam theory can transform a 3-D problem into a sectional 2-D analysis and a 1-D beam analysis, but in the process they end up making a lot of assumptions. It is not explicitly written but even the simplest theories by Euler-Bernoulli or St. Venant, which aim to solve for extension, bending and torsion in beam, also follow the aforementioned dimensional reduction procedure.

These are just a few dominant modes of deformation out of the many possibilities are most commonly observed. Then, Timoshenko introduced the transverse shear deformations by considering the rotations of the cross-sections with independent degrees of freedom. Also, Vlasov [165] showed the effect of restrained warping at the boundaries, penetrating the interior solutions in thin-walled open section beams. Even though these beam theories attempt to capture some of the deformation modes which require deep understanding of the behavior of beams, there are still some assumptions made a priori which affect the accuracy of the solution as the complexity in the original problem increases. Some of the beam theories have inconsistencies within the assumptions or presuppose decoupling of the different modes of deformation, leading to inaccuracies. A comprehensive set of information on this and other developments related to beam theories is given by Hodges [69].

1.2 Existing Literature on Beam Theories

As discussed, for a complete solution of a beam problem, we need the results from a sectional analysis and a 1-D beam analysis. Several outstanding methods can determine the sectional constants and recover 3-D outputs once the 1D variables are solved for. Among the first ones, Borri and his co-workers [20, 51] based their approach on linear elasticity and extracted a 6×6 cross-sectional stiffness matrix using the principle of virtual work. Well-known tools such as BECAS [19] and NABSA [51] are based on this approach. Ghiringelli et al. [50] introduced a novel approach where the sectional properties are obtained by modeling the cross section as a slice of 3-D finite elements. In a recent work [14], Bauchau and Han performed the cross-sectional analysis aligned with the three-dimensional elasticity based on a Hamiltonian formalism. This approach involves the use of finite elements as well and was further updated by them in Ref. [59] to include nonlinearities. Another rigorous methodology is the Formal Asymptotic Method (FAM) wherein the asymptotic analysis is applied directly to the governing equations as opposed to a variational equivalent. The analysis begins by using the slenderness ratio to define a ‘slow’ and ‘fast’ set

of coordinates; for example, the slow coordinates, would refer to the cross-sectional coordinates divided by the slenderness ratio; and the axial coordinate. Buannic and Cartaraud [21] employ the FAM to develop a theory for beams whose elastic moduli varied periodically along the beam. Ref. [76] presents a structural model based on a mixed force and displacement method. The results were validated for both open and closed section beams. The method of extraction of cross-sectional properties followed by Dong and his co-workers [44, 45, 83] is to obtain the displacements from 3D elasticity (such as Iesan's solutions [73]), from which equivalent section properties are obtained. Another method, which performs a rigorous dimensional reduction using the ideas of an axiomatic hypothesis and an asymptotic expansion method is Carrera Unified Formulation (CUF) [24]. The displacement field is written as a series using Maclaurin polynomials for the cross-sectional coordinates with unknown coefficients dependent on the axial coordinate. These are then evaluated using a finite element approach. In order to reduce the computational effort, an asymptotic analysis is used to detect and eliminate the degrees of freedom which are not relevant to the problem. Various cross sections have been studied using this method [26] and it was shown that the model was able to satisfactorily predict natural frequencies [23]. Silvestre and Camotim [154, 155] construct a Generalized Beam Theory (GBT) for composite thin-walled beams starting from classical plate theory. The kinematics are developed based on the thin plate assumptions of the Love-Kirchhoff model and the principle of virtual work is used to obtain the final governing equations of the problem. Two models are developed: a first-order theory for geometrically linear analysis and a second-order theory for linear stability analysis by including the appropriate nonlinear terms in the kinematics.

Apart from the research articles mentioned above, there is a plethora of extraordinary research articles concerning the geometrically exact equations pertaining to the 1D beam analysis. Some of the research works that serve as a background or even remotely relate to the work done in this thesis, are mentioned in this section. Reissner [141] was one of the first works to present a large-displacement finite-strain beam theory. The finite rota-

tions in this work were described using Rodrigues rotation parameters. The concept of intrinsic equations was also introduced. Wempner [177], in his work related to mechanics of thin bodies, developed the equations for thin, curved and twisted rods using the principle of virtual work. The 1-D geometrically nonlinear beam equations of Hodges [67] have found application in the mixed-variational formulation of GEBT (Geometrically Exact Beam Theory) [186] which is used to solve the 1-D beam problems in this work. The work by Hodges [67] supersedes the well known research works in the literature on rotating beams i.e. Refs. [71] and [66]. Those 1-D beam equations are also the foundation of the fully intrinsic form used in NATASHA (Nonlinear Aeroelastic Trim and Stability of HALE Aircraft) [130].

Despite the presence of the above-mentioned works, a significant amount of time is being spent by people in industry as well as academia while working to develop or use composite beam theories with *ad hoc* assumptions. A study of the literature over the last few years leads to several developments which are based on assumptions that simply render the theories useless for complex problems. For example, in Ref. [110], the cross section is assumed to be rigid and the out-of-plane warping to be the St. Venant solution for isotropic beams, though the development is for composite materials. The Euler-Bernoulli formula for the deflection of a simply supported beam is used for the analysis of a reinforced concrete beam with carbon fiber reinforced composites [157]. Further usage of the Euler-Bernoulli beam theory is seen in Refs. [29, 89, 178] for studies of vibration suppression in structures with complex deformation phenomena. For micro- and nano-scale structures, Refs. [7, 36, 109, 168] provide solutions based on beam theories with couple-stresses, strain gradients, etc.

1.3 Scope of the Present Work

In this work, unlike many existing beam theories and modeling approaches, the Variational Asymptotic Method (VAM), formulated by Berdichevsky [15], and the Decomposition of

Rotation Tensor (DRT), by Danielson and Hodges [42], are proposed for complex beam-like structures. This allows for a beam-like formulation that is free of ad hoc assumptions. This is a synergistic approach where the computationally inexpensive nature of beam modeling using the VAM is combined with modeling procedures using *sectional* finite elements to obtain reliable models for high-fidelity, multiphysics simulations. The result is a systematic derivation of the cross-sectional constitutive relations and a set of geometrically exact, one-dimensional (1-D) beam equations of motion. Variational Asymptotic Beam Section (VABS) is a computationally efficient yet asymptotically correct tool for the cross-sectional analysis. It has been developed with the objective of capturing the cross-sectional behavior of composite beams. Additionally, it can recover detailed 3-D stress and strain fields for the entire structure using inputs from the 1-D global analysis. The 1-D nonlinear beam analysis can be done using a tool called GEBT based on the mixed formulation of the geometrically exact beam theory.

Through the present work, significant advancements to the overall framework i.e. the cross-sectional analysis and the stress-strain recovery using VABS as well as the capabilities of the 1-D beam analysis using GEBT, are described. The cross-sectional analysis through VABS led to non-physical results while solving initially curved thin-walled beams or beams with thin composite layers. Chapter II contains information on a detailed investigation of these non-physical effects, lists various ways to solve the problem and finally proposes fundamental changes to be implemented in the current formulation. The chapter also evaluates results obtained from thin-walled beam theory against VABS and 3-D FEM. Further, suitable methodologies to implement damping and understand piezoelectric effects have been worked upon and demonstrated in Ch. V. This is done by modifying the underlying theory behind 1-D Geometrically Exact Beam Theory (GEBT). Another methodology for storing and retrieving time histories of stresses and strain through automated high-fidelity stress-strain recovery has been carried out in Ch. VII and compared against 3-D FEM. Apart from this, a methodology has been developed to solve beam-like

structures such as aircraft wings, which have complex 3-D internal geometry with aperiodicity and inhomogeneity. Such a technique facilitates an accurate analysis of aircraft wings which is a daunting, time-consuming task. It is generally considered during detailed design phase and is suitable for an optimization framework. This unique methodology has been demonstrated in Ch. VIII. Finally, a summary of all the accomplishments in this dissertation is present in Ch. IX along with interesting ideas, applications and diverse branches of the 'tree of innovation' where the present work can find suitable applications. Overall, the present additions not only improve the existing features of the tools but also expand the scope of the underlying theory for computationally effective structural analysis.

Part 2

Cross-Sectional Analysis (2-D)

CHAPTER II

VARIATIONAL ASYMPTOTIC METHOD

2.1 Introduction

The entire 3-D analysis for a beam-like structure is summarized in Fig. 2.1. As described in Chapter I, with the help of decomposition of rotation tensor, the overall 3-D analysis is split into two parts, viz. the 2-D cross sectional analysis using VAM and the 1-D beam analysis done using GEBT. This is followed by 3-D recovery where 3-D stresses, strains, and displacements for the beam are obtained. The 2-D sectional analysis requires information on cross-sectional geometry, material properties and information on the initial twist and curvatures, if any. The 6×6 stiffness and mass matrices contain the 1-D sectional elastic and inertia constants obtained from 2-D sectional analysis, for a given cross section. These matrices are used as inputs to GEBT to solve for 1-D displacements variables of the beam reference line. Finally, the 3-D variables are computed using cross-sectional recovery process which uses the 2-D warping solutions from the sectional analysis, the material matrix and the 1-D displacements.

This chapter specifically deals with improvements in the 2-D sectional analysis. In VAM, the strain energy density of a cross section is written in terms of small parameters. These small parameters typically include $b << l$ and $b << R$, where b is a characteristic cross-sectional dimension, l is the wavelength of deformation and R is the radius of curvature/twist. The VAM applies an asymptotic expansion in terms of these small parameters

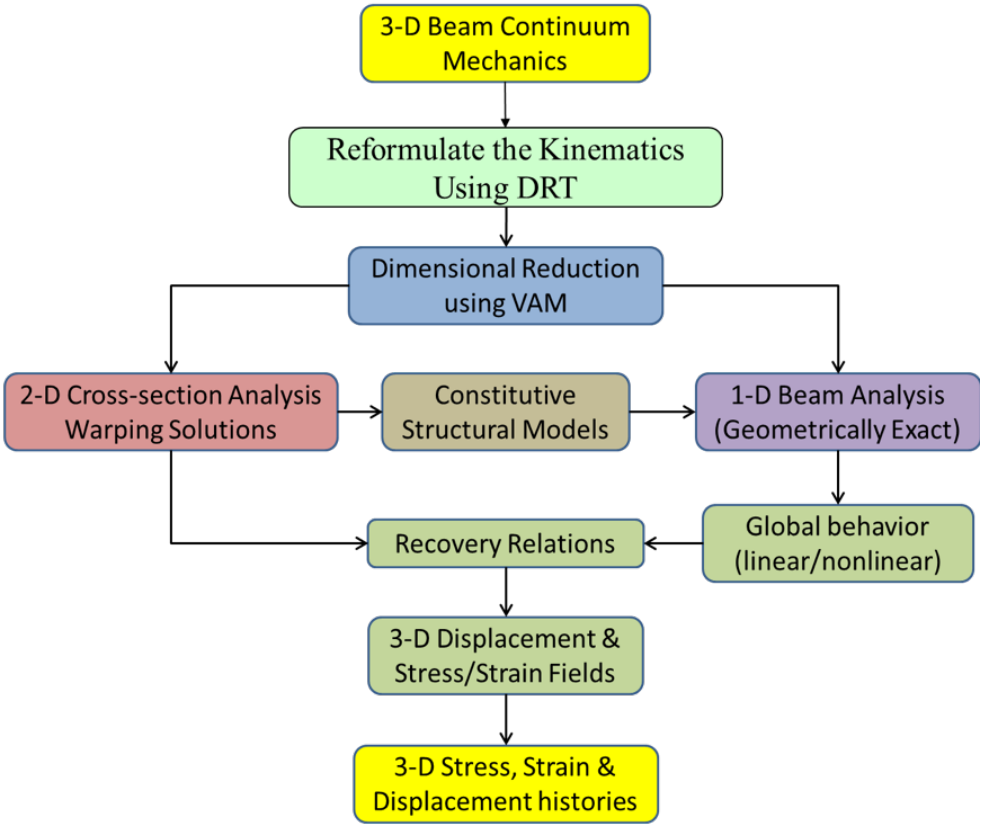

Figure 2.1: Summary of the existing beam analysis procedure

of the energy functional instead of the system of differential equations, thereby making the modeling procedure more compact, less cumbersome, versatile and variationally consistent. This cross-sectional modeling capability was later extended to include refinements such as transverse shear and effects of initial curvature and twist [27, 28, 133, 188]. An update on the variational asymptotic procedure with many such developments was provided by Yu et al. [187] and by Ho [65]. Some recent advancements to the cross-sectional analysis with regards to cross-sectional obliqueness and high-fidelity stress-strain recovery have been made by Rajagopal [138]. VAM has been proven effective and efficient to analyze sections such as strips, initially curved and/or twisted strips, open- and closed-section beams, springs and even initially curved and twisted asymmetric thin-walled, open-section beams in several papers [147, 189, 87, 55]. A comprehensive validation study for a VAM-based beam analysis against 3-D FEA for rotor blades is presented by Chen et al. [34].

These results are sufficient to demonstrate that a VAM based technique can produce results with an accuracy comparable to that of the 3-D FEA while reducing computational effort.

2.2 Beam Kinematics

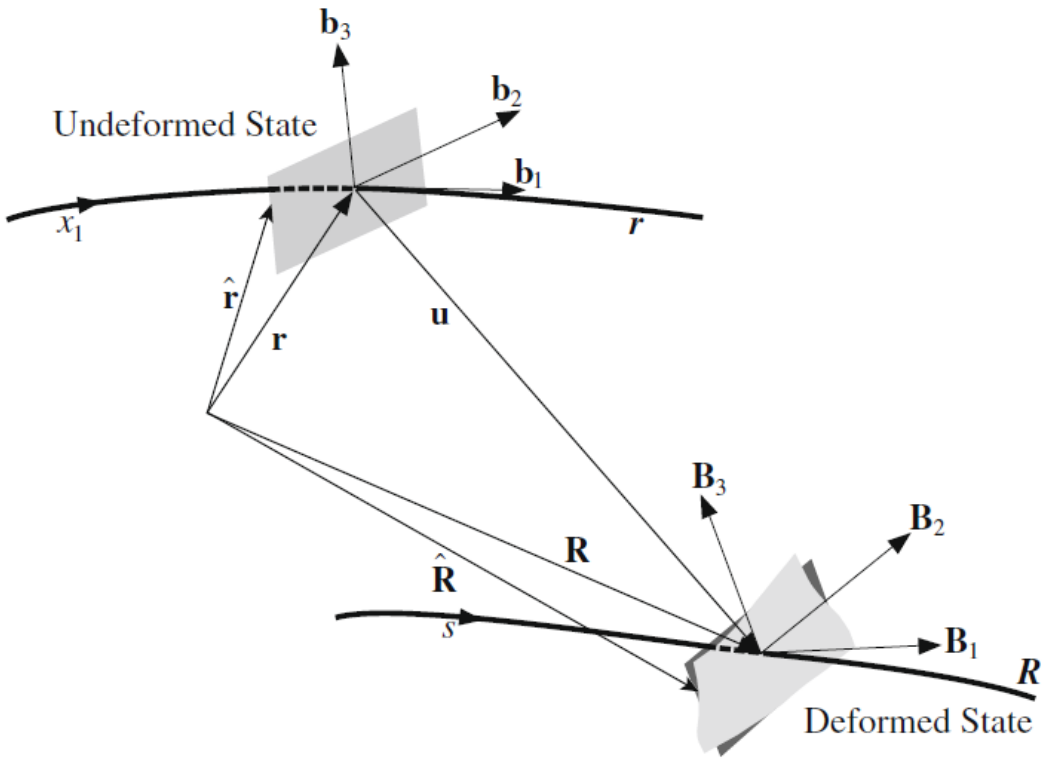

Figure 2.2: Schematic of Beam Deformation

In the present approach, a beam as seen in Figure 2.2, can be represented by a reference line r in the undeformed state and an undeformed reference cross section at x_1. The sectional co-ordinates are x_α, where $\alpha = \{2, 3\}$. The beam undergoes deformation such that the reference line in deformed state is represented by R and the cross section is allowed to warp. To simplify and facilitate the understanding of cross-sectional analysis, the present work neglects the obliqueness of the cross section that may be present in a given beam geometry. The present approach makes use of three coordinate frames (a, b and B) following Hodges [69], with a as a global body-attached frame, b as the undeformed beam reference

frame and B as the deformed beam reference frame. The orthonormal triad of unit vectors $\mathbf{b}_i$ is specified at each point along r, such that, $\mathbf{b}_1(x_1)$ always remains tangential to the undeformed reference curve. The position vector of any point in the undeformed beam $\hat{\mathbf{r}}$ is given as

$$\hat{\mathbf{r}}(x_1, x_2, x_3) = \mathbf{r}(x_1) + x_\alpha \mathbf{b}_\alpha(x_1) \tag{2.1}$$

where $\mathbf{r}$ is the position vector of the points along the reference line. After deformation, the particle that had position vector $\hat{\mathbf{r}}$ in the undeformed state now has the position vector $\hat{\mathbf{R}}$ in the deformed state. Another orthonormal triad $\mathbf{B}_i$ for deformed configuration are specified at each point along $\mathbf{R}$ which is related to $\mathbf{b}_i$ as $\mathbf{B}_i = C_{ij}^{Bb}\mathbf{b}_j = C_{ij}\mathbf{b}_j$. The position vector of an arbitrary point in the deformed state denoted by $\hat{\mathbf{R}}(x_1, x_2, x_3)$ can now be expressed as

$$\hat{\mathbf{R}}(x_1, x_2, x_3) = \mathbf{R}(x_1) + x_\alpha \mathbf{B}_\alpha(x_1) + w_i(x_1, x_2, x_3)\mathbf{B}_i(x_1) \tag{2.2}$$

where the functions w_i are the warping displacements, subject to constraints

$$\begin{aligned} \langle w_i(x_1, x_2, x_3)\rangle &= 0 \\ \langle w_{2,3}(x_1, x_2, x_3) - w_{3,2}(x_1, x_2, x_3)\rangle &= 0 \end{aligned} \tag{2.3}$$

for unique warping solutions, where

$$\langle\cdot\rangle = \int_{-\frac{b}{2}}^{\frac{b}{2}} \int_{-\frac{h}{2}}^{\frac{h}{2}} (\cdot)\, dx_2 dx_3$$

Using the decomposition of rotation tensor [42], the Jaumann-Biot-Cauchy strain tensor can be expressed as

$$\Gamma_{ij} = \frac{1}{2}(\chi_{ij} + \chi_{ji}) - \delta_{ij} \tag{2.4}$$

where δ_{ij} is the Kronecker symbol, and χ_{ij} is the mixed-basis component of the deforma-

tion gradient tensor, defined by Ogden (Ref. [126]), such that

$$\chi_{ij} = \mathbf{B}_i \cdot \mathbf{G}_k \mathbf{g}^k \cdot \mathbf{b}_j \tag{2.5}$$

with $\mathbf{G}_k$ as the covariant base vectors of the deformed configuration and $\mathbf{g}^k$ as the contravariant base vectors of the undeformed configuration, which are tangent to the coordinate curves. The covariant base vectors of the undeformed configuration can be obtained from beam kinematics as

$$\begin{gathered} \mathbf{g}_1 = \mathbf{b}_1 + x_\alpha \mathbf{b}'_\alpha = (1 - x_2 k_3 + x_3 k_2)\mathbf{b}_1 - k_1 x_3 \mathbf{b}_2 + x_2 k_1 \mathbf{b}_3, \\ \mathbf{g}_\alpha = \mathbf{b}_\alpha \end{gathered} \tag{2.6}$$

where $\alpha = \{2, 3\}$. The contravariant base vectors of the undeformed configuration, which are normal to the coordinate curves are described by Wempner [177] as

$$\mathbf{g}^i = \frac{1}{2\sqrt{g}} e_{ijk}(\mathbf{g}_j \times \mathbf{g}_k) \tag{2.7}$$

where

$$g = \det \begin{bmatrix} \mathbf{g}_1 \cdot \mathbf{g}_1 & \mathbf{g}_1 \cdot \mathbf{g}_2 & \mathbf{g}_1 \cdot \mathbf{g}_3 \\ \mathbf{g}_2 \cdot \mathbf{g}_1 & \mathbf{g}_2 \cdot \mathbf{g}_2 & \mathbf{g}_2 \cdot \mathbf{g}_3 \\ \mathbf{g}_3 \cdot \mathbf{g}_1 & \mathbf{g}_3 \cdot \mathbf{g}_2 & \mathbf{g}_3 \cdot \mathbf{g}_3 \end{bmatrix} = \det(\mathbf{g}_i \cdot \mathbf{g}_j) \tag{2.8}$$

Further evaluation of the expression above yields

$$\sqrt{g} = \underbrace{1}_{g_0} - \underbrace{x_2 k_3 + x_3 k_2}_{g_1} = g_0 + g_1 \tag{2.9}$$

The categorization of the terms in Eq. (2.9) is done based on the order of the terms involved. For example, $g_0 = \mathcal{O}(\epsilon^0)$, zeroth order in strain, subsequently, $g_i = \mathcal{O}(\epsilon^i)$, where i is a non-

negative integer. The inverse of $\sqrt{g}$ can be expanded using Taylor series

$$\begin{aligned}\frac{1}{\sqrt{g}} =& \frac{1}{1 - x_2 k_3 + x_3 k_2} \\ =& 1 + (x_2 k_3 - x_3 k_2) + (x_2 k_3 - x_3 k_2)^2 + O(k_i^3) \\ =& g_0 + g_1 + g_2 + O(k_i^3)\end{aligned} \tag{2.10}$$

This equation was expanded up through the linear term by Yu et al. [187]. But Rajagopal [139] demonstrated the need for expansion up through the quadratic term for an asymptotically correct expansion of the strain energy in problems involving initial curvature. Further, it is shown in [138] that this term needs to be expanded up through the fourth order in curvatures for a 3-D recovery of higher fidelity as described in Sec. 7.1. So, Eq. (2.10) now becomes

$$\begin{aligned}\frac{1}{\sqrt{g}} =& 1 + (x_2 k_3 - x_3 k_2) + (x_2 k_3 - x_3 k_2)^2 + (x_2 k_3 - x_3 k_2)^3 + (x_2 k_3 - x_3 k_2)^4 + O(k_i^5) \\ =& g_0 + g_1 + g_2 + g_3 + g_4 + O(k_i^5)\end{aligned} \tag{2.11}$$

Further, the 1D generalized strain measures can be defined in the intrinsic form as

$$\boldsymbol{\gamma} = \boldsymbol{C}^{bB} \cdot \mathbf{R}' - \mathbf{r}' \tag{2.12a}$$

$$\boldsymbol{\kappa} = \boldsymbol{C}^{bB} \cdot \boldsymbol{K} - \boldsymbol{k} \tag{2.12b}$$

where the $\boldsymbol{C}$ quantities are rotation tensors, $\boldsymbol{K}$ is the curvature vector of the deformed beam reference line, $\boldsymbol{k}$ is the curvature vector of the undeformed beam reference line, γ_{11} is the extensional strain, κ_1 is the elastic twist, κ_2 and κ_3 are the elastic bending curvatures. These quantities represent the kinematics of the beam deformation and are the same as whether

the beam is thin-walled or not. Furthermore, $\boldsymbol{K}$ and $\boldsymbol{k}$ can be written as:

$$\widetilde{\boldsymbol{K}} = (\boldsymbol{C}^{BA})' \cdot \boldsymbol{C}^{AB} \tag{2.13a}$$

$$\widetilde{\boldsymbol{k}} = (\boldsymbol{C}^{bA})' \cdot \boldsymbol{C}^{Ab} \tag{2.13b}$$

From Eqs. (2.12) and (2.13), the generalized strain displacement relations [68] can be obtained as

$$\gamma = C(e_1 + u' + \widetilde{k}u) - e_1 \tag{2.14a}$$

$$\widetilde{K} = -C'C^T + C\widetilde{k}C^T \tag{2.14b}$$

where $\kappa = K - k$, $k = \lfloor\, k_1 \; k_2 \; k_3 \,\rfloor^T$, $e_1 = \lfloor\, 1 \; 0 \; 0 \,\rfloor^T$ and C is the transformation matrix based on Wiener-Milenković rotation parameters. Also, it is to be noted that $C^{Ba} = C^{ba}C$.

2.3 Mathematical Formulation

The behavior of beams is governed by the extended Hamilton's Principle as shown

$$\int_{t_1}^{t_2} [\delta(\mathcal{K} - \mathcal{U}) + \overline{\delta\mathcal{W}}]dt = 0 \tag{2.15}$$

where t_1 and t_2 are arbitrary fixed times, $\mathcal{K}$ is the kinetic energy, $\mathcal{U}$ is the strain energy, δ is the Lagrangian variation for a fixed time, and $\overline{\delta\mathcal{W}}$ is the virtual work by applied loads. Here the bar on $\delta\mathcal{W}$ indicates that it is a single quantity and not the variation of a functional $\mathcal{W}$. Strain energy is written as

$$\mathcal{U} = \int_0^L \langle\langle \sigma^T \Gamma \rangle\rangle dx_1 \tag{2.16a}$$

$$\langle\langle \bullet \rangle\rangle = \langle \bullet \sqrt{g} \rangle \tag{2.16b}$$

assuming that the material is linearly elastic and thus satisfies Hooke's law

$$\sigma = \mathcal{D}\Gamma \tag{2.17}$$

where Γ is the 3-D strain and is written as $\Gamma = \begin{bmatrix} \Gamma_{11} & 2\Gamma_{12} & 2\Gamma_{13} & \Gamma_{22} & 2\Gamma_{23} & \Gamma_{33} \end{bmatrix}^T$. Here, x_i represents the beam coordinate frame such that the unit vector x_1 points along the span of the beam and x_2, x_3 are corresponding cross-sectional coordinates for the cross section. Warping functions are assumed to be of the order of the strain with assumption of small local rotations. Thus, the product of warping and 1-D generalized strains may be neglected and the 3-D strain field can be written as

$$\Gamma = \Gamma_a w + \Gamma_\epsilon \bar{\epsilon} + \Gamma_R w + \Gamma_\ell w' \tag{2.18}$$

where Γ_a is a 6×3 matrix, sparsely populated with operators of derivatives with respect to the cross-sectional coordinates as described in Eq. (2.19). The other symbols (i.e., Γ_e, Γ_R and Γ_ℓ) are defined in Eqs. (2.20), (2.21) and (2.22) respectively. These symbols in Eq. (2.18) are further defined and derived in Ref. [69].

$$\Gamma_a = \begin{bmatrix} 0 & 0 & 0 \\ \frac{\partial}{\partial x_2} & 0 & 0 \\ \frac{\partial}{\partial x_3} & 0 & 0 \\ 0 & \frac{\partial}{\partial x_2} & 0 \\ 0 & \frac{\partial}{\partial x_3} & \frac{\partial}{\partial x_2} \\ 0 & 0 & \frac{\partial}{\partial x_3} \end{bmatrix} \tag{2.19}$$

$$\Gamma_\epsilon = \frac{1}{\sqrt{g}} \begin{bmatrix} 1 & 0 & x_3 & -x_2 \\ 0 & -x_3 & 0 & 0 \\ 0 & x_2 & 0 & 0 \\ 0 & 0 & 0 & 0 \\ 0 & 0 & 0 & 0 \\ 0 & 0 & 0 & 0 \end{bmatrix} = \frac{1}{\sqrt{g}} \overline{\Gamma}_\epsilon = \sum_{i=0}^{4} g_i \overline{\Gamma}_\epsilon \tag{2.20}$$

$$\Gamma_\ell = \frac{1}{\sqrt{g}} \begin{bmatrix} 1 & 0 & 0 \\ 0 & 1 & 0 \\ 0 & 0 & 1 \\ 0 & 0 & 0 \\ 0 & 0 & 0 \\ 0 & 0 & 0 \end{bmatrix} = \frac{1}{\sqrt{g}} \overline{\Gamma}_\ell = \sum_{i=0}^{3} g_i \overline{\Gamma}_\ell \tag{2.21}$$

$$\Gamma_R = \frac{1}{\sqrt{g}} \begin{bmatrix} \Gamma_{hR} & -k_3 & k_2 \\ k_3 & \Gamma_{hR} & -k_1 \\ -k_2 & k_1 & \Gamma_{hR} \\ 0 & 0 & 0 \\ 0 & 0 & 0 \\ 0 & 0 & 0 \end{bmatrix} = \frac{1}{\sqrt{g}} \overline{\Gamma}_R = \sum_{i=0}^{3} g_i \overline{\Gamma}_R \tag{2.22}$$

where

$$\Gamma_{hR} = k_1 \left(x_3 \frac{\partial}{\partial x_2} - x_2 \frac{\partial}{\partial x_3} \right) \tag{2.23}$$

A detailed derivation of the 3-D strains and the expressions for strain energy density (strain energy per unit length) is presented in Ref. [69]. The derivation was updated by Yu et al. [187]. Further, to do the dimensional reduction, one must rely on the inherent small parameters that are generally present in a beam geometry. Denoting the characteristic radius of initial curvature or twist by R, the two small geometric parameters are b/l and b/R. Also, there can be additional small parameters associated with the beam problem depending on the beam geometry and material properties which are discussed in Sec. IV. Therefore, using the finite element discretization of the warping field [69]

$$\begin{aligned} w\left(x_1, x_2, x_3\right) &= S\left(x_2, x_3\right) V\left(x_1\right) \\ w &= \lfloor w_1 \quad w_2 \quad w_3 \rfloor^T \end{aligned} \tag{2.24}$$

where $S(x_2, x_3)$ are the finite-element shape functions, the expression for the strain energy from Eq. (2.16) can be rewritten as

$$\begin{aligned} 2U =& V^T E V + 2V^T(D_{a\epsilon}\overline{\epsilon} + D_{aR}V + D_{a\ell}V') + \overline{\epsilon}^T D_{\epsilon\epsilon}\overline{\epsilon} + V^T D_{RR} V \\ &+ V'^T D_{\ell\ell} V' + 2V^T D_{R\epsilon}\overline{\epsilon} + 2V'^T D_{\ell\epsilon}\overline{\epsilon} + 2V^T D_{R\ell} V' \end{aligned} \tag{2.25}$$

The matrices in the above equation are defined carefully with the order of magnitude written in subscript as

$$\begin{aligned} D_{a\epsilon} &= \langle (\Gamma_a S)^T D \overline{\Gamma}_\ell S \rangle \\ &= \langle (\Gamma_a S)^T D \overline{\Gamma}_\epsilon \rangle \end{aligned} \tag{2.26}$$

$$D_{aR} = \langle (\Gamma_a S)^T D \overline{\Gamma}_R S \rangle \tag{2.27}$$

$$D_{a\ell} = \langle (\Gamma_a S)^T D \overline{\Gamma}_\ell S \rangle \tag{2.28}$$

$$
\begin{aligned}
D_{\epsilon\epsilon} &= \langle\langle \Gamma_\epsilon^T D\Gamma_\epsilon \rangle\rangle \\
&= \langle \frac{1}{\sqrt{g}} \overline{\Gamma}_\epsilon^T D\overline{\Gamma}_\epsilon \rangle \\
&= \langle g_0 \overline{\Gamma}_\epsilon^T D\overline{\Gamma}_\epsilon \rangle + \langle g_1 \overline{\Gamma}_\epsilon^T D\overline{\Gamma}_\epsilon \rangle + \langle g_2 \overline{\Gamma}_\epsilon^T D\overline{\Gamma}_\epsilon \rangle \\
&\qquad + \langle g_3 \overline{\Gamma}_\epsilon^T D\overline{\Gamma}_\epsilon \rangle + \langle g_4 \overline{\Gamma}_\epsilon^T D\overline{\Gamma}_\epsilon \rangle \\
&= D_{\epsilon\epsilon_0} + D_{\epsilon\epsilon_1} + D_{\epsilon\epsilon_2} + D_{\epsilon\epsilon_3} + D_{\epsilon\epsilon_4}
\end{aligned}
\tag{2.29}
$$

$$
\begin{aligned}
D_{RR} &= \langle\langle (\Gamma_R S)^T D\Gamma_R S \rangle\rangle \\
&= \langle \frac{1}{\sqrt{g}} (\overline{\Gamma}_R S)^T D\overline{\Gamma}_R S \rangle \\
&= \langle g_0 (\overline{\Gamma}_R S)^T D\overline{\Gamma}_R S \rangle + \langle g_1 (\overline{\Gamma}_R S)^T D\overline{\Gamma}_R S \rangle + \langle g_2 (\overline{\Gamma}_R S)^T D\overline{\Gamma}_R S \rangle \\
&= D_{RR_2} + D_{RR_3} + D_{RR_4}
\end{aligned}
\tag{2.30}
$$

$$
\begin{aligned}
D_{\ell\ell} &= \langle\langle (\Gamma_\ell S)^T D\Gamma_\ell S \rangle\rangle \\
&= \langle \frac{1}{\sqrt{g}} (\overline{\Gamma}_\ell S)^T D\overline{\Gamma}_\ell S \rangle \\
&= \langle g_0 (\overline{\Gamma}_\ell S)^T D\overline{\Gamma}_\ell S \rangle + \langle g_1 (\overline{\Gamma}_\ell S)^T D\overline{\Gamma}_\ell S \rangle + \langle g_2 (\overline{\Gamma}_\ell S)^T D\overline{\Gamma}_\ell S \rangle \\
&= D_{\ell\ell_2} + D_{\ell\ell_3} + D_{\ell\ell_4}
\end{aligned}
\tag{2.31}
$$

$$
\begin{aligned}
D_{R\epsilon} &= \langle\langle (\Gamma_R S)^T D\Gamma_\epsilon \rangle\rangle \\
&= \langle \frac{1}{\sqrt{g}} (\overline{\Gamma}_R S)^T D\overline{\Gamma}_\epsilon \rangle \\
&= \langle g_0 (\overline{\Gamma}_R S)^T D\overline{\Gamma}_\epsilon \rangle + \langle g_1 (\overline{\Gamma}_R S)^T D\overline{\Gamma}_\epsilon \rangle + \langle g_2 (\overline{\Gamma}_R S)^T D\overline{\Gamma}_\epsilon \rangle + \langle g_3 (\overline{\Gamma}_R S)^T D\overline{\Gamma}_\epsilon \rangle \\
&= D_{R\epsilon_1} + D_{R\epsilon_2} + D_{R\epsilon_3} + D_{R\epsilon_4} \\
D_{R\epsilon_{i+1}} &= \langle g_i (\overline{\Gamma}_R S)^T D\overline{\Gamma}_\epsilon \rangle
\end{aligned}
\tag{2.32}
$$

$$
\begin{aligned}
D_{\ell\epsilon} &= \langle\langle (\Gamma_\ell S)^T D\Gamma_\epsilon \rangle\rangle \\
&= \langle \frac{1}{\sqrt{g}} (\overline{\Gamma}_\ell S)^T D\overline{\Gamma}_\epsilon \rangle \\
&= \langle g_0 (\overline{\Gamma}_\ell S)^T D\overline{\Gamma}_\epsilon \rangle + \langle g_1 (\overline{\Gamma}_\ell S)^T D\overline{\Gamma}_\epsilon \rangle + \langle g_2 (\overline{\Gamma}_\ell S)^T D\overline{\Gamma}_\epsilon \rangle + \langle g_3 (\overline{\Gamma}_\ell S)^T D\overline{\Gamma}_\epsilon \rangle \\
&= D_{\ell\epsilon_1} + D_{\ell\epsilon_2} + D_{\ell\epsilon_3} + D_{\ell\epsilon_4}
\end{aligned}
\tag{2.33}
$$

$$
\begin{aligned}
D_{R\ell} &= \langle\langle (\Gamma_R S)^T D\Gamma_\ell S \rangle\rangle \\
&= \langle \frac{1}{\sqrt{g}} (\overline{\Gamma}_R S)^T D\overline{\Gamma}_\ell S \rangle \\
&= \langle g_0 (\overline{\Gamma}_R S)^T D\overline{\Gamma}_\ell \rangle + \langle g_1 (\overline{\Gamma}_R S)^T D\overline{\Gamma}_\ell \rangle + \langle g_2 (\overline{\Gamma}_R S)^T D\overline{\Gamma}_\ell \rangle \\
&= D_{R\ell_2} + D_{R\ell_3} + D_{R\ell_4}
\end{aligned}
\tag{2.34}
$$

and finally,

$$\begin{aligned} E =& \langle\langle (\Gamma_a S)^T D \Gamma_a S \rangle\rangle \\ =& \langle (\Gamma_a S)^T D (\Gamma_a S) \sqrt{g} \rangle \\ =& \underbrace{\langle (\Gamma_a S)^T D \Gamma_a S g_0 \rangle}_{E_0} + \underbrace{\langle (\Gamma_a S)^T D \Gamma_a S g_1 \rangle}_{E_1} \\ =& E_0 + E_1 \end{aligned} \tag{2.35}$$

After substituting the values obtained above in Eq. (2.25), the total strain energy that is to be considered is therefore

$$\begin{aligned} 2U =& (V_0 + V_1 + V_2)^T (E_0 + E_1)(V_0 + V_1 + V_2) \\ &+ 2(V_0 + V_1 + V_2)^T (D_{a\epsilon}) \overline{\epsilon} \\ &+ 2(V_0 + V_1 + V_2)^T (D_{aR})(V_0 + V_1 + V_2) \\ &+ 2(V_0 + V_1 + V_2)^T (D_{a\ell})(V_0' + V_1' + V_2') \\ &+ \overline{\epsilon}^T (D_{\epsilon\epsilon_0} + D_{\epsilon\epsilon_1} + D_{\epsilon\epsilon_2} + D_{\epsilon\epsilon_3} + D_{\epsilon\epsilon_4}) \overline{\epsilon} \\ &+ (V_0 + V_1 + V_2)^T (D_{RR_2} + D_{RR_3} + D_{RR_4})(V_0 + V_1 + V_2) \\ &+ (V_0' + V_1' + V_2')^T (D_{\ell\ell_2} + D_{\ell\ell_3} + D_{\ell\ell_4})(V_0' + V_1' + V_2') \\ &+ 2(V_0 + V_1 + V_2)^T (D_{R\epsilon_1} + D_{R\epsilon_2} + D_{R\epsilon_3} + D_{R\epsilon_4}) \overline{\epsilon} \\ &+ 2(V_0' + V_1' + V_2')^T (D_{\ell\epsilon_1} + D_{\ell\epsilon_2} + D_{\ell\epsilon_3} + D_{\ell\epsilon_4}) \overline{\epsilon} \\ &+ 2(V_0 + V_1 + V_2)^T (D_{R\ell_2} + D_{R\ell_3} + D_{R\ell_4})(V_0' + V_1' + V_2') \end{aligned} \tag{2.36}$$

The terms are now split into orders for the asymptotic analysis. There are two important observations to be noted. First, the definitions of the symbols are such that the order of any symbol is the sum of all the numbers that appear as subscripts in that symbol. Second, the order of magnitude separation of terms in the strain energy expression, Eq. (2.36) is done by considering only the terms of different orders in 3-D strain given by Eq. (2.18). This can potentially cause an issue in determining correct orders of terms in the strain

energy expression as each term in that expression contains contribution from the kinematic variables and material properties. If the multiplication of 3-D strain expression with the material properties in Eq. (2.16) results in a changed order of magnitudes for the same terms characterized in Eq. (2.36), then there is a chance that some terms being eliminated from the strain energy expression at a particular order, are not higher order terms and ought to be retained. More details on this observation are provided in Sec. 4.2. While minimizing the strain energy, one needs to also consider the constraints due to warping mentioned in Eq. (2.3) which are represented in terms of discretized warping variables as

$$V^T D_c = 0 \tag{2.37}$$

The kernel of Γ_a, ψ, from Hodges [69] can be used during the development such that

$$\begin{aligned} \Gamma_a \psi = 0 \implies E_0 \Psi = 0 \\ \psi = S\Psi \end{aligned} \tag{2.38}$$

2.3.1 Zeroth-Order Analysis

From Eq. (2.36), the zeroth-order energy can be obtained as

$$2U_0 = V_0^T E_0 V_0 + 2V_0^T D_{a\epsilon} \bar{\epsilon} + \bar{\epsilon}^T D_{\epsilon\epsilon_0} \bar{\epsilon} \tag{2.39}$$

Keeping track of the warping constraints, the final equation for zeroth-order warping is therefore

$$E_0 V_0 + D_{a\epsilon} \bar{\epsilon} = 0 \tag{2.40}$$

After considering singularities of E_0 [69], the final solution is

$$V_0 = \hat{V}_0 \bar{\epsilon} \tag{2.41}$$

2.3.2 First-Order Analysis

The warping is now perturbed and substituted back in the strain energy. Now, the relevant terms in the strain energy are those through second-order. However, after the substitution of the zeroth-order warping solutions in the strain energy expression, the zeroth-order strain energy is a constant and does not feature in the first-order warping calculation. So, the expression for strain energy after removing the zeroth-order terms can be written as

$$\begin{aligned} 2U_1 =& \bar{\epsilon}^T D_{\epsilon\epsilon_1} \bar{\epsilon} + (V_0'^T D_{\ell\epsilon_1} + V_0^T D_{R\epsilon_1})\bar{\epsilon} \\ &+ 2V_0^T D_{aR_1} V_0 + \cancel{V_1^T E_0 V_0} + V_0^T E_1 V_0 + \cancel{V_0^T E_0 V_1} + 2V_0^T D_{a\ell_1} V_0' \end{aligned} \tag{2.42}$$

Further, the second-order terms in the strain energy can be combined and written in the following expression as

$$\begin{aligned} 2U_2 =& \bar{\epsilon} D_{\epsilon\epsilon_2} \bar{\epsilon} + (\cancel{2V_2^T D_{a\epsilon}} + 2V_1'^T D_{\ell\epsilon_1} + 2V_0'^T D_{\ell\epsilon_2} + 2V_1^T D_{R\epsilon_1} + 2V_0^T D_{R\epsilon_2})\bar{\epsilon} \\ &+ 2V_1^T D_{aR_1} V_0 + V_0^T D_{RR_2} V_0 + \cancel{V_2^T E_0 V_0} + V_1^T E_1 V_0 + 2V_0^T D_{aR} V_1 \\ &+ V_1^T E_0 V_1 + V_0^T E_1 V_1 + \cancel{V_0^T E_0 V_2} + 2V_1^T D_{a\ell} V_0' \\ &+ 2V_0^T D_{R\ell_2} V_0' + 2V_0^T D_{a\ell} V_1' \end{aligned} \tag{2.43}$$

The canceled terms in the above two equations are results of Eq. (2.40). As expected the second-order warping plays no part in the second-order strain energy (a fact stated in Ref. [185]). After considerations of the warping constraints, the final equation for V_1 is

$$\begin{aligned} E_0 V_1 =& (D_c(\Psi^T D_c)^{-1}\Psi^T - \Delta)(D_R \bar{\epsilon} + D_S \bar{\epsilon}') \\ D_R =& E_1 \hat{V}_0 + (D_{aR} + D_{aR}^T)\hat{V}_0 + D_{R\epsilon_1} \\ D_S =& (D_{a\ell} - D_{a\ell}^T)\hat{V}_0 - D_{\ell\epsilon_1} \end{aligned} \tag{2.44}$$

The solution after removing the singularities of E_0 may be written as

$$V_1 = V_{1R}\overline{\epsilon} + V_{1S}\overline{\epsilon}' \tag{2.45}$$

Only the terms related with V_1 are relevant in the process of the minimization of the strain energy. After performing integration by parts with respect to x_1 to get rid of the derivatives of V_1, the relevant terms are

$$\begin{aligned}
\mathcal{F} =& V_1^T E_0 V_1 + 2V_1^T(E_1 V_0 + D_{a\epsilon_1}\overline{\epsilon} + (D_{aR} + D_{aR}^T)V_0 + D_{R\epsilon_1}\overline{\epsilon}) \\
&+ 2V_1^T((D_{a\ell} - D_{a\ell}^T)V_0' - D_{\ell\epsilon_1}\overline{\epsilon}') \\
=& V_1^T E_0 V_1 + 2V_1^T(E_1\hat{V}_0 + (D_{aR} + D_{aR}^T)\hat{V}_0 + D_{R\epsilon_1})\overline{\epsilon} \\
&+ 2V_1^T((D_{a\ell} - D_{a\ell}^T)\hat{V}_0 - D_{\ell\epsilon_1})\overline{\epsilon}' \\
=& V_1^T E_0 V_1 + 2V_1^T D_R\overline{\epsilon} + 2V_1^T D_S\overline{\epsilon}'
\end{aligned} \tag{2.46}$$

Keeping the constraints in mind, one can use the standard procedure of the calculus of variations to solve for the warping field. Hence

$$\begin{aligned}
E_0 V_1 =& (D_c(\Psi^T D_c)^{-1}\Psi^T - \Delta)(D_R\overline{\epsilon} + D_S\overline{\epsilon}') \\
V_1 =& V_{1R}\overline{\epsilon} + V_{1S}\overline{\epsilon}'
\end{aligned} \tag{2.47}$$

where Ψ is the kernel matrix for E_0 and D_c is the constraint matrix associated with warping (i.e., $E_0\Psi = 0$ and $V^T D_c = 0$, respectively). Using this, we may now obtain the second-order asymptotically correct strain energy as

$$2U = \overline{\epsilon}^T A\overline{\epsilon} + 2\overline{\epsilon}^T B\overline{\epsilon}' + \overline{\epsilon}'^T C\overline{\epsilon}' + 2\overline{\epsilon}^T D\overline{\epsilon}'' \tag{2.48}$$

The matrices in the above equation are defined as

$$\begin{aligned}
A =& \hat{V_0}^T D_{a\epsilon} + D_{\epsilon\epsilon_0} + \hat{V_0}^T E_1 \hat{V}_0 + 2\hat{V_0}^T D_{aR_1}\hat{V}_0 + D_{\epsilon\epsilon_1} + 2\hat{V_0}^T D_{R\epsilon_1} \\
& + D_{\epsilon\epsilon_2} + \hat{V_0}^T D_{RR_2}\hat{V}_0 + 2\hat{V_0}^T D_{R\epsilon_2} + V_{1R}^T \overline{D}_R \\
B =& \hat{V_0}^T D_{a\ell_1}\hat{V}_0 + D_{\ell\epsilon_1}^T \hat{V}_0 + D_{\ell\epsilon_2}^T \hat{V}_0 + \hat{V_0}^T D_{R\ell_2}\hat{V}_0 + \frac{1}{2}(V_{1R}^T \overline{D}_S + D_R^T V_{1S}) \\
& + (\hat{V_0}^T D_{a\ell_1} + D_{\ell\epsilon_1}^T) V_{1R} \\
C =& \hat{V_0}^T D_{\ell\ell_2}\hat{V}_0 + V_{1S}^T \overline{D}_S \\
D =& (\hat{V_0}^T D_{a\ell} + D_{\ell\epsilon_1}^T) V_{1S}
\end{aligned} \tag{2.49}$$

where

$$\begin{aligned}
\overline{D}_R =& (D_c(\Psi^T D_c)^{-1}\Psi^T + \Delta) D_R \\
\overline{D}_S =& (D_{a\ell} + D_{a\ell}^T)\hat{V}_0 + D_{\ell\epsilon_1}
\end{aligned} \tag{2.50}$$

To summarize the minimization process, the strain energy functional thus formed in Eq. (2.36) is minimized with respect to the warping functions and the warping solutions are further perturbed to obtain asymptotically correct second order approximations of the strain energy, Eq. (2.48), respectively. The Generalized Timoshenko (GT) transformation now follows as that given in Ref. [64] and [65] to convert Eq. (2.48) into the following form

$$2U = \epsilon^T X \epsilon + 2\epsilon^T Y \gamma_s + \gamma_s^T G \gamma_s \tag{2.51}$$

where X, Y and G are unknowns to be found to fit Eq. (2.48) in the GT (i.e. shear deformable) model, Eq. (2.51). Here matrices X, Y, and G are of the size 4×4, 4×4, and 2×2, respectively. The transformation procedure involves applying 1-D kinematic equations, constitutive law, and static equilibrium equations. The result is a system of nonlinear algebraic equations with unknowns consisting of stiffness matrices X, Y, and G. Because the strain energy, Eq. (2.51) is a quadratic form involving generalized strain measures, one

obtains a physically linear one-dimensional model. The cross-sectional stress resultants are linear in the 1-D generalized strains and can be written in the form

$$\begin{Bmatrix} F_1 \\ F_2 \\ F_3 \\ M_1 \\ M_2 \\ M_3 \end{Bmatrix} = \begin{bmatrix} X & Y \\ Y^T & G \end{bmatrix} \begin{Bmatrix} \epsilon \\ \gamma_s \end{Bmatrix} \tag{2.52}$$

After rearranging the terms in the equation above, one obtains a 1-D constitutive law relating the 1-D generalized resultant forces on the beam cross section to the 1-D generalized strains as

$$\begin{Bmatrix} F_1 \\ F_2 \\ F_3 \\ M_1 \\ M_2 \\ M_3 \end{Bmatrix} = \underbrace{\begin{bmatrix} S_{11} & S_{12} & S_{13} & S_{14} & S_{15} & S_{16} \\ S_{21} & S_{22} & S_{23} & S_{24} & S_{25} & S_{26} \\ S_{31} & S_{32} & S_{33} & S_{34} & S_{35} & S_{36} \\ S_{41} & S_{42} & S_{43} & S_{44} & S_{45} & S_{46} \\ S_{51} & S_{52} & S_{53} & S_{54} & S_{55} & S_{56} \\ S_{61} & S_{62} & S_{63} & S_{64} & S_{65} & S_{66} \end{bmatrix}}_{S} \begin{Bmatrix} \gamma_{11} \\ 2\gamma_{12} \\ 2\gamma_{13} \\ \kappa_1 \\ \kappa_2 \\ \kappa_3 \end{Bmatrix} \tag{2.53}$$

where S is the 6×6 sectional stiffness matrix. The Eq. (2.53) can be written in a condensed form as

$$\begin{Bmatrix} F \\ M \end{Bmatrix} = \begin{bmatrix} A & B \\ B^T & D \end{bmatrix} \begin{Bmatrix} \gamma \\ \kappa \end{Bmatrix} \tag{2.54}$$

where A,B and D are the 3× sub-matrices of the stiffness matrix S and have no relation with the matrices used in laminate theory. $F = \begin{bmatrix} F_1 & F_2 & F_3 \end{bmatrix}^T$, $M = \begin{bmatrix} M_1 & M_2 & M_3 \end{bmatrix}^T$, $\gamma = \begin{bmatrix} \gamma_{11} & 2\gamma_{12} & 2\gamma_{13} \end{bmatrix}^T$ and $\kappa = \begin{bmatrix} \kappa_1 & \kappa_2 & \kappa_3 \end{bmatrix}^T$ as shown. Apart from this, one also obtains the 6×6 inertia matrix $[I]$ from the cross-sectional analysis as part of the Eq. (2.55) which is written

as

$$\left\{ \begin{array}{c} P \\ H \end{array} \right\} = [I] \left\{ \begin{array}{c} V \\ \Omega \end{array} \right\} \tag{2.55}$$

CHAPTER III

THIN-WALLED BEAM THEORY

Thin-walled structures consist of thin-walled beams, plates, and shells. The aerospace industry led the evolution in the design of thin-walled structures followed by other industries in order to reduce weight for similar or higher load-bearing capacity. In general, beams have one dimension much larger than the other two dimensions, commonly referred to as cross-sectional dimensions. Some of the examples in the aviation industry are the high aspect-ratio wings or rotor blades. In the case of a thin-walled beam, all the three dimensions are significantly different from each other by at least an order of magnitude. For example, the length of a thin-walled beam is termed as the largest dimension in the geometry and the wall thickness is the smallest, with the characteristic dimension of the cross section in between. Such thin-walled beams can be analyzed in multiple ways. The thin-walled beam theory presented by Bauchau and Craig in Ref. [13] is popular and is being widely used for engineering applications. It makes an assumption that the non-vanishing components of stresses are the axial component and the transverse shear component tangential to the contour of the cross section. Using nonlinear composite beam theory described in Sec. 2.3 developed by Hodges et al. [69], this work presents results for a Z-section beam as shown in Sec. 3.1. The thickness of the Z-section beam is treated as a parameter and is varied over a range of values. The results obtained from the VAM are then compared with thin-walled beam theory solutions and solutions obtained from commercially available 3-D

finite element tools.

Through this work, an exhaustive use and verification of VABS based on the VAM is presented for thin-walled beams especially the thin-walled structures with asymmetry and an open section. Note that, for thin-walled open section beams, there exists another capability in VABS to model using Generalized Vlasov (GV) theory which provides a 5×5 stiffness matrix as opposed to a 6×6 stiffness matrix obtained by using Generalized Timoshenko (GT) model which captures shear deformation effects. The cases presented did not involve torsional loads so a GT model was used to obtain shear stress variations in the cross section of the Z-section thin-walled beam.

Results in Sec. 3.1 show that thin-walled beam theory is asymptotically correct but is limited to modeling thin-walled beams as a combination of lines or curves as opposed to areas in VABS. Obtaining asymptotically correct solutions with variations in the cross section along with a capability to model beams made up of composite materials easily and efficiently as compared to 3-D FEM, provides a reason to use VABS over any other simulation tool for engineering applications.

3.1 Thin-Walled Beam Theory vs. VAM

This work presents a comparison of the solutions obtained using VAM to those obtained using the TWBT, for a specific case of a Z-section thin-walled beam. Cases for thin-walled beams using the variational asymptotic method have been analyzed and presented in several papers [147, 87, 189]. These include simple sections such as strips, initially curved and/or twisted strips, I-section beams as open sections, box beams as closed sections, and springs as initially twisted and curved beams. These are sufficient to demonstrate that VABS can produce results with an accuracy comparable to that of 3-D finite element codes (and thin-walled beam theory/elasticity solutions, when available). The purpose of this work is to present results for a thin-walled Z-section beam and compare results with thin-walled beam theory solutions and Finite Element Methods (FEM). Z-section beams are not

very common, but the most important application as purlins is quite common in the civil engineering field. Soon, thin-walled Z-section beams may appear as spars in aerospace engineering applications, but that would depend on whether the saving in weight is significant compared to the loss in strength to compensate with a different design of beam. In this work, a thin-walled Z-section beam is considered with a parametric variation in the web angle with respect to the horizontal axis (x_2) and a parametric variation of the ratio b/h (referred to as β in this text), which is the ratio of the flange length to the web length for the Z-section as shown in Fig. 3.1. Initially, the web angle is set at α = $60°$, and the parameter

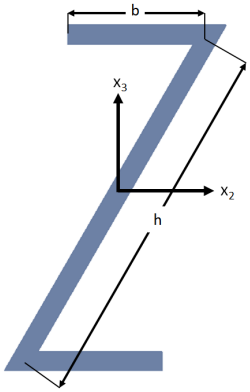

Figure 3.1: Sample Z-section with notations

$\beta = b/h = 3/8$. In that scenario, a solution using the thin-walled beam theory as described in Ref. [13] shows that the shear flow along the web is constant. The shear flows in the two flanges of the Z section and the web, have been obtained and verified to be correct through the thin-walled beam theory. When the parameter β is manipulated from 0.5 to 1.0, the shear flow along the web approaches a constant at a particular value of $\beta = b/h = 3/8$ and when the web angle of Z section with the horizontal is $60°$. It appears that this constant shear flow, is due to the alignment of the principal axis of bending with the web for this case, and therefore there is no axial stress along the web.

It is observed that for a particular value of β, there exists a specific value of web angle where the shear flow along the web attains a constant value. In a case where the angle of the web with respect to the horizontal is different from $60°$, e.g., α= $45°$, the principal axis

of bending aligns itself along the web at a different value of $\beta = \frac{3}{(4\sqrt{2})}$ (for $\alpha = 45°$) and at that particular value of β, the shear flow in the web is also found to be a constant, as shown in Fig. 3.2b. Figure 3.2a shows the case where the angle of the web is $60°$ with the horizontal. The shear flow is constant along the web when $\beta = 3/8$ and it has been seen that the principal axis of bending is aligned along the web as well.

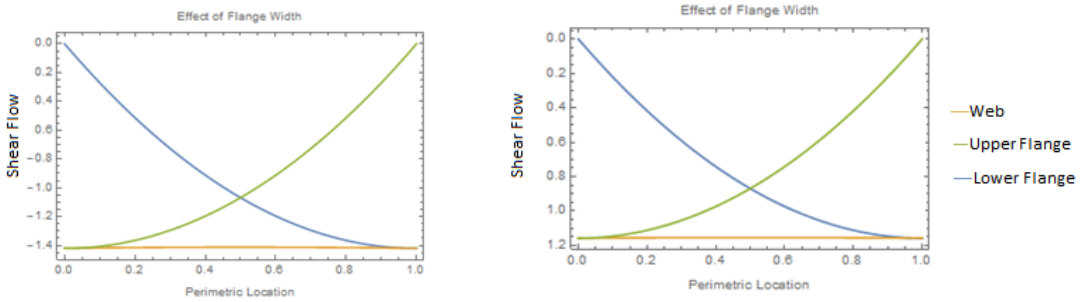

(a) α = 60°; $\beta = \frac{3}{8}$

(b) α = 45°; $\beta = \frac{3}{(4\sqrt{2})}$

Figure 3.2: Shear Flows obtained from thin-walled beam theory in a Z-section beam with different web angles (α) and flange-web length ratios ($\beta = \frac{b}{h}$)

Now, it is important to know if this strange behavior is observed while solving this problem using Variational Asymptotic Beam Sectional Analysis (VABS)/VAM or the 3-D FEM as well. For this, various cases were tested out. There were effects of different variations studied:

1. Variation in the angle of the web (α) with the horizontal
2. Variation in web thickness/cross-sectional thickness (t)

Geometries with different web angle with respect to horizontal axis were executed using VABS. The stresses obtained from VABS are in the form of σ_{11}, σ_{22}, σ_{33}, σ_{12}, σ_{23}, σ_{13}. The stress tensor needs to be rotated to obtain the shear stress/shear flow along the web. For the rotation of the stress tensor by the angle α, an appropriate rotation matrix needs to be used but as the stress components to be rotated are in a plane perpendicular to x_1, they can be multiplied with a standard direction cosine matrix to obtain the stresses along the web as shown

$$[\sigma]^{\text{web}} = [Q]^T \cdot [\sigma] \cdot [Q] \tag{3.1}$$

where, the rotation matrix is defined as

$$[Q] = \begin{bmatrix} 1 & 0 & 0 \\ 0 & \cos\theta & -\sin\theta \\ 0 & \sin\theta & \cos\theta \end{bmatrix} \tag{3.2}$$

finally, the stress components rotated for the co-ordinate frame such that x_2 is aligned with the web can be derived as

$$\begin{aligned} \sigma_{11}^{\text{web}} =& \sigma_{11} \\ \sigma_{22}^{\text{web}} =& \sigma_{22}\cos^2\theta + \sigma_{33}\sin^2\theta + \sigma_{23}\sin 2\theta \\ \sigma_{33}^{\text{web}} =& \sigma_{22}\sin^2\theta + \sigma_{33}\cos^2\theta - \sigma_{23}\sin 2\theta \\ \sigma_{12}^{\text{web}} =& \sigma_{12}\cos\theta + \sigma_{13}\sin\theta \\ \sigma_{13}^{\text{web}} =& -\sigma_{12}\sin\theta + \sigma_{13}\cos\theta \\ \sigma_{23}^{\text{web}} =& -\frac{1}{2}\left[\sigma_{22}\sin 2\theta + \sigma_{33}\sin 2\theta\right] + \sigma_{23}\cos 2\theta \end{aligned} \tag{3.3}$$

3.1.1 Case I: Variation in Angle of the Web (α) with the horizontal

This case assumes that the analysis is done at a cross-sectional thickness which is of the order of 20 times smaller than the length of the web, i.e., h/20. Further, the variation was carried out with four different cases considering $\alpha = 50°$, 55°, 60°, 65°.

3.1.2 Case II: Variation in the Cross-Sectional Thickness (t)

This case assumes that the analysis is done at a value of web angle which is α= 60°. Further, the variation is carried out with the thickness of the cross section as $t = h/10$, $t = h/15$, $t = h/18$, $t = h/20$, $t = h/22$, $t = h/25$, $t = h/100$. Figure 3.7 shows a summary of shear stress variation with change in the beam thickness. Parabolic variation in the shear stresses along the web is present but visible in figures attached later.

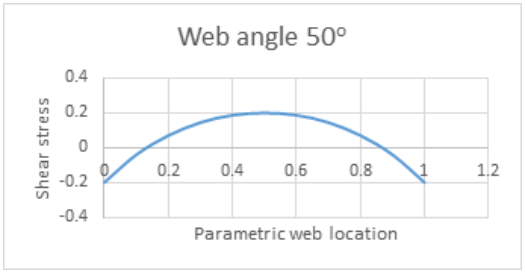

(a) Shear stress variation along the web

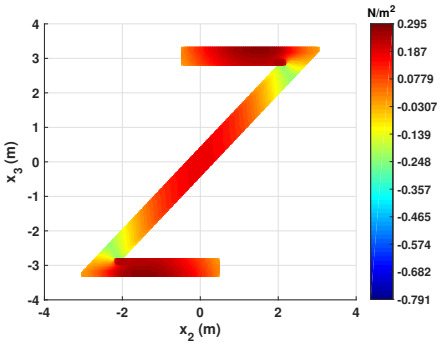

(b) Shear stress contour plot

Figure 3.3: Shear stress (σ_{12}) variation in the web and contour plot when the stress tensor is rotated by the web angle, $50°$

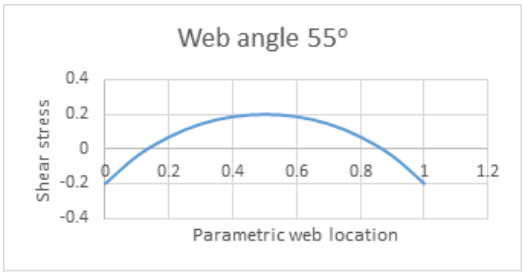

(a) Shear stress variation along the web

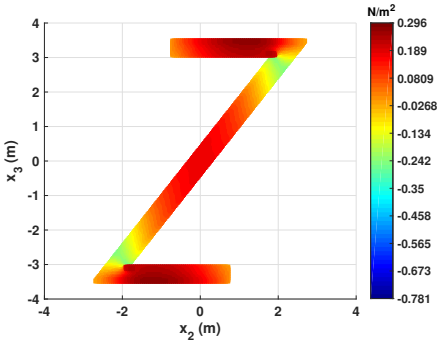

(b) Shear stress contour plot

Figure 3.4: Shear stress (σ_{12}) variation in the web and contour plot when the stress tensor is rotated by the web angle, $55°$

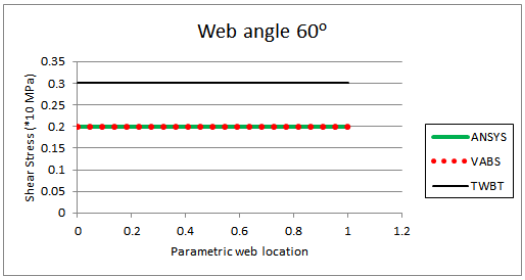

(a) Shear stress variation along the web

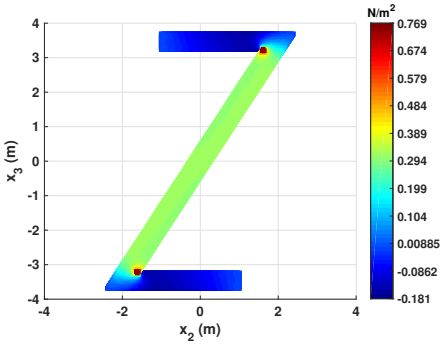

(b) Shear stress contour plot

Figure 3.5: Shear stress (σ_{12}) variation in the web and contour plot when the stress tensor is rotated by the web angle, $60°$

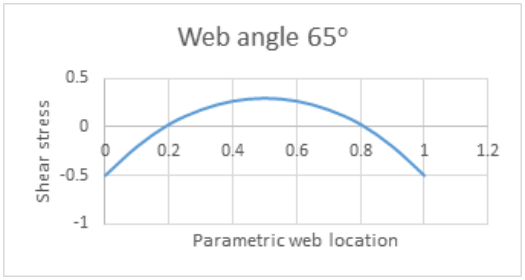

(a) Shear stress variation along the web

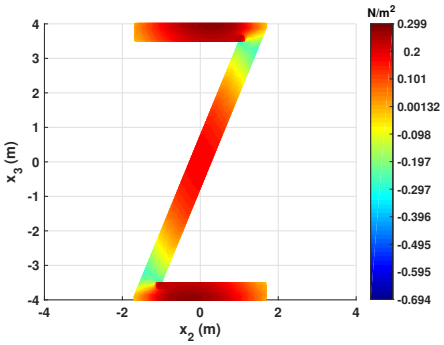

(b) Shear stress contour plot

Figure 3.6: Shear stress (σ_{12}) variation in the web and contour plot when the stress tensor is rotated by the web angle, $65°$

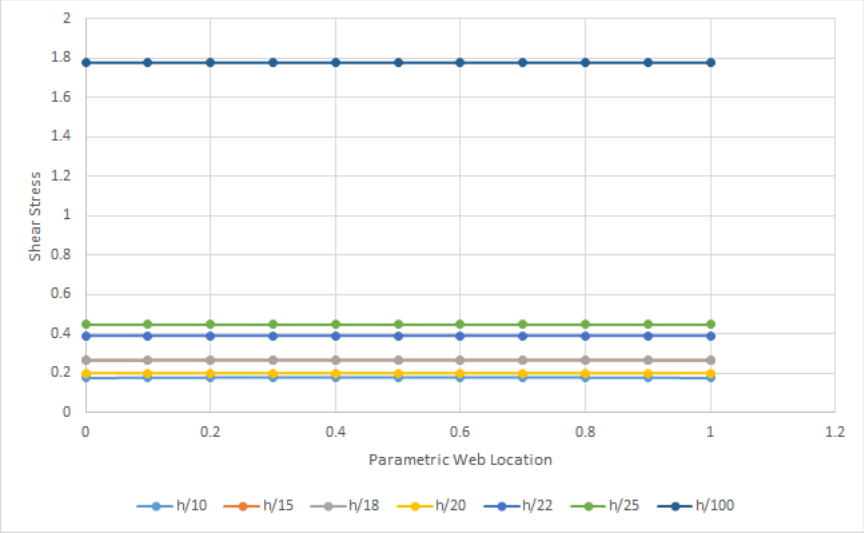

Figure 3.7: Shear Stresses along the web with variation in the thickness of the beam as a fraction of the length of the web

3.2 Results

Figure 3.5a shows a comparison between the shear stress results obtained from Thin-Walled Beam Theory (TWBT), VABS and 3-D FEM solutions obtained from ANSYS. As shown in the figures from 3.3a-3.6a, the solution obtained from analytical VAM is similar to the one obtained from the thin-walled beam theory in the sense that the shear stresses are obtained to be constant and the shear flow is shear stress times the thickness (constant in our formulation for the Z section beam) only at $\alpha = 60°$. For all other orientations of the

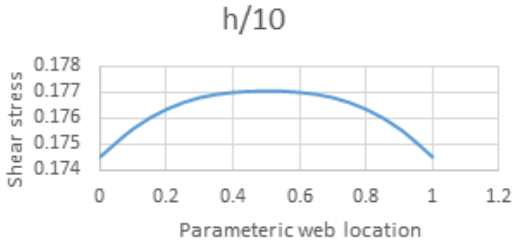

(a) Shear stress variation along the web

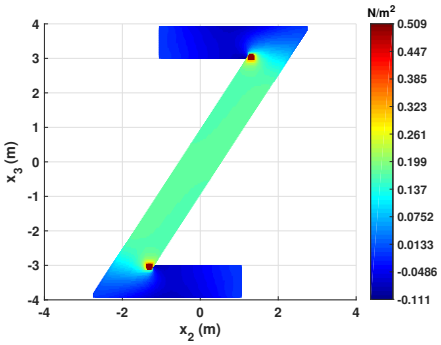

(b) Shear stress contour plot

Figure 3.8: Shear stress (σ_{12}) variation in the web and contour plot when the stress tensor is rotated by the web angle, 60° with wall thickness, $t = h/10$

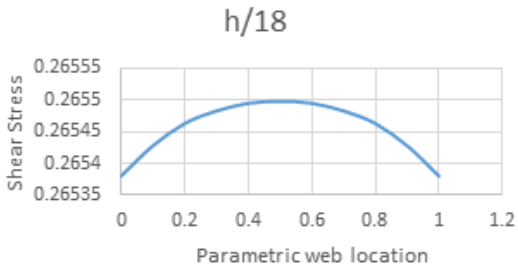

(a) Shear stress variation along the web

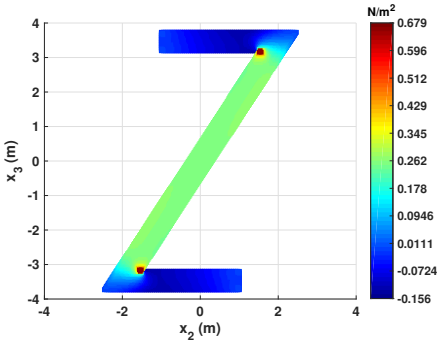

(b) Shear stress contour plot

Figure 3.9: Shear stress (σ_{12}) variation in the web and contour plot when the stress tensor is rotated by the web angle, 60° with wall thickness, $t = h/15$

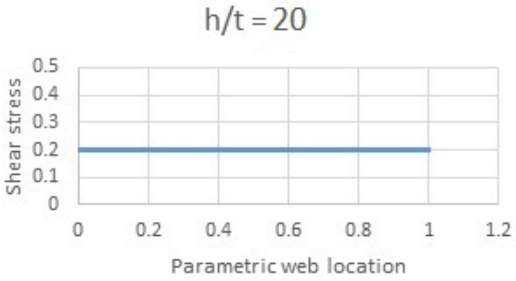

(a) Shear stress variation along the web

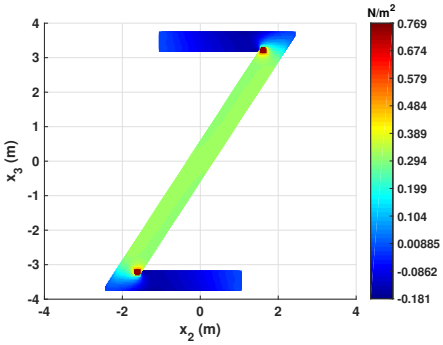

(b) Shear stress contour plot

Figure 3.10: Shear stress (σ_{12}) variation in the web and contour plot when the stress tensor is rotated by the web angle, 60° with wall thickness, $t = h/18$

web with respect to the horizontal, the shear flow exists in the web with a variation as a parabola, as shown. This proves the asymptotic correctness of thin-walled beam theory.

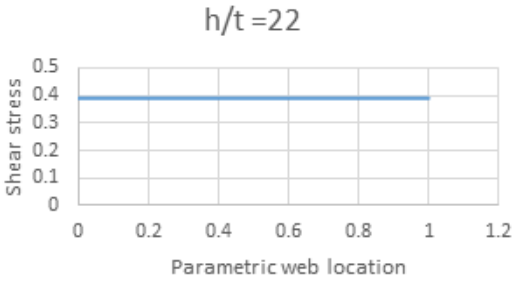

(a) Shear stress variation along the web

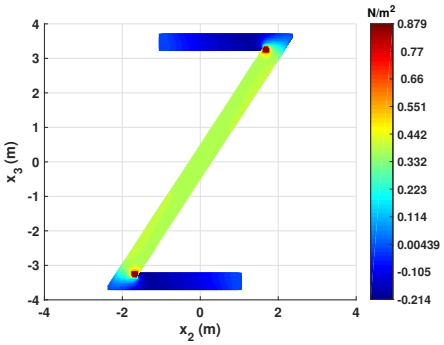

(b) Shear stress contour plot

Figure 3.11: Shear stress (σ_{12}) variation in the web and contour plot when the stress tensor is rotated by the web angle, $60°$ with wall thickness, $t = h/22$

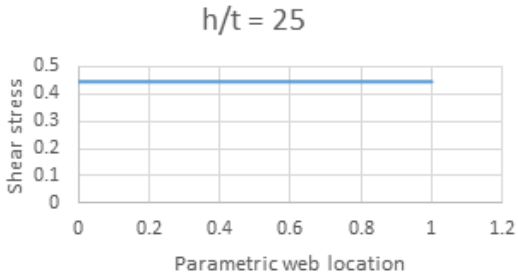

(a) Shear stress variation along the web

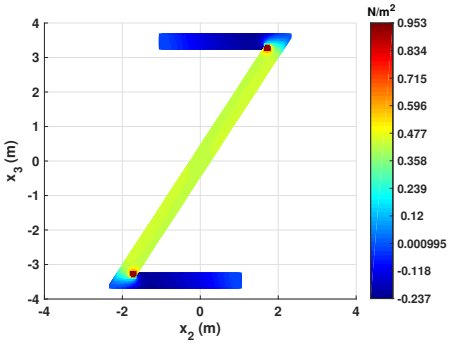

(b) Shear stress contour plot

Figure 3.12: Shear stress (σ_{12}) variation in the web and contour plot when the stress tensor is rotated by the web angle, $60°$ with wall thickness, $t = h/25$

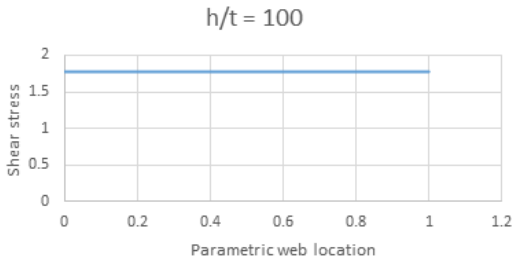

(a) Shear stress variation along the web

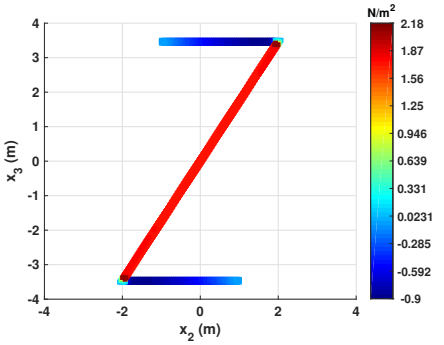

(b) Shear stress contour plot

Figure 3.13: Shear stress (σ_{12}) variation in the web and contour plot when the stress tensor is rotated by the web angle, $60°$ with wall thickness, $t = h/100$

As shown in the Figs. 3.8a – 3.13a, when a beam is solved using VAM, as the thickness of the cross section is decreased, a constant shear flow along the web is obtained once the

characteristic dimension of the cross section, web length (h) in the presented case, is at least 20 times the thickness of the cross section. Beyond that point, the beam behaves as a thick walled beam and the thin-walled beam theory is not valid. This is also proved by Hodges[69]. Further, thin-walled beam theory isn't capable of providing stress concentration locations in the cross section as clearly as a variational asymptotic approach can (demonstrated in Fig. 3.5b). Because both analytical VAM and VABS recover 3-D displacements and stresses, it is possible to capture the effect of thickness on the results as well. Furthermore, with TWBT, only results along the thickness, can be obtained, thus, it is nearly impossible for the thin-walled beam theory to capture the variation in shear stress through the thickness because the thickness term cancels out at an intermediate step. Moreover, it is less time consuming and less exhaustive to study numerous cases using the presented approach as compared to using 3-D FEM where each case needs separate pre-processing.

CHAPTER IV

NON-PHYSICAL BEHAVIOR IN THE SECTIONAL ANALYSIS USING VAM

4.1 Problem Description

With VABS, the advantage is not only expressible in terms of computational efficiency, but also in terms of evolving the underlying theory for structural analysis. The results obtained from VABS are proven to consider higher order terms while evaluating a set of elastic constants for a given cross section when compared to traditional beam theories without making any assumptions a priori, in the analysis. Recently, however, a few cases have been identified in which VABS yields negative values for some of the diagonal elements in the stiffness matrix associated with generalized Timoshenko theory [138]. This is nonphysical and clearly indicative of something that requires attention. Rajagopal [138] outlines that this phenomenon is due to the interaction of two small parameters affecting results of a cross-sectional analysis, thus producing in erroneous stiffness matrix. For example, in the case of a graphite-epoxy strip $[45/0]_{3s}$ whose section measures 1.182×0.0579 in. and is initially curved out of its plane by 0.1 rad/in., VABS outputs the bending stiffness in the stiffer direction to be -9.31×10^4 lb-in^2. Initially, this issue was observed in the cross-sectional analysis of thin composite strips, but later on, it was observed in thin orthotropic strips as well with small to moderate initial curvature. For example, consider a graphite-epoxy orthotropic strip of size 1.2×0.06 in. made up axially oriented fibers with Young's modulus of E_1 and $E_2 = E_3$ which have value 20×10^6 psi and 1×10^5 psi, respectively. It also

has an initial out-of-plane curvature of 0.08 rad/in. In this case, negative in-plane stiffness values were observed as well. From the preliminary study, one can draw a conclusion that this non-physical behavior is caused by extreme values of a few distinct factors involved. Identification of a root cause of this issue, becomes both challenging as well as critical. It is important to conduct a detailed investigation of this issue while understanding the behavior of the stiffness matrix generated by VABS while comparing it to the desired or expected values of the stiffness values. This study would not only help in getting more information for finding the root cause, but also potentially lead to filling gaps in the literature where the trends in stiffness values are studied with variation in different factors. More details on this case and many other cases which are part of a detailed study of this issue, are presented in Sec. 4.2.

Rajagopal [138] also pointed out that one of the main reasons for this issue could be that the asymptotic analysis is not set up to take advantage of the ratio of wall thickness to the maximum cross section dimension h/b during the process of minimizing strain energy functional asymptotically. The detailed study in Sec. 4.2 also reveals that the other factor causing this issue is that the ratio between material properties of orthotropic materials such as E_1/E_2 or E_1/E_3 becomes very high which introduced their inverse as independent small parameters for the variational problem. Rao [140] developed an approach in which the Young's moduli ratio of different components in a plate is chosen as a small parameter. Rao [140] considers the ratio of Young's modulus of the core to the Young's modulus of the face sheets. Through this work, such parameters would be used in a beam analysis where the ratio of Young's modulus in two different directions for an orthotropic material is chosen to be the small parameter. In this section, methods to tackle the destructive interaction between the small parameters are presented along with the drawbacks and the benefits of each.

4.2 Detailed Investigation

The nonphysical effects observed (Sec. 4.1) in the computations of VABS indicate that there are multiple factors leading to such behavior. This behavior of the stiffness matrix is associated with three factors, viz., the thin-walled nature of the beam cross section or the layers within a composite beam's cross section, initial curvatures and material properties of orthotropic, anisotropic or composite materials such that the material has a very high Young's modulus in the axial direction as compared to the transverse directions. To study the trends or the variation in stiffness values of beam cross sections through VABS with respect to these factors under consideration leads to a very complex domain of analysis. Thus, a study has been conducted by varying one factor at a time as a variable to study the trends in stiffness values obtained from the existing VABS version.

4.2.1 Varying Width of the Beam Section

In this section, a square beam with cross-sectional dimensions of 0.06×0.06 in. (dimensions along x_2 and x_3, x_1 points to the span/length of the beam) is chosen with an initial curvature of 0.08 rad/in. about x_2, which is is changing the shape of the cross section from square to thin-walled by varying the width from 0.06 in. to 2.4 in. which is 40 times the height. The beam has an out-of-plane curvature i.e. k_2, curvature about x_2 of 0.08 rad/in.

Initially, the beam is made of an isotropic material, with Young's Modulus 20.59×10^6 psi. Figure 4.1 shows the variation in the in-plane stiffness obtained from VABS for each beam as the width is increased while keeping the thickness, out-of-plane curvature and material properties fixed. The width is increased such that the width-to-thickness ratio increases ranges from 1 to 20. It is observed that the in-plane stiffness increases gradually as the width is increased because the material is being added, making the beam larger. It is observed that there is no appearance of non-physical effects such as negative stiffness even if the width is increased to almost 40 times the thickness. Further, this result has been

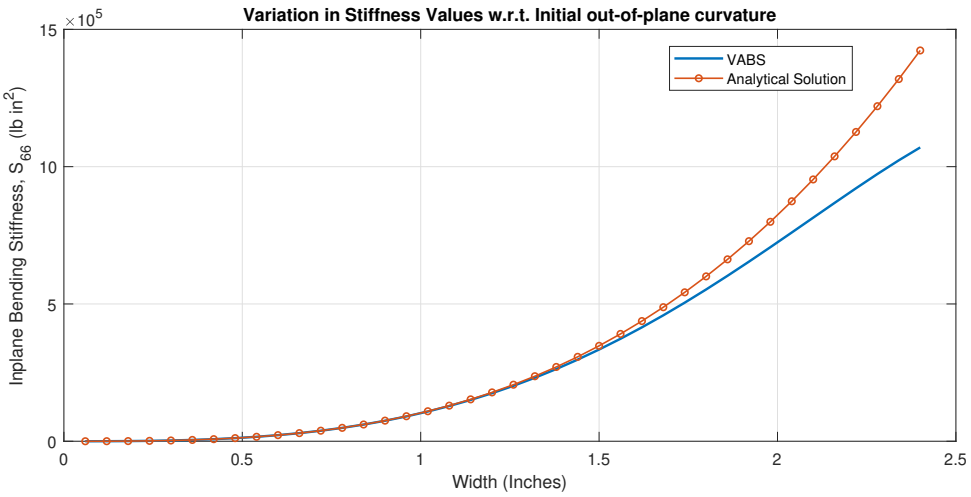

Figure 4.1: Variation in the S_{66} stiffness when an isotropic beam's width is increased from 0.06 in. to 1.2in.

compared to the analytical solution obtained from Ref. [69] and there the results obtained from VABS start to deviate from the analytical solution when width-to-thickness ratio is increased beyond 20 as shown in Fig. 4.1.

Now, instead of the isotropic material, the beam is made of orthotropic material with Young's Modulus $E_1 = 20.59 \times 10^6$ psi and $E_2 = E_3 = 1 \times 10^5$ psi, bulk modulus, $G_{12} = G_{13} = G_{23} = 8 \times 10^6$ psi and Poisson's ratio, $\nu_{12} = \nu_{13} = 0.3$ and $\nu_{23} = 0.335$.

Figure 4.2 shows how the in-plane stiffness value increased as the width was increased, but the rate of increase in the stiffness reduced and it eventually started decreasing when the width became 0.9 in.Ḟurther it went negative as the width was subsequently increased. Clearly, this is something non-physical, as the in-plane stiffness can neither decrease for a beam of larger cross-sectional area nor it can be a negative value. In this case, it is not necessary to generate analytical closed-form solution involving orthotropic materials and initial curvature, for comparison. The negative values of S_{66} are evidence to the non-physical behavior in the formulation.

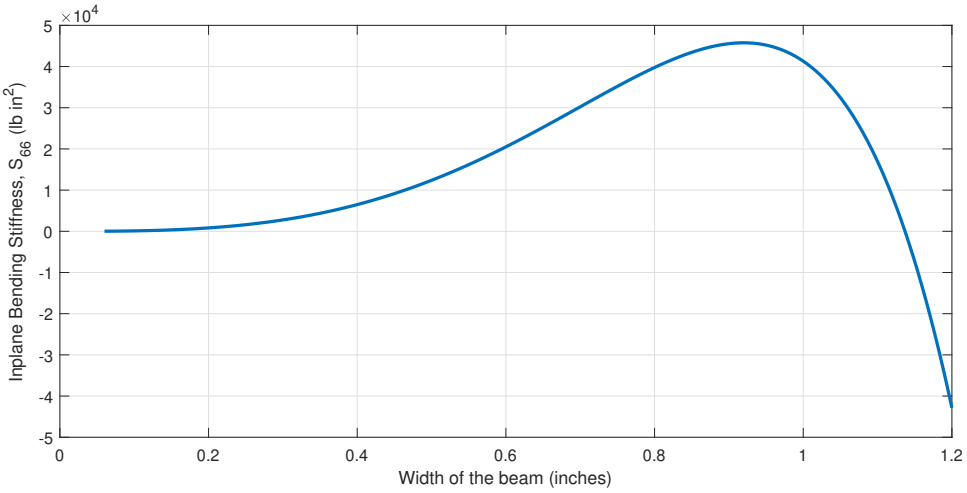

Figure 4.2: Variation in the S_{66} stiffness when an orthotropic beam's width is increased from 0.06 in. to 1.2in.

4.2.2 Variation in Initial Curvature

In this case, the trends of the in-plane stiffness while varying the initial out-of-plane curvature value as input, is studied. For this purpose, a beam of cross-sectional dimension 1.2×0.06 in. is chosen such that the width is 20 times the thickness so that it becomes a thin-walled beam section. Further, the material properties are chosen as the same orthotropic properties taken in the previous case. The initial out-of-plane curvature is increased from 0.001 to 0.08 rad/in.

Figure 4.3 represents the behavior of the in-plane stiffness as the curvature value is increased. The plot depicts that the in-plane stiffness starts to decrease as soon as the initial curvature about x_2 is increased. It is hard to say what should really happen to the in-plane stiffness values, but it should not be negative at any point. However, it is becoming negative as soon as the initial curvature about x_2 is increased beyond 0.041 rad/in. During this study, it also has been observed that the increase in the in-plane initial curvature does not lead to any negative stiffness values in the stiffness matrix as long as the curvature value leads to a physically possible cross section and satisfies $\sqrt{g} > 0$, refer Eq. (2.10).

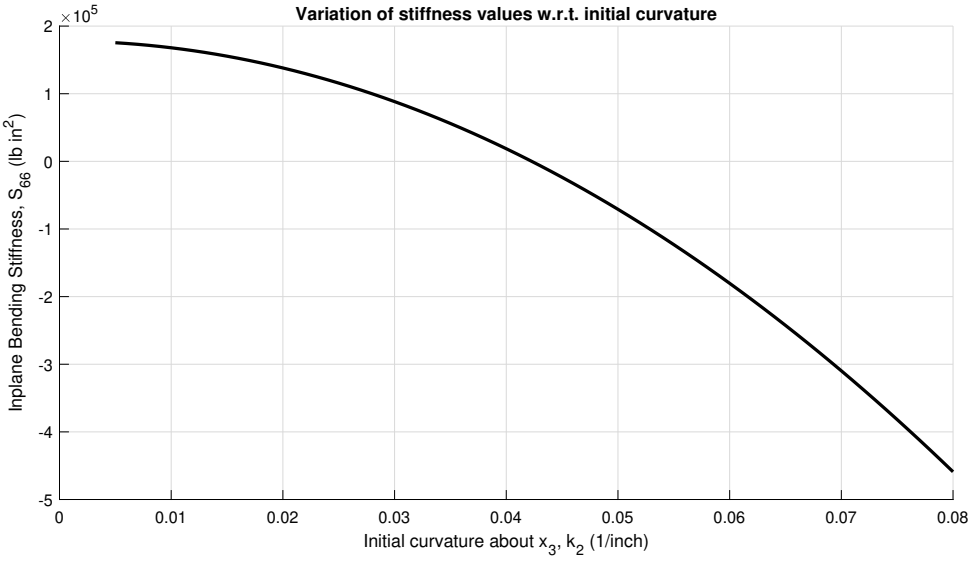

Figure 4.3: Variation in the S_{66} stiffness in a thin-walled orthotropic beam when initial out-of-plane curvature (k_2) is increased from 0.001 to 0.08 rad/in.

4.2.3 Variation in Ratio of the Material Properties

So far, the variation in the in-plane stiffness has been studied with respect to the changes in the width-to-thickness ratio and the initial out-of plane curvature. Section 4.1 outlines that the ratio of the Young's moduli in different directions is also another factor to be considered while trying to identify the cause of this issue of obtaining negative stiffness values. Also, it is known that the in-plane bending stiffness is largely dependent on the Young's modulus in the axial direction as bending in any direction introduces axial stresses in the beam. So, in this case, the changes in the in-plane bending stiffness with changes in E_1/E_2 are studied. This is essentially the ratio of Young's modulus in the axial direction to the Young's modulus in the transverse direction x_2, about which there is an initial out-of-plane curvature of 0.08 rad/in. The cross-sectional dimensions are the same dimensions of a thin-walled beam as taken in the previous case, with a width-to-thickness ratio of 20. The trends in the in-plane bending stiffness, S_{66}, are plotted in Fig. 4.4 on a semi-log plot as the horizontal co-ordinate is a ratio. Here, the ratio is increased from 0.01 to 200. This

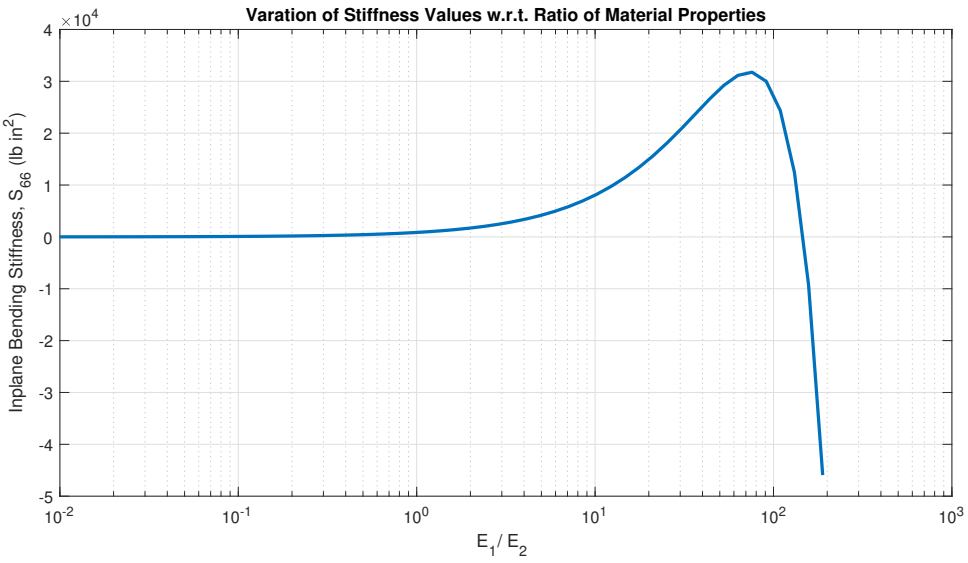

Figure 4.4: Variation in the S_{66} stiffness in an initially curved, thin-walled beam when E_1/E_2 is increased from 0.01 to 200

is important because initially, E_2 is 100 times larger than E_1 and finally, the simulation ends when E_1 is 200 times E_2. This covers both the aspects when a material property in one direction is higher than the one in the other. It is observed that the value of in-plane bending stiffness doesn't change with the increase in E_1/E_2 till the ratio is 1, implying that the in-plane bending stiffness starts increasing as soon as E_1 becomes greater than E_2. However, a non-physical effect crops up when this increase is slowed down and followed by a decrease in the in-plane bending stiffness value. This happens when E_1 is larger than E_2 by 20 times or more. In another study, the variation in the in-plane stiffness is studied when the ratio E_1/E_3 is increased from 0.01 to 200 in a beam with all other characteristics kept the same as the previous case such as moderate out-of-plane initial curvature. A semi-log plot for the in-plane stiffness in Fig. 4.5 demonstrates that there is no appearance of any negative stiffness value as the ratio is increased. So, clearly the non-physical effect is associated with the terms involving the out-of plane initial curvature and the ratio E_1/E_2. This observation helps to reduce the number of permutations or combinations in which the accuracy can be affected. One may wonder, why are we even considering materials with

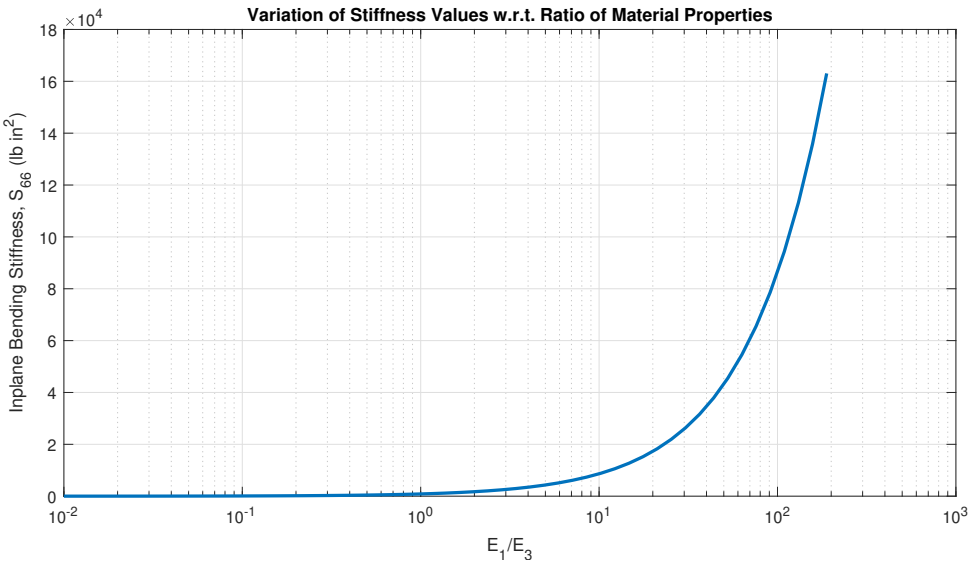

Figure 4.5: Variation in the S_{66} stiffness in an initially curved, thin-walled beam when E_1/E_3 is increased from 0.01 to 200

such a large difference between the values of Young's moduli in different directions? It is then important to note that such a disparity between various moduli values is very common in fiber reinforced composites typically in fiber reinforced plastics/polymers. So, the reason behind the non-physical behavior in stiffness matrix is very important to be identified.

4.2.4 Example of a Thick Composite Beam

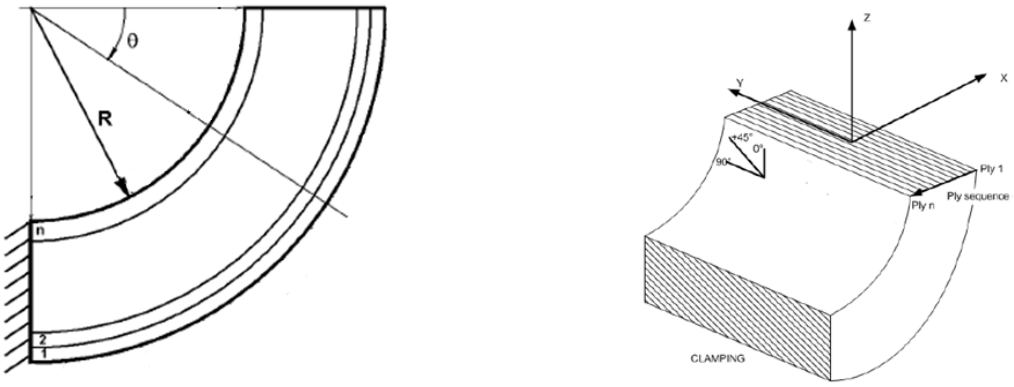

(a) Initially curved cantilever beam (b) Layup directions

Figure 4.6: Geometric characteristics of the chosen, thick composite beam

Table 4.1: Geometric and material properties of the composite cross section

(a) Sectional geometric properties

Property	value [mm]
Thickness	4.416
Width	15
Internal radius (R)	5
Ply thickness	0.184
Number of plies	24

(b) Sectional material properties

Property	value
E_{11}[MPa]	152800
$E_{22} = E_{33}$[MPa]	8700
$G_{12} = G_{13}$[MPa]	4200
G_{23}[MPa]	3150
$\nu_{12} = \nu_{13}$	0.335
ν_{23}	0.380

In a very recent analysis, another issue is identified which could potentially be linked to this study of small parameters in a beam that is not thin-walled. In Figs. 4.6a and 4.6b a curved beam consisting of 24 layers with geometric and material properties found in Tables 4.1a and 4.1b, respectively, with detailed layup information present in Table 4.2.

Table 4.2: Layup Sequence

Layup No.	Angle	No.	Angle	No.	Angle	No.	Angle	No.	Angle	No.	Angle
1	-45	5	90	9	45	13	0	17	0	21	-45
2	0	6	-45	10	-45	14	90	18	45	22	45
3	45	7	-45	11	90	15	-45	19	45	23	0
4	-45	8	0	12	45	16	45	20	90	24	-45

When the cross-sectional analysis is performed for the curved beam using VABS, it is observed that negative stiffness is obtained for bending stiffness about x_3 (i.e., element S_{66} of the 6×6 Timoshenko stiffness matrix obtained from VABS). It is worth noting that this beam is not thin-walled. The width is almost three times of the thickness of the beam, where according to prior studies, a beam that has a width 20 times its thickness is regarded as a thin-walled beam. Further, different cases analyzed are presented along with arguments to help find out the reasons of this problem.

By modifying the geometry and material properties, different cases were chosen and checked for nonphysical effects. As shown in Table 4.3, Case 1 is the original problem, the bending stiffness S_{66} of which is compared to that of three other cases. Those cases are chosen by reducing the width-to-height value (which is same as height in Case 2), by having

zero curvature in Case 3 and by having isotropic material properties instead of orthotropic properties in Case 4.

Table 4.3: Summary of different cases analyzed for a composite beam

S. No.	Width	Curvature	Material Properties	Bending stiffness about x_3
1	3×height	Out-of-plane curvature	different orders	-1.1989374300E+08
2	height	Out-of-plane curvature	different orders	1.7061040168E+06
3	3×height	zero curvature	different orders	6.6490623635E+07
4	3×height	out-of-plane curvature	isotropic	8.3941114032E+07

It is observed from Cases 2 – 4 that the bending stiffness is no longer negative. This clearly shows that there are multiple factors influencing nonphysical effects in the current problem. Those factors are associated with the coordinate x_2 which is associated with the width of the beam, the out-of-plane curvature and the material properties, especially the different orders of magnitude for E_{11} and E_{22}.

4.2.5 Investigating the Accuracy of Perturbation Solution

Section 2.3 describes how a Generalized Timoshenko (GT) model with a 6×6 stiffness matrix is obtained by transforming the asymptotically correct strain energy (Eq. (2.48) to fit the GT form in Eq. (2.51). Ho et al. [64] laid out a system of exact non-linear equations that were derived with the help of 1-D equilibrium equations. These exact equations can be solved using an iterative method to solve a system of nonlinear equations and are an upgrade to the existing analytical perturbation solution developed by Yu [188]. An updated version of this perturbation solution is also present in the appendix of Ref. [64] and [187]. The motivation behind employing an approximate perturbation solution to obtain the 6×6 Timoshenko stiffness matrix is that the perturbation solution is several orders of magnitude faster than a solution obtained after convergence of a suitable iterative method needed to solve the exact equations. Besides, in almost all of the prior research as well as in the research works by Ho et al. [64, 65], the perturbation solutions also satisfied the system of exact energy transformation equations, demonstrating accuracy with respect to the chosen

benchmark platform. In recent studies only, we have seen nonphysical phenomenon being demonstrated by the results obtained from perturbation solution. This motivated the work in this section to test whether perturbation solution is the culprit for the negative stiffness values obtained from the sectional analysis.

For this investigation, we take the case of a thick composite beam whose sectional aspect ratio is 3 (i.e., with width three times the thickness of the beam). Again, the beam has 24 layers through the thickness with layup information and material properties listed in Tables 4.2 and 4.1b respectively. Also, the important geometric properties required to set up the problem are mentioned in Table 4.1a. Upon solving the case of a composite beam using VABS, we obtain the sectional properties. Because of the nature of the issue in this investigation, however, we primarily care about the 4×4 classical stiffness matrix (analogous to the Euler-Bernoulli Beam Theory), the 6×6 Timoshenko stiffness matrix (Eq. (2.53)) and the intermediate matrices containing stiffness coefficients (i.e., A, B, C, and D) which are a part of the asymptotically correct strain energy, Eq. (2.48). These intermediate matrices are not obtained as direct outputs from the commercial version of VABS, but are obtained by modifying the outputs in a research/developer version of VABS. Equations (4.1) and (4.2) represent the classical and the Generalized Timoshenko stiffness (S) matrices respectively.

$$\text{Classical} = \begin{bmatrix} 3.600145\text{E+06} & -1.380141\text{E+05} & 1.179389\text{E+06} & 3.357514\text{E+06} \\ & 6.505714\text{E+06} & 3.874839\text{E+05} & 3.857667\text{E+06} \\ \text{symmetric} & & 6.207977\text{E+06} & 4.737591\text{E+06} \\ & & & 6.970872\text{E+07} \end{bmatrix} \tag{4.1}$$

$$S = \begin{bmatrix} 3.647381\text{E+06} & -1.708112\text{E+03} & 3.511881\text{E+09} & -1.282763\text{E+05} & 1.214635\text{E+06} & -4.701320\text{E+06} \\ & 4.930850\text{E+06} & -9.237700\text{E+07} & -1.320848\text{E+06} & -7.345899\text{E+04} & 3.581949\text{E+06} \\ & & 2.239325\text{E+05} & 1.846219\text{E+07} & 3.916592\text{E+08} & -1.426791\text{E+05} \\ & & & 6.847468\text{E+06} & 9.563367\text{E+05} & -6.371848\text{E+06} \\ & \text{symmetric} & & & 6.669813\text{E+06} & -7.134774\text{E+06} \\ & & & & & -1.198937\text{E+08} \end{bmatrix} \tag{4.2}$$

It can be observed that the GT stiffness matrix contains a negative value in the diagonal term S_{66}, the in-plane bending stiffness. On the other hand, the classical stiffness matrix does not contain any non-physical effects. The readers are being reminded that the three things which affect the value of the in-plane bending stiffness in a GT model as compared to the classical Euler-Bernoulli beam model are the presence of initial curvatures, the terms correct up to the second-order in the strain energy expression and the implementation of the perturbation solution to obtain the GT model from the asymptotically correct strain energy.

In this section, the accuracy of the perturbation solution is being investigated, so we need the intermediate coefficient stiffness matrices A, B, C and D which are present in the asymptotically correct strain energy expression, Eq. (2.48). The matrices obtained from VABS for this case are listed as follows

$$A = \begin{bmatrix} 3.647380\text{E+06} & -1.287338\text{E+05} & 1.214610\text{E+06} & -4.698046\text{E+06} \\ & 6.493647\text{E+06} & 9.366589\text{E+05} & -5.452370\text{E+06} \\ \text{symmetric} & & 6.668719\text{E+06} & -7.065225\text{E+06} \\ & & & -1.199846\text{E+08} \end{bmatrix} \tag{4.3}$$

$$B = \begin{bmatrix} 0.000000\text{E+00} & -2.148574\text{E+06} & 0.000000\text{E+00} & 0.000000\text{E+00} \\ & 0.000000\text{E+00} & -5.416408\text{E+07} & -1.312553\text{E+02} \\ \text{symmetric} & & 0.000000\text{E+00} & 0.000000\text{E+00} \\ & & & 0.000000\text{E+00} \end{bmatrix} \tag{4.4}$$

$$C = \begin{bmatrix} 2.914103\text{E+05} & 0.000000\text{E+00} & -8.734874\text{E+00} & -1.731360\text{E+04} \\ & 5.838136\text{E+07} & 0.000000\text{E+00} & 0.000000\text{E+00} \\ \text{symmetric} & & 1.025906\text{E+07} & 4.243790\text{E+06} \\ & & & 1.241374\text{E+10} \end{bmatrix} \tag{4.5}$$

$$D = \begin{bmatrix} -2.497440\text{E+06} & 0.000000\text{E+00} & -8.130894\text{E+07} & -1.724915\text{E+04} \\ & 2.416621\text{E+06} & 0.000000\text{E+00} & 0.000000\text{E+00} \\ \text{symmetric} & & 2.981732\text{E+06} & 6.497951\text{E+06} \\ & & & 1.215736\text{E+10} \end{bmatrix} \tag{4.6}$$

Using these matrices from VABS, the perturbation solution generates the GT model (Eq. (2.51), matrix S). The matrix A is also referred to as the corrected classical matrix as it is a 4×4 matrix, with degrees of freedom analogous to the E-B matrix, but includes the corrections mentioned above. It is important to note that there is a negative value on the diagonal of classical stiffness matrix primarily for in-plane bending stiffness, which is alarming.

To test the validity of the perturbation solution, the exact transformation equations derived by Ho in Ref. [64] are used. The exact equations are essentially a system of nonlinear equations which are derived for the transformation to the GT model with the help of the 1-D equilibrium equations. Now, to solve this set of exact nonlinear transformation equations

an iterative method is employed by Ho et al. Now, we try to derive the GT stiffness matrix with the help of the exact equations instead of the perturbation solution, but the chosen initial guess for the iterative method is the solution from the perturbation solution itself. These are the guesses are for the matrices X, Y and G

$$X = \begin{bmatrix} 3.647380\text{E+06} & -1.287338\text{E+05} & 1.214610\text{E+06} & -4.698046\text{E+06} \\ & 6.493647\text{E+06} & 9.366589\text{E+05} & -5.452370\text{E+06} \\ \text{symmetric} & & 6.668719\text{E+06} & -7.065225\text{E+06} \\ & & & -1.199846\text{E+08} \end{bmatrix} \tag{4.7}$$

$$Y = \begin{bmatrix} -1.708112\text{E+03} & 3.511881\text{E+09} \\ -1.320848\text{E+06} & 1.846219\text{E+07} \\ -7.345899\text{E+04} & 3.916592\text{E+08} \\ 3.581949\text{E+06} & -1.426791\text{E+05} \end{bmatrix} \tag{4.8}$$

$$G = \begin{bmatrix} 4.930850\text{E+06} & -9.237700\text{E+07} \\ -9.237700\text{E+07} & 2.239325\text{E+05} \end{bmatrix} \tag{4.9}$$

It is observed from this activity that the iterative method in this case doesn't converge when the solution from perturbation solution is chosen as the starting point. Ideally, it should have converged within a few iterations. An approach to obtain solutions to the exact nonlinear equations developed by Ho [65] might be feasible if a more efficient iterative method is employed, else the time consumed to solve the exact equations would render the entire solution, computationally inefficient.

4.2.6 Conclusion from the Extensive Study

In the previous few sections, we see an extensive investigation on the various cases where non-physical effects such as negative values of the diagonal elements in the stiffness matrix. In this section, the observations from the detailed investigation are discussed. With

relevant evidence, various parameters were varied to study the trends of the stiffness values. Initially, the effect of change in an isotropic beam's geometry is studied by increasing the width to eventually make it a thin-walled beam. Further, the initial out-of-plane curvature and ratio of Young's modulus in different directions is altered in a thin-walled beam and the effect on in-plane stiffness is studied. Then, the case of a thick composite beam is presented which demonstrates negative stiffness values as well. It is important to understand that the composite beam considered in the study is made of 24 very thin layers and the ratio of Young's modulus in different directions is significantly large, large enough for negative stiffness values to show up. Finally, the case of a composite beam is used to test the perturbation solution used to evaluate the warping solutions during the 2-D sectional analysis.

From the study, it is clear that the perturbation solution is incorrect for specific cases which involve moderate initial curvatures, large differences between directional Young's modulus values and large geometric aspect ratios. The perturbation solution depends on an accurate identification of the order of magnitude of the terms involved in the transformation. Even, the entire sectional analysis is dependent on the correct order of magnitude analysis as terms which are considered to be of higher orders magnitude are left out from the analysis at each step of the application of variational asymptotic method. Another important yet alarming observation that the classical corrected matrix, obtained from the variational asymptotic method by considering the second order terms in the strain energy expression, also has negative values in the diagonal term representing the in-plane stiffness. This also leads to the conclusion that certainly, there are issues with the order of magnitude analysis that are affecting both the values in the classical corrected stiffness matrix and perturbation solution for the transformation to the GT model.

So, a key conclusion is to look at the order of magnitude analysis in detail to avoid missing any terms which are significantly large in magnitude and were neglected as higher order terms. The order of magnitudes of various 3-D strain terms in a variational asymp-

totic approach as described in Sec. 2.3 are classified based on the order of small parameters associated with the problem. So far, the small parameters associated with strain, and curvature are considered in the sectional analysis. Several works by Volovoi [166] and Harursampath [60] do make an attempt to consider small parameters associated with the thickness-to-width ratio of a thin-walled beam as well. Some of the following sections derive ideas from these works and attempt to solve the problem of negative stiffness values.

It can also be concluded from the various examples that if at least one of the three small parameters such as the curvature, thickness-to-width ratio and material properties are eliminated from the problem, the results of the GT model employing perturbation solution, do not demonstrate any non-physical behavior. This is observed in the first three cases when the three parameters were altered individually and it is clear in various cases of thick-composite beam that were studied. The stiffness values were positive unless, there was a moderate initial curvature, a large gap between the Young's modulus values in different directions and a high aspect ratio in the geometry, altogether. So, the next few sections attempt to eliminate at least one of the small parameters from the overall 2-D sectional analysis without making any *ad hoc* assumptions. Further, the findings, benefits and drawbacks of the techniques are discussed.

4.3 Methods to Avoid the Non-Physical Behavior

4.3.1 Approach 1: Classical Laminate Plate Theory

In this section, a theoretical framework is developed that considers a priori the small parameters associated with the wall thickness. This approach examines and modifies the underlying analytical procedure. It is noted that some interactions of small parameters occurred in cases where Classical Laminated Plate Theory [CLPT] or Classical Laminated Shell Theory [CLST] were used as starting points. This means that the beam generalized 3-D strains are written in terms of shell or plate generalized 2-D strains using a suitable transformation. Further, the variational-asymptotic procedure is applied with the help of

small parameters in the transformed problem. It is seen that certain terms, where small parameters appeared in the denominator, are now retained. This is unlike the beam formulation where they were being considered as higher-order terms and hence neglected, leading to a destructive interaction of small parameters. This subsection discusses such an approach in detail.

As mentioned above, one of the small parameters is considered ab inito but the analysis in the present work does not include the nonlinear effects such as trapeze effects as included in the approach presented in Hodges et al. [70] but might include nonlinear terms in the expressions of 3-D beam generalized strains as opposed to what is mentioned in [138]. In this approach, the undeformed strip geometry is considered as a potential candidate for this problem of interaction of small parameters. The coordinates and nomenclature follow from the description in Sec. 2.3. The domain of the strip-beam is $0 \leq x_1 \leq L$, $-\frac{b}{2} \leq x_2 \leq \frac{b}{2}$, and $-\frac{h}{2} \leq x_3 \leq \frac{h}{2}$. While the position vector of an arbitrary material point in the strip is same as Eq. (2.1), the position vector $\hat{\mathbf{R}}(x_1, x_2, x_3)$ of an arbitrary material point in the deformed configuration is different from Eq. (2.2) owing to the fact that the starting point would be a CLST and can be represented as

$$\hat{\mathbf{R}}(x_1, x_2, x_3) = \mathbf{R}(x_1) + x_\alpha \mathbf{B}_\alpha(x_1) + \overline{w}_i(x_1, x_2, x_3)\mathbf{B}_i(x_1) \tag{4.10}$$

Here, it is important to note that the representation of the warping field is normal to the local shell surface and is constituted of terms as follows:

$$\overline{w}_\alpha(x_1, x_2, x_3) = w_\alpha(x_1, x_2) + x_3\phi_\alpha(x_1, x_2) + \Delta_\alpha(x_1, x_2, x_3) \tag{4.11a}$$

$$\overline{w}_3(x_1, x_2, x_3) = \overline{w}_3(x_1, x_2) + \Delta_3(x_1, x_2, x_3) \tag{4.11b}$$

The Δ_i's represent the unknown variation and the remaining components in the equations 4.11a and 4.11b are warping and local rotations "averaged" across the thickness. As the

warping field is split, it needs to satisfy additional constraints as mentioned below:

$$\int_{-\frac{h}{2}}^{\frac{h}{2}} \Delta_{\alpha}(x_1, x_2, x_3)\, dx_3 = 0, \tag{4.12}$$

$$\int_{-\frac{h}{2}}^{\frac{h}{2}} \Delta_{3}(x_1, x_2, x_3)\, dx_3 = 0, \tag{4.13}$$

and

$$\int_{-\frac{h}{2}}^{\frac{h}{2}} \Delta_{\alpha,3}(x_1, x_2, x_3)\, dx_3 = 0 \tag{4.14}$$

These constraints are also required to be satisfied in addition to the constraints on warping variables. Further, the expression for the 3-D strain field in the terms of beam generalized strains and unknown warping functions can be obtained as

$$\begin{aligned}
\Gamma_{11} &= \frac{1}{1 + x_3 k_2 - x_2 k_3}(\overline{\gamma}_{11} - x_2\overline{\kappa}_3 + x_3\overline{\kappa}_2 - k_1 x_2 \overline{w}_{1,3} + k_1 x_3 \overline{w}_{1,2} + k_2\overline{w}_3 - k_3\overline{w}_2 + \overline{w}_{1,1}) \\
2\Gamma_{12} &= \frac{1}{1 + x_3 k_2 - x_2 k_3}(-x_3\overline{\kappa}_1 - k_1 x_2 \overline{w}_{2,3} + k_1 x_3 \overline{w}_{2,2} - k_1\overline{w}_3 + k_2 x_3 \overline{w}_{1,2} - k_3 x_2 \overline{w}_{1,2} + k_3\overline{w}_1 + \overline{w}_{1,2} + \overline{w}_{2,1}) \\
2\Gamma_{13} &= \frac{1}{1 + x_3 k_2 - x_2 k_3}(x_2\overline{\kappa}_1 + k_1\overline{w}_2 - k_1 x_2 \overline{w}_{3,3} + k_1 x_3 \overline{w}_{3,2} + k_2 x_3 \overline{w}_{1,3} - k_2\overline{w}_1 - k_3 x_2 \overline{w}_{1,3} + \overline{w}_{1,3} + \overline{w}_{3,1}) \\
\Gamma_{22} &= \overline{w}_{2,2} \\
2\Gamma_{23} &= \overline{w}_{2,3} + \overline{w}_{3,2} \\
\Gamma_{33} &= \overline{w}_{3,3}
\end{aligned} \tag{4.15}$$

For the sake of simplicity of the procedure, the strip has a initial twist rate k_1 and initial curvature k_2 about x_2 is considered, thus making the problem a 2-D problem by neglecting

k_3. Thus, the 3-D strain field can be represented as

$$\begin{aligned}
\Gamma_{11} &= \frac{1}{1+x_3k_2}(\overline{\gamma}_{11} - x_2\overline{\kappa}_3 + x_3\overline{\kappa}_2 - k_1x_2\overline{w}_{1,3} + k_1x_3\overline{w}_{1,2} + k_2\overline{w}_3 + \overline{w}_{1,1}) \\
2\Gamma_{12} &= \frac{1}{1+x_3k_2}(-x_3\overline{\kappa}_1 - k_1x_2\overline{w}_{2,3} + k_1x_3\overline{w}_{2,2} - k_1\overline{w}_3 + k_2x_3\overline{w}_{1,2} + \overline{w}_{1,2} + \overline{w}_{2,1}) \\
2\Gamma_{13} &= \frac{1}{1+x_3k_2}(x_2\overline{\kappa}_1 + k_1\overline{w}_2 - k_1x_2\overline{w}_{3,3} + k_1x_3\overline{w}_{3,2} + k_2x_3\overline{w}_{1,3} - k_2\overline{w}_1 + \overline{w}_{1,3} + \overline{w}_{3,1}) \\
\Gamma_{22} &= \overline{w}_{2,2} \\
2\Gamma_{23} &= \overline{w}_{2,3} + \overline{w}_{3,2} \\
\Gamma_{33} &= \overline{w}_{3,3}
\end{aligned} \tag{4.16}$$

The warping field variables can be shown to be of the order $w_\alpha = \mathcal{O}(\epsilon b)$, $w_3 = \mathcal{O}(\frac{\epsilon b}{\delta_h})$ where $\mathcal{O}(\epsilon)$ is the order of maximum strain. These are verified once the final solution of warping is obtained. Using the two Eqs. (4.11a) and (4.11b) in the set of Eq. (4.16) followed by a phantom explained in Hodges et al. [70]. There, the terms violating the constraints mentioned in Eqs. (4.12), (4.13) and (4.14) are killed, leading to determination of the order of $\Delta_i's$ as $\mathcal{O}(\epsilon\delta_h b)$. The geometry also implies a relation among unknown warping variables as

$$(\Delta_{1,3} + \phi_1)^2 + (\Delta_{2,3} + \phi_2)^2 + (1 + \Delta_{3,3})^2 = (1+e)^2 \tag{4.17}$$

where $e = \mathcal{O}(\epsilon)$. A consequence of this relation in Eq. (4.17) is that $\phi_1 = -x_2\kappa_1 + \mathcal{O}(\epsilon)$ and $\phi_2 = -w_{3,2} + \mathcal{O}(\epsilon)$. Thus, these higher order terms do not appear in the classical analysis but do appear in the shear deformable beam analysis. Now, the 3-D beam strain measures can be represented in the form of 2-D shell strain measures with the help of the equation

$$\Gamma_{\alpha\beta} = \epsilon_{\alpha\beta} + x_3\rho_{\alpha\beta} \tag{4.18}$$

where $\epsilon_{\alpha\beta}$ are the membrane strains and $\rho_{\alpha\beta}$ are the middle surface bending curvatures. The expressions for these 2-D strain and curvature measures for a classical analysis (where all terms with order of magnitude higher than $\mathcal{O}(\epsilon)$, $\mathcal{O}(\frac{\epsilon\delta_t}{\delta_h})$ and $\mathcal{O}(\frac{\epsilon^2}{\delta_h^2})$ are neglected and

terms with these orders of magnitude are retained, which involve the interaction of small parameters) are represented as

$$\begin{aligned}
\epsilon_{11} &= \overline{\gamma}_{11} - x_2\overline{\kappa}_3 + k_1 x_2^2 \overline{\kappa}_1^2 \\
2\epsilon_{12} &= k_1(x_2 w_{3,2} - w_3) + w_{1,2} \\
\epsilon_{22} &= w_{2,2} \\
\rho_{11} &= \overline{\kappa}_2 \\
\rho_{22} &= -w_{3,22} \\
2\rho_{12} &= -2\overline{\kappa}_1
\end{aligned} \tag{4.19}$$

As the strip is being considered as a 2-D elastic body, the strain energy density (i.e., energy per unit middle surface area) can be written as

$$\mathcal{U}_{2D} = \frac{1}{2} \begin{Bmatrix} \epsilon_{11} \\ \epsilon_{22} \\ 2\epsilon_{12} \\ \rho_{11} \\ \rho_{22} \\ 2\rho_{12} \end{Bmatrix}^T \begin{bmatrix} A' & B' \\ B'^T & D' \end{bmatrix} \begin{Bmatrix} \epsilon_{11} \\ \epsilon_{22} \\ 2\epsilon_{12} \\ \rho_{11} \\ \rho_{22} \\ 2\rho_{12} \end{Bmatrix} \tag{4.20}$$

where A', B' and D' are 3×3 matrices for membrane, bending and coupling stiffness effects, respectively. The beam strain energy density is given by $\mathcal{U}_{1D} = \langle \mathcal{U}_{2D} \rangle$. In order to carry out this integration, it is required to obtain the unknown functions of x_2 in Eq. (4.20). These are obtained by minimizing the strain energy functional $\mathcal{U} = \int_0^l \mathcal{U}_{1D} dx_1$ subject to the constraints provided in Eqs. (2.4), (4.12), (4.13) and (4.14). Finally, the warping field obtained after minimization (for closed form expressions, maximum permissible order of k_2 is $\mathcal{O}(\frac{\sqrt{\epsilon}}{b})$) is written in Eq. (4.21). It shows that the initial twist and curvature enter into the solution for the zeroth-order warping solution leading to a strain energy correct up to

the first order due to the presence of δ_h in the denominator. Thus,

$$\begin{aligned}
w_1 &= -\frac{1}{6}(k_1\nu x_2(b^2+x_2)^2\overline{\kappa}_2 \\
w_2 &= -\frac{1}{6}\nu\left(k_2\nu x_2\left(x_2^2-b^2\right)\overline{\kappa}_2+\left(b^2-3x_2^2\right)\overline{\kappa}_3+2k_1x_2^3\overline{\kappa}_1+6x_2\overline{\gamma}_{11}\right) \\
w_3 &= -\frac{1}{6}\nu\left(b^2-3x_2^2\right)\overline{\kappa}_2+3k_1\left(\nu^2-1\right)x_2\left(7b^4-10b^2x_2^2+3x_2^4\right)
\end{aligned} \tag{4.21}$$

For the CLST or CLPT, the sectional strain energy for this problem is obtained as:

$$\mathcal{U}_{1D}=\frac{1}{2}\left\{\begin{array}{c}\overline{\gamma}_{11}\\ \overline{\kappa}_1\\ \overline{\kappa}_2\\ \overline{\kappa}_3\end{array}\right\}^T[S_{cl}]\left\{\begin{array}{c}\overline{\gamma}_{11}\\ \overline{\kappa}_1\\ \overline{\kappa}_2\\ \overline{\kappa}_3\end{array}\right\} \tag{4.22}$$

where the non-zero components of the classical stiffness matrix are

$$\begin{aligned}
(S_{11})_{cl} &= 2Embh \\
(S_{12})_{cl} &= \frac{2}{3}Emk_1b^3h \\
(S_{22})_{cl} &= \frac{bEmh\left(6b^4k_1^2(\nu+1)+5h^2\right)}{15(\nu+1)} \\
(S_{33})_{cl} &= \frac{1}{6}Emb^3h\left[1+\frac{4\nu b^4k_2^2}{15h^2}\right] \\
(S_{44})_{cl} &= \frac{2}{3}Emb^3h\left[1-\frac{8\left(1-\nu^2\right)b^4k_2^2}{105h^2}\right]
\end{aligned} \tag{4.23}$$

In this section, a theoretical framework was developed that considers the small parameters associated with the wall thickness a priori. It was followed by use of Classical Laminated Plate Theory [CLPT] or Classical Laminated Shell Theory [CLST] as starting point. Further, the variational-asymptotic procedure is applied with the help of small parameters in the transformed problem. Here the classical stiffness matrix is obtained in which the in-plane bending stiffness does not demonstrate any non-physical phenomenon. Though this approach solves the issue of obtaining a negative stiffness value, there are a few draw-

backs. This approach is not feasible to be incorporated into the existing VABS framework. It may not handle arbitrary cross-sectional geometries. It can accommodate wide range of problems which are plate-like or shell-like geometries, but it cannot be applied to solve the problem of obtaining negative stiffness values in the thick composite beams demonstrated in Sec. 4.2.

4.3.2 Approach 2: Segmentation of the Cross Section

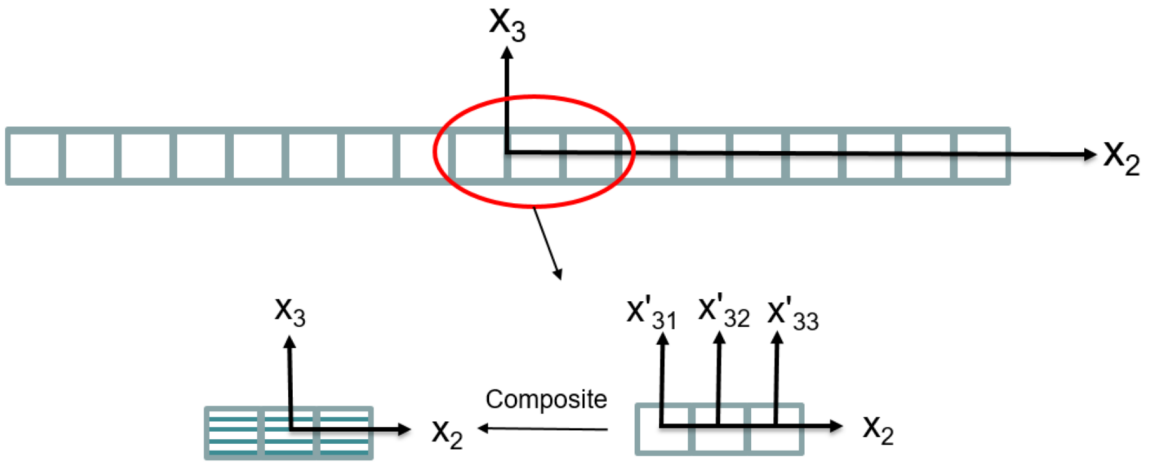

Figure 4.7: Generalized technique avoiding small parameters entering the formulation

Though the approach mentioned in Section 4.3.1 captures the effect of destructive interference of small parameters, it is not yet feasible to incorporate into the existing VABS framework for an arbitrary cross-sectional geometry. To avoid this issue, an approach similar to the Mechanics of Structural Genome (MSG) [107], is implemented. From the detailed investigation in Sec. 4.2, it is observed, if one of the three small parameters (h/b, bk_2 or E_2/E_1) is eliminated from the problem, the analysis doesn't incur any non-physical effects. While the approach employing the CLPT or CLST attempts to capture the interaction of two small parameters in the cross section, this approach aims to take away the effect of the small parameter associated with the thickness of a thin-walled beam (i.e., h/b where h is the thickness and b is the width of the beam). In this approach, the sectional analysis of thin-walled geometry is discretized into a number of smaller components, with an aspect

ratio that avoids the interaction of two small parameters in the order of magnitude analysis by eliminating one of the small parameters entirely. A schematic for this approach is provided in Fig. 4.7. The next step is an application of the variational-asymptotic approach as laid out in Sec. 2.3, on each of these discretized elements along with appropriate continuity and constraints on warping variables and their derivatives with respect to the cross-sectional coordinates. This methodology is implemented on the cases used in Sec. 4.2 for investigating the causes of negative stiffness values in the Timoshenko stiffness matrix. Results from those cases are discussed in various subsections below following the order from Sec. 4.2.

Varying Width of the Beam Section

In this case, we took a square beam section of dimensions 0.06×0.06 in. along with an initial curvature of 0.08 rad/in and orthotropic material properties chosen in Sec. 4.2.1. Then, the width is increased from 0.06 in. to 1.2 in. which is 20 times the height, thus making it gradually turn into a thin-walled beam section. Finally, the in-plane bending stiffness is obtained for the beam section while increasing the width. Fig. 4.8 shows that the non-physical behavior of the beam was eliminated and the in-plane stiffness value (S_{66}) was no longer decreasing with the increase in the width.

Variation in the Initial Curvature

For this case, a thin-walled beam of sectional dimensions 1.2×0.06 in. is chosen as the width is 20 times the thickness. The material properties are chosen to be the same as previous case and the out-of-plane initial curvature is increased from 0.001 to 0.08 rad/in. Figure 4.9 plots the change in the in-plane bending stiffness, S_{66}, as the initial curvature is increased. There is no appearance of any non-physical effect. There is a very slight increase in the in-plane bending stiffness with the increase in out-of-plane initial curvature whereas it started decreasing with an increase in the initial curvature when computed with VABS. Figure 4.10 shows that difference between the solutions obtained from the segmentation

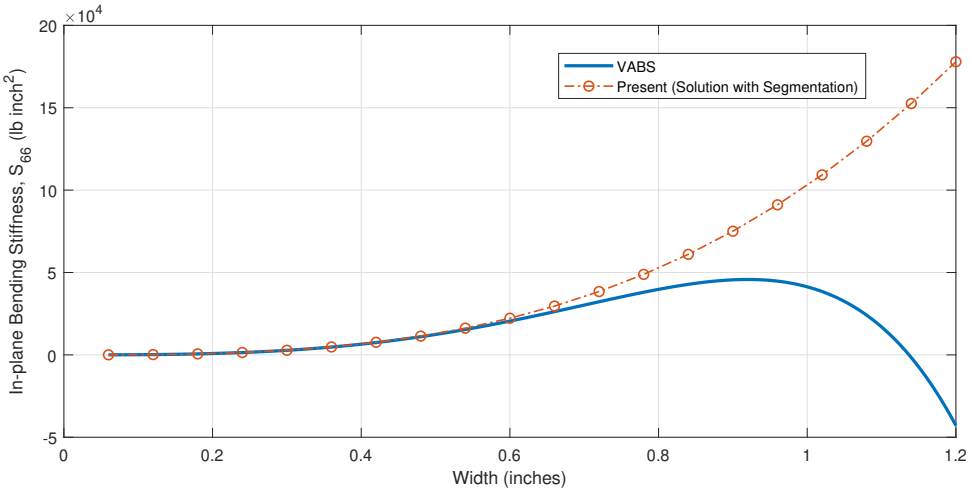

Figure 4.8: Variation in the S_{66} stiffness obtained after segmentation vs. the solution from VABS when an orthotropic beam's width is increased from 0.06 in. to 1.2in.

approach (current approach) and VABS.

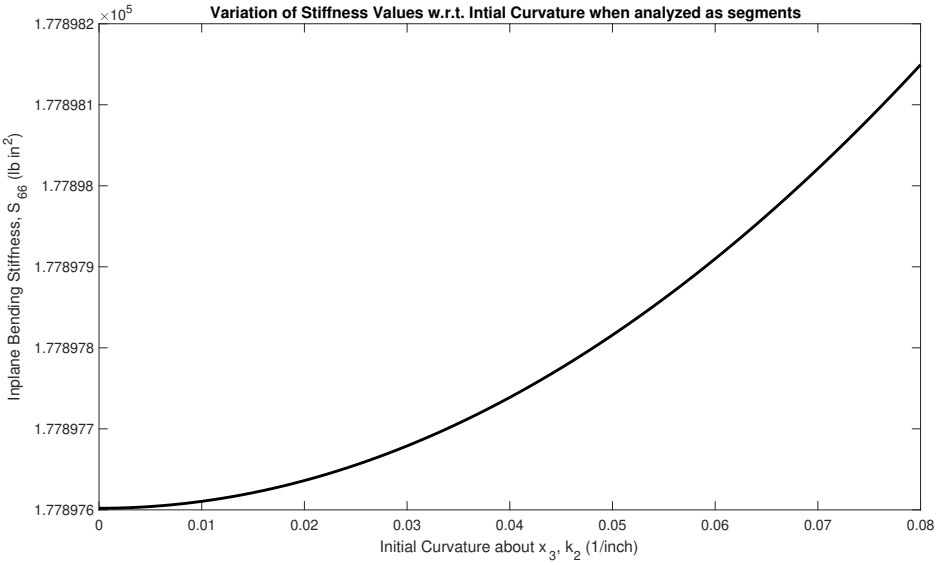

Figure 4.9: Variation in the S_{66} stiffness obtained after segmentation when an orthotropic beam's initial out-of-plane curvature is increased from 0.001 to 0.08 rad/in.

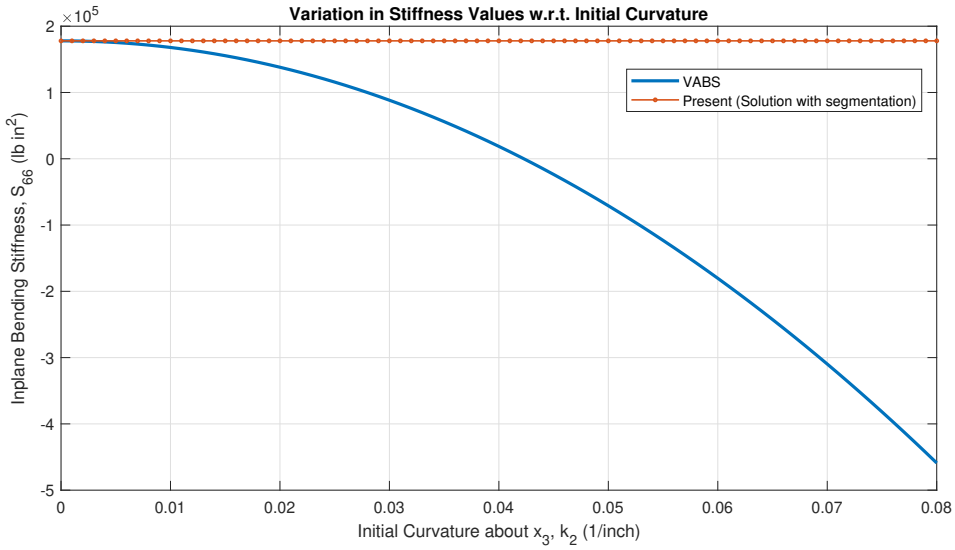

Figure 4.10: Variation in the S_{66} stiffness obtained after segmentation vs. the solution from VABS when an orthotropic beam's initial out-of-plane curvature is increased from 0.001 to 0.08 rad/in.

Variation in Ratio of the Material Properties

Finally, the current approach is applied for solving the problems where the ratio of material properties E_1/E_2 or E_1/E_3 is altered. For these cases, a thin-walled beam of the same cross-sectional dimensions in the previous case with an out-of-plane initial curvature of 0.08 rad/in. With the present approach, negative stiffness values are not obtained when the ratio of material properties, E_1/E_2 is increased from 0.01 to 200. The plot for the change in the in-plane stiffness is present in Fig. 4.11. Also, Fig. 4.12 provides a comparison of the results obtained from the present approach and VABS. During the investigation, we considered another case where the ratio of material properties E_1/E_3 was altered. Figure 4.13 contains plots of the in-plane bending stiffness values when E_1/E_3 is increased from 0.01 to 200 when the solution is obtained from the present approach and VABS. The percentage difference between the two results when compared to the results obtained from VABS is depicted in Fig. 4.14. The maximum difference in the values obtained by the present approach as compared to VABS is less than 0.04%. This indicates that the results obtained

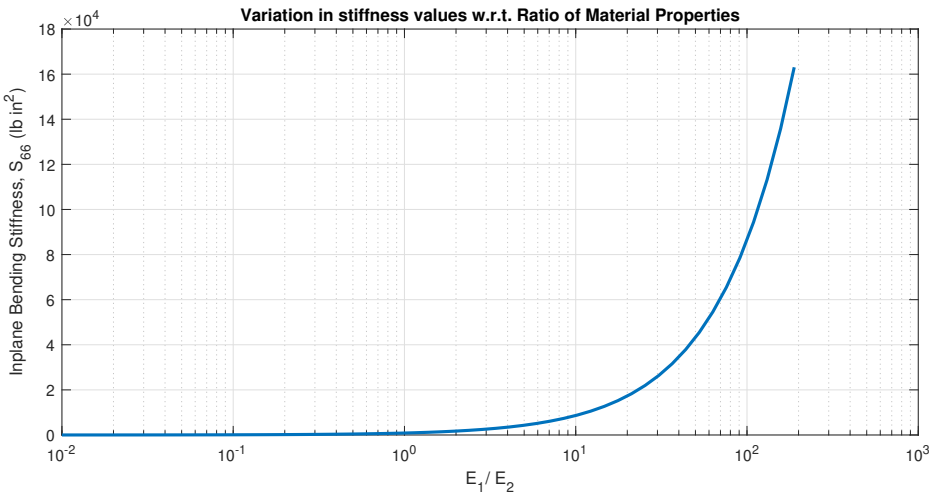

Figure 4.11: Variation in the S_{66} stiffness obtained after segmentation when E_1/E_3 is increased from 0.01 to 200 in an initially curved, thin-walled beam

from VABS for the stiffness values when material ratio E_1/E_3 is increased, are correct and do not have any discrepancy as observed in other cases discussed.

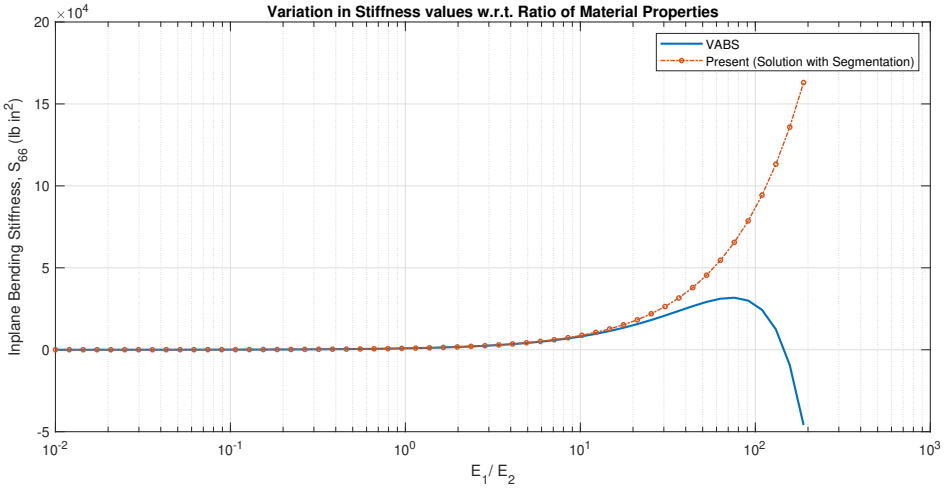

Figure 4.12: Variation in the S_{66} stiffness obtained after segmentation vs. the solution from VABS when E_1/E_2 is increased from 0.01 to 200 in an initially curved, thin-walled beam

The methodology mentioned in this does take care of the non-physical behavior of VABS, but there are still some issues concerning the results. It has been observed that the overall results for torsional stiffness and the stiffness values of the terms coupled with

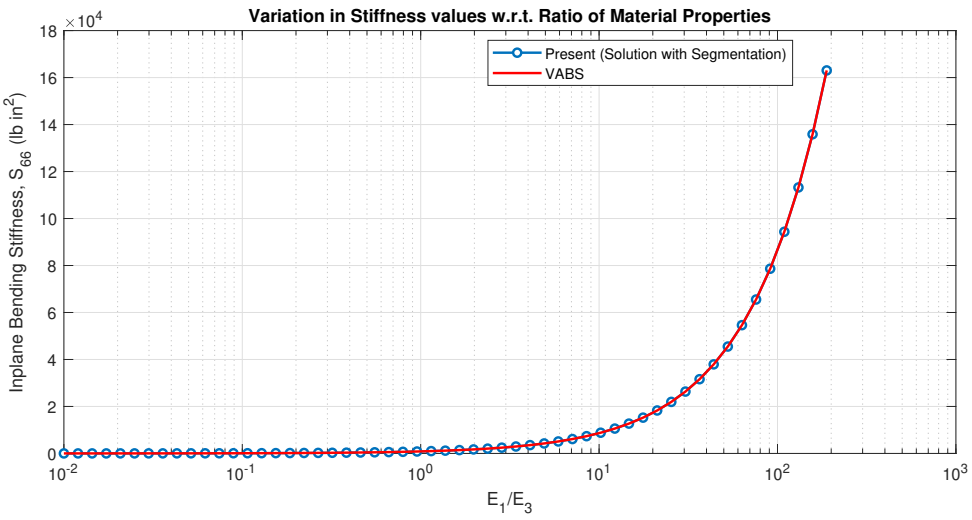

Figure 4.13: Variation in the S_{66} stiffness obtained after segmentation vs. the solution from VABS when E_1/E_3 is increased from 0.01 to 200 in an initially curved, thin-walled beam

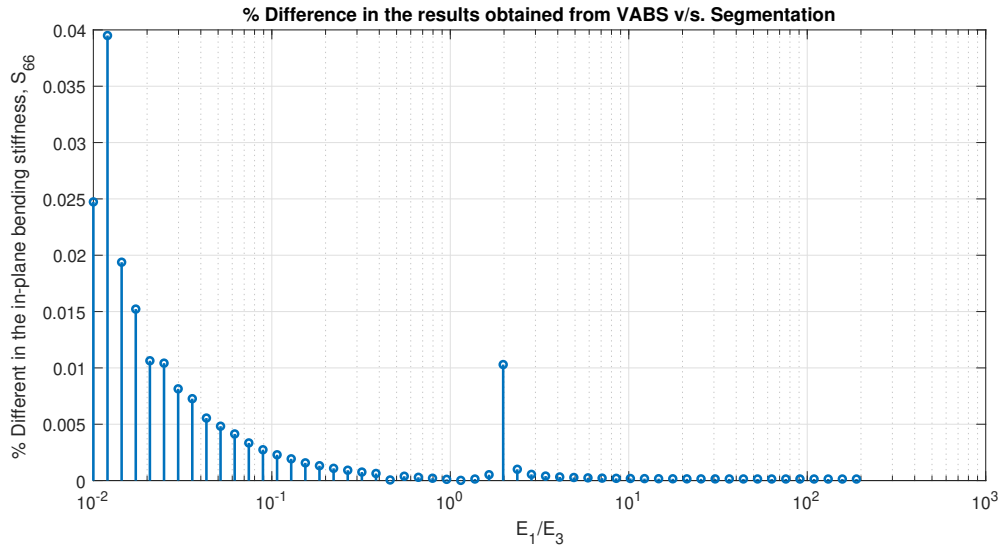

Figure 4.14: Percentage difference in the results obtained from VABS vs. the segmentation methodology when E_1/E_3 is increased from 0.01 to 200 in an initially curved, thin-walled beam

torsion are not satisfactory. For example, let's take an isotropic beam of dimensions 0.06×0.06 in. along with an initial curvature of 0.08 rad/in and Young's modulus 20.49×10^6 psi. It has already been established that results obtained from VABS are accurate for isotropic materials so this case considers an orthotropic material. Then, the width is increased from

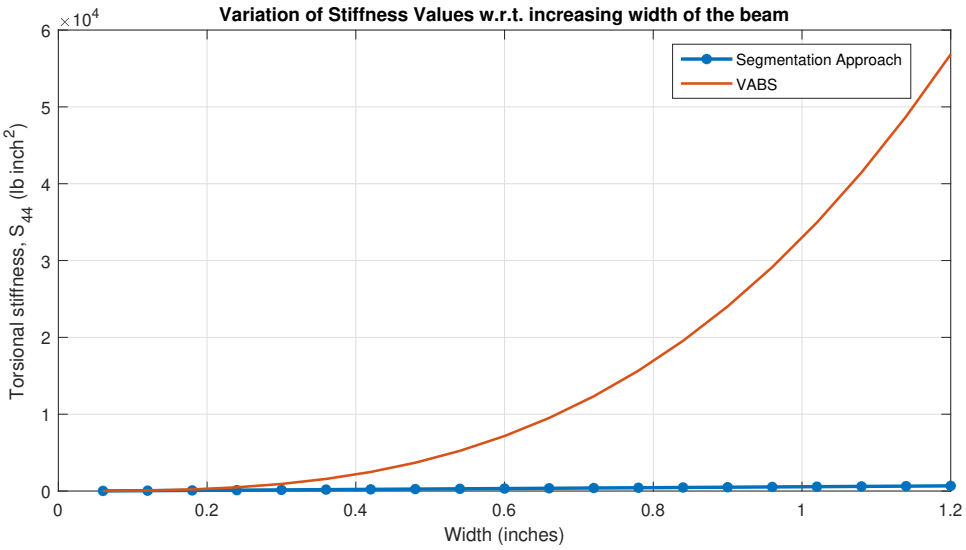

Figure 4.15: Variation in the S_{44} stiffness obtained after segmentation vs. the solution from VABS when a beam's width is increased from 0.06 in. to 1.2in.

0.06 in. to 1.2 in. which is 20 times the height, thus making it gradually turn into a thin-walled beam section. Figure 4.15 show how the approach employing segmentation of a thin-walled section is not able to recover the correct torsional stiffness values that VABS is able to generate. Because of this, the segmentation approach can not be used to solve the problems involving this non-physical behavior of the stiffness matrix.

4.3.3 Approach 3: Theoretical Modification

From the implementation of different approaches mentioned in the previous sections and the results obtained from the respective chosen test cases, it is inferred that the effort to either make use of the thickness-to-width ratio is a small parameter or completely eliminate it from the problem is not sufficient as it doesn't satisfy the requirement of generality or provide completely correct results. Moreover, the approaches tried previously do not address the issue of negative stiffness values for the in-plane stiffness in the cases of thick composite beams because in that problem, the small parameter related to thickness-to-width ratio should not appear. Hence, it is important to perform a robust order of magnitude analysis

before truncating the strain energy expression for zeroth-order and second-order strain energies for application of the VAM. It is speculated that some terms which have significantly large magnitudes are being skipped in the computation of strain energy. This error in the orders of magnitude analysis is potentially caused by not accounting for different orders of magnitude of material constants such as Young's moduli in different directions. Seemingly, those terms appear because of the interaction of various small parameters (i.e., curvature, thickness-to-width ratio and the material properties).

As shown in Sec. 4.2, the ratio of material properties such as E_2/E_1 affects the current problem. In the VAM formulation till now, this small parameter was not being considered at all. Equation 2.16 represents the strain energy expression which is further expanded with in Eq. (2.36) were the orders of magnitudes are listed. From the derivation, it is evident that the material matrix (D) remains intact in the entire process and the terms are separated by their orders of magnitudes in the expressions for 3-D strain. This leads to truncation of strain energy expression based on the order of magnitude of terms in the expression of 3-D strain only, which is inconsistent. In case of isotropic material, the ratio of material properties in different directions would possess a value of unity. When this multiplies a term with geometric small parameter cubed, it would have been neglected in zeroth-order and second-order analysis in the previous approach. Now, however, in the current approach, this term needs to be retained based on the orders of magnitude for E_1 and E_2. For example, for an orthotropic material, the material matrix is obtained as

$$\begin{bmatrix} 2.05157 \times 10^7 & 0. & 0. & 42911. & 0. & 42911. \\ 0. & 7.88077 \times 10^6 & 0. & 0. & 0. & 0. \\ 0. & 0. & 7.88077 \times 10^6 & 0. & 0. & 0. \\ 42911. & 0. & 0. & 109980. & 0. & 33056.8 \\ 0. & 0. & 0. & 0. & 7.88077 \times 10^6 & 0. \\ 42911. & 0. & 0. & 33056.8 & 0. & 109980. \end{bmatrix} \tag{4.24}$$

whereas for an isotropic material

$$\begin{bmatrix} 2.75827 \times 10^7 & 0. & 0. & 1.18212 \times 10^7 & 0. & 1.18212 \times 10^7 \\ 0. & 7.88077 \times 10^6 & 0. & 0. & 0. & 0. \\ 0. & 0. & 7.88077 \times 10^6 & 0. & 0. & 0. \\ 1.18212 \times 10^7 & 0. & 0. & 2.75827 \times 10^7 & 0. & 1.18212 \times 10^7 \\ 0. & 0. & 0. & 0. & 7.88077 \times 10^6 & 0. \\ 1.18212 \times 10^7 & 0. & 0. & 1.18212 \times 10^7 & 0. & 2.75827 \times 10^7 \end{bmatrix} \tag{4.25}$$

Equation (4.24) represents how the orders of some magnitudes change drastically in the case of orthotropic material as compared to the terms in material matrix for an isotropic material, Eq. (4.25). It is important to consider this change as the 3-D strain expressions are multiplied with the material matrix for the evaluation of strain energy.

So, a new approach for the variational formulation identifies terms in the strain energy expression to be retained based on a more robust order of magnitude analysis. A detailed study of the terms associated with both geometric and material properties is carried out. Further, the terms are characterized based on their order of magnitudes in terms of strains and the appropriate terms were chosen to be retained in a specific order of strain energy during the VAM process. The details of this process are present in Appendix A. Eventually, the implementation of this process leads to an integrated solution of the current and previous problems associated with small parameters. Through this work, a specific case was solved which considers an orthotropic strip (1.2×0.06 in.) with out-of-plane initial curvature of 0.08 rad/in. The material properties of the strip are such that Young's Moduli $E_1 = 20.59 \times 10^6$ psi and $E_2 = E_3 = 1 \times 10^5$ psi, bulk modulus, $G_{12} = G_{13} = G_{23} = 8 \times 10^6$ psi, and Poisson's ratio, $\nu_{12} = \nu_{13} = 0.3$ and $\nu_{23} = 0.335$. Figure 4.16 represents the 3-D displacement field along the span of the orthotropic strip such that u_1, u_2 and u_3 are plotted at the midpoint of the top edge in each cross section along the span. The maximum error in the results obtained from modified VABS and 3-D FEM is 0.02%. It is observed that the non-physical effects are now absent and the sectional

analysis is able to obtain correct stiffness values and hence recover correct displacement results.

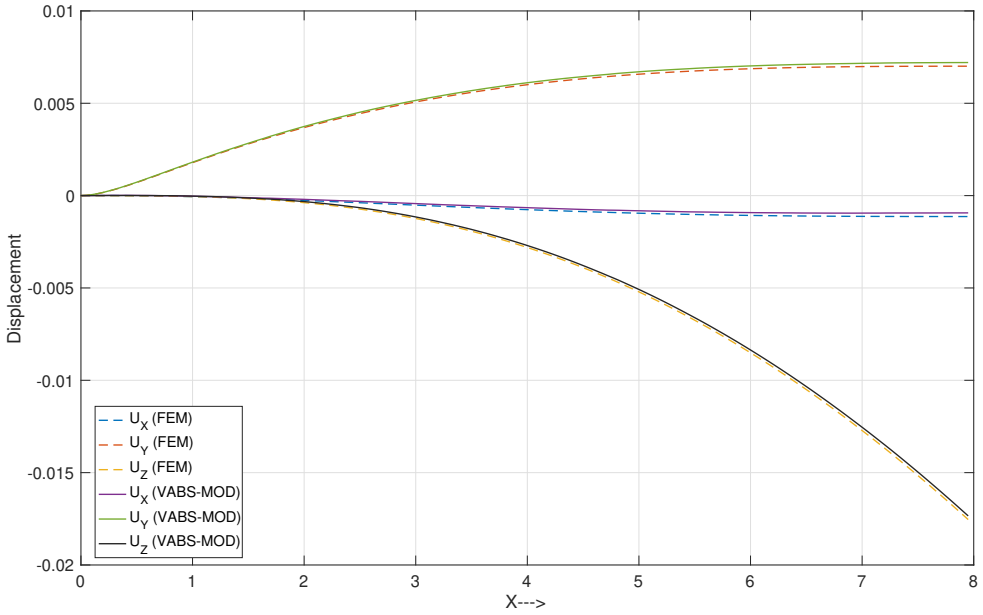

Figure 4.16: Displacement field for an orthotropic strip with out-of-plane initial curvature under a tip transverse load

Part 3

Nonlinear Beam Analysis (1-D)

CHAPTER V

NONLINEAR 1-D BEAM ANALYSIS WITH STRUCTURAL DAMPING

With the 2-D cross-sectional analysis complete, it is now important to execute the 1-D beam theory to complete the beam analysis so that the overall 3-D results can be computed for a given beam problem. It is interesting to note that the stiffness/flexibility matrix obtained from the 2-D cross-sectional analysis has the best set of elastic constants for any composite beam. The matrix is fully populated in case of a beam without any geometrical symmetries and made of generally anisotropic materials. Thus, all the fundamental deformation modes, including extension, shear, torsion and bending could be elastically coupled. In this chapter, enhancements to the Geometrically Exact Beam Theory (GEBT) are laid out in the form of a methodology to implement damping and the next chapter accommodates piezoelectric effects.

5.1 Introduction

Damping has been used as a micro-structural research tool for clarifying mechanisms that lead to inelastic behavior and energy dissipation in materials. Damping is essentially a rheological property involving 'deformation' and 'flow' of matter. Deformation is a generic term which refers to the alteration of the shape or size of a collection of matter under application of external forces. The term 'flow' is used when deformation is dependent on time. In this paper, the term rheology encompasses all stress-strain-time properties of

material and structural systems. For example, comparing different materials A and B under the same conditions (same boundary conditions, same geometrical dimensions), the same magnitude of periodic forcing function with the same frequency of excitation, material A may oscillate longer (or shorter) with larger (or smaller) amplitude than material B. This is primarily due to differences in material properties. The damping force due to internal molecular friction in material A could be less (or more) than the damping force due to internal molecular friction in material B. This kind of damping is called material damping, and on a macro-scale it brings in a widely studied effect, viz., structural damping.

Another type of damping encountered in a vibrating system is introduced through the surrounding medium in which the vibration takes place. For example, a vibratory structural system will oscillate much longer in air than in water. This kind of damping is frequently modeled as viscous damping, the force of which depends on properties of the surrounding medium and the motion. In general, then, one can classify damping into two basic categories: material and non-material damping or internal and external damping.

5.1.1 Structural Damping

In the modeling of the dynamics of rotor blades, external damping is taken into account mostly by the modeling of aerodynamic loads. However, to incorporate structural damping into a geometrically exact beam model is a challenge and is the subject of this paper. Here, structural damping refers to the capacity of a structure or structural component to dissipate energy or to remove structural vibration or some of the energy associated therewith. Beside intermolecular friction there are many other factors that may lead to structural damping. These include disordered atomic arrays such as grain and sub-grain boundaries, inclusions, point defect relaxations, certain types of dislocation motions, macro-thermoelasticity, stress amplitude, internal forces, number of cycles, quality of the surface, temperature and other imperfections in microstructure that display inelastic micromechanisms, the behavior of which may be nonlinear [94].

It becomes very important to understand structural damping even though to do so requires implementing a suitable 3D damping model into a complex formulation. This is mainly because structural damping affects the dynamic behavior of structures as demonstrated by Merett [115] and vibration damping has become an important area of research and application in the recent past as explained in detail by Sun and Liu [159]. Banks and Inman [11] studied damping in composite cantilever beams, performing dynamic tests for various types damping phenomenon. These included air damping, strain-rate damping (Kelvin-Voigt model type), spatial hysteresis damping (differential rates of rotation causing internal friction) and time hysteresis damping (time history of strain is considered). Finally, they used the method of least squares to identify damping coefficients and concluded that a spatial hysteresis model combined with a viscous damping model will result in best quantitative agreement. A recent two-part book by Adhikari [2, 4] offered descriptions of almost all known types of damping models, as well as providing details of analysis techniques for those models. Additionally, the text also includes other phenomenological models proposed by Lesieutre and Kosmatka as well as a method based on integro-patial-differential equations by Friswell et al., explained later in this section.

Lazan [94] provides a general constitutive law for a linear viscoelastic material, in other words, a constitutive law for a material with linear damping can be written as:

$$\begin{aligned}\left[a_0 + a_1\left(\frac{\partial}{\partial t}\right) + a_2\left(\frac{\partial^2}{\partial t^2}\right) + \cdots + a_n\left(\frac{\partial^n}{\partial t^n}\right)\right]\sigma = \\ \left[b_0 + b_1\left(\frac{\partial}{\partial t}\right) + b_2\left(\frac{\partial^2}{\partial t^2}\right) + \cdots + b_n\left(\frac{\partial^n}{\partial t^n}\right)\right]\epsilon\end{aligned} \tag{5.1}$$

where $a_1, a_2, \ldots, a_n$ and $b_1, b_2, \ldots, b_n$ are constants and could have influence on material properties and constants. For a reduced-order Kelvin-Voigt Model, higher-order derivatives (second order or higher in ϵ and first- or higher-order in σ) are neglected in equation (5.1) to obtain:

$$a_0\sigma = \left[b_0 + b_1\left(\frac{\partial}{\partial t}\right)\right]\epsilon \tag{5.2}$$

Similarly, neglecting different higher-order terms in the same expression results in different rheological models, such as the Maxwell model

$$\left[a_0 + a_1\left(\frac{\partial}{\partial t}\right)\right]\sigma = b_0\epsilon \tag{5.3}$$

and the linear solid model

$$\left[a_0 + a_1\left(\frac{\partial}{\partial t}\right)\right]\sigma = \left[b_0 + b_1\left(\frac{\partial}{\partial t}\right)\right]\epsilon \tag{5.4}$$

A linear solid model is also sometimes referred to as combination of Kelvin-Voigt and Maxwell models, and sometimes as a Zener model. Many researchers have compared these above models for applications to various problems.

Hoseini [137] uses a generalized Hooke's law for viscoelastic materials,

$$\begin{Bmatrix} \sigma_1(x_1,x_2,t) \\ \sigma_2(x_1,x_2,t) \\ \sigma_3(x_1,x_2,t) \end{Bmatrix} = \int_{-\infty}^{t} \begin{bmatrix} c_{11}(t-\tau) & c_{12}(t-\tau) & 0 \\ c_{21}(t-\tau) & c_{22}(t-\tau) & 0 \\ 0 & 0 & c_{66}(t-\tau) \end{bmatrix} \begin{Bmatrix} \dot{\epsilon}_1(x_1,x_2,t) \\ \dot{\epsilon}_2(x_1,x_2,t) \\ \dot{\epsilon}_3(x_1,x_2,t) \end{Bmatrix} d\tau \tag{5.5}$$

which has a new form of constitutive equation that is claimed to bridge the differential and integral form of linear elasticity. Use of a Kelvin-Voigt model in prior art is criticized and the article uses Maxwell and Zener models in the theoretical formulation.

Moczo et al. [88] compare the use of aforementioned common rheological models and perform a comparative study as well. Some researchers do present phenomenological models to suit a particular experiment or problem. Lesieutre [100] claims that experiments on typical built-up, lightly damped aerospace structures show weak frequency dependent damping, but the rheological models mentioned above are strongly dependent on frequency. Based on this fact, a rotation-based phenomenological model is proposed in which internal shear force, for a beam in bending, e.g., is proportional to the time rate of change of the slope.

Lesieutre [99] extended such phenomenological models to include membrane loads.

Beyond this, it is important to note, of all the relationships or models used to describe rheological behavior of materials, the most commonly used one for viscoelastic materials is the complex notation method, but it is less relevant for rotor blade like structures. However, Bilasse [17] proposed a complex mode based numerical method in which the harmonic balance method is coupled to a one-mode Galerkin procedure to develop a nonlinear amplitude-frequency and amplitude-loss factor relationship for nonlinear vibrations in sandwich beams.

On the other hand, Mendiguren [114] made use of fractional derivatives, use of which basically modifies the Kelvin-Voigt model to have the form $\sigma = a\frac{d^{\alpha}\epsilon}{dt^{\alpha}}$ where α takes a value between 0 and 1. It is demonstrated that fractional derivative model is better in representing the elastic to elasto-plastic transition but the drawback is the requirement of huge computational power to solve the problem. Another method demonstrated by Kienholz [75] uses viscous damping to build a finite element model for a three-layer laminate consisting a viscoelastic material layer and modal damping ratios are obtained by using modal strain energy method. This method was also used [84] to tackle problems in which viscoelastic patches in a fan blade were introduced to increase the damping in the chord-wise bending modes, thus enhancing blade fatigue characteristics. Similarly, in other articles [16, 85] a simple viscous damping model is used for viscoelastic beams and co-cured laminates to conclude that damping coefficients are affected by mode number and applied loads, but not significantly by cure cycle temperatures. Friswell et al. [98] considered dynamics of Euler-Bernoulli beams with non-local and non-viscous damping by considering a formulation based on integro-partial-differential equations. Adhikari et al. [153] uses an exponential form in order to model non-viscous damping with symmetric nonlinearities in a forced Duffing oscillator, such as when the damping force is written as

$$f_d(t) = \int_0^t c\mu e^{-\mu(t-\tau)} d\tau \tag{5.6}$$

The governing differential equation can be written as

$$m\frac{d^2x}{d\hat{t}^2} + c\int_{\hat{\tau}=0}^{\hat{\tau}=\hat{t}} \mu e^{-\mu(\hat{t}-\hat{\tau})}\frac{dx}{d\hat{\tau}}d\hat{\tau} + kx + \alpha k x^3 = A\cos(\Omega\hat{t}) \tag{5.7}$$

Erturk et al. [96] introduce softening and dissipative nonlinearities and based on the model chosen, backbone curves with a linear $(-x^2\text{sgn}(x))$ or quadratic variation $(-x^3)$ of the peak response frequency versus response amplitude are obtained. Damping terms are introduced through the virtual work done by non-conservative forces, viz.,

$$\overline{\delta\mathcal{W}} = -\int_0^l \left[\hat{b}_1 u_3\ \text{sgn}(u_3) + \hat{b}_2 u_3^2\right]\text{sgn}(\dot{u}_3)\delta u_3 dx_1 \tag{5.8}$$

Note that the overbar indicates that $\overline{\delta\mathcal{W}}$ is one quantity and not variation of a functional $\mathcal{W}$. Using the damping terms contributing to the expression of virtual work done by non-conservative forces for a bimorph, the governing equation is obtained as:

$$\ddot{x} + \Big(b_1 x\ \text{sgn}(x) + b_2 x^2\Big)\text{sgn}(\dot{x}) + k_1 x + k_2 x^2\text{sgn}(x) = -m\ddot{z}(t) \tag{5.9}$$

There also have been other researchers who have attempted to implement a nonlinear damping model. Alijani et al. [8] considers out-of-plane excitation and resulting nonlinear vibrations of thin rectangular plates and curved panels. Alijani et al. use Donnell's nonlinear shell theory and the governing equations contain quadratic and cubic nonlinear stiffness terms. It has been observed that structures display larger dissipation in large amplitude vibrations, resulting in smaller increases in peak amplitudes of successive forces. This phenomenon is due to a nonlinear change of damping during large amplitude vibrations. This shows that larger damping is observed in large amplitude vibrations and provides motivation to consider nonlinear damping. While Lakes presented viscoelastic measurement techniques [91], the authors of Ref. [11, 84, 88, 94, 114, 115, 137, 159] have provided experimental validations as well.

5.2 Mixed Formulation of the GEBT with Structural Damping

The beam theory implemented in DYMORE [12], a tool for multibody dynamic simulations, is based on a formulation that regards displacement and rotation as the fundamental variables. On the other hand, work presented in various articles [30, 69, 148] demonstrate the utility of including intrinsic variables, such as force and moment variables. In the present approach, a mixed formulation [186] implemented in a tool named GEBT is modified to accommodate structural damping.

The behavior of beams is governed by the extended Hamilton's Principle as shown

$$\int_{t_1}^{t_2} [\delta(\mathcal{K} - \mathcal{U}) + \overline{\delta\mathcal{W}}]dt = 0 \tag{5.10}$$

where t_1 and t_2 are arbitrary fixed times, $\mathcal{K}$ is the kinetic energy, $\mathcal{U}$ is the internal energy, δ is the Lagrangian variation for a fixed time, and $\overline{\delta\mathcal{W}}$ is the virtual work by applied loads.To implement a mixed formulation for the 1-D beam analysis, variables in Eq. (5.10) are represented in terms of the intrinsic variables. So, the variation of strain energy can be written as:

$$\int_0^l \delta\mathcal{U}dx_1 = \int_0^l \left[\delta\gamma^T \left(\frac{\partial\mathcal{U}}{\partial\gamma}\right)^T + \delta\kappa^T \left(\frac{\partial\mathcal{U}}{\partial\kappa}\right)^T\right] dx_1 \tag{5.11}$$

where

$$F = \left(\frac{\partial\mathcal{U}}{\partial\gamma}\right)^T \tag{5.12a}$$

$$M = \left(\frac{\partial\mathcal{U}}{\partial\kappa}\right)^T \tag{5.12b}$$

Substituting values from Eq. (5.12) into Eq. (5.11), one obtains

$$\int_0^l \delta\mathcal{U}dx_1 = \int_0^l [\delta\gamma^T F + \delta\kappa^T M]dx_1 \tag{5.13}$$

The virtual rotation can then be expressed as:

$$\widetilde{\overline{\delta\psi}} = -\delta C C^T \tag{5.14}$$

Upon differentiating with respect to x_1 and using relation $\delta\kappa = \delta K$ obtained by operating on Eq. (2.13b), from Eq. (2.14b) one may obtain the variation of the generalized moment strains as

$$\delta\kappa = \overline{\delta\psi}' + \widetilde{K}\overline{\delta\psi} \tag{5.15}$$

To obtain variation of the generalized force strain measures, using derivation from Hodges [69], the variation of Eq. (2.14a) is expressed as

$$\delta\gamma = \delta C(e_1 + u' + \widetilde{k}u) + C(\delta u' + \widetilde{k}\delta u) \tag{5.16}$$

To eliminate u, a column matrix of virtual displacements $\overline{\delta\mathbf{q}} = {}^b\delta(\mathbf{u})$ is introduced which is only in the b basis just like the displacement vector. Subsequently, one obtains

$$\delta\gamma = \overline{\delta q}' + \widetilde{K}\overline{\delta q} + (\widetilde{e}_1 + \widetilde{\gamma})\overline{\delta\psi} \tag{5.17}$$

After substituting values for $\delta\gamma$ from (5.17) and for $\delta\kappa$ from (5.15) into Eq. (5.13), the variation in strain energy density is represented as:

$$\int_0^l \delta\mathcal{U} dx_1 = \int_0^l \left[\left[\overline{\delta q}' + \widetilde{K}\overline{\delta q} + (\widetilde{e}_1 + \widetilde{\gamma})\overline{\delta\psi}\right]^T F + \left[\overline{\delta\psi}' + \widetilde{K}\overline{\delta\psi}\right]^T M \right] dx_1 \tag{5.18}$$

Similar to the strain energy, the variation in kinetic energy can also be expressed in intrinsic quantities as

$$\int_0^l \delta\mathcal{K} dx_1 = \int_0^l \left[\delta V^T \left(\frac{\partial\mathcal{K}}{\partial V}\right)^T + \delta\Omega^T \left(\frac{\partial\mathcal{K}}{\partial\Omega}\right)^T \right] dx_1 \tag{5.19}$$

Just like the forces and moments in Eq. (5.12), sectional linear and angular momenta P and H are written as

$$P = \left(\frac{\partial \mathcal{K}}{\partial V}\right)^T = \mu(V - \widetilde{\overline{\xi}}\Omega) \tag{5.20a}$$

$$H = \left(\frac{\partial \mathcal{K}}{\partial \Omega}\right)^T = i\Omega + \mu\widetilde{\overline{\xi}}V \tag{5.20b}$$

Using the velocity and angular velocity relationships from Hodges [69], variations of those quantities are obtained as

$$\delta V = \dot{\overline{\delta q}} + \widetilde{\Omega}\overline{\delta q} + \widetilde{V}\overline{\delta\psi} \tag{5.21a}$$

$$\delta\Omega = \dot{\overline{\delta\psi}} + \widetilde{\Omega}\overline{\delta\psi} \tag{5.21b}$$

The variation in kinetic energy density can be rewritten as:

$$\delta\mathcal{K} = \delta V^T P + \delta\Omega^T H \tag{5.22a}$$

$$\delta\mathcal{K} = \left(\dot{\overline{\delta q}} + \widetilde{\Omega}\overline{\delta q} + \widetilde{V}\overline{\delta\psi}\right)^T P + \left(\dot{\overline{\delta\psi}} + \widetilde{\Omega}\overline{\delta\psi}\right)^T H \tag{5.22b}$$

Known body forces and tractions over the surface of the smart beam can have virtual work equivalent to that of distributed applied forces and moments as shown by [42]. The virtual work equivalent, because of the applied loads and moments per unit length (i.e., f and m), is given by

$$\overline{\delta\mathcal{W}} = \int_0^l (\overline{\delta q}^T f + \overline{\delta\psi}^T m) dx_1 \tag{5.23}$$

The variational statement in Eq. (5.10), after substituting values from equations (5.13),

(5.22a) and (5.23), is rewritten as

$$\begin{aligned}\int_{t_1}^{t_2}\int_0^l \Big\{\delta V^T P + \delta\Omega^T H - \delta\gamma^T F - \delta\kappa^T M + \overline{\delta q}^T f \\ +\overline{\delta\psi}^T m\Big\}dx_1 dt = \int_0^l \left(\overline{\delta q}^T \hat{P} + \overline{\delta\psi}^T \hat{H}\right)\Big|_{t_1}^{t_2} dx_1 \\ -\int_{t_1}^{t_2}\left(\overline{\delta q}^T \hat{F} + \overline{\delta\psi}^T \hat{M}\right)\Big|_0^l dt\end{aligned} \tag{5.24}$$

If the intrinsic formulation is chosen, then one integrates (5.24) by parts with respect to t and x_1 and uses the 1-D kinematical relations to obtain

$$\begin{aligned}\int_{t_1}^{t_2}\int_0^l \Big\{\overline{\delta q}^T\Big(F' + \widetilde{K}F - \dot{P} - \widetilde{\Omega}P + f\Big) + \\ \overline{\delta\psi}^T\Big(M' + \widetilde{K}M + (\widetilde{e_1} + \widetilde{\gamma})F - \dot{H} - \widetilde{\Omega}H - \widetilde{V}P \\ +m\Big)\Big\}dx_1 dt = \int_0^l \left[\overline{\delta q}^T\Big(\hat{P} - P\Big) + \overline{\delta\psi}^T\Big(\hat{H} - H\Big)\right]\Big|_{t_1}^{t_2} dx_1 \\ -\int_{t_1}^{t_2}\left[\overline{\delta q}^T\Big(\hat{F} - F\Big) + \overline{\delta\psi}^T\Big(\hat{M} - M\Big)\right]\Big|_0^l dt\end{aligned} \tag{5.25}$$

Furthermore, the Euler-Lagrange equations can be extracted from (5.25) which are the intrinsic equations of motion and are written as

$$F' + \widetilde{K}F + f = \dot{P} + \widetilde{\Omega}P \tag{5.26a}$$

$$M' + \widetilde{K}M + (\widetilde{e_1} + \widetilde{\gamma})F + m = \dot{H} + \widetilde{\Omega}H + \widetilde{V}P \tag{5.26b}$$

The intrinsic kinematical equations required to solve a problem using intrinsic formulations are derived by Hodges [69] and are written as

$$\dot{\gamma} = V' + \widetilde{K}V + (\widetilde{e_1} + \widetilde{\gamma})\Omega \tag{5.27a}$$

$$\dot{\kappa} = \Omega' + \widetilde{K}\Omega \tag{5.27b}$$

where $V(x_1)$ is the column matrix of velocity measures expressed in the beam cross-

sectional frame and $\Omega(x_1)$ is the column matrix of angular velocities.

To implement a suitable damping methodology, however, the mixed formulation is used. The variational statement in Eq. (5.10), after substituting values from equations (5.18), (5.22b) and (5.23), is rewritten as a variational statement in the mixed formulation

$$\begin{aligned}\int_{t_1}^{t_2}\int_0^l \Big\{ \Big(\dot{\overline{\delta q}}^T + \widetilde{\Omega}\overline{\delta q} + \widetilde{V}\overline{\delta\psi}\Big)P + \Big(\dot{\overline{\delta\psi}}^T + \widetilde{\Omega}\overline{\delta\psi}\Big)H \\ -\Big(\overline{\delta q}'^T + \widetilde{K}\overline{\delta q} + (\widetilde{e}_1+\widetilde{\gamma})\overline{\delta\psi}\Big)F - \Big(\overline{\delta\psi}'^T + \widetilde{K}\overline{\delta\psi}\Big)M \\ +\overline{\delta q}^T f + \overline{\delta\psi}^T m\Big\}dx_1 dt = \int_0^l \Big(\overline{\delta q}^T\hat{P} + \overline{\delta\psi}^T\hat{H}\Big)\Big|_{t_1}^{t_2} dx_1 \\ -\int_{t_1}^{t_2}\Big(\overline{\delta q}^T\hat{F} + \overline{\delta\psi}^T\hat{M}\Big)\Big|_0^l dt\end{aligned} \tag{5.28}$$

The constitutive law obtained from the 2-D sectional analysis in Eq. (2.53) provides an expression for elastic forces and moments such that

$$\begin{Bmatrix} F_e \\ M_e \end{Bmatrix} = \begin{bmatrix} A & B \\ B^T & D \end{bmatrix} \begin{Bmatrix} \gamma \\ \kappa \end{Bmatrix} \tag{5.29}$$

Using the Kelvin-Voigt model from Eq. (5.2) to include structural damping, one obtains the modified constitutive law as

$$\underbrace{\begin{Bmatrix} F \\ M \end{Bmatrix}}_{\text{Variables}} = \underbrace{\begin{bmatrix} A & B \\ B^T & D \end{bmatrix} \begin{Bmatrix} \gamma \\ \kappa \end{Bmatrix}}_{\text{Elastic Forces}} + \underbrace{\begin{bmatrix} A & B \\ B^T & D \end{bmatrix} [\mu] \begin{Bmatrix} \dot{\gamma} \\ \dot{\kappa} \end{Bmatrix}}_{\text{Dissipative Forces}} \tag{5.30}$$

Rearranging terms in Eq. (5.30) to obtain

$$\begin{Bmatrix} \gamma \\ \kappa \end{Bmatrix} + [\mu] \begin{Bmatrix} \dot{\gamma} \\ \dot{\kappa} \end{Bmatrix} = \begin{bmatrix} R & Z \\ Z^T & T \end{bmatrix} \begin{Bmatrix} F \\ M \end{Bmatrix} \tag{5.31}$$

where the flexibility matrix is defined as

$$\begin{bmatrix} R & Z \\ Z^T & T \end{bmatrix} = \begin{bmatrix} A & B \\ B^T & D \end{bmatrix}^{-1} \tag{5.32}$$

Now, we need to identify the coefficients of the 3-D damping matrix. The stiffness matrix-based proportional damping is not sufficient to model a correct damping behavior. Hence, there is a need for 3-D damping model. As mentioned in section 2.3 that most researchers use experimental techniques to obtain damping coefficients. This approach may not be appropriate in this case because performing experiments with excitation to obtain response in different modes of deformation may not be feasible to study dissipation characteristics.

The plan is to leverage the information on material damping available through experiments or standard data books as well as the information processed during cross-sectional analysis in Sec. 2.3. For the application of a K-V model, the basic damping matrix without the 3-D effects would look like

$$[\mu] = \begin{bmatrix} \mu & 0 & 0 & 0 & 0 & 0 \\ 0 & \mu & 0 & 0 & 0 & 0 \\ 0 & 0 & \mu & 0 & 0 & 0 \\ 0 & 0 & 0 & \mu & 0 & 0 \\ 0 & 0 & 0 & 0 & \mu & 0 \\ 0 & 0 & 0 & 0 & 0 & \mu \end{bmatrix} \tag{5.33}$$

where μ is either a material damping coefficient obtained from experiments or a Rayleigh's dissipation coefficient for a given material.

Using Lazan's monograph [94] and considering the shape factors, volume, surface area and peak stress information obtained from VABS, we identify a normalized damping integral which will be used to treat the μ in the original damping matrix to finally create this

reformed 3-D damping matrix.

$$[\mu] = \begin{bmatrix} \mu_1 & 0 & 0 & 0 & 0 & 0 \\ 0 & \mu_2 & 0 & 0 & 0 & 0 \\ 0 & 0 & \mu_3 & 0 & 0 & 0 \\ 0 & 0 & 0 & \mu_4 & 0 & 0 \\ 0 & 0 & 0 & 0 & \mu_5 & 0 \\ 0 & 0 & 0 & 0 & 0 & \mu_6 \end{bmatrix} \tag{5.34}$$

This represents a 3-D damping matrix where the effect of damping on deformations of various degrees of freedom is not the same. It is important to note that (5.31) is a linear ordinary differential equation of first-order in time. One can obtain the exact solution of that Eq. of the form

$$\begin{Bmatrix} \gamma \\ \kappa \end{Bmatrix} = [f(t)] \begin{bmatrix} R & Z \\ Z^T & T \end{bmatrix} \begin{Bmatrix} F \\ M \end{Bmatrix} \tag{5.35}$$

where $[f(t)]$ is a 6×6 matrix with elements as functions of the time t. All the variables in the ODE are inherently functions of x_1 and t. To further derive the mixed formulation, the kinematic differential relations are incorporated into the variational statement (5.31) with the help of Lagrange multipliers and using calculus of variations. These kinematic differential equations may either be derived or directly used from equations (2.14) and (5.27). Rearranging the γ Eq. (2.14a), one obtains

$$u' = C^{bB}(e_1 + \gamma) - e_1 - \tilde{k}u \tag{5.36a}$$

$$\dot{u} = C^{bB}V - v - \tilde{\omega}u \tag{5.36b}$$

$$c' = Q^{-1}(\kappa + k - C^{bB}k) \tag{5.36c}$$

$$\dot{c} = Q^{-1}(\Omega - C^{bB})\omega \tag{5.36d}$$

where Eqs. (5.36a) and (5.36c) can be derived from Eq. (2.14). However, Eqs. (5.36b)

and (5.36d) need additional information from Ref. [67] for derivation. Also,

$$Q = \frac{1}{(4 - c_0^2)} \left[\big(4 - \frac{1}{4} c^T c\big)\Delta - 2\tilde{c} + \frac{1}{2} c c^T \right] \tag{5.37}$$

from Wang and Yu [170], such that

$$Q^{-1} = \big(1 - \frac{1}{16} c^T c\big)\Delta + \frac{1}{2}\tilde{c} + \frac{1}{8} c c^T \tag{5.38}$$

and

$$c_0 = 2\Big(1 - \tan^2 \frac{\phi}{4}\Big) \tag{5.39}$$

The variational statement with λ_i's as the Lagrange multipliers, incorporating the kinematic differential equations, becomes

$$\begin{aligned}
&\int_{t_1}^{t_2} \int_0^l \Big\{ \delta V^T P + \delta \Omega^T H - \delta \gamma^T F - \delta \kappa^T M + \overline{\delta q}^T f \\
&+ \overline{\delta \psi}^T m + \delta \Big[\lambda_1 \big(u' - C^{bB}(e_1 + \gamma) + e_1 + \tilde{k} u \big) \Big] \\
&+ \delta \Big[\lambda_2 \big(\dot{u} - C^{bB} V + v + \tilde{\omega} u \big) \Big] \\
&+ \delta \Big[\lambda_3 \big(c' - Q^{-1}(\kappa + k - C^{bB} k) \big) \Big] \\
&+ \delta \Big[\lambda_4 \big(\dot{c} - Q^{-1}(\Omega - C^{bB}) \big) \Big] \Big\} dx_1 dt \\
= &\int_0^l \Big(\overline{\delta q}^T \hat{P} + \overline{\delta \psi}^T \hat{H} \Big) \Big|_{t_1}^{t_2} dx_1 - \int_{t_1}^{t_2} \Big(\overline{\delta q}^T \hat{F} + \overline{\delta \psi}^T \hat{M} \Big) \Big|_0^l dt
\end{aligned} \tag{5.40}$$

If the damping solution is not obtained in Eq. (5.35), then Eq. (5.31) can be incorporated

into the variational statement along with additional Lagrange multipliers as shown here:

$$
\begin{aligned}
&\int_{t_1}^{t_2}\int_0^l \Big\{\delta V^T P + \delta\Omega^T H - \delta\gamma^T F - \delta\kappa^T M + \overline{\delta q}^T f \\
&+ \overline{\delta\psi}^T m + \delta\Big[\lambda_1\big(u' - C^{bB}(e_1+\gamma) + e_1 + \tilde{k}u\big)\Big] \\
&+ \delta\Big[\lambda_2\big(\dot{u} - C^{bB}V + v + \tilde{\omega}u\big)\Big] \\
&+ \delta\Big[\lambda_3\big(c' - Q^{-1}(\kappa + k - C^{bB}k)\big)\Big] \\
&+ \delta\Big[\lambda_4\big(\dot{c} - Q^{-1}(\Omega - C^{bB})\big)\Big] \\
&+ \delta\Big[\lambda_5\big(\gamma + [\mu].\dot{\gamma} - [R \quad Z]F\big) \\
&+ \delta\Big[\lambda_6\big(\kappa + [\mu].\dot{\kappa} - [Z^T\ T]M\big)\Big\} dx_1 dt \\
&= \int_0^l \Big(\overline{\delta q}^T \hat{P} + \overline{\delta\psi}^T \hat{H}\Big)\Big|_{t_1}^{t_2} dx_1 - \int_{t_1}^{t_2}\Big(\overline{\delta q}^T \hat{F} + \overline{\delta\psi}^T \hat{M}\Big)\Big|_0^l dt
\end{aligned}
\tag{5.41}
$$

However, incorporating additional Lagrange multipliers introduces complexity in the variational statement. Following Wang and Yu [170], after identifying Lagrange multipliers in (5.40), one obtains

$$
\begin{aligned}
&\int_0^l \Big\{\delta u_a'^T F_a + \overline{\delta\psi}_a'^T M_a + \delta u_a^T(\dot{P}_a + \tilde{\omega}_a P_a) \\
&+ \overline{\delta\psi}_a^T\Big[\dot{H}_a + \tilde{\omega}_a H_a + \tilde{V}_a P_a - C^{aB}(\tilde{e}_1 + \tilde{\gamma})F_B\Big] \\
&- \overline{\delta F}_a^T\Big[C^{aB}(e_1+\gamma) - C^{ab}e_1\Big] - \overline{\delta F}_a'^T u_a - \overline{\delta M}_a'^T c_a \\
&- \overline{\delta M}_a^T Q_a^{-1} C^{ab}\kappa + \overline{\delta P}_a^T(-\dot{u}_a + V_a - v_a - \tilde{\omega}_a u_a) \\
&+ \overline{\delta H}_a^T(\Omega_B - \omega_B - C^{ba}Q_a\dot{c}_a) - \delta u_a^T f_a - \overline{\delta\psi}_a^T m_a\Big\} dx_1 \\
&= \Big(\delta u_a^T \hat{F}_a + \overline{\delta\psi}_a^T \hat{M}_a - \overline{\delta F}_a^T \hat{u}_a - \overline{\delta M}_a^T \hat{c}_a\Big)\Big|_0^l
\end{aligned}
\tag{5.42}
$$

Here the strains and curvatures are obtained from (5.35) and are not dependent only on elastic forces and moments. In this equation, the time derivatives of virtual quantities are removed through integrations by parts and $Q_a = C^{ab}QC^{ba}$.

To further complete the solution of the variational statement using the mixed formula-

tion, shape functions of lowest possible order are chosen. For two-noded beam elements of length ΔL_i,one can introduce a general coordinate ξ such that

$$\xi = \frac{x_1 - L_i}{\Delta L_i} \qquad dx_1 = \Delta L_i d\xi \qquad ()' = \frac{1}{\Delta L_i}\frac{\partial()}{\partial \xi} \tag{5.43}$$

where L_i is the x_1 coordinate of the starting node. Introducing the following linear shape functions for these variables as only first-order derivatives appear in the formulation and constants for other test functions, one obtains

$$\begin{aligned} \delta u_a = (1-\xi)\delta u_i + \xi \delta u_j \quad \overline{\delta\psi}_a = (1-\xi)\overline{\delta\psi}_i + \xi\delta\overline{\delta\psi}_j \\ \delta F_a = (1-\xi)\delta F_i + \xi \delta F_j \quad \overline{\delta M}_a = (1-\xi)\overline{\delta M}_i + \xi\delta\overline{\delta M}_j \end{aligned} \tag{5.44}$$

with i as the starting and j as the ending node. Dividing the beam into N elements with the starting node of the i^{th} element numbered as i and the ending is numbered as $i+1$, one obtains the finite element equations as

$$f^-_{u_1} - F^*_1 = 0 \tag{5.45}$$

$$f^-_{\psi_1} - M^*_1 = 0 \tag{5.46}$$

$$f^-_{F_1} - \hat{u}_1 = 0 \tag{5.47}$$

$$f^-_{M_1} - \hat{c}_1 = 0 \tag{5.48}$$

at the starting node, and

$$f^+_{u_N} - F^*_{N+1} = 0 \tag{5.49}$$

$$f^+_{\psi_N} - M^*_{N+1} = 0 \tag{5.50}$$

$$f^+_{F_N} + \hat{u}_{N+1} = 0 \tag{5.51}$$

$$f^+_{M_N} + \hat{c}_{N+1} = 0 \tag{5.52}$$

at the ending node. The starred quantities are the external forces and moments balancing the internal resultants. Further, at each intermediate node, the following continuity equations are imposed:

$$f^+_{u_i} + f^-_{u_{i+1}} = 0 \tag{5.53}$$

$$f^+_{\psi_i} + f^-_{\psi_{i+1}} = 0 \tag{5.54}$$

$$f^+_{F_i} + f^-_{F_{i+1}} = 0 \tag{5.55}$$

$$f^+_{M_i} + f^-_{M_{i+1}} = 0 \tag{5.56}$$

$$f_{P_i} = 0 \tag{5.57}$$

$$f_{H_i} = 0 \tag{5.58}$$

Carrying out the integration of Eq. (5.42), analytically after using the shape functions written in Eq. (5.44), one obtains

$$\begin{aligned}
&\sum_{i=1}^{N} \Big\{ \delta u_i^T f^-_{u_i} + \delta u^T_{i+1} f^+_{u_i} + \overline{\delta\psi}_i^T f^-_{\psi_i} + \overline{\delta\psi}^T_{i+1} f^+_{\psi_i} + \overline{\delta F}_i^T f^-_{F_i} \\
&+ \overline{\delta F}^T_{i+1} f^+_{F_i} + \overline{\delta M}_i^T f^-_{M_i} + \overline{\delta M}^T_{i+1} f^+_{M_i} + \overline{\delta P}_i^T f^-_{P_i} + \overline{\delta H}_i^T f^-_{H_i} \Big\} \\
&= \delta u^T_{N+1} \hat{F}_{N+1} + \overline{\delta\psi}^T_{N+1} \hat{M}_{N+1} - \delta F^T_{N+1} \hat{u}_{N+1} \\
&- \overline{\delta M}^T_{N+1} \hat{c}_{N+1} - \delta u_1^T \hat{F}_1 - \overline{\delta\psi}_1^T \hat{M}_1 + \delta F_1^T \hat{u}_1 + \overline{\delta M}_1^T \hat{c}_1
\end{aligned} \tag{5.59}$$

with

$$f_{u_i}^{\mp} = \mp C^T C^{ab} F_i$$
$$-\overline{f}_i^{\mp} + \frac{\Delta L_i}{2}\left[\tilde{\omega}_a C^T C^{ab} P_i + \overline{\dot{C^T C^{ab}} P_i}\right] \tag{5.60}$$

$$f_{\psi}^{\mp} = \mp C^T C^{ab} M_i - \overline{m}_i^{\mp} + \frac{\Delta L_i}{2}\Big[\tilde{\omega}_a C^T H_i$$
$$+\overline{\dot{C^T C^{ab}} H_i} + C^T C^{ab}(\tilde{V}_i P_i - (\tilde{e}_1 + \tilde{\gamma}_i) F_i)\Big] \tag{5.61}$$

$$f_{F_i}^{\mp} = \pm u_i - \frac{\Delta L_i}{2}\Big[C^T C^{ab}(e_1 + \gamma_i) - C^{ab} e_1\Big] \tag{5.62}$$

$$f_M^{\mp} = \pm c_i - \frac{\Delta L_i}{2} Q_a^{-1} C^{ab} \kappa_i \tag{5.63}$$

$$f_{P_i} = C^T C^{ab} V_i - v_i - \tilde{\omega}_a u_i - \dot{u}_i \tag{5.64}$$

$$f_{H_i} = \Omega_i - C^{ba} C \omega_a - C^{ba} Q_a \dot{c}_i \tag{5.65}$$

and

$$\overline{f}_i^{-} = \int_0^1 (1-\xi) f_a \Delta L_i d\xi \tag{5.66}$$

$$\overline{f}_i^{+} = \int_0^1 \xi f_a \Delta L_i d\xi \tag{5.67}$$

$$\overline{m}_i^{-} = \int_0^1 (1-\xi) m_a \Delta L_i d\xi \tag{5.68}$$

$$\overline{m}_i^{+} = \int_0^1 \xi m_a \Delta L_i d\xi \tag{5.69}$$

Governing equations (5.45) – (5.58) can be written compactly in the form

$$\mathcal{F}(X, \dot{X}) = 0 \tag{5.70}$$

where $\mathcal{F}$ is a system of $18N + 6M$ equations and X is a vector containing $18N + 6M$ unknowns. Specifically, equations corresponding to f_u and f_ψ are the equations of motion, f_F and f_M are the strain-displacement equations and the equations corresponding to f_P and f_H are velocity-displacement kinematical equations. The system of nonlinear equations are

solved using Newton-Raphson method along with line search algorith to guarantee global convergence. A suitable Newmark time-marching scheme derived for this purpose is shown below for a generic function of time, A:

$$A(t+\delta t) = A(t) + \dot{A}(t)\delta t + [(1-2\alpha)\ddot{A}(t+\delta t) + 2\alpha\ddot{A}(t+\delta t)]\frac{(\delta t)^2}{2} \tag{5.71}$$

$$\dot{A}(t+\delta t) = \dot{A}(t) + [(1-c)\ddot{A}(t) + c\ddot{A}(t+\delta t)]\delta t \tag{5.72}$$

where δt is the time increment. Substituting (5.71) into (5.72) one obtains

$$\dot{A}(t+\delta t) = \Big(1-\frac{c}{\alpha}\Big)\dot{A}(t) + \Big(1-\frac{c}{2\alpha}\Big)\delta t\ddot{A}(t) + \frac{c}{\alpha\delta t}[A(t+\delta t) - A(t)] \tag{5.73}$$

Following Yu [186], if one chooses $\frac{c}{2\alpha} = 1$, the above formulation can be simplified as

$$\dot{A}(t+\delta t) = \frac{2[A(t+\delta t) - A(t)]}{\delta t} - \dot{A}(t) \tag{5.74}$$

Equations (5.60), (5.61), (5.64), and (5.65) are modified to further carry out time marching. Starred quantities appearing in the developed equations such as $(\ )^*$ are evaluated at

time t and the others are evaluated at time step $t + \delta t$, such that

$$f_{u_i}^{\mp} = \mp C^T C^{ab} F_i - \overline{f}_i^{\mp} + \frac{\Delta L_i}{2}\Big[\Big(\tilde{\omega_a} + \frac{2}{\delta t}\Delta\Big)C^T C^{ab} H_i - \frac{2}{\delta t}(C^T C^{ab} P_i)^* - (\dot{\overline{C^T C^{ab} P_i}})^*\Big] \tag{5.75}$$

$$f_{\psi_i}^{\mp} = \mp C^T C^{ab} M_i - \overline{m}_i^{\mp} + \frac{\Delta L_i}{2}\Big[\Big(\tilde{\omega_a} + \frac{2}{\delta t}\Delta\Big)C^T C^{ab} P_i - \frac{2}{\delta t}(C^T C^{ab} H_i)^* - (\dot{\overline{C^T C^{ab} H_i}})^* + C^T C^{ab}(\tilde{V}_i P_i - (\tilde{e}_1 + \tilde{\gamma}_i)F_i)\Big] \tag{5.76}$$

$$f_{P_i} = C^T C^{ab} V_i - v_i - \Big(\tilde{\omega}_a + \frac{2}{\delta t}\Delta\Big)u_i + \frac{2}{\delta t}u_i^* + \dot{u}_i^* \tag{5.77}$$

$$f_{H_i} = \Omega_i - C^{ba} C\omega_a - C^{ba}\frac{\Delta - \tilde{c}_i/2}{1 + c_i c_i^T/4}\Big[\frac{2}{\delta t}(c_i - c_i^*) - \dot{c}_i^*\Big] \tag{5.78}$$

In the overall implementation of damping in the mixed formulation using the K-V model, incorporation of structural damping has been done by allowing the strain and curvatures variables to be represented in the form of total force and total moment variables. In prior work, those variables were represented only in the terms of elastic force and moment variables. This modification has been made to an in-house version of GEBT and a verification study is presented in the next section.

5.3 Verification

In this section of the article, a verification of the proposed theory against 3-D Finite Element Method (FEM) is provided. It is important to note that commercially available 3-D FEM tools are only equipped with proportional damping. That is, these tools accept only a constant coefficient proportional either to the mass matrix, the stiffness matrix or both. A generalized form of proportional damping was proposed by Adhikari [3]. 3-D FEM tools require just one coefficient to proportionate the entire mass or stiffness matrix as compared to the proposed formulation where 3-D damping coefficients can be provided, so that an entire 6×6 matrix can be populated to model 3-D damping in realistic composite beam like

structures.

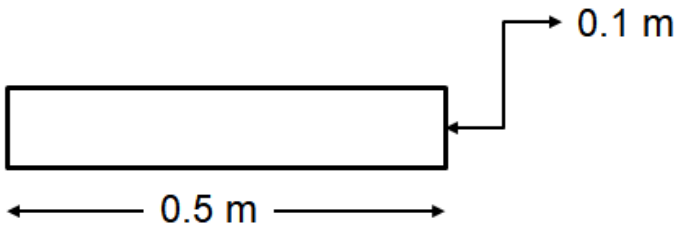

Figure 5.1: Cross section details of the cantilever beam

So, in order to validate results, the present formulation is modified to generate a special case of stiffness-proportional damping to represent a problem with the simplest form of structural damping and subsequently compare the damped frequencies obtained from this formulation with those obtained from 3-D FEM. For example, a typical cantilever beam made of aluminum, with cross-sectional dimensions 0.5 m$\times$0.1 m, as shown in Fig. 5.1, Young's modulus of 70×10^9 Pa, Poisson's ratio 0.327 and density of 2700 kg/m^3 is chosen for a damped frequency eigenvalue analysis using the formulation implemented in VABS+GEBT along with 3-D FEM. Results for damped frequencies demonstrating the agreement between present approach as well as 3-D FEM is presented in Table 5.1.

Table 5.1: Damped Frequency: 3-D FEM vs. VABS+GEBT

Frequency (ω_d)	3-D FEM[1] Undamped	3-D FEM[1] Damped	VABS+GEBT Damped
1	0.20415	0.1970	0.19707893
2	1.0203	1.0050	1.0050081
3	1.2792	1.2352	1.2352704
4	3.581	3.4599	3.4599691
5	6.3748	6.2820	6.2820758
6	7.0158	6.7838	6.7838326
7	11.593	11.2224	11.222416
8	14.488	13.9702	13.970275
9	17.311	16.7799	16.779962
10	17.765	17.5190	17.519074

[1]3-D FEM calculations are performed in ANSYS Inc. 18.0

As mentioned above, to perform this analysis, the present approach is reduced to incor-

porate a stiffness-based proportional damping using the Kelvin-Voigt model from equation (5.2) to include structural damping, one obtains the modified constitutive law as

$$\underbrace{\begin{Bmatrix} F \\ M \end{Bmatrix}}_{\text{Variables}} = \underbrace{\begin{bmatrix} A & B \\ B^T & D \end{bmatrix} \begin{Bmatrix} \gamma \\ \kappa \end{Bmatrix}}_{\text{Elastic Forces}} + \underbrace{\begin{bmatrix} A & B \\ B^T & D \end{bmatrix} [\mu] \begin{Bmatrix} \dot{\gamma} \\ \dot{\kappa} \end{Bmatrix}}_{\text{Dissipative Forces}} \tag{5.79}$$

Rearranging terms in equation (5.79) to obtain

$$\begin{Bmatrix} \gamma \\ \kappa \end{Bmatrix} + [\mu] \begin{Bmatrix} \dot{\gamma} \\ \dot{\kappa} \end{Bmatrix} = \begin{bmatrix} R & Z \\ Z^T & T \end{bmatrix} \begin{Bmatrix} F \\ M \end{Bmatrix} \tag{5.80}$$

where flexibility matrix

$$\begin{bmatrix} R & Z \\ Z^T & T \end{bmatrix} = \begin{bmatrix} A & B \\ B^T & D \end{bmatrix}^{-1} \tag{5.81}$$

It is important to note that Eq. (5.80) is a linear ordinary differential equation of first-order in time. One can obtain the exact solution of that equation of the form

$$\begin{Bmatrix} \gamma \\ \kappa \end{Bmatrix} = [f(t)] \begin{bmatrix} R & Z \\ Z^T & T \end{bmatrix} \begin{Bmatrix} F \\ M \end{Bmatrix} \tag{5.82}$$

where $[f(t)]$ is a 6×6 matrix with elements as functions of time t. All the variables in the ODE are inherently functions of x_1 and t. For the purpose of solving the present example, the damping coefficient of 2×10^{-4} s obtained from standard material data tables instead of using. 3-D damping matrix. Thus, Eq. (5.80) is suitably modified to obtain

$$\begin{Bmatrix} \gamma \\ \kappa \end{Bmatrix} + \mu \begin{Bmatrix} \dot{\gamma} \\ \dot{\kappa} \end{Bmatrix} = \begin{bmatrix} R & Z \\ Z^T & T \end{bmatrix} \begin{Bmatrix} F \\ M \end{Bmatrix} \tag{5.83}$$

The solution to the ordinary differential equation is obtained as

$$\begin{Bmatrix} \gamma \\ \kappa \end{Bmatrix} = (1 - e^{\frac{\tau}{\mu}t}) \begin{bmatrix} R & Z \\ Z^T & T \end{bmatrix} \begin{Bmatrix} F \\ M \end{Bmatrix} \tag{5.84}$$

For isotropic beams such as the one demonstrated in the validation studies, $\tau = E$ and $\frac{\mu}{\tau} = \beta$ where β is the stiffness proportional Rayleigh's dissipation coefficient, so equation (5.84) becomes

$$\begin{Bmatrix} \gamma \\ \kappa \end{Bmatrix} = (1 - e^{\frac{t}{\beta}}) \begin{bmatrix} R & Z \\ Z^T & T \end{bmatrix} \begin{Bmatrix} F \\ M \end{Bmatrix} \tag{5.85}$$

which is then incorporated in the eigenvalue analysis and the Newmark scheme for time marching analysis.

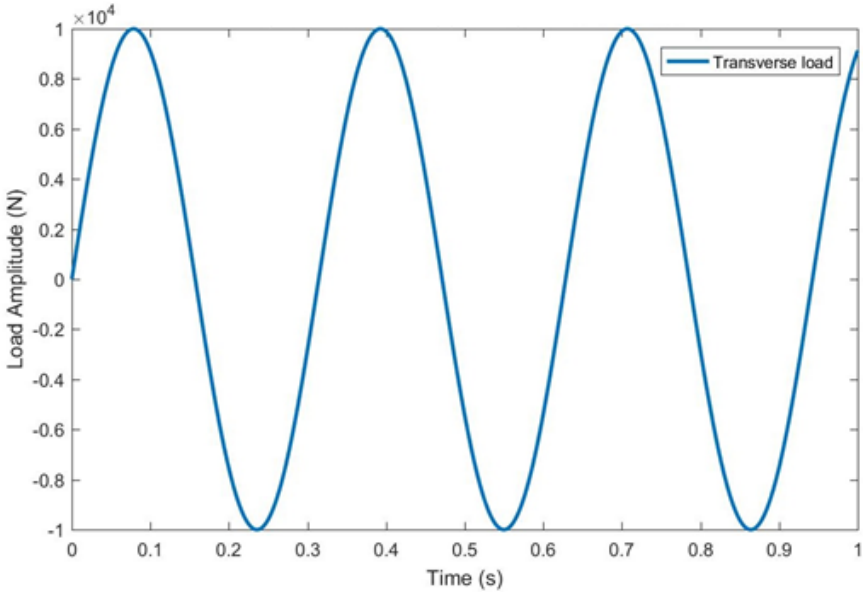

Figure 5.2: Representation of applied tip transverse load

In another case, the tip of a cantilever beam with cross section as shown in Fig. 5.1 is subjected to a dynamic load of magnitude $f_3 = 10^4 \sin(20t)$. Detailed characteristics of the applied load are shown in Fig. 5.2. The response of the beam is plotted from time 0 to 1 seconds is shown in Fig. 5.3. Results from 3-D FEM are also presented alongside. It is important to note that the results obtained from GEBT are 1-D results until 3-D displacements

are recovered with the help of the warping calculated during the cross-sectional analysis. To appropriately compare 1-D results obtained from GEBT and 3-D results obtained from FEA, the 3-D results are averaged over the cross section and then plotted in Fig. 5.3. It is observed that the results with damping obtained from the present approach agree with the results obtained from FEA, providing an evidence that the current implementation of Kelvin-Voigt model is appropriate at least for problems involving structural damping that can be modeled with stiffness-proportional damping.

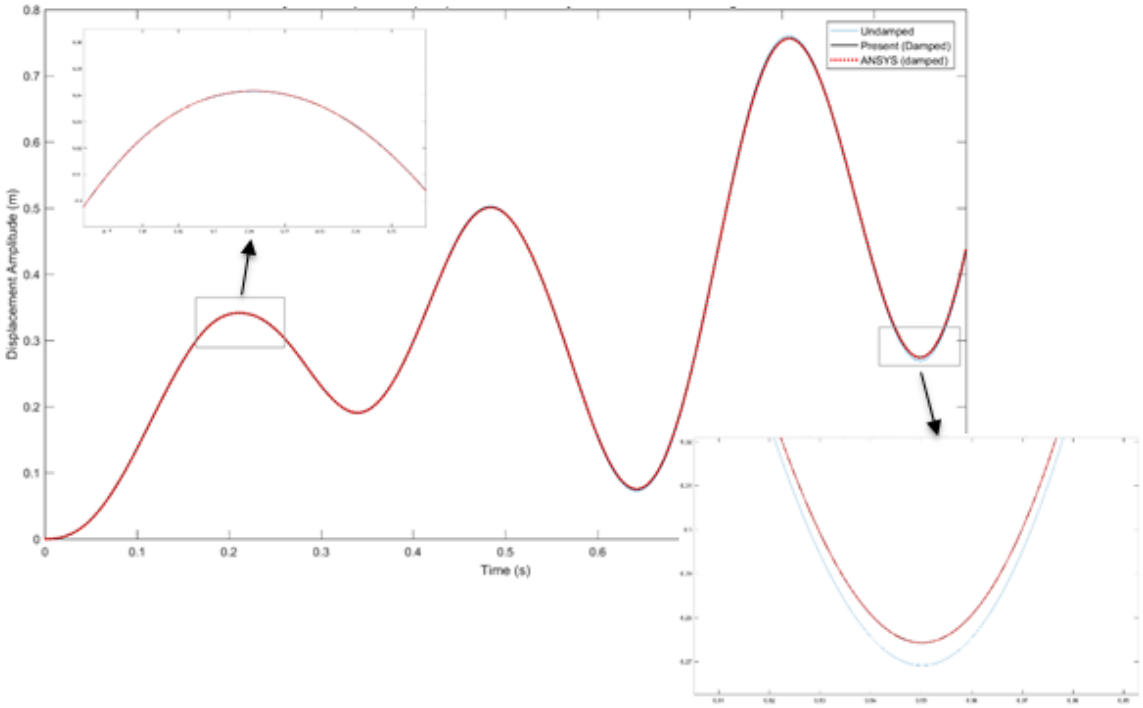

Figure 5.3: Dynamic response: Tip displacement under dynamic transverse loading

CHAPTER VI

INITIALLY CURVED AND PRE-TWISTED SMART BEAMS

In recent times the use of smart structures has skyrocketed. Smart structures can sense and respond to stimuli. These are made up of active materials like the Shape Memory Alloys (SMAs), electrostrictives, magnetostrictives, piezoelectric materials etc. After integration into the structures, these can be used as self-controllable and monitorable systems [61]. Among these active materials, more focus is given to piezoelectric materials, as they can be used both as actuators as well as sensors by relating external stimuli to strains and vice-versa [37].

Chee et al. [32], Loewy [108], Chopra [37] and Giurgiutiu [52] discuss this promising technology. Despite all the research being done, the analytical capabilities to predict the response of smart structures is quite limited as compared to conventional composite structures. Most of the active structural components can be analyzed using beam models, which have one dimension much larger than the other two. Hence, these structures are termed as smart beams.

In the literature, models are classified into engineering models, which are based on a priori kinematic assumptions, and asymptotic models, which are based on asymptotic expansion of three-dimensional (3D) quantities. Engineering models are widely used in the modeling of smart beams. A review of these models is presented by Mackerle [111, 112] and Chopra [37]. These can be studied by considering only the main induced effect

in the model (uncoupled) [31, 41, 128, 144], or by considering both the actuation and sensing capabilities simultaneously (coupled) [97, 136, 150, 161]. These models rely on a priori kinematic assumptions, mainly based on intuition and have clear physical meaning. However, these cannot be easily extended to heterogeneous structures. On the other hand, the asymptotic method does not rely on any a priori assumptions and can reduce the 3D problem into a sequence of 1D beam models by taking advantage of small parameters [9].

The Variational Asymptotic Method (VAM) [15] includes the benefits of both these above mentioned methods. The 3D beam theory is dimensionally reduced into a 2D cross-sectional analysis and a 1D beam theory. VAM has been successfully applied to 2D cross-sectional analysis of smart beams.Wang [169] applied VAM to model the multiphysics behavior of smart beams. Roy et al. [147] developed the classical model for smart beams. Roy and Yu [146] added on by developing the refined generalized Timoshenko model. However, the work related to the incorporation of smart beam capabilities into the 1D beam theory remains limited.

Robbins and Reddy [144] used a layer-wise displacement theory to analyze actuators within beams using piezoelectric materials. Saravanos and Heyliger [149] developed approximate finite element solutions for the static and free-vibration analysis of beams with the capability to model both sensory and active composite laminates with embedded piezoelectric layers. Han et al. [58] used DYMORE for the non-linear dynamic simulation modeling for smart beams involving piezoelectric materials. Ajitsaria et al. [6] showed the modeling of a bimorph piezoelectric cantilever beam for voltage generation. A finite element formulation for vibration control of a laminated plate with piezoelectric sensors/actuators is presented by Hwang and Park [72]. A finite element model for the static and dynamic analysis of a piezoelectric bimorph is developed by Wang [171] in 2004.

In the present study, analytical predictive capabilities for smart beams have been incorporated into the geometrically exact intrinsic equations derived by Hodges [69]. A unified solution to predict the 1D linear response of smart beams for both sensing and actuation

cases is presented. This method uses the 2D coupled cross-sectional parameters obtained from the variational asymptotic smart beam theory developed by Neto et al. [119] as inputs into the modified equations. Le [95] proposed a classification of smart beams based upon the arrangement of electrodes for the piezoelectric materials into an Axial Field Problem (end surfaces of smart beams are fully or partially electroded) and a Radial Field Problem (surfaces parallel to the axis of smart beams are electroded). Initially curved and twisted Radial Field Problems are considered in the present work such that the electroded surfaces form equi-potential surfaces with prescribed electric potential. A commercially available finite element code ABAQUS is used to validate the results obtained from the modified linear1D beam equations. Excellent agreement is found between the present work and the 3D FEM results for both the actuation and sensor cases of different beam geometries.

6.1 Modifications to the Theoretical Framework

This section explains the modification made to the sectional and the 1-D beam analysis to solve problems involving piezo-composite beams. As we already know by now that the behavior of smart beams is governed by Hamilton's Principle where the total internal energy will be determined by the mechanical field, along with one or more other fields as opposed to the strain energy in Eq. (5.10).

$$\int_{t_1}^{t_2} [\delta(\mathcal{K} - \mathcal{U}) + \overline{\delta\mathcal{W}}]dt = 0 \tag{6.1}$$

where t_1 and t_2 are arbitrary fixed times, $\mathcal{K}$ is the kinetic energy, $\mathcal{U}$ is the internal energy, δ is the Lagrangian variation for a fixed time, and $\overline{\delta\mathcal{W}}$ is the virtual work by applied load and electrical charges. As usual, the bar indicates that the virtual work need not be the variation of a functional.

For piezoelectric smart beams, from Ref. [95], the electrical enthalpy is

$$\mathcal{U} = \frac{1}{2}\int_{\mathcal{V}} (\mathbf{\Gamma^T} : \mathbf{C^E} : \mathbf{\Gamma} - \mathbf{2E} \cdot \mathbf{e} : \mathbf{\Gamma} - \mathbf{E^T} \cdot \varepsilon^{\mathbf{\Gamma}} \cdot \mathbf{E}) d\mathcal{V} \tag{6.2}$$

where $\mathbf{\Gamma}$ is the 3-D strain tensor, $\mathbf{C^E}$ is the elastic tensor at constant electric field, which is further described in Appendix B, $\mathbf{e}$ is the piezoelectric tensor, $\mathbf{E}$ is the electric field vector, $\varepsilon^{\mathbf{\Gamma}}$ is dielectric tensor at constant strain field and $\mathcal{V}$ is the volume of smart beam. For smart beams with no initial curvature or twist, the constitutive relation matrix (9×9) is

$$\mathcal{U} = \frac{1}{2}\int_0^L \langle \Gamma^{\mathcal{T}} \mathcal{C} \Gamma \rangle dx_1 \tag{6.3}$$

where

$$\mathcal{C} = \begin{bmatrix} \mathbf{C^E} & -\mathbf{e^T} \\ \mathbf{e} & -\varepsilon^{\mathbf{\Gamma}} \end{bmatrix} \tag{6.4}$$

Now, a variational asymptotic expansion can be carried out as described in Sec. 2.3. This procedure was first carried out for piezoelectric beams by Roy et al. [145]. Following the method stated in Valliappan et al. [163], constraints on warping and electric potential can be specified. Upon the minimization of the equivalent 1-D strain energy per unit length with respect to the unknown warping field variables results in the 1-D constitutive law. Following the steps given by [146] to obtain asymptotically correct second-order strain energy and carrying out transformation into the generalized Timoshenko smart beam model, we get 1D constitutive law relating the 1D generalized resultant forces on the beam cross-section with the 1D generalized strains given by

$$\begin{bmatrix} F \\ M \end{bmatrix} = \begin{bmatrix} A & B \\ B^T & D \end{bmatrix} \begin{bmatrix} \gamma \\ \kappa \end{bmatrix} - \begin{bmatrix} F_a \\ M_a \end{bmatrix} \tag{6.5}$$

With the stiffness and mass matrices obtained from the sectional analysis, next step is to use the mixed formulation as laid out in Sec. 5.2 or the intrinsic equations for the beam

derived in Eq. 5.25 and also given by

$$F' + \widetilde{K}F + f = \dot{P} + \widetilde{\Omega}P \tag{6.6a}$$

$$M' + \widetilde{K}M + (\widetilde{e_1} + \widetilde{\gamma})F + m = \dot{H} + \widetilde{\Omega}H + \widetilde{V}P \tag{6.6b}$$

The solution procedure is taken from Yu and Blair [186], which makes use of a constitutive law using a flexibility matrix instead of a stiffness matrix given by

$$\begin{Bmatrix} \gamma \\ \kappa \end{Bmatrix} = \begin{bmatrix} R & Z \\ Z^T & T \end{bmatrix} \begin{Bmatrix} F \\ M \end{Bmatrix} \tag{6.7}$$

and the intrinsic kinematic partial differential equations

$$\dot{\gamma} = V' + \widetilde{K}V + (\widetilde{e_1} + \widetilde{\gamma})\Omega \tag{6.8a}$$

$$\dot{\kappa} = \Omega' + \widetilde{K}\Omega \tag{6.8b}$$

where $V(x_1, t)$ is the column matrix of velocity measures expressed in the beam cross-sectional frame and $\Omega(x_1, t)$ is the column matrix of angular velocities. Further derivation of the intrinsic formulation are presented by Hodges [68]. For the purpose of validation, these formulations are simplified for static cases resulting into linear equations and are used in the next section. Also, short derivations and relevant details are included as part of the solution of the example problems presented in next section, Sec. 6.2.

6.2 Validation Studies

In order to verify the formulated theory, three different cases that were taken into consideration are prismatic, initially twisted and initially curved smart beams. To investigate the static characteristics, each of the cases was validated for when used as an actuator and as a sensor. Cross-sectional analysis tool VABS [145] is used to obtain the cross-sectional con-

stants and actuation terms which serve as input parameters into the formulated equations. The results obtained were compared with the 3D FEM analysis done in ABAQUS [63].

6.2.1 Straight Smart Beam

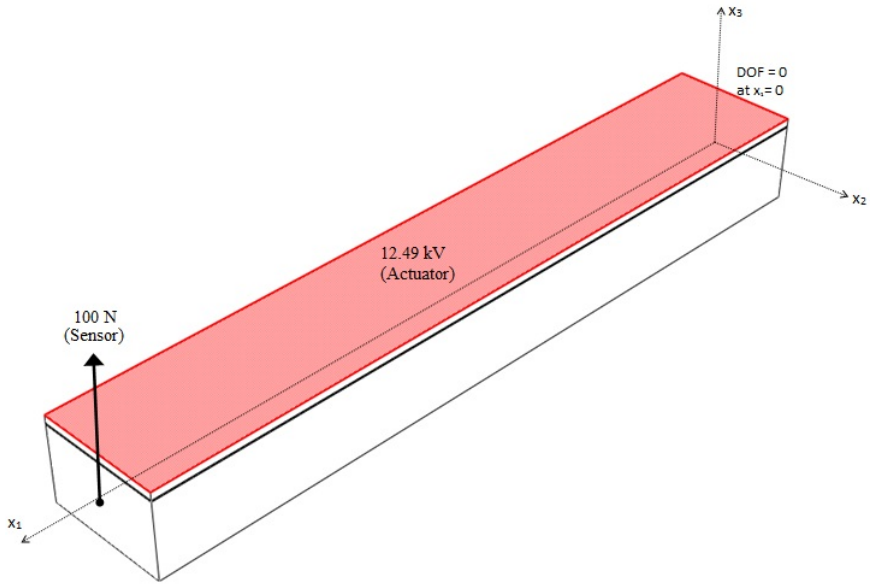

Figure 6.1: Three-layer straight smart beam

Actuator

A three-layer piezo-composite smart beam is studied in the literature [144, 149, 58, 33]. This cantilevered smart beam is made up of a piezoelectric layer on the top, followed by an adhesive layer fixing it to an aluminum substrate as shown in Fig. 6.1. Table 6.1 shows the geometrical and material properties of the beam. Robbins [144] provided only the mechanical properties of the piezoelectric material and assumed 0.1% induced strain actuation for calculations. [33] and [58] applied 12.49 kV across the piezoelectric layer which resulted in the same average axial strain. So for the purpose of actuation, a constant electric voltage of 12.49 kV is applied on the top surface of piezoelectric layer and the bottom surface of the piezoelectric layer is grounded.

Table 6.1: Geometry and material properties of three-layer smart beam

Properties	Piezoelectric	Adhesive	Aluminum
E_{11} (GPa)	68.9	6.9	68.9
$E_{22} = E_{33}$ (GPa)	48.3	6.9	68.9
$G_{12} = G_{13} = G_{23}$ (GPa)	20.7	2.46	27.6
ν_{13}	0.25	0.4	0.25
e_{31}(C m^{-2})	-6.54	0	0
e_{32} (C m^{-2})	-4.14	0	0
e_{33} (C m^{-2})	11.58	0	0
ϵ_{11}=ϵ_{22}=ϵ_{33} (C V^{-1} m^{-1})	11.53×10^{-9}	11.53×10^{-9}	10.18×10^{-11}
Thickness (mm)	1.524	0.254	15.24
Width (mm)	25.4	25.4	25.4
Length (mm)	152.4	152.4	152.4
Density (kg m^{-3})	7600	1662	2769

Table 6.2: Cross-sectional constants of three-layer straight smart beam

S	1	2	3	4	5	6
1	2.9324×10^{7}	0.691675	2.4937	0.0390635	-2575.85	1481.36
2	0.691675	9.54803×10^{6}	9545.66	3401.75	0.048804	-0.00634431
3	2.4937	9545.66	9.57643×10^{6}	-492.044	11.2683	0.50928
4	0.0390635	3401.75	-492.044	625.46	-0.0201041	-0.000224116
5	-2575.85	0.048804	11.2683	-0.0201041	698.577	-4.23373
6	1481.36	-0.00634431	0.50928	-0.000224116	-4.23373	1570.39

First, the cross-sectional constants are obtained from VABS as listed in Table 6.2. These along with the actuation terms $F_{a_1} = 2.76337 \times 10^3$ N and $M_{a_2} = 2.314 \times 10^1$ Nm, obtained specifically from VABS version 4.0 are used as inputs into the equations. The accuracy of results also depend upon the accuracy of these cross-sectional constants. ABAQUS is used for the 3D FEM analysis. The cross-section is meshed with seven elements along the thickness of aluminum layer and two elements along the thickness of both piezoelectric and adhesive layers. Ten elements are specified along the width and twenty elements along the length of each layer. The aluminum and adhesive layers contain 8-node linear brick elements, with reduced integration and hourglass control (C3D8R). The piezoelectric layer has 8-node linear piezoelectric bricks (C3D8E). A general contact interaction is present between all the layers having interaction properties such that there is no slip (tangential behavior) and there exists a hard contact without separation (normal behavior). The linear, intrinsic equations for static case are given by:

$$\begin{aligned} F' + \widetilde{k}F + f = 0 \\ M' + \widetilde{k}M + \widetilde{e_1}F + m = 0 \end{aligned} \tag{6.9}$$

where

$$\begin{aligned} \widetilde{K} &= \begin{bmatrix} 0 & -k_3 & k_2 \\ k_3 & 0 & -k_1 \\ -k_2 & k_1 & 0 \end{bmatrix} \\ \widetilde{e_1} &= \begin{bmatrix} 0 & 0 & 0 \\ 0 & 0 & -1 \\ 0 & 1 & 0 \end{bmatrix} \end{aligned} \tag{6.10}$$

Here, f and m are the uniform distributed force and moment column matrices, respectively. F and M are the force and moment column matrices, respectively. The kinematic equations

can be simplified as:

$$\gamma = u' + \widetilde{k}u + \widetilde{e_1}\theta \tag{6.11a}$$

$$\kappa = \theta' + \widetilde{k}\theta \tag{6.11b}$$

On solving the constitutive Eq. (5.31), the intrinsic Eq. (6.9) and the kinematic Eq. (6.11), values of displacements and rotations can be obtained. Two sets of boundary conditions (BC) are possible. One set could be either applied at x_1 = 0 or the other which is applied at $x_1 = L$. It would be simpler to apply boundary conditions at $x_1 = L$ as shown

$$BC \text{ at } x_1 = L, \quad \begin{cases} F_1(L) = \hat{F}_1, \;\; M_1(L) = \hat{M}_1 \\ F_2(L) = \hat{F}_2, \;\; M_2(L) = \hat{M}_2 \\ F_3(L) = \hat{F}_3, \;\; M_3(L) = \hat{M}_3 \end{cases} \tag{6.12}$$

Moreover, it would make sense to use the local coordinate frame to solve the equations as the actuation and distributed load variables are present in that frame. Later on, the results can be converted back into the global coordinate frame easily using a direction consine matrix. Using the boundary condition sets, Eq. (6.9) can be solved for given F and M matrices, so that

$$F = \begin{Bmatrix} \hat{F}_1 + F_{a_1} + f_1(L - x_1) \\ \hat{F}_2 + F_{a_2} + f_2(L - x_1) \\ \hat{F}_3 + F_{a_3} + f_3(L - x_1) \end{Bmatrix} \tag{6.13}$$

$$M = \begin{Bmatrix} \hat{M}_1 + M_{a_1} + m_1(L - x_1) \\ \hat{M}_2 + M_{a_2} - \frac{1}{2}(L - x_1)(f_3(L - x_1) + 2(F_3 - m_2)) \\ \hat{M}_3 + M_{a_3} + \frac{1}{2}(L - x_1)(f_2(L - x_1) + 2(F_2 + m_3)) \end{Bmatrix} \tag{6.14}$$

By substituting Eqs. (6.13) and (6.14) into Eqs. (6.15) and (6.16), and specifying boundary conditions such that the displacements and rotation terms are zero at the fixed end $(x_1 = 0)$,

the values of displacement and rotations can be obtained along the beam length directly in the global frame because the beam is straight. For this particular case, because the beam is straight and prismatic, $k_1 = k_2 = k_3 = 0$, no external tip forces and moments are acting, and column matrices $\hat{F} = 0$ and $\hat{M} = 0$. Finally, no distributed loads are applied so column matrices $f = 0$ and $m = 0$.

$$\left\{ \begin{array}{c} {u_1}'(x_1) \\ {u_2}'(x_1) - \theta_3(x_1) \\ \theta_2(x_1) + {u_3}'(x_1) \end{array} \right\} = RF + ZM \tag{6.15}$$

$$\left\{ \begin{array}{c} {\theta_1}'(x_1) \\ {\theta_2}'(x_1) \\ {\theta_3}'(x_1) \end{array} \right\} = Z^{\mathsf{T}}F + TM \tag{6.16}$$

Here, $u(x_1)$ is the column matrix of displacement measures expressed in the beam cross-sectional frame and $\theta(x_1)$ is the column matrix of infinitesimal cross-sectional rotations.

Table 6.3 shows the tip displacement values computed by [144], [149], ABAQUS and the present work at the midpoint of the cross section $(H/2)$. It can be observed that the results obtained from present equations are more close to the results obtained from the 3D FEM. Figures 6.2 and 6.3 show the variations in the displacement results obtained along the beam length. Figure 6.4 shows the rotation (in radians) for each section along the beam length.

Table 6.3: Tip displacements of straight smart beam

Displacement (m)	Robbins et al.	Saravanos et al.	ABAQUS	Present
$U_1(\times 10^5)$	1.365	1.361	1.485	1.481
$U_3(\times 10^4)$	-3.470	-3.299	-3.889	-3.888

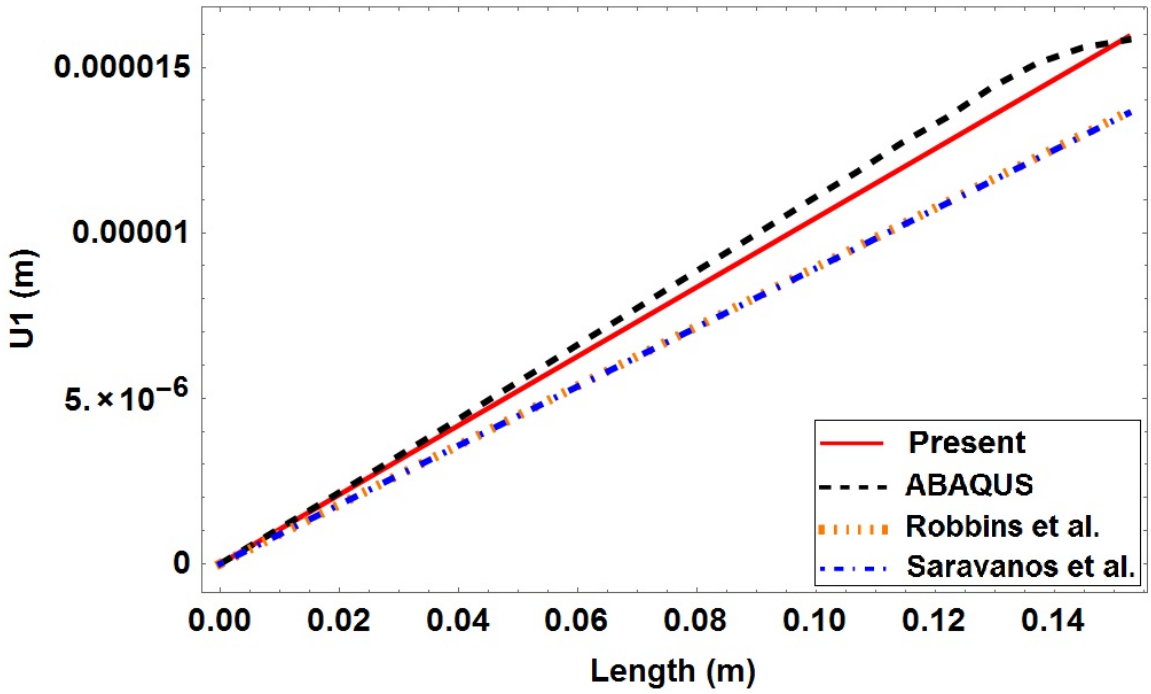

Figure 6.2: Displacement in x_1 direction (straight actuator)

Sensor

The same three-layer, straight, piezo-composite cantilevered beam is studied as a sensor. All the material and geometrical properties remain the same as specified earlier in Table 6.1. The cross-sectional constants given by VABS are also the same as shown in Table 6.2. The only difference from the actuator case is that no electric voltage is applied on the piezoelectric layer, which means that all the actuation terms are now zero. Instead, a point load of 100 N is applied at the midpoint of the tip section towards the positive x_3 direction as seen in Fig. 6.1. The value of $\hat{F}_3 = 100$ N; and all other loads, moments and curvatures are specified as zero in Eqs. (6.13) – (6.16) for the straight smart beams. The displacement and rotation values along the beam length are compared with the 3D FEM results as shown in Figs. 6.5 and 6.6. These values could be further used as inputs to recover the distribution in voltage, stress and strain in each section along the beam length.

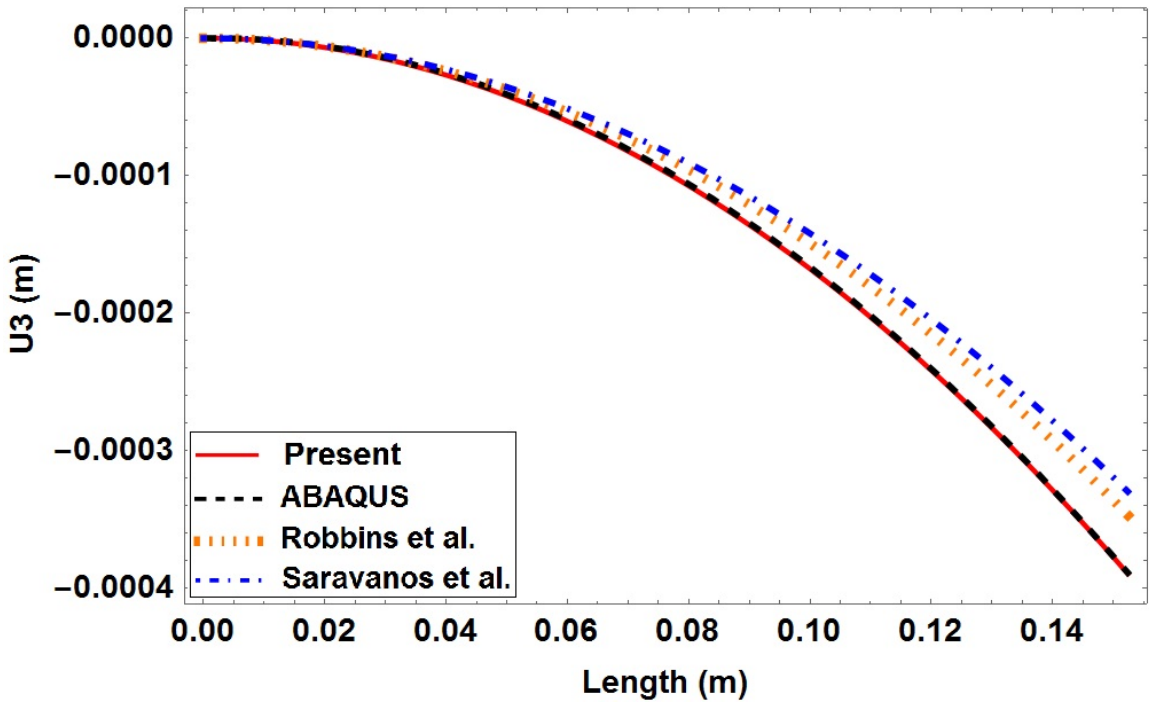

Figure 6.3: Displacement in x_3 direction (straight actuator)

6.2.2 Twisted Smart Beam

Actuator

In order to analyze the effect of initial twist, the straight smart beam analyzed in Case 1 is provided with an initial twist of $20°$ about x_1 as seen in Fig. 6.7. The material and geometrical parameters remain the same as specified earlier in Table 6.1. For actuation, the same constant electric voltage of 12.49 kV is applied on the top of piezoelectric layer having its bottom surface grounded.

VABS version 4.0 is used to obtain new cross-sectional constants for this initially twisted smart beam as specified in Table 6.4. These along with actuation terms $F_{a_1} = 2.722 \times 10^3$ N and $M_{a_2} = 2.2915 \times 10^1$ Nm are used as inputs into the equations. The direction of these terms remain the same with respect to the local coordinate frame of each section hence they are easily accommodated in the equations. The cross section contains 110 elements and 20 elements present along the length and width of each layer, respec-

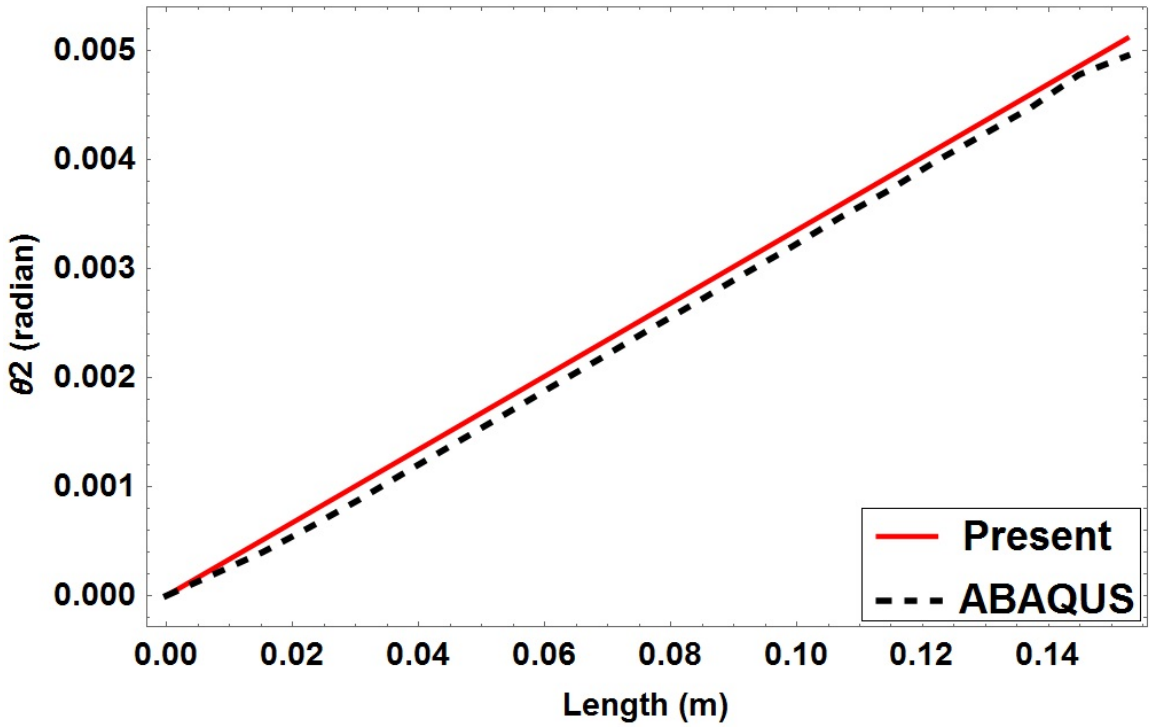

Figure 6.4: Rotation about x_2 axis (straight actuator)

tively, with the same element types as specified in Case 1.

Because of the lack of literature available for initially twisted and curved smart beams, 3D FEM analysis done in ABAQUS is used to verify the results obtained from the modified equations. The initial twist $k_1 = \pi/(9L)$ rad/m, and the curvatures $k_2 = k_3 = 0$. No external tip forces and moments are acting, so column matrices $\hat{F}$ and $\hat{M}$ are both equal to zero. Similarly, no distributed loads are applied, so column matrices $f = 0$ and $m = 0$. On solving Eq. (5.31), (6.9), (6.11), and (6.12), the Eqs. (6.13) – (6.16) specified in Case 1 are now changed into Eqs. (6.17) – (6.22) for the initially twisted beam. It is simpler to calculate the displacement and rotations for each section in the local coordinate frame (x_2', x_3') because of the presence of actuation terms in that frame.

$$F = \begin{Bmatrix} \hat{F}_1 + F_{a_1} + f_1(L - x_1) \\ \frac{\mathcal{G}_1 \sin(k_1(L-x_1)) + \mathcal{G}_2 \cos(k_1(L-x_1)) - f_3}{k_1} + F_{a_2} \\ \frac{\mathcal{G}_2 \sin(k_1(L-x_1)) - \mathcal{G}_1 \cos(k_1(L-x_1)) + f_2}{k_1} + F_{a_3} \end{Bmatrix} \tag{6.17}$$

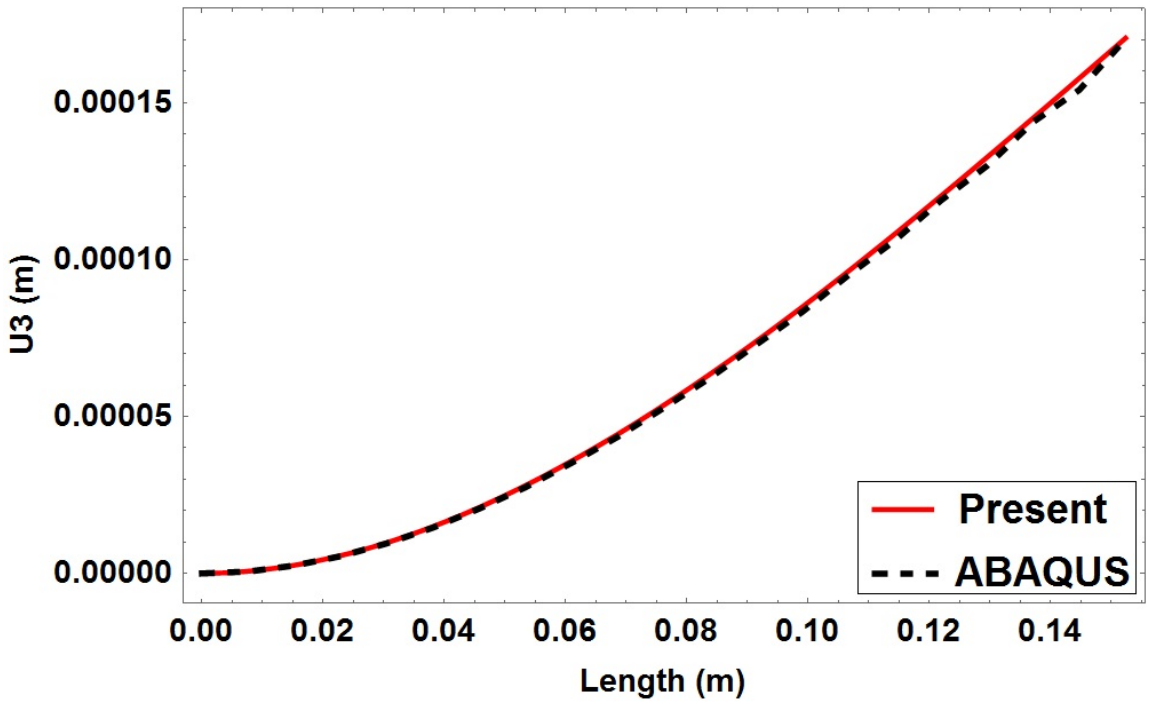

Figure 6.5: Displacement in x_3 direction (straight sensor)

Table 6.4: Cross-sectional constants of three-layer twisted smart beam

S	1	2	3	4	5	6
1	2.93241×10^7	-4910.74	-4416.08	-3.9026	-2577.35	1481.29
2	-4910.74	9.54987×10^6	9506.6	3413.33	-283.869	9.42858
3	-4416.08	9506.6	9.58203×10^6	-491.905	19.3503	-934.201
4	-3.9026	3413.33	-491.905	625.469	0.485259	-0.139093
5	-2577.35	-283.869	19.3503	0.485259	698.749	-4.23138
6	1481.29	9.42858	-934.201	-0.139093	-4.23138	1571.14

where

$$\begin{aligned} \mathcal{G}_1 &= f_2 - \hat{F}_3 k_1 \\ \mathcal{G}_2 &= f_3 + \hat{F}_2 k_1 \end{aligned} \tag{6.18}$$

$$M = \left\{ \begin{array}{c} \hat{M}_1 + M_{a_1} + m_1(L - x_1) \\ \frac{\mathcal{T}_1 \cos(k_1(L-x_1)) - \mathcal{T}_2 \sin(k_1(L-x_1)) + f_3 - m_3 k_1}{{k_1}^2} + M_{a_2} \\ \frac{\mathcal{T}_2 \cos(k_1(L-x_1)) + \mathcal{T}_1 \sin(k_1(L-x_1)) - f_2 + m_2 k_1}{{k_1}^2} + M_{a_3} \end{array} \right\} \tag{6.19}$$

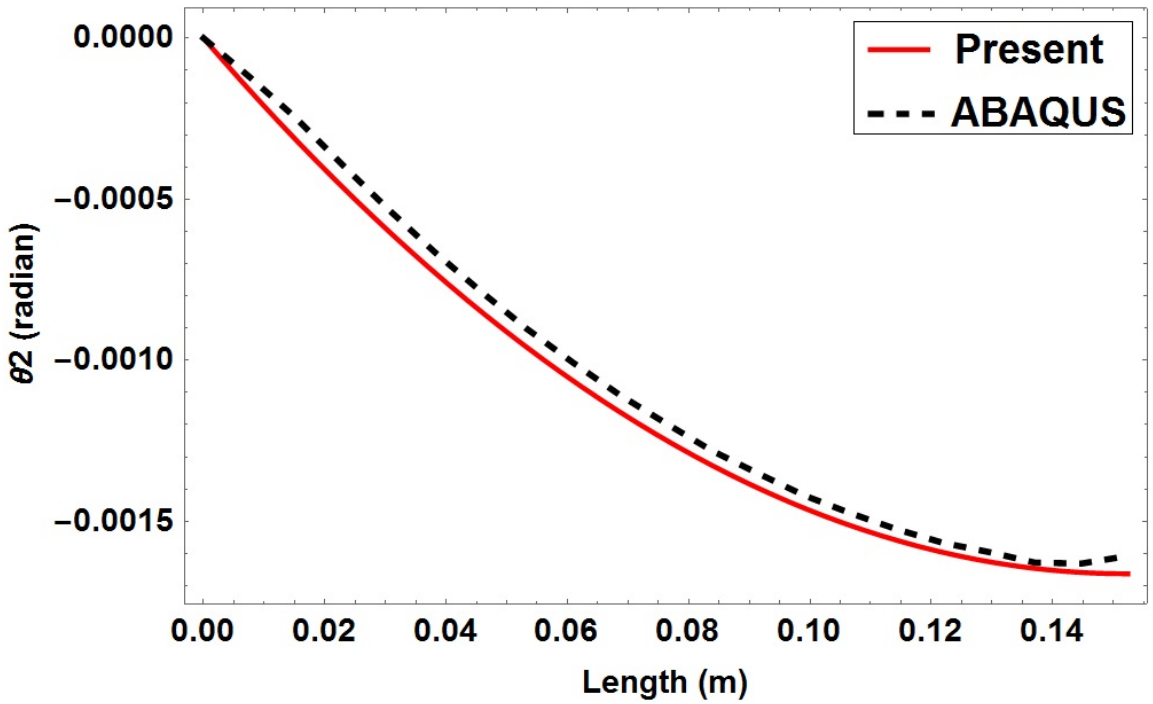

Figure 6.6: Rotation about x_2 axis (straight sensor)

where

$$\begin{aligned} \mathcal{T}_1 &= -f_3 + k_1(m_3 + \hat{M}_2 k_1 + \mathcal{G}_1(L - x_1)) \\ \mathcal{T}_2 &= f_2 + k_1(-m_2 + \hat{M}_3 k_1 + \mathcal{G}_2(L - x_1)) \end{aligned} \tag{6.20}$$

$$\left\{ \begin{array}{c} {u_1}'(x_1) \\ -k_1 u_3(x_1) - \theta_3(x_1) + {u_2}'(x_1) \\ k_1 u_2(x_1) + \theta_2(x_1) + {u_3}'(x_1) \end{array} \right\} = RF + ZM \tag{6.21}$$

$$\left\{ \begin{array}{c} {\theta_1}'(x_1) \\ {\theta_2}'(x_1) - k_1 \theta_3(x_1) \\ k_1 \theta_2(x_1) + {\theta_3}'(x_1) \end{array} \right\} = Z^{\mathsf{T}} F + TM \tag{6.22}$$

The results for each section are transformed back into the global coordinate frame (x_2,x_3)

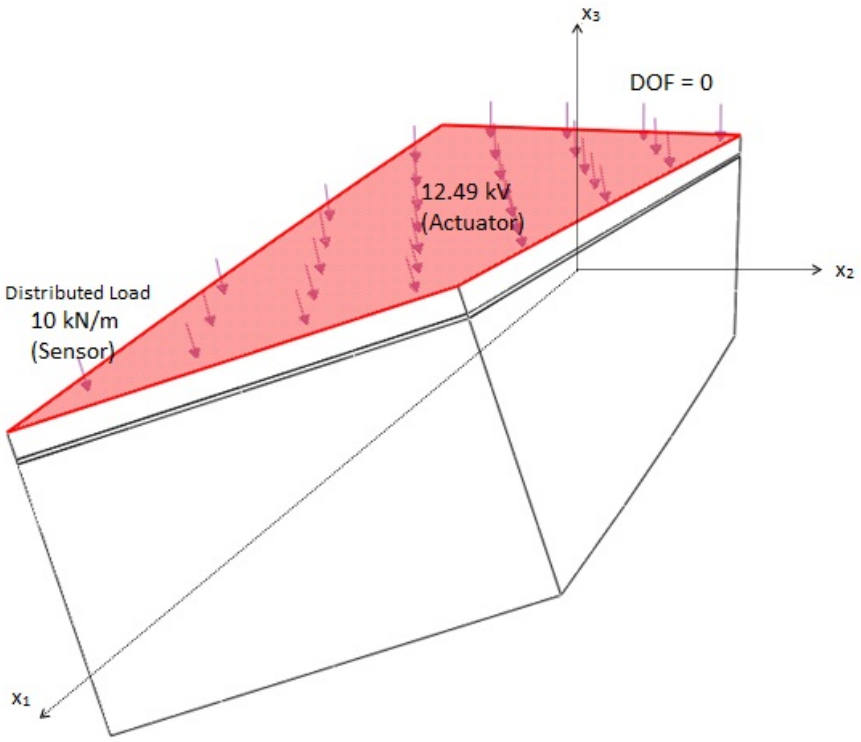

Figure 6.7: Three-layer twisted smart beam

using the rotation matrix $\bar{\mathcal{R}}$.

$$\bar{\mathcal{R}} = \begin{bmatrix} 1 & 0 & 0 \\ 0 & \cos(k_1 x_1) & -\sin(k_1 x_1) \\ 0 & \sin(k_1 x_1) & \cos(k_1 x_1) \end{bmatrix} \tag{6.23}$$

Results obtained from the present work are compared with those obtained from ABAQUS as shown in Figs. 6.9 – 6.12.

Sensor

The same curved beam is analyzed as a sensor. Since no electric potential is predefined, all the actuation terms go to zero. This time, a uniform distributed load of 10 kN/m is applied on the top of the piezoelectric layer in the negative local x_3 direction (i.e., $f_3 = -10,000$) as seen in Fig. 6.7 where the distributed load remains perpendicular to the surface. Since we

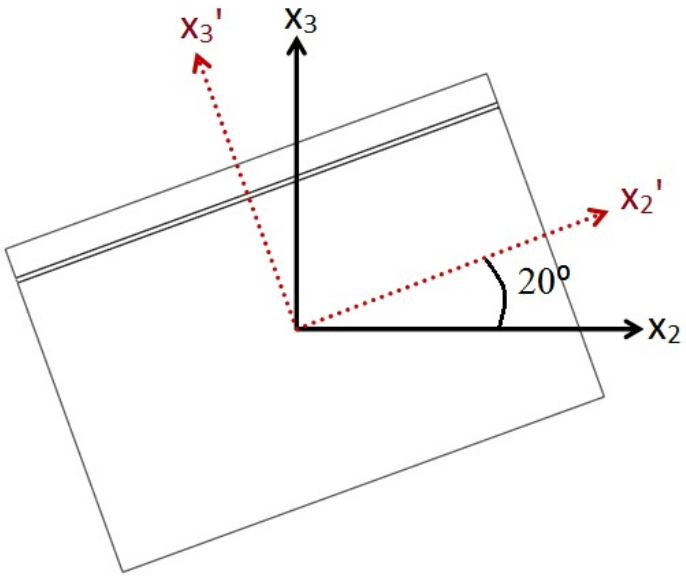

Figure 6.8: Rotation from local to global frame

are solving the equations in the local frame, no modifications in either boundary conditions or equations are required. It should be noted that in ABAQUS a total distributed load of 1524 N is applied for analysis. If a tip load was applied in the positive global x_3 direction, then we would have to specify its components in the local frame. The results obtained from solving Eqs. (6.17) – (6.22) are plotted in Figs. 6.13 – 6.15, which could be further used as inputs to recover 3D results.

6.2.3 Curved Smart Beam

Actuator

A curved cantilevered piezo-composite smart beam is modeled as shown in Fig. 6.16. The same straight smart beam as discussed in Case 1 is provided with an initial curvature of 0.0023 rad/mm about x_3. The beam is defined by an arc of 152.4 mm length making $20°$ with the center located on the positive x_2 axis. The geometrical and material properties remain the same as given in Table 6.1. The elements in each layer remain the same with 1400 elements in aluminum, 400 in adhesive and 400 in piezoelectric layer. For actuation, 12.49

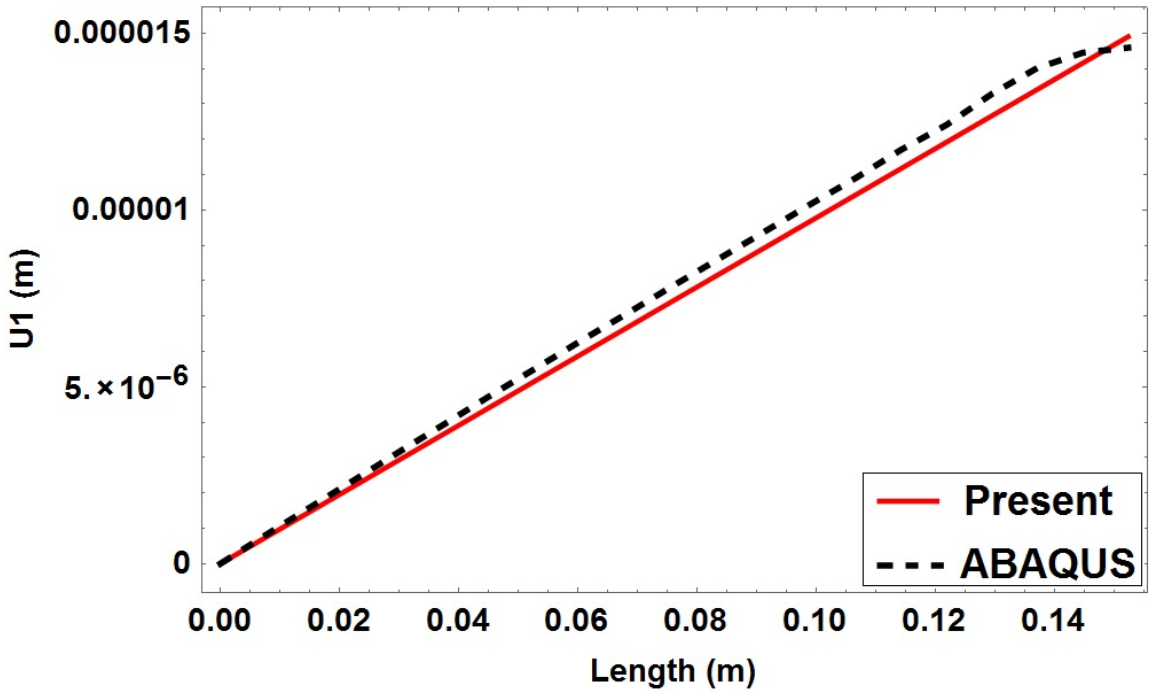

Figure 6.9: Displacement in x_1 direction (twisted actuator)

Table 6.5: Cross-sectional constants of three-layer curved smart beam

S	1	2	3	4	5	6
1	2.92844 $\times 10^7$	0.779926	0.37095	0.0106538	-2563.01	-2340.98
2	0.779926	9.54986$\times 10^6$	7224.5	3401.41	0.0300371	-0.00898333
3	0.37095	7224.5	9.57984$\times 10^6$	672.544	11.15	0.557241
4	0.0106538	3401.41	672.544	625.599	-0.0210691	-0.000236855
5	-2563.01	0.0300371	11.15	-0.0210691	698.613	-3.89356
6	-2340.98	-0.00898333	0.557241	-0.000236855	-3.89356	1570.66

kV of potential difference is applied across the piezoelectric layer. The cross-sectional constants for this initially twisted beam are obtained from VABS version 4.0, as specified in Table 6.5. The actuation terms $F_{a_1} = 2.8928 \times 10^3$ N and $M_{a_2} = 2.2733 \times 10^1$ Nm are used as inputs into the equations. The direction of actuation terms remains the same with respect to the local coordinate frame. Note that $k_3 = \pi/(9L)$ rad/m and $k_1 = k_2 = 0$, and no external tip forces and moments are acting. The column matrices $\hat{F} = 0$ and $\hat{M} = 0$, and no uniform distributed loads are applied, so that, the column matrices $f = 0$ and $m = 0$. On solving Eqs. (5.31), (6.9), (6.11), and (6.12), Eqs. (6.13) – (6.16) for the initially curved beam are now changed to

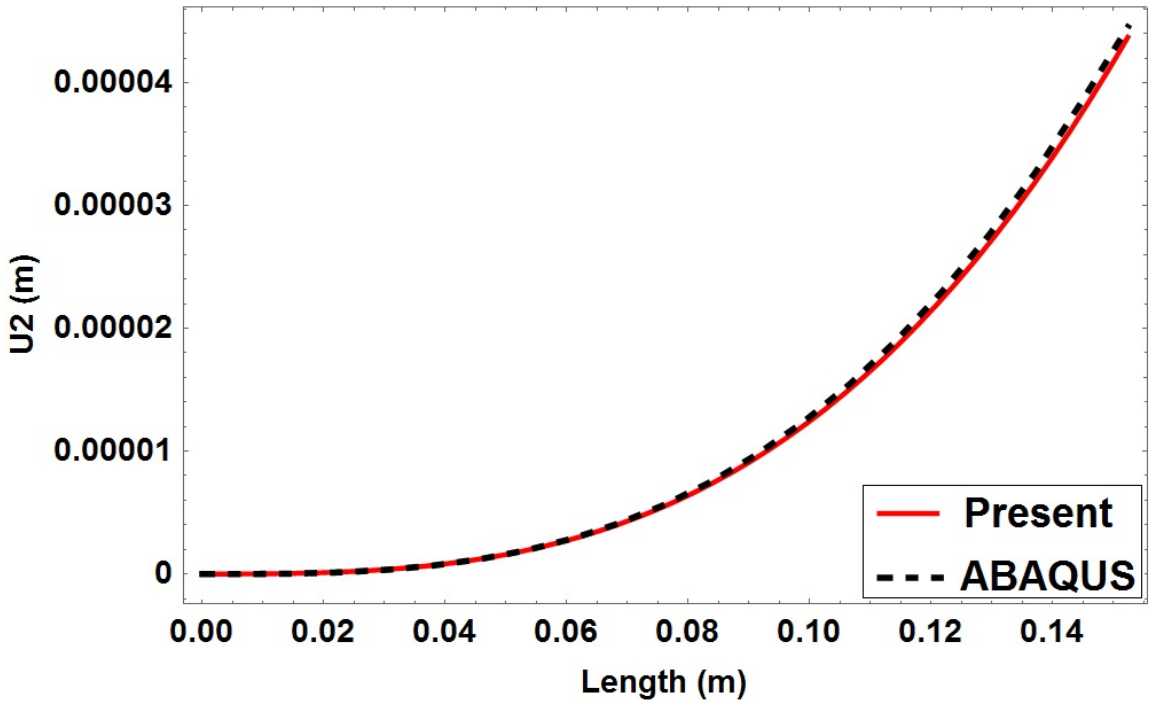

Figure 6.10: Displacement in x_2 direction (twisted actuator)

$$F = \left\{ \begin{array}{c} \frac{\mathcal{G}_1 \sin(k_3(L-x_1))+\mathcal{G}_2 \cos(k_3(L-x_1))-f_2}{k_3} + F_{a_1} \\ \frac{\mathcal{G}_2 \sin(k_3(L-x_1))-\mathcal{G}_1 \cos(k_3(L-x_1))+f_1}{k_3} + F_{a_2} \\ \hat{F}_3 + F_{a_3} + f_3(L-x_1) \end{array} \right\} \tag{6.24}$$

where

$$\begin{aligned} \mathcal{G}_1 &= f_1 - \hat{F}_2 k_3 \\ \mathcal{G}_2 &= f_2 + \hat{F}_1 k_3 \end{aligned} \tag{6.25}$$

$$M = \left\{ \begin{array}{c} \frac{\mathcal{T}_3+\mathcal{T}_1 \cos(k_3(L-x_1))-\mathcal{T}_2 \sin(k_3(L-x_1))}{{k_3}^2} + M_{a_1} \\ \frac{\mathcal{T}_4+\mathcal{T}_2 \cos(k_3(L-x_1))+\mathcal{T}_1 \sin(k_3(L-x_1))}{{k_3}^2} + M_{a_2} \\ \frac{\mathcal{T}_5-\mathcal{G}_2 \cos(k_3(L-x_1))-\mathcal{G}_1 \sin(k_3(L-x_1))}{{k_3}^2} + M_{a_3} \end{array} \right\} \tag{6.26}$$

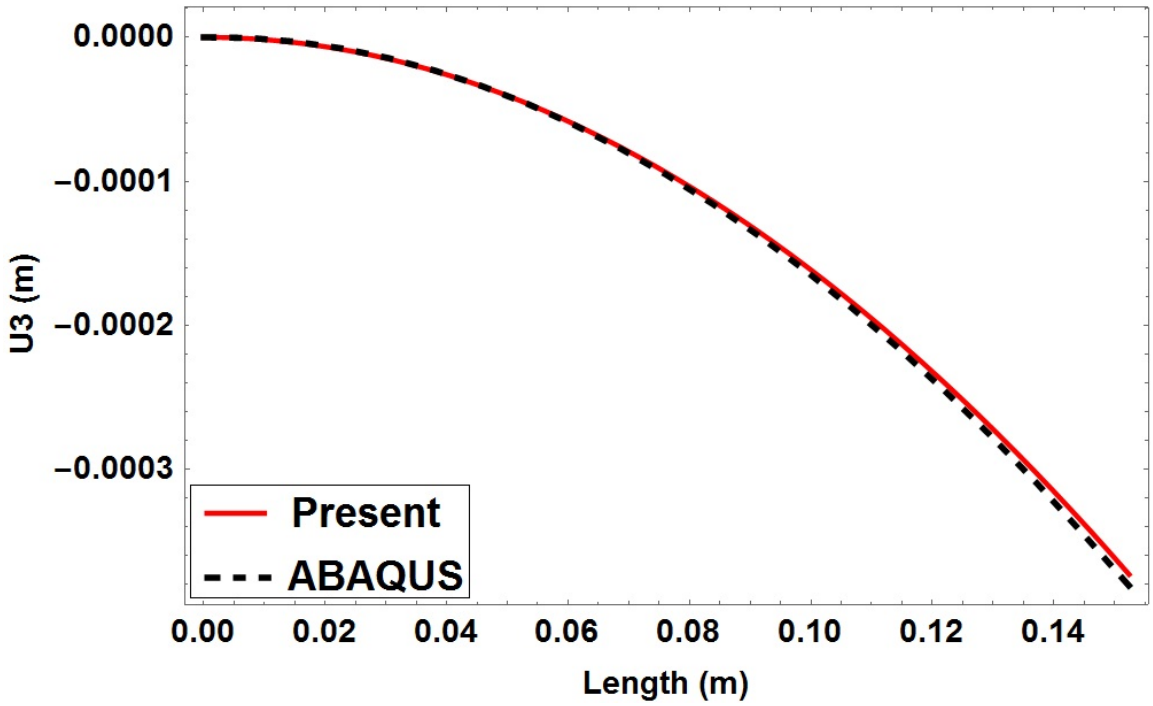

Figure 6.11: Displacement in x_3 direction (twisted actuator)

where

$$\begin{aligned}
\mathcal{T}_1 &= k_3(-\hat{F}_3 + m_2 + \hat{M}_1 k_3) \\
\mathcal{T}_2 &= f_3 + k_3(\hat{M}_2 k_3 - m_1) \\
\mathcal{T}_3 &= k_3(\hat{F}_3 - m_2 + f_3(L - x_1)) \\
\mathcal{T}_4 &= m_1 k_3 - f_3 \\
\mathcal{T}_5 &= {k_3}^2(\hat{M}_3 + m_3(L - x_1)) + k_3(\hat{F}_1 + f_1(L - x_1)) + f_2
\end{aligned} \tag{6.27}$$

$$\begin{Bmatrix} {u_1}'(x_1) - k_3 u_2(x_1) \\ k_3 u_1(x_1) - \theta_3(x_1) + {u_2}'(x_1) \\ \theta_2(x_1) + {u_3}'(x_1) \end{Bmatrix} = RF + ZM \tag{6.28}$$

$$\begin{Bmatrix} {\theta_1}'(x_1) - k_3\theta_2(x_1) \\ {\theta_2}'(x_1) + k_3\theta_1(x_1) \\ {\theta_3}'(x_1) \end{Bmatrix} = Z^{\mathsf{T}}F + TM \tag{6.29}$$

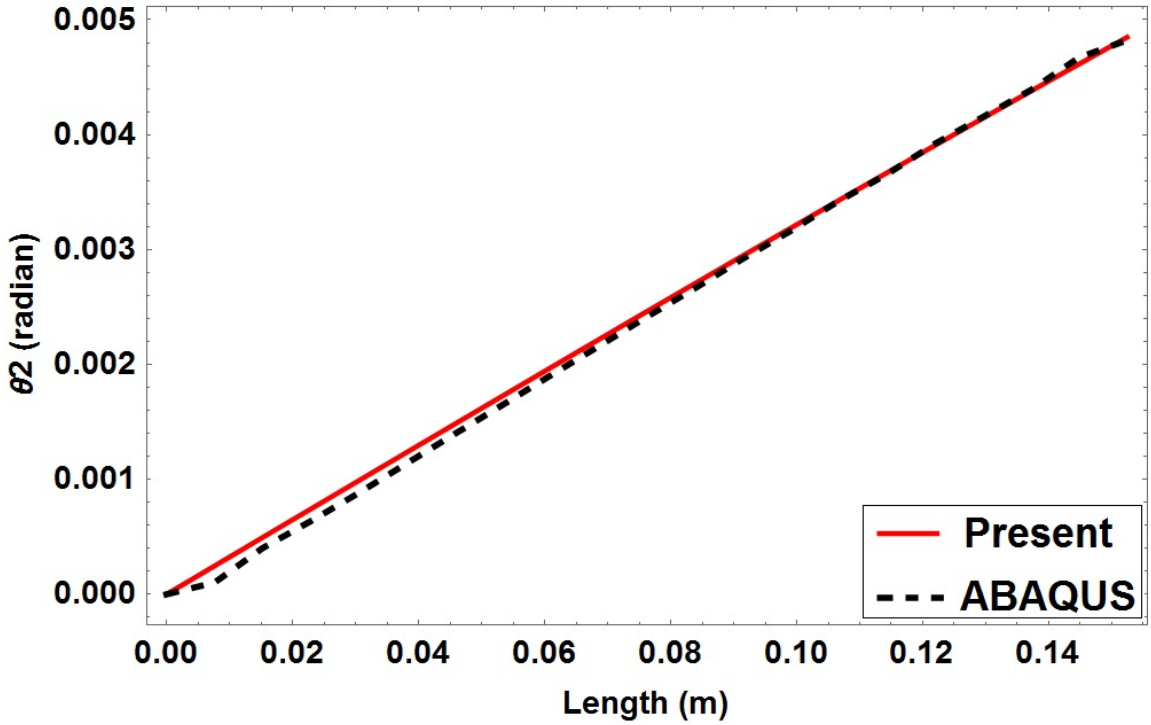

Figure 6.12: Rotation about x_2 axis (twisted actuator)

The results for each section are transformed back into the global coordinate frame using the rotation matrix $\bar{\mathcal{R}}$.

$$\bar{\mathcal{R}} = \begin{bmatrix} \cos(k_3 x_1) & -\sin(k_3 x_1) & 0 \\ \sin(k_3 x_1) & \cos(k_3 x_1) & 0 \\ 0 & 0 & 1 \end{bmatrix} \tag{6.30}$$

The displacements and rotations obtained in all three directions are plotted in Figs. 6.17 and 6.18. It can be observed that the results obtained from present work are in good agreement with the results obtained from 3D FEM.

Sensor

The same smart beam is analyzed as a sensor. To analyze the full capabilities of the formulated equations, for this case, electrical loads are applied on the curved beam that are equipotential to the mechanical loads applied in the case of an actuator. As seen in Fig. 6.16,

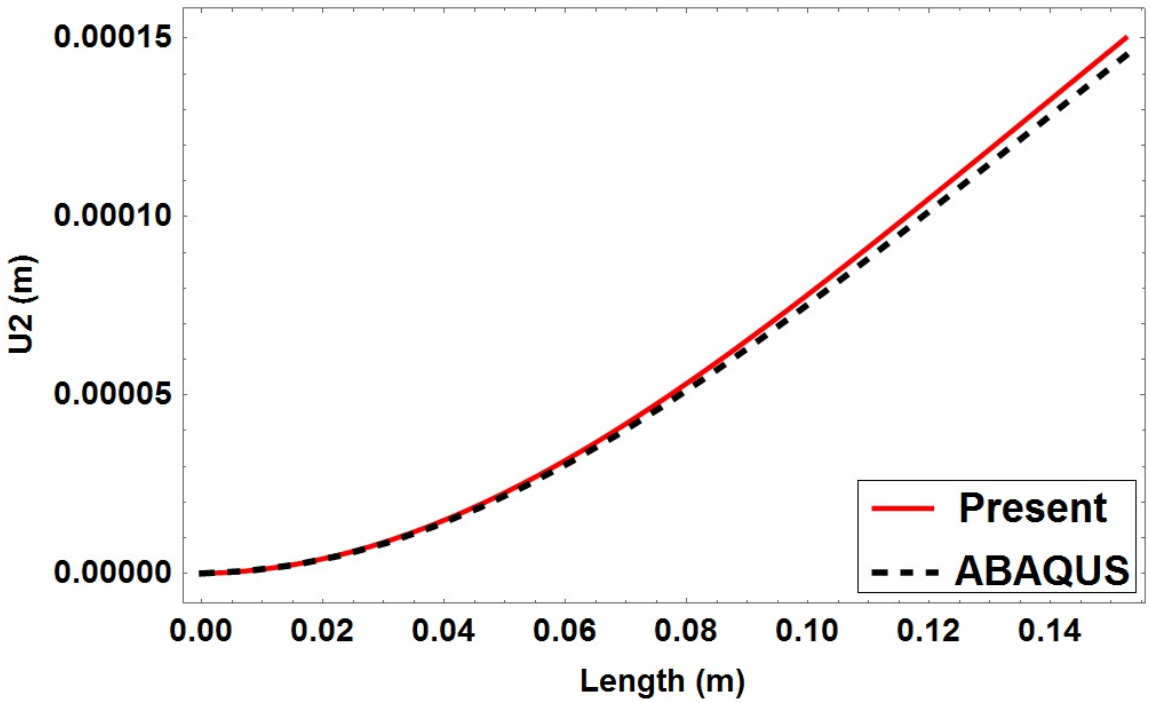

Figure 6.13: Displacement in x_2 direction (twisted sensor)

in addition to a tip point load of 100 N in the positive x_3 direction, the curved beam is also subjected to a uniform distributed load of 10 kN/m towards positive local x_2 direction. From comparison with 3D FEM results, it is observed that these equations can predict the displacements and rotations quite accurately in all three directions. The displacements and rotations obtained in all three directions are plotted in Figs. 6.19 and 6.20. These accurate 1D results could be further used as inputs to recover unknown 3D displacements, stresses and electric potentials.

Nonlinear Transient Analysis

In this case, we take the three-layer straight smart beam which was the subject of interest in Case 1 as well. Here, the straight smart beam is treated as an actuator. As a reminder to the readers, this cantilevered smart beam is made up of a piezoelectric layer on the top, followed by an adhesive layer fixing it to an aluminum substrate as shown in Fig. 6.1. Table 6.1 shows the geometrical and material properties of the beam. For the purpose of

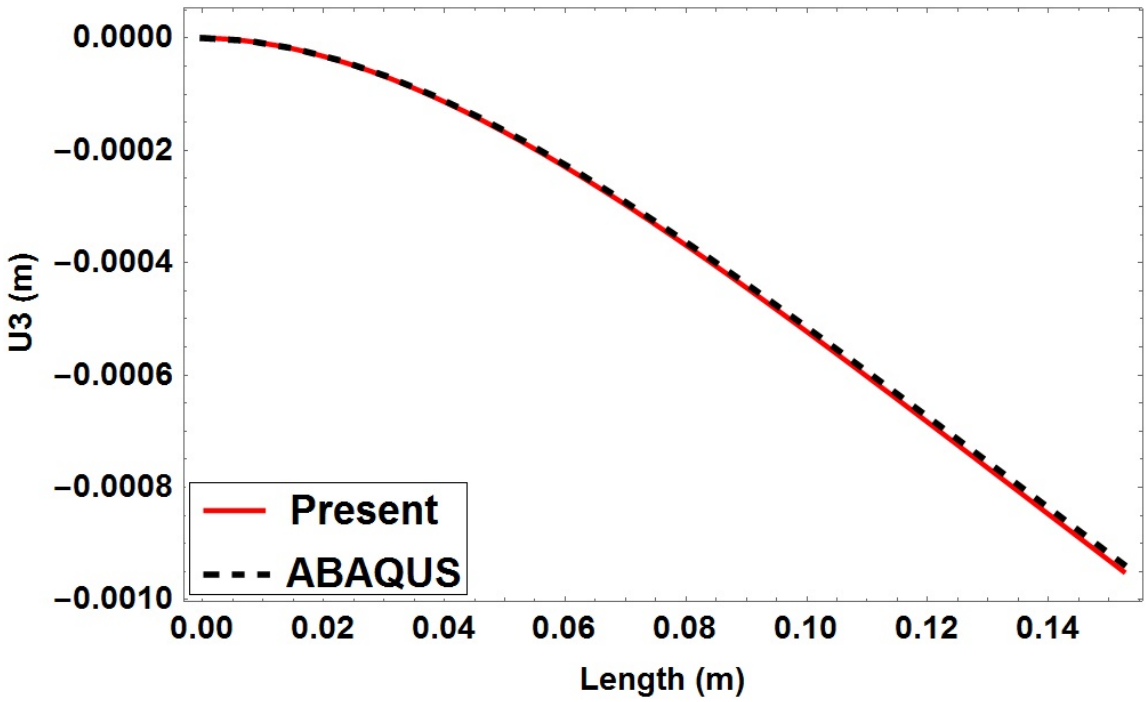

Figure 6.14: Displacement in x_3 direction (twisted sensor)

actuation, a dynamic electric potential of $12.49\sin(20t)$ kV is applied on the top surface of piezoelectric layer and the bottom surface of the piezoelectric layer is grounded.

As usual, the cross-sectional constants in the form of the 6×6 Generalized Timoshenko stiffness matrix are obtained from VABS as listed in Table 6.2. These along with the actuation terms $F_{a_1} = 2.76337 \times 10^3$ N and $M_{a_2} = 2.314 \times 10^1$ Nm which are obtained by considering the amplitude of the electrical load are used as inputs into the equations. As this problem involves a dynamic load, we employ a modified form of the mixed formulation discussed in Sec. 5.2 for a nonlinear transient electro-mechanical analysis. So, during the 1-D beam analysis using mixed-formulation, the constitutive law is modified as shown in Eq. (6.5) to accommodate dynamic actuator fores and moments as $F_{a_1} = 2.76337 \times 10^3 \sin(20t)$ N and $M_{a_2} = 2.314 \times 10^1 \sin(20t)$ Nm, respectively. Again, ABAQUS is used for the 3D FEM analysis in a similar way as used in Case 1. Figure 6.21 compares the tip displacement of the straight beam treated as an actuator undergoing dynamic electrical loads. As seen from the plot, results obtained from the present methodol-

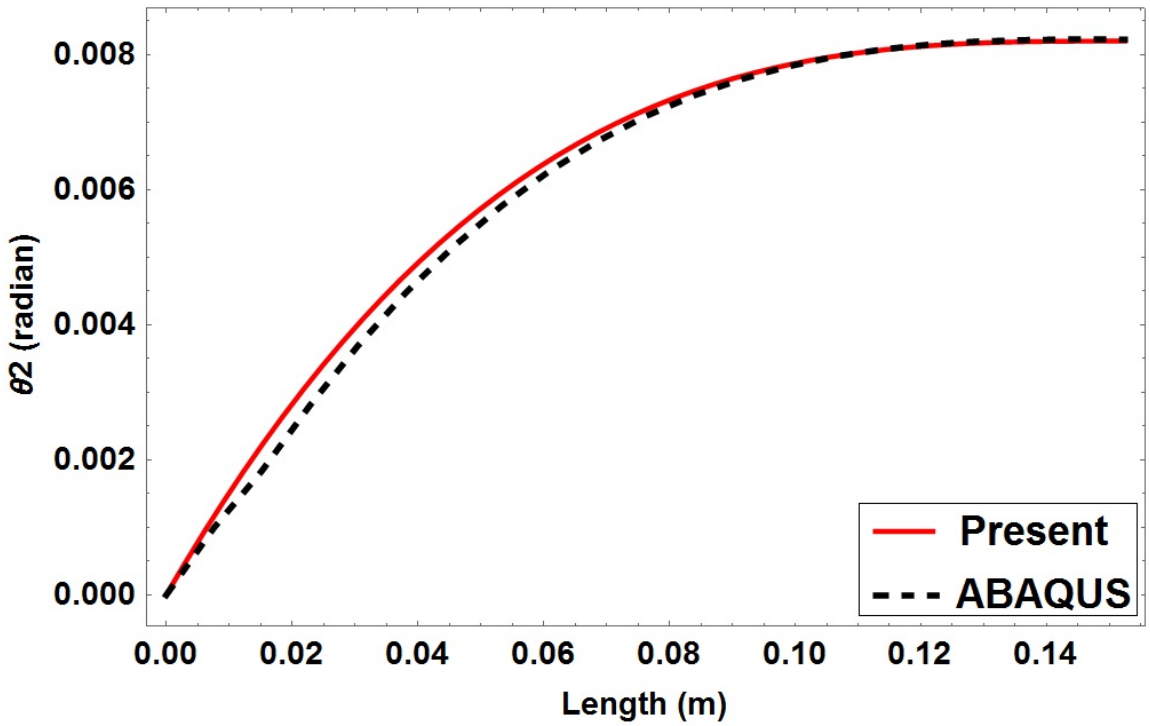

Figure 6.15: Rotation about x_2 axis (twisted sensor)

ogy are in very good agreement with results obtained from 3-D FEM.

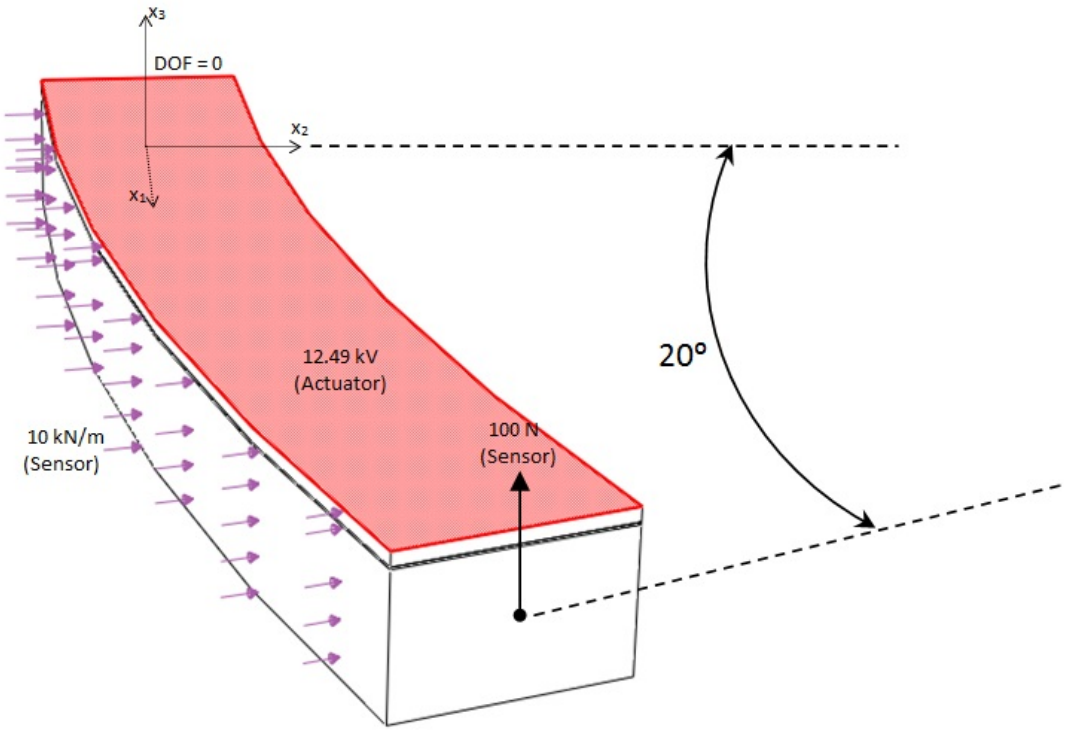

Figure 6.16: Three-layer curved smart beam

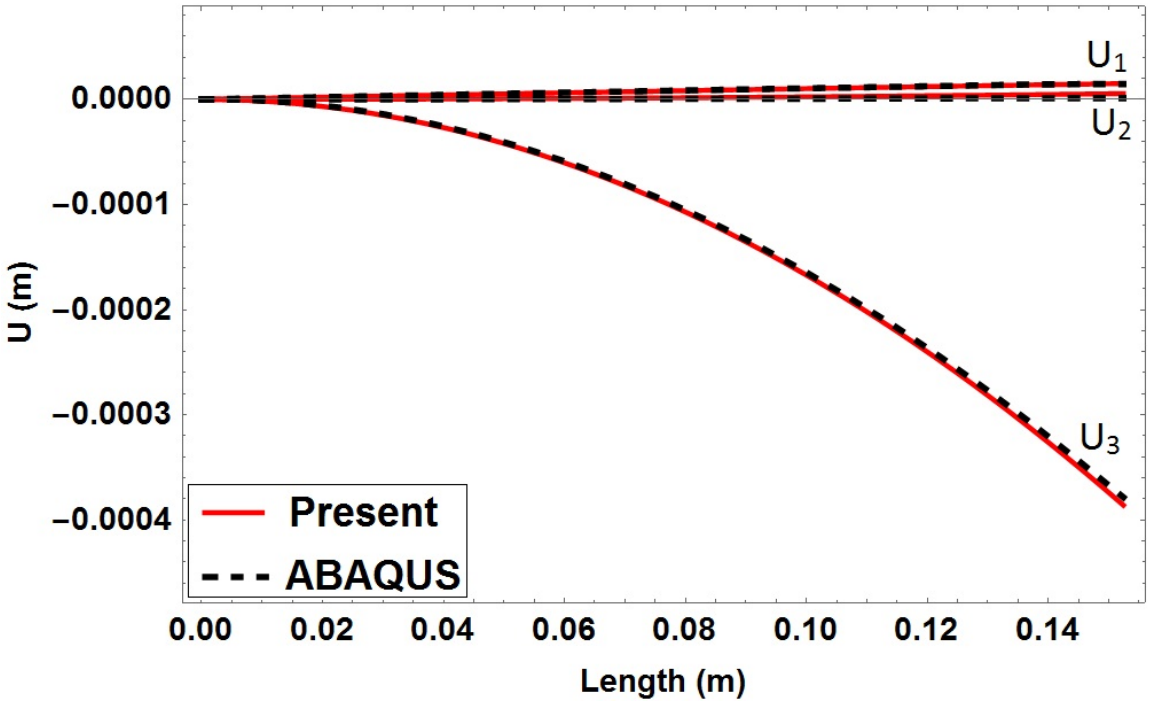

Figure 6.17: Displacement in all three directions (curved actuator)

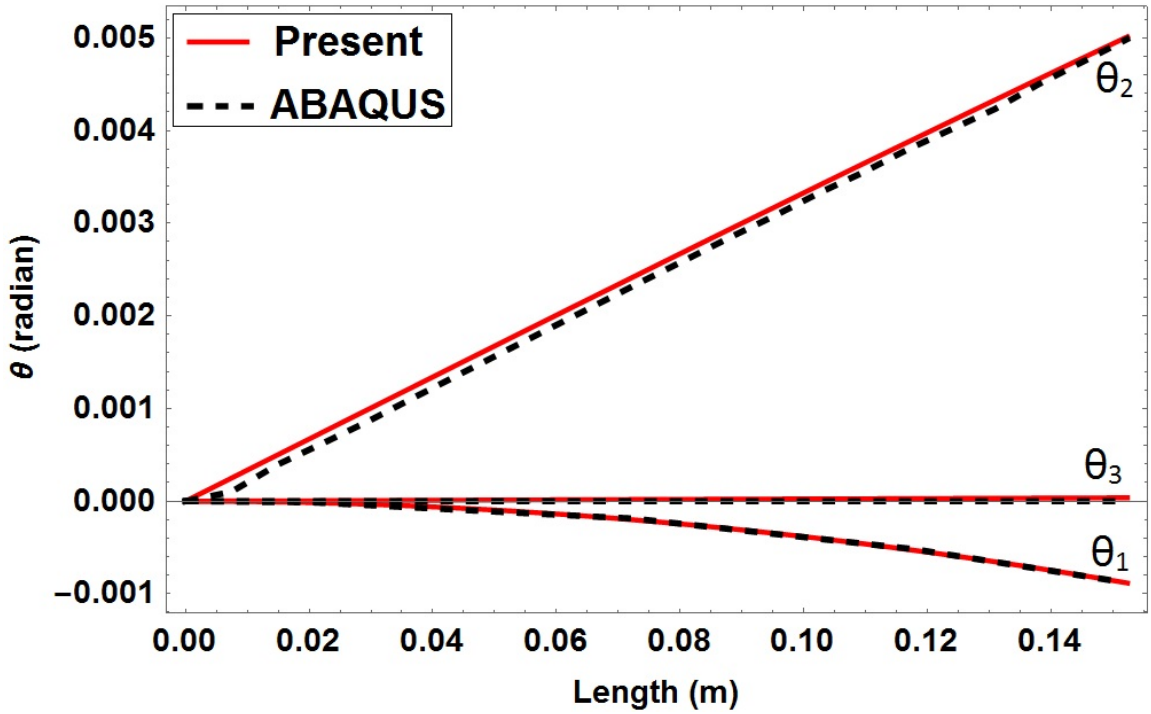

Figure 6.18: Rotations about all three axes (curved actuator)

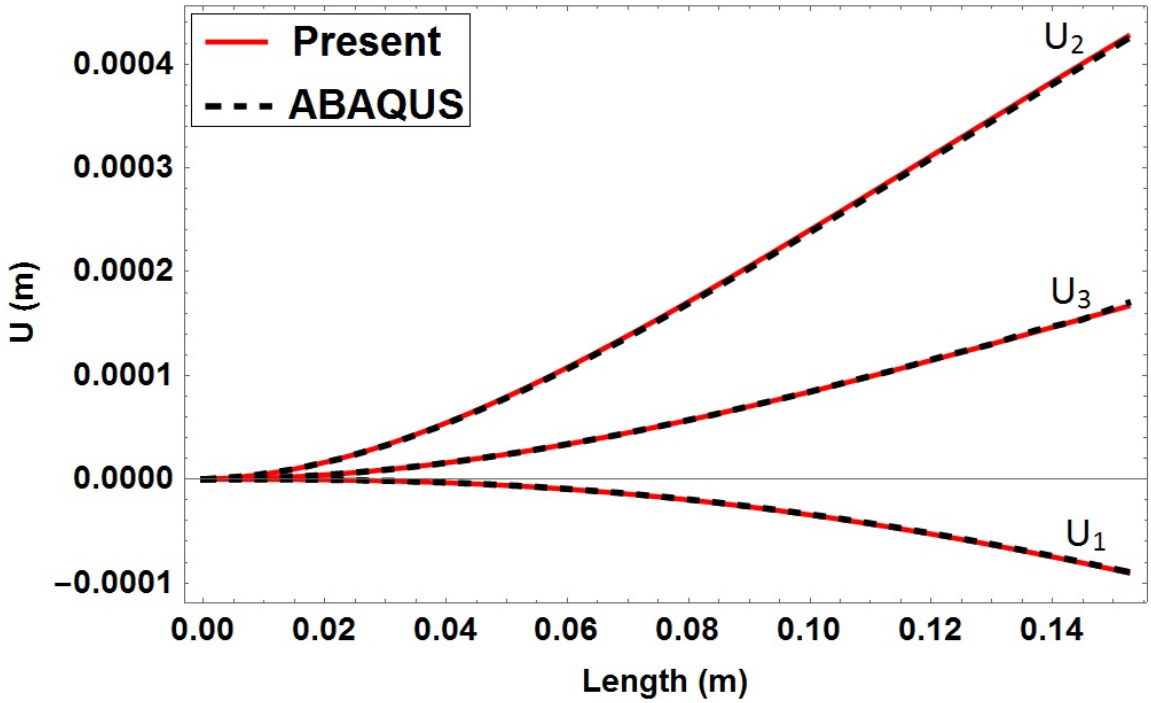

Figure 6.19: Displacement in all three directions (curved sensor)

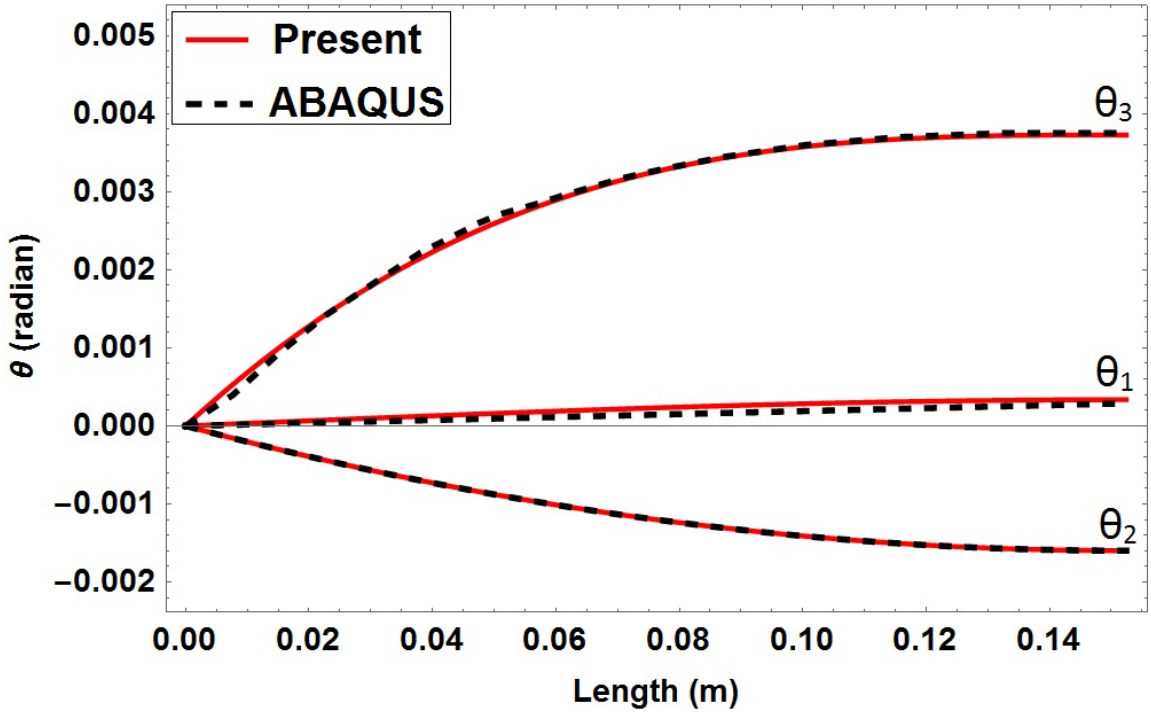

Figure 6.20: Rotations about all three axes (curved sensor)

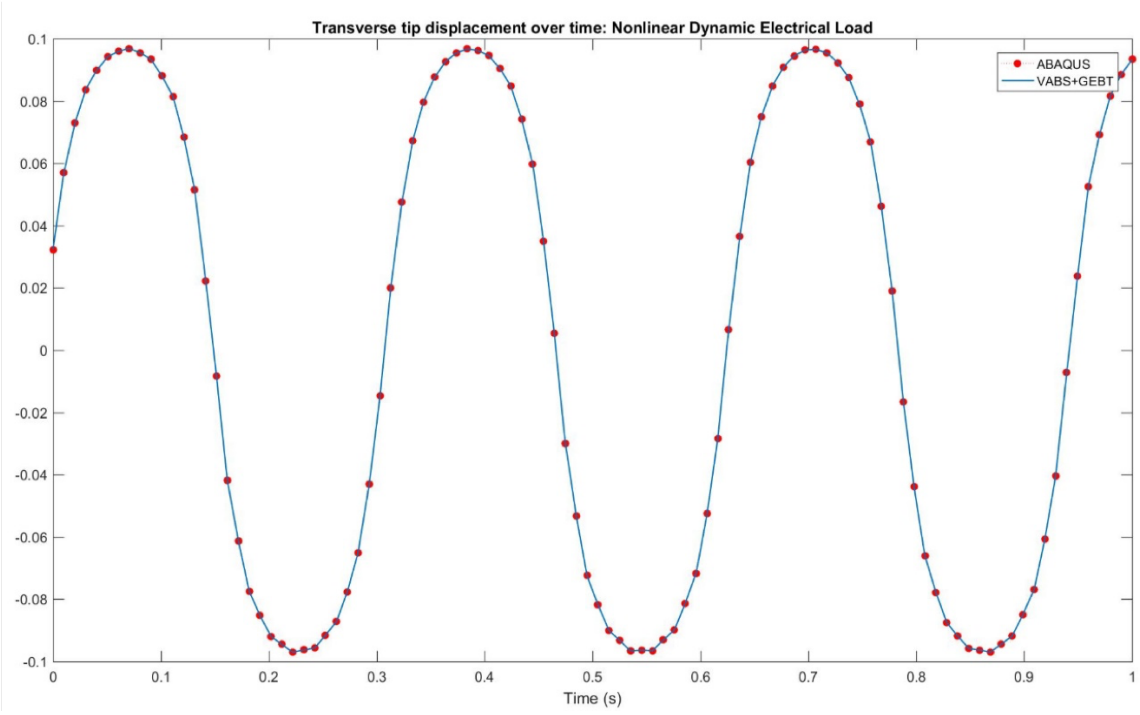

Figure 6.21: Tip displacement under dynamic electrical loads in the actuator

Part 4

Recovery of 3-D Variables

CHAPTER VII

DYNAMIC HISTORIES OF 3-D STRESSES IN NONLINEAR TRANSIENT ANALYSIS

The efficient, high-fidelity cross-sectional analysis tool, VABS developed out of the methodology researched at Georgia Tech, is the only analysis of its kind. VABS provides a variety of engineering models including structural models in the form of generalized classical, Timoshenko, and Vlasov models along with various non-classical effects for cross-sectional analysis of composite beams made with arbitrary geometry. As described in Ch. I, to perform structural analysis, one must determine the input information such as structural loads, geometry, boundary conditions, and material properties. The results of such an analysis typically include stresses, strains and displacements. It is also important for VABS to provide a high fidelity recovery for 3-D variables such as stresses using results from GEBT. A detailed account of the equations involved in the background of VABS and GEBT can be found in the references [138, 187, 186] and [69]. Also, from Ch. II and Ch V details on the theoretical framework of VABS and GEBT, respectively, can be obtained. This chapter provides a closure to the entire structural analysis of beam-like structures in aerial vehicles such as rotor blades. Here, a new framework is developed for the analysis based on VABS and GEBT that is robust and applicable to a wide range of problems, specifically problems with beams made of composite materials under dynamic loading. Existing capabilities of VABS include calculation of the mass matrix, the stiffness matrix from a second-order

asymptotically correct strain energy and a stress-strain displacement recovery which incorporates second-order warping solutions. This work to derive the second order warping solutions has been completed by Rajagopal [138] and is suitably modified for a transient analysis in the present framework as shown in Sec. 7.1.2. Perturbing the warping to the second-order results in a subsequent evaluation of the stress, strain and displacement to a higher fidelity. Since the stiffness matrix is correct up to second-order, evaluation of the second-order warping is sufficient to capture the second-order terms in the final expressions for recovery. Therefore, the current recovery procedure is consistent with the same level of fidelity as the stiffness matrix.

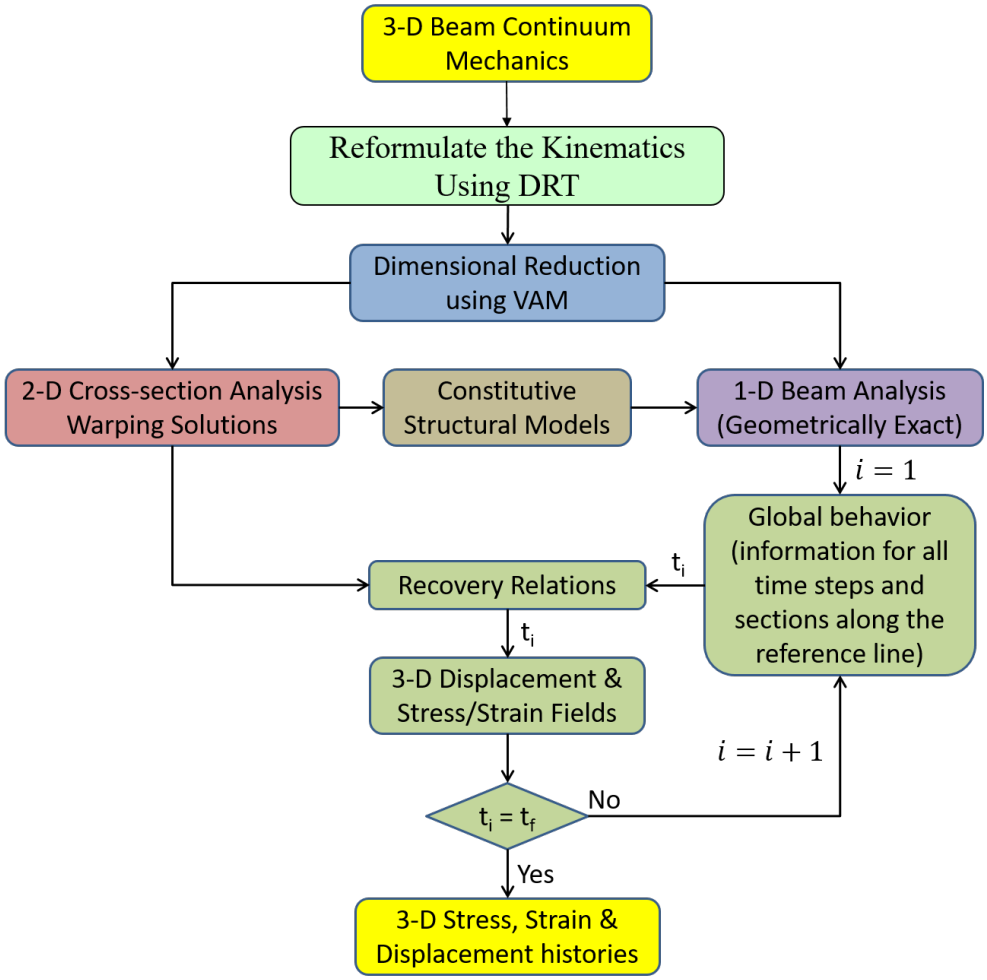

Figure 7.1: Flowchart for obtaining the complete 3-D stress-strain-displacement history for the dynamic analysis of composite beams

For the dynamic analysis, a transient structural problem is solved by dividing the simulation range into numerous small time-steps. Furthermore, the unknowns and the 3-D variables are evaluated at each time-step of this dynamic analysis, that makes use of the values at previous time-steps. Through the present work, a framework to obtain histories of 3-D variables is proposed. That is, we focus on recovery of 3-D stresses and strains at each time-step in a nonlinear transient structural analysis as shown in Fig. 7.1. The outputs from this framework are similar to the outputs from 3-D FEM and are a good resource for comparison. This framework aims to generate, store, retrieve, visualize and analyze the large amount of data generated at each time-step for providing an ability to understand material deformation and failure.

Visualizing stress and strain has always been an attractive option for engineers to understand the behavior of a component and make an engineering judgment about the location of stress concentrations. Also, analyzing values of stresses and strains at all the time-steps involved in the analysis can assist in the design process, especially in determining adherence to the failure criteria. It is, however, not possible to accomplish this task using conventional FEM tools due to excessive computational costs and lack of memory to handle the large amount of data generated by a 3-D FEM solver. This chapter demonstrates the capability of VABS and GEBT as computationally efficient, yet accurate tools for accomplishing the task to recover the 3-D stress and strain fields for all the locations in a 3-D beam at any given instant of time in the simulation range. This chapter also contains all the equations needed for obtaining a higher-order recovery of stress, strain and displacement in VABS for a nonlinear transient structural analysis. Finally, some results from the new framework are presented to demonstrate the 3-D stress histories in nonlinear transient analysis with validation against 3-D FEM.

7.1 Formulation for the 3-D Recovery

The Generalized Timoshenko (GT) model (note Eq. (2.52)) is obtained from the asymptotically correct strain energy in two steps. Initially, the coefficient matrices are obtained by differentiating terms in the asymptotically correct second order strain energy with respect to the strain. This process is followed by the application of nonlinear transformation equations with the help of 1-D equilibrium equations to make the coefficient matrices represent the shear strains instead of the 2-D beam generalized strain derivatives. As described in Ch. II, Sec. 2.3, the warping solutions obtained are asymptotically correct up to the first order of strain terms. These first-order warping solutions lead to the asymptotically correct second order strain energy. Further, for a higher fidelity recovery for 3-D variables such as stresses, strains and displacements, warping solutions are desired to be asymptotically correct up to the second order i.e. same order as that of the strain energy for the GT model.

7.1.1 Second-Order Analysis

This section develops higher order strain energy expressions for minimization with respect to the warping variables perturbed to the second order. Thus, the procedure in this section are directly following Sec. 2.3.2. For this purpose, the relevant terms in the strain energy would now be fourth-order terms. The warping solutions for second order would be very long and even longer would be the fourth-order strain energy expressions. However, our interest is only to evaluate the second-order warping solutions so, some simplifications can be made. Some terms in the strain energy expression are asymptotically correct up to the second-order. These terms are obtained by substituting the first-order warping solutions, so those terms would not enter the minimization problem for the computation of the second-order perturbations (V_2) to the first-order warping solutions. Also, the terms in the third- and fourth-order strain energy can be simplified to exclude the terms that do not contain V_2 because V_0 and V_1 are already identified. Thus, an expression for the third-order terms in

the strain energy can be written in terms of the warping variables (V_2) as

$$\begin{aligned}2U_3 =&(2V_2^T D_{a\epsilon_1} + 2V_2'^T D_{\ell\epsilon_1} + 2V_2^T D_{R\epsilon_1})\overline{\epsilon} + 2V_2^T D_{aR_1} V_0 + V_2^T E_1 V_0 + V_2^T E_0 V_1 \\ &+ 2V_0^T D_{aR_1} V_2 + V_1^T E_0 V_2 + V_0^T E_1 V_2 + 2V_2^T D_{a\ell_1} V_0' + 2V_0^T D_{a\ell_1} V_2' \\ =&2V_2^T (E_0 V_1 + D_R \overline{\epsilon} + D_S \overline{\epsilon}')\end{aligned} \tag{7.1}$$

The above simplification comes from Eq. (2.44). Also, the fourth-order terms in the strain energy expression can be compiled as

$$\begin{aligned}2U_4 =&(2V_2^T(D_{a\epsilon_2} + D_{R\epsilon_2}) + 2V_2'^T D_{\ell\epsilon_2})\overline{\epsilon} + 2V_2^T D_{aR_2} V_0 + V_2^T D_{RR_2} V_0 + V_2^T E_2 V_0 \\ &+ 2V_2^T D_{aR_1} V_1 + V_2^T E_1 V_1 + 2V_1^T D_{aR_1} V_2 + 2V_0^T D_{aR_2} V_2 + V_0^T D_{RR_2} V_2 \\ &+ V_2^T E_0 V_2 + V_1^T E_1 V_2 + V_0^T E_2 V_2 + V_2^T D_{a\ell_2} V_0' + V_2'^T D_{\ell\ell_2} V_0' + 2V_2^T D_{R\ell_2} V_0' \\ &+ 2V_2^T D_{a\ell_1} V_1' + 2V_1^T D_{a\ell_1} V_2' + 2V_0^T D_{a\ell_2} V_2' + V_0'^T D_{\ell\ell_2} V_2' + 2V_0^T D_{R\ell_2} V_2' \\ =&V_2^T E_0 V_2 + 2V_2^T \{[D_{a\epsilon_2} + D_{R\epsilon_2} + (D_{aR_2} + D_{RR_2} + E_2 + D_{aR_2}^T)\hat{V}_0 \\ &+ (E_1 + D_{aR_1} + D_{aR_1}^T)V_{1R}]\overline{\epsilon} + [-D_{\ell\epsilon_2} + (D_{a\ell_2} - D_{a\ell_2}^T + D_{R\ell_2} - D_{R\ell_2}^T)\hat{V}_0 \\ &+ (E_1 + D_{aR_1} + D_{aR_1}^T)V_{1S} + (D_{a\ell_1} - D_{a\ell_1}^T)V_{1R}]\overline{\epsilon}' + [(D_{a\ell_1} - D_{a\ell_1}^T)V_{1S} - D_{\ell\ell_2}\hat{V}_0]\overline{\epsilon}''\}\end{aligned} \tag{7.2}$$

Therefore, the final truncated functional to be minimized, is

$$\begin{aligned}\mathcal{F} =&V_2^T E_0 V_2 + 2V_2^T (D_0 \overline{\epsilon} + D_1 \overline{\epsilon}' + D_2 \overline{\epsilon}'') + 2V_2^T D_c \Lambda \\ &+ 2V_2^T (E_0 V_1 + D_R \overline{\epsilon} + D_S \overline{\epsilon}')\end{aligned} \tag{7.3}$$

The coefficient matrices in the equation above are defined as

$$
\begin{aligned}
D_0 &= D_{a\epsilon_2} + D_{R\epsilon_2} + (D_{aR_2} + D_{RR_2} + E_2 + D_{aR_2}^T)\hat{V}_0 + (E_1 + D_{aR_1} + D_{aR_1}^T)V_{1R} \\
D_1 &= -D_{\ell\epsilon_2} + (D_{a\ell_2} - D_{a\ell_2}^T + D_{R\ell_2} - D_{R\ell_2}^T)\hat{V}_0 + (E_1 + D_{aR_1} + D_{aR_1}^T)V_{1S} \\
&\quad + (D_{a\ell_1} - D_{a\ell_1}^T)V_{1R} \\
D_2 &= (D_{a\ell_1} - D_{a\ell_1}^T)V_{1S} - D_{\ell\ell_2}\hat{V}_0
\end{aligned}
\tag{7.4}
$$

The third-order terms cancel out after determination of the Lagrange multiplier in the variational problem with the subsequent substitution for V_1. After the use of the warping constraints, the final equation for second-order warping can be written as

$$
E_0 V_2 = [D_c(\Psi^T D_c)^{-1}\Psi^T - \Delta](D_0\overline{\epsilon} + D_1\overline{\epsilon}' + D_2\overline{\epsilon}'') \tag{7.5}
$$

After elimination of the singularities associated with E_0, the final expression for the second-order warping is

$$
V_2 = V_{20}\overline{\epsilon} + V_{21}\overline{\epsilon}' + V_{22}\overline{\epsilon}'' \tag{7.6}
$$

7.1.2 3-D Recovery in a Nonlinear Transient Analysis

As it is described in Sec. 2.1, the entire 3-D analysis for any beam problem is split into a 2-D cross-sectional analysis and a 1-D beam analysis. The 2-D sectional analysis, as shown in Fig. 7.1, provides the 2-D sectional elastic and inertia constants in the form of 6×6 stiffness and mass matrices, respectively, if a Generalized Timoshenko model-based analysis is invoked. While the sectional stiffness and mass matrices are the primary output data from a VABS execution, the output files also include solutions to the warping variables demonstrated in Sec. 7.1 which assist in recovery of 3-D displacements once the solution of 1-D variables such as the 1-D displacements, forces and moments are available at each time step. Further, the information can be used to compute and visualize the 3-D stress-strain state on the cross section as well. Given a set of six section stress resultants (the axial

force, the two shear forces, the twisting moment, and the two transverse bending moments), which define the load acting on the section, it is a relatively simple computation to obtain the stress distribution corresponding to a particular sectional load at a given cross section along the span of the beam. This step can be repeated for all the sections to obtain values for 3-D variables for the entire 3-D geometry at all time steps.

The 3-D quantities are recovered at each node on the cross-section. After calculation of 1-D displacements from GEBT at each time step, the 3-D displacements for each time steps at any point in a given cross section can be evaluated using

$$U_i^{(t_k)}(x_1, x_2, x_3 = u_i^{(t_k)}(x_1) + x_\alpha[C_{\alpha i}(x_1) - \delta_{\alpha i}] + C_{ij}(x_1)w_j(x_1, x_2, x_3) \tag{7.7}$$

where u_i are the 1-D displacements for the beam cross section obtained from GEBT (1-D beam analysis outlined in Ch. V) at a time step t_k and C_{ij} are the components of the direction cosine matrix representing the finite rotation of the cross-sectional frame of the deformed beam. The warping w_j can be obtained from

$$w(x_1, x_2, x_3) = S(x_2, x_3)\left[(\hat{V}_0 + V_{1R} + V_{20})\overline{\epsilon} + (V_{1S} + V_{21})\overline{\epsilon}' + V_{22}\overline{\epsilon}''\right] \tag{7.8}$$

Now, we need to evaluate the 1D generalized strain measures and their derivatives. A quick summary of the various notations for the 1D generalized strain measures and the relations between them at each time step is as follows:

$$\begin{aligned}
\overline{\epsilon}^{(t_k)} &= \lfloor \overline{\gamma}_{11} \;\; \overline{\kappa}_1 \;\; \overline{\kappa}_2 \;\; \overline{\kappa}_3 \rfloor^T \\
\epsilon^{(t_k)} &= \lfloor \gamma_{11} \;\; \kappa_1 \;\; \kappa_2 \;\; \kappa_3 \rfloor^T \\
\gamma_s^{(t_k)} &= \lfloor 2\gamma_{12} \;\; 2\gamma_{13} \rfloor^T \\
\varepsilon^{(t_k)} &= \lfloor \gamma_{11} \;\; 2\gamma_{12} \;\; 2\gamma_{13} \;\; \kappa_1 \;\; \kappa_2 \;\; \kappa_3 \rfloor^T \\
\overline{\epsilon}^{(t_k)} &= \epsilon^{(t_k)} + Q^{(t_k)}\gamma_s' + P^{(t_k)}\gamma_s
\end{aligned} \tag{7.9}$$

Hence, to determine $\bar{\epsilon}$, one needs ϵ and ϵ', and the strain recovery needs ε, ε', ε'', ε''' and $\varepsilon^{(IV)}$. After lumping the inertial terms with the applied loads, the 1D beam equations can be obtained from Eq. (5.26). Further,

$$
\begin{aligned}
&\mathcal{F}' + \mathcal{R}\mathcal{F} + \phi = 0 \\
&\mathcal{F}^{(t_k)} = \lfloor F_1^{(t_k)} \quad F_2^{(t_k)} \quad F_3^{(t_k)} \quad M_1^{(t_k)} \quad M_2^{(t_k)} \quad M_3^{(t_k)} \rfloor^T \\
&\mathcal{R}^{(t_k)} = \mathcal{R}^{(t_k)}(\varepsilon) = \begin{bmatrix} \tilde{K} & 0 \\ \tilde{e_1} + \tilde{\gamma} & \tilde{K} \end{bmatrix} \\
&\phi^{(t_k)} = \begin{Bmatrix} f^{(t_k)} \\ m^{(t_k)} \end{Bmatrix}
\end{aligned}
\tag{7.10}
$$

Note that the $\mathcal{F}^{(t_k)}$ is not to be confused with the minimization functional used in Ch. II, Sec. 2.3]. The 6×6 cross-sectional flexibility matrix (Φ) of the GT model is employed as follows:

- $\varepsilon^{(t_k)} = \Phi\mathcal{F}^{(t_k)} \implies \mathcal{R}^{(t_k)}$ can be evaluated
- $\mathcal{F}'^{(t_k)} = -\mathcal{R}^{(t_k)}\mathcal{F}^{(t_k)} - \phi$; $\varepsilon'^{(t_k)} = \Phi\mathcal{F}'^{(t_k)}$

  $\implies \mathcal{R}'^{(t_k)}$ can be evaluated
- $\mathcal{F}''^{(t_k)} = -\mathcal{R}'^{(t_k)}\mathcal{F}^{(t_k)} - \mathcal{R}^{(t_k)}\mathcal{F}'^{(t_k)} - \phi'$; $\varepsilon''^{(t_k)} = \Phi\mathcal{F}''^{(t_k)}$

  $\implies \mathcal{R}''^{(t_k)}$ can be evaluated
- $\mathcal{F}'''^{(t_k)} = -\mathcal{R}''^{(t_k)}\mathcal{F}^{(t_k)} - \mathcal{R}^{(t_k)}\mathcal{F}''^{(t_k)} - 2\mathcal{R}'^{(t_k)}\mathcal{F}'^{(t_k)} - \phi''$; $\varepsilon'''^{(t_k)} = \Phi\mathcal{F}'''^{(t_k)}$

  $\implies \mathcal{R}'''^{(t_k)}$ can be evaluated
- $\mathcal{F}^{(IV)(t_k)} = -\mathcal{R}'''^{(t_k)}\mathcal{F}^{(t_k)} - 3\mathcal{R}''^{(t_k)}\mathcal{F}'^{(t_k)} - 3\mathcal{R}'^{(t_k)}\mathcal{F}''^{(t_k)} - \mathcal{R}^{(t_k)}\mathcal{F}'''^{(t_k)} - \phi'''$;

  $\varepsilon^{(IV)(t_k)} = \Phi\mathcal{F}^{(IV)(t_k)}$

Finally, the expression for strain is obtained as

$$\begin{aligned}\Gamma^{(t_k)} =&\Gamma_{a\beta}w + \Gamma_\epsilon\overline{\epsilon}^{(t_k)} + \Gamma_R w + \Gamma_\ell w' \\ =&\Gamma_{a\beta}S(V_0 + V_1 + V_2) + \Gamma_\epsilon\overline{\epsilon}^{(t_k)} + \Gamma_R S(V_0 + V_1 + V_2) + \Gamma_\ell(V_0' + V_1' + V_2') \\ =&\left[(\Gamma_{a\beta} + \Gamma_R)S(\hat{V}_0 + V_{1R} + V_{20}) + \Gamma_\epsilon\right]\overline{\epsilon}^{(t_k)} \\ &+ \left[(\Gamma_{a\beta} + \Gamma_R)SV_{22} + \Gamma_\ell S(V_{1S} + V_{21})\right]\overline{\epsilon}''^{(t_k)} \\ &+ \left[(\Gamma_{a\beta} + \Gamma_R)S(V_{1S} + V_{21}) + \Gamma_\ell S(\hat{V}_0 + V_{1R} + V_{20})\right]\overline{\epsilon}'^{(t_k)} + \Gamma_\ell SV_{22}\overline{\epsilon}'''^{(t_k)}\end{aligned} \tag{7.11}$$

The final expression for stress is simply

$$\sigma^{(t_k)} = D\Gamma^{(t_k)} \tag{7.12}$$

Hence, the formulation for the second-order 3-D stress, strain and displacement recovery for a nonlinear transient analysis for generally anisotropic and initially curved and/or twisted beams is complete. The information of 3-D variables is stored at each time step and can be retrieved for visualization and analysis as demonstrated in Sec. 7.3

7.2 Store and Retrieve Histories of 3-D Recovery

In the present work, tools developed from equations presented in Refs. [187] and [186] (viz., VABS and GEBT, respectively), are being used after suitable modification by Rajagopal [138] to include recovery with a higher fidelity of sectional warping solutions. This section provides the details of the framework developed for the purpose of generating time histories of 3-D stress/strain. The process of obtaining the time histories primarily involves the following steps:

1. Use a preprocessor such as PreVABS, a commercially available meshing tool or the Delaunay triangulation to generate 2-D elements in a given beam cross section.

2. Use the information about the mesh along with the material properties and layup information for composite materials to write the VABS input file.

3. Execute VABS to obtain the 6×6 mass and stiffness matrices which are needed for the 1-D analysis.

4. The derived matrices are then used to prepare an input file for GEBT to generate the 1-D displacement field, the corresponding forces, moments and their derivatives.

5. This data is used in VABS along with the solution for the warping variables for recovery of 3-D variables such as the 3-D stress, strain and displacement fields.

To avoid the hassle of communicating between different tools using input files, the present framework integrates the 1-D analysis directly in VABS, so that the information about 1-D variables is available directly to the user. Further, all these steps are linked using sophisticated MATLAB scripts, which is also used for transforming the data in neat contour plots that are visually appealing and easy to interpret as compared to large matrices with numbers. Figure 7.1 shows the steps involved in obtaining the complete 3-D stress, strain and displacement history for a composite beam. Analysis in GEBT provides the 1-D variables for all time instants t_k at each location x_i along the length of the beam which are now directly transferred to VABS. Scripts and macros have been developed to automate the execution of VABS recovery relations for each time-step to obtain the corresponding 3-D variables. This procedure is repeated for all time-steps to get the complete evolution of the 3-D variables during the entire time domain.

7.3 Validation Studies

To demonstrate the evolution of the 3-D variables under different loading conditions we use an isotropic cantilever beam and a composite beam as shown in Figs. 7.2 and 7.13.

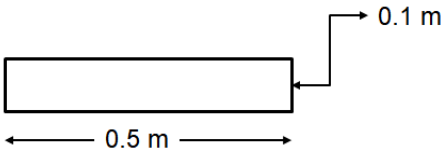

Figure 7.2: Sectional details of the cantilever isotropic beam

7.3.1 Isotropic Beam

First, we use the example of a straight cantilever beam having a rectangular cross section as shown in Fig. 7.2. Since, isotropic beams are well understood we particularly chose this example to demonstrate the various features of the present work in detail and also for numerical validation with other finite element analysis (FEA) tools. The geometric and material properties of the beam are given in Table 7.1. The beam is subject to a vertical transverse tip loading $f(t) = 1000\sin(4\pi t)$ N. i.e., loading in the direction of x_3 at $x_1 = L$, where L is the length of the beam.

Table 7.1: Geometric and material properties for the isotropic cantilever beam

Property	value
Thickness	0.1 m
Width	0.5 m
Length (L)	2 m
Elastic modulus	69×10^9 Pa
Poisson's ratio	0.327
Density	2700 kg/m^3

Figure 7.3 shows exactly how the dominant stress components σ_{11}, σ_{12} and σ_{13} evolve at the mid-section of the beam, along with the corresponding load values over the duration of the applied load as shown in Fig. 7.4.

Similar graphs can be obtained for the stress components σ_{22}, σ_{23} and σ_{33}, but for the given transverse loading and symmetry in the cross section, these stress components are negligible compared to the dominant stress components. Figures 7.5a–c, show the comparison of the the maximum and minimum values of σ_{11}, σ_{12} and σ_{13}, respectively, at the mid-section, against 3D FEA (ANSYS) at all time steps.

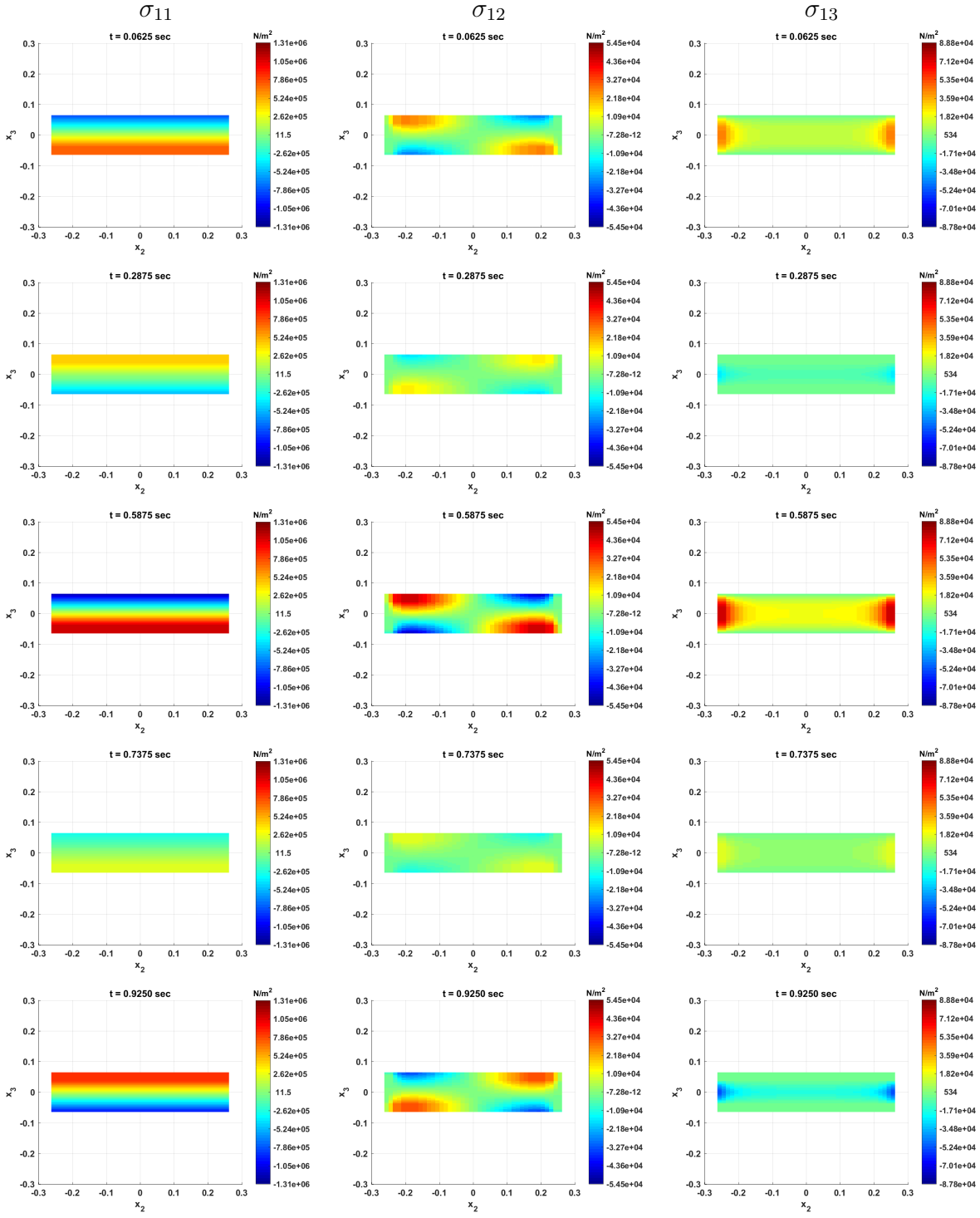

Figure 7.3: Some snapshots of the stress components σ_{11}, σ_{12} and σ_{13} at the mid-section of a cantilever beam over a time domain of 1 secs, corresponding to the applied load shown in Fig. 7.4

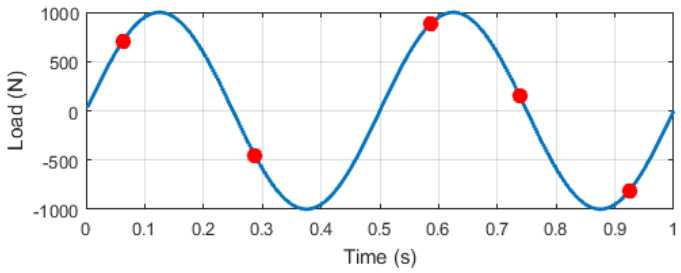

Figure 7.4: Snapshot of the loading function; the red dots correspond to the time steps when the stress plots are generated in Fig. 7.3

The present analysis does not involve any structural damping. An important observation here, is that even though the input force is sinusoidal in nature, the output stress has a certain number of sub-peaks apart from the main peaks. Upon further investigation it is revealed that the dynamic response of the beam constitutes a higher harmonic which may or may not be avoided by the presence of structural damping. After performing an eigenvalue analysis to obtain natural frequencies and mode shapes through VABS and GEBT, the natural frequencies for the first two bending modes are identified to be 19.46 and 120.91 rad/s. When the axial stress (σ_{11}) amplitude is converted in frequency domain (as shown in Fig. 7.6) with the help of a Fourier series transformation, it is found that the stress amplitude is picking up two main harmonics in entire transient analysis which correspond to the first two bending modes obtained from eigenvalue analysis as the natural frequency $\omega = 2\pi f$. However, from the plots in Fig. 7.5, it is evident from the main peaks that the participation of the fundamental mode is higher as compared to the second bending mode because the excitation frequency is 4π. So, the sub-peaks are obtained due to the small but significant participation of a higher mode.

Another important observation is related to the inclusion of inertia effects. Figure 7.7 demonstrates a comparison between the results obtained from the present framework, 3-D FEA and results from the present framework for a quasi-static analysis instead of a transient analysis in the two aforementioned cases. A quasi-static analysis has been studied in the past as an analysis where the forces change very slowly with respect to time, essentially

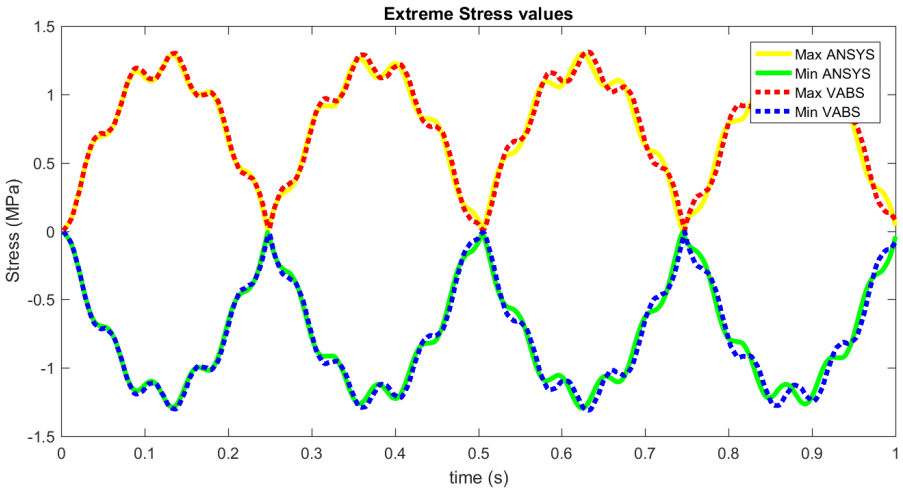

(a) Maximum and minimum values of σ_{11} at the mid-section

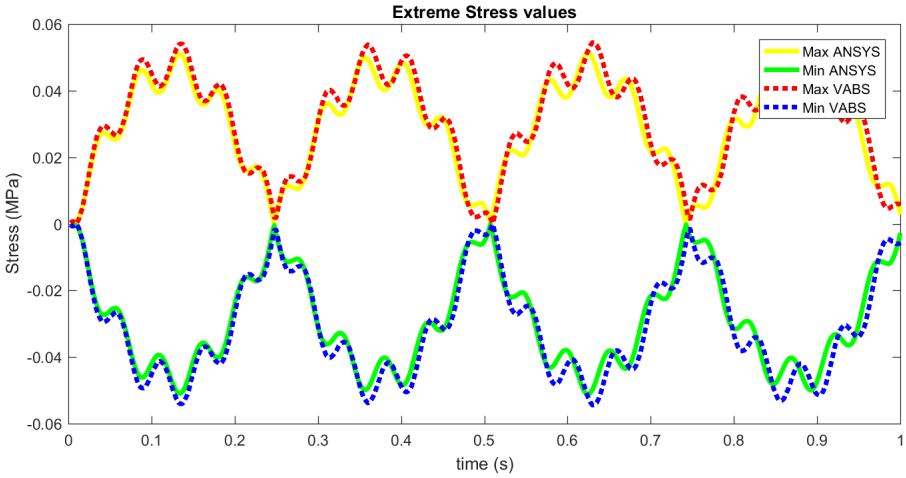

(b) Maximum and minimum values of σ_{12} at the mid-section

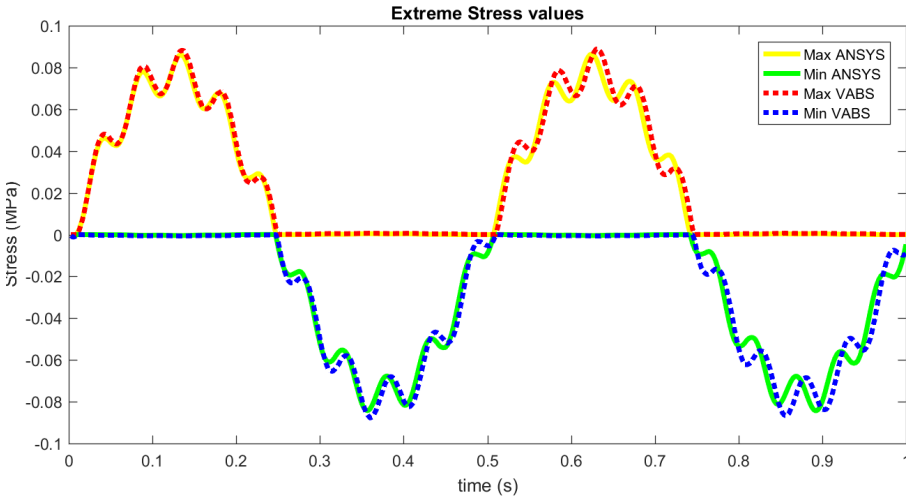

(c) Maximum and minimum values of σ_{13} at the mid-section

Figure 7.5: Validation of the the maximum and minimum values of dominant stress components at the mid-section, against 3D FEA (ANSYS)

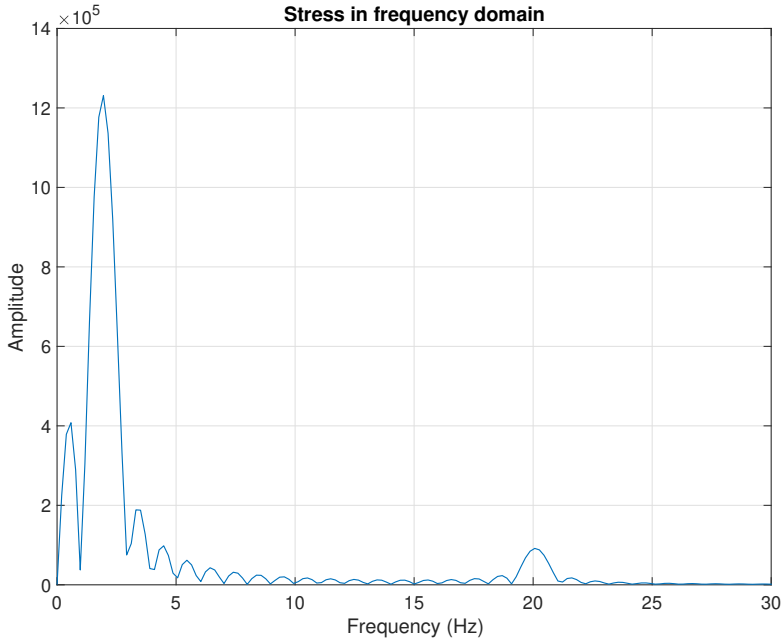

Figure 7.6: Stress (σ_{11}) amplitude in frequency domain

neglecting the inertia effects. When inertia effects are neglected, the dynamic behavior which is captured by the present analysis and the 3-D FEA can not be captured accurately. Inability to include inertia effects in a nonlinear transient analysis is likely to underestimate the stresses a rotor blade is subjected to and may result in failure if that blade is designed without taking inertia effects into account.

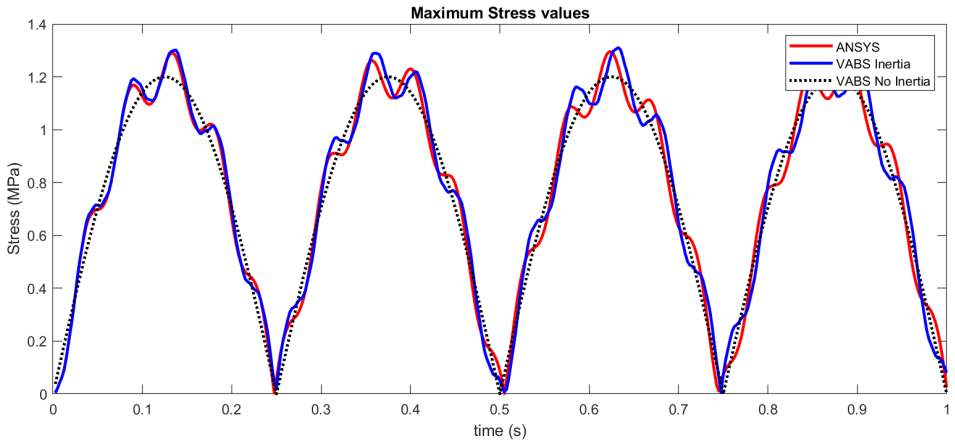

Figure 7.7: Comparison of the the maximum values of σ_{11} at the mid-section obtained from the present framework, without inertia effects and with 3D FEA (ANSYS)

Further, a quantitative plot for the relative error in peak stresses, obtained from the two methods, is presented in Fig. 7.8. The maximum error in determining the peak stress amplitude through the present framework against 3-D FEA is less than 1.5% throughout the entire nonlinear transient analysis.

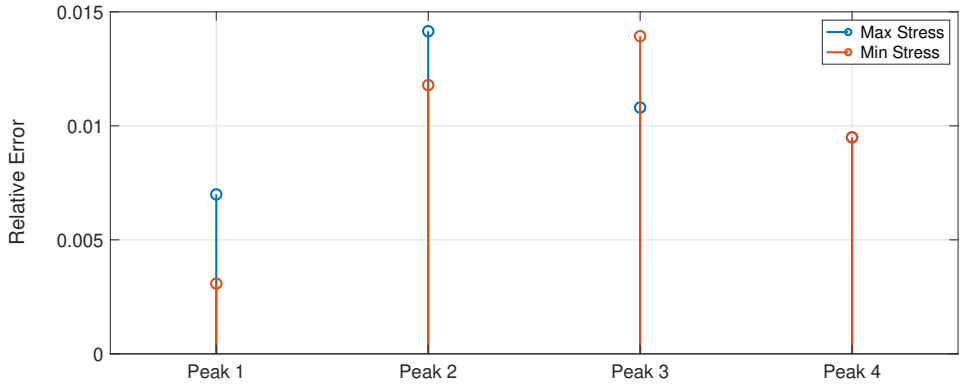

Figure 7.8: Relative error in the values of stress (σ_{11}) amplitude obtained from the present framework when compared to 3-D FEA

As far as the location of peak values is concerted, Figs. 7.9–7.12 show the comparison between the stress distributions obtained from VABS and ANSYS at the mid-section of the beam, corresponding to the peak stress values. It is evident that the present framework accurately identifies locations for peak stresses when compared with the ones obtained from 3-D FEA in ANSYS. This is a really important feature when designing any new components.

Table 7.2 shows some of the key features of the two types of approaches in determining the 3-D variables - VABS/GEBT and 3-D FEA (ANSYS). The present framework, not only provides high fidelity recovery of 3-D variables without any ad-hoc assumptions, but it is also much faster and requires minimum computational resources to achieve the same level of results as compared to 3-D FEA software, which is our main motivation for the development of the current work. A number of important results can be extracted from the stored data depending on the requirements of the design like exact location of the maximum/minimum stress over the entire time domain, maximum displacement, 1-D force and

moment variables for all time-steps, and much more.

Table 7.2: Comparison of computation variables (VABS vs 3-D FEM)

Comparable	VABS + GEBT	3-D FEM (ANSYS)
Duration of Analysis	1 s	1 s
Time-Steps	400	400
Number of Elements	480 (2-D); 100 (1-D)	500 oct. elements/section
Memory (RAM) used	2 GB; 1-core	16 GB, 2-cores
Computation Time (Solver)	$\sim$ 20 min	$\sim$ 7.5 hrs
Storage Requirements	$\sim$ 100 MB	$\sim$ 60 GB

7.3.2 Composite Beam

In this section, a 24-layer composite beam is chosen the geometric and material properties of which are mentioned in Tables 7.3 and 7.4, respectively, with detailed layup information present in Table 7.5. Once again, the beam is subject to a vertical loading $f(t) = 1000\sin(4\pi t)$ for a duration of 1 second at the tip of the beam, as shown in Fig. 7.13. Figure 7.14 shows a snapshot from the dynamics time history data of all the six stress components at the mid-section of the composite beam at $t = 0.502$ sec. We can observe how the different layers are stressed differently. Using these contour plots, a user distinctly recognizes the layer which has the maximum stress under the given loading. Consequently, the ply angle or the layup sequence can be modified to mitigate the design problem. Figure 7.15 shows the variation of the maximum and minimum values of the stress component σ_{11} for all time-steps. It is important to note that even with reduction in externally applied load to zero, there are locations in the mid-section which are stressed at all times. Hence, we can observe that both the inertia effects and the couplings between various modes of deformation are quite dominant, primarily due to the complex layup of the composite beam.

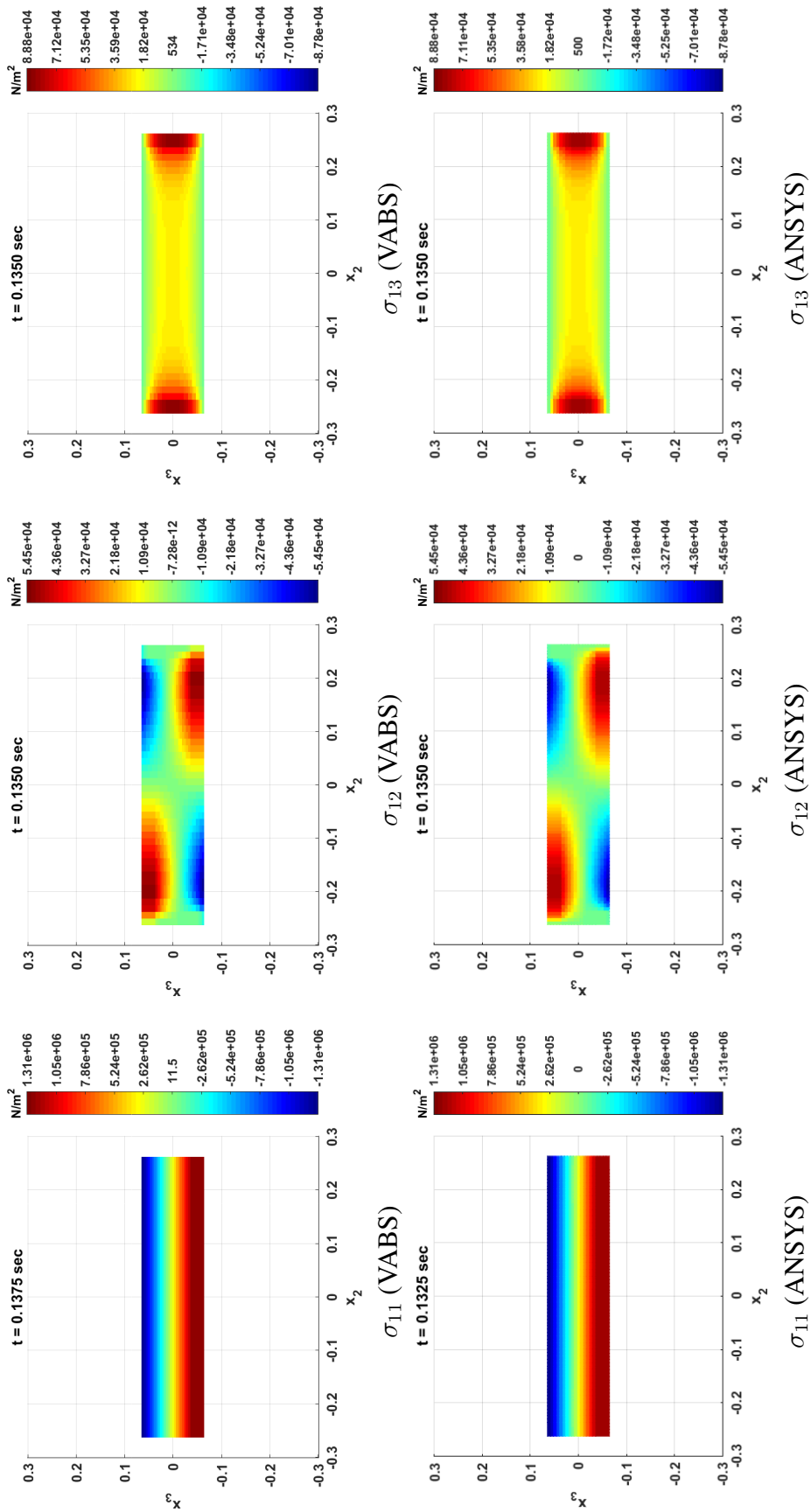

Figure 7.9: Comparison of the contour plots of the the dominant stress components at the mid-section of the beam obtained from VABS and ANSYS, corresponding to the first peak in Fig. 7.5

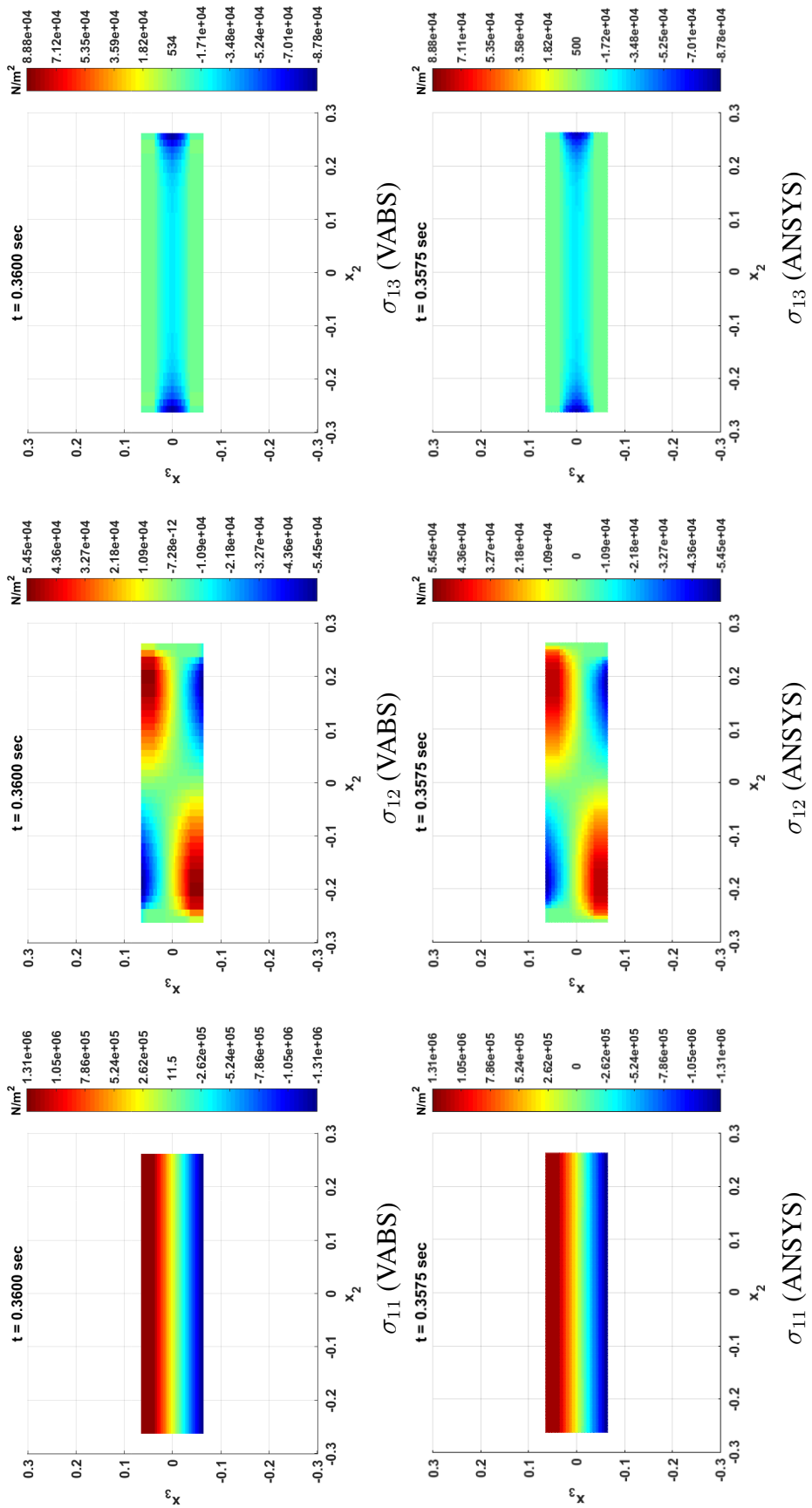

Figure 7.10: Comparison of the contour plots of the the dominant stress components at the mid-section of the beam obtained from VABS and ANSYS, corresponding to the second peak in Fig. 7.5

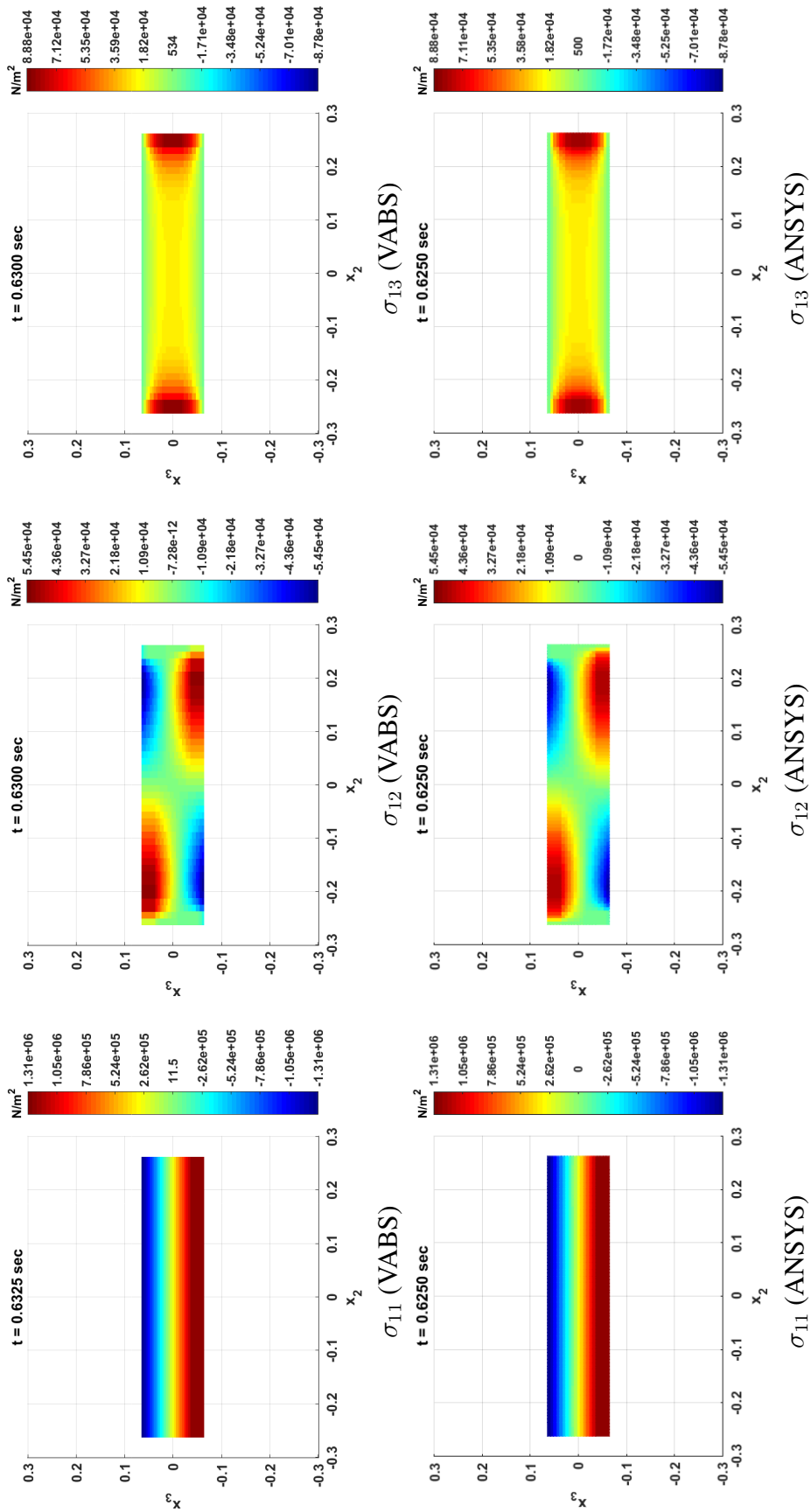

Figure 7.11: Comparison of the contour plots of the the dominant stress components at the mid-section of the beam obtained from VABS and ANSYS, corresponding to the third peak in Fig. 7.5

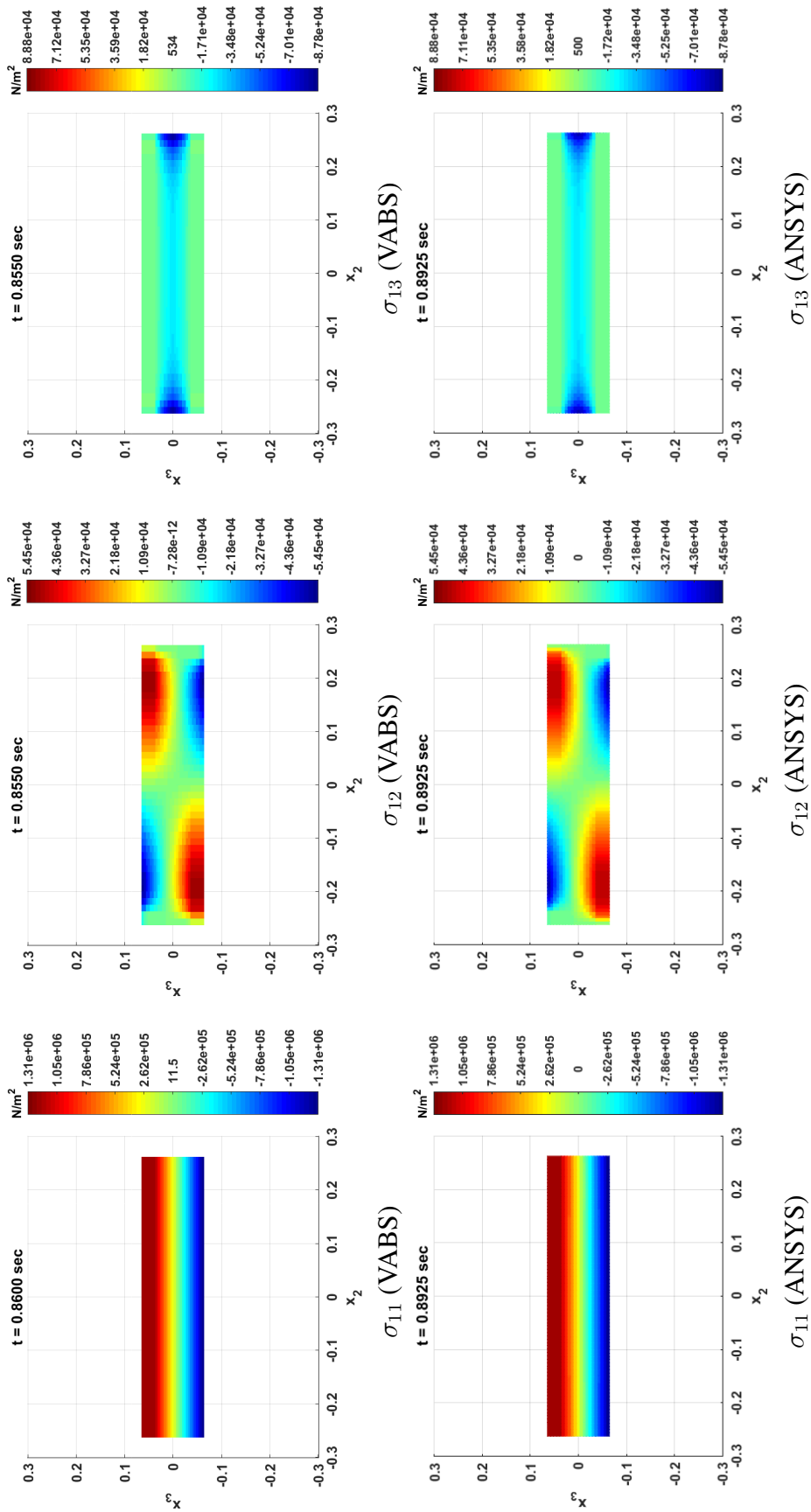

Figure 7.12: Comparison of the contour plots of the the dominant stress components at the mid-section of the beam obtained from VABS and ANSYS, corresponding to the fourth peak in Fig. 7.5

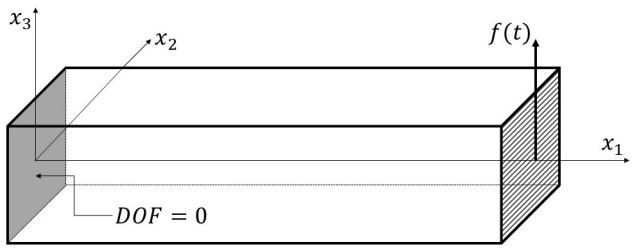

Figure 7.13: Schematic of a cantilever composite beam

Table 7.3: Geometric properties

Property	value [mm]
Thickness	4.416
Width	5
Length (L)	11.32
Internal radius (R)	5
Ply thickness	0.184
Number of plies	24

Table 7.4: Material Properties

Property	Value
E_{11}	152800 MPa
$E_{22} = E_{33}$	8700 MPa
$G_{12} = G_{13}$	4200 MPa
G_{23}	3150 MPa
$\nu_{12} = \nu_{13}$	0.335
ν_{23}	0.380

Table 7.5: Layup Sequence

Layup No.	Angle	No.	Angle	No.	Angle	No.	Angle	No.	Angle	No.	Angle
1	-45	5	90	9	45	13	0	17	0	21	-45
2	0	6	-45	10	-45	14	90	18	45	22	45
3	45	7	-45	11	90	15	-45	19	45	23	0
4	-45	8	0	12	45	16	45	20	90	24	-45

7.3.3 Realistic Wind Turbine Rotor Blade

So far, this chapter demonstrates the capabilities of the present framework for beam sections with fairly simple geometric properties, such as those with rectangular cross sections. However, the present framework is built on the foundations of tools designed for a composite beam with arbitrary cross-sectional geometry and layup. In the concluding portion of this chapter, a nonlinear transient structural analysis of a wind turbine rotor blade is carried out in the present framework. Figure 7.17 demonstrates a typical wind turbine blade's cross section as taken from Chen [34]. The entire structure is divided into multiple skin segments and web segments known as spars. This blade under consideration for the present study is

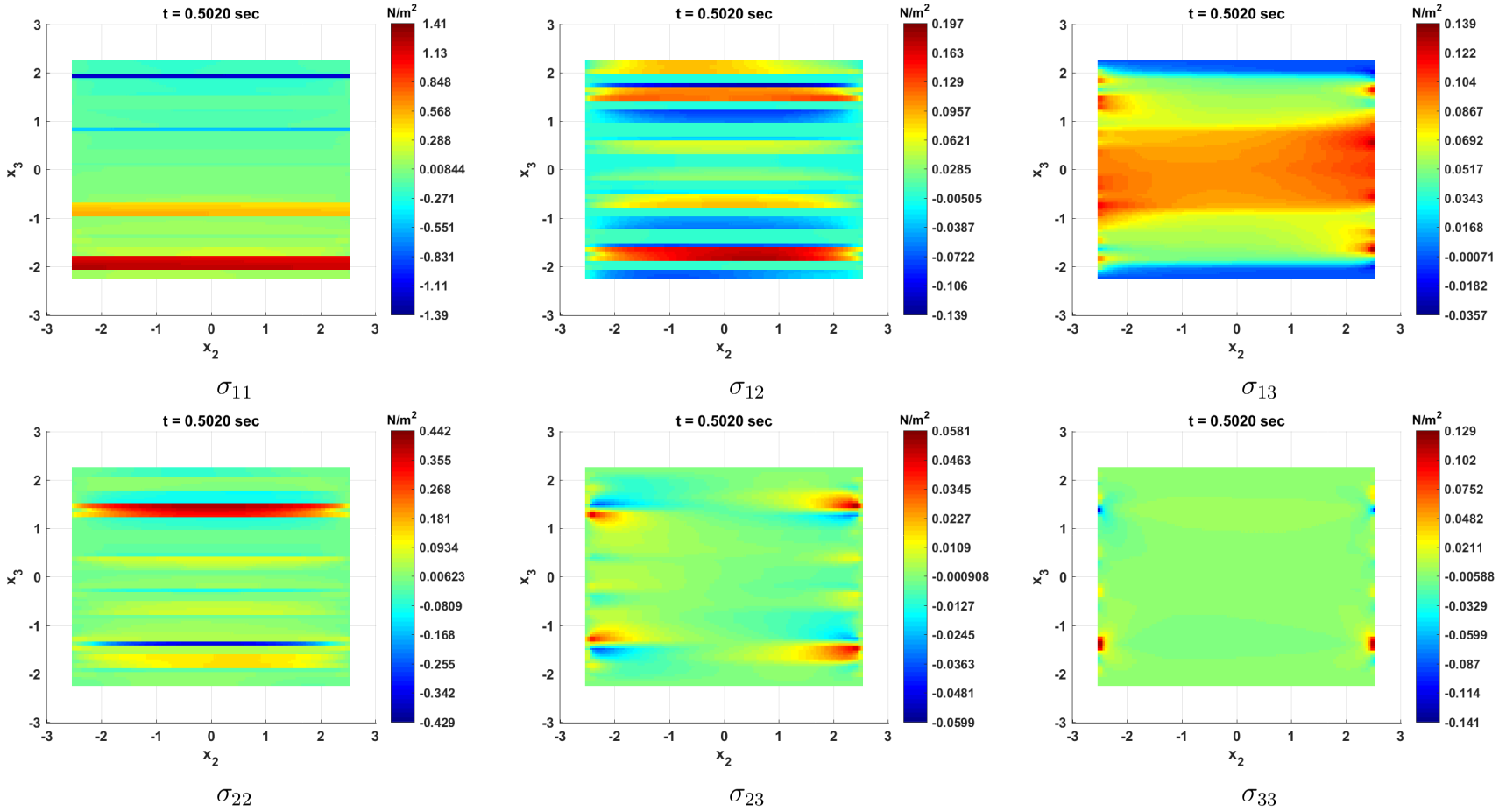

Figure 7.14: Snapshot of the six components of the 3-D stress field at the mid-section of a composite beam at $t = 0.502$ sec

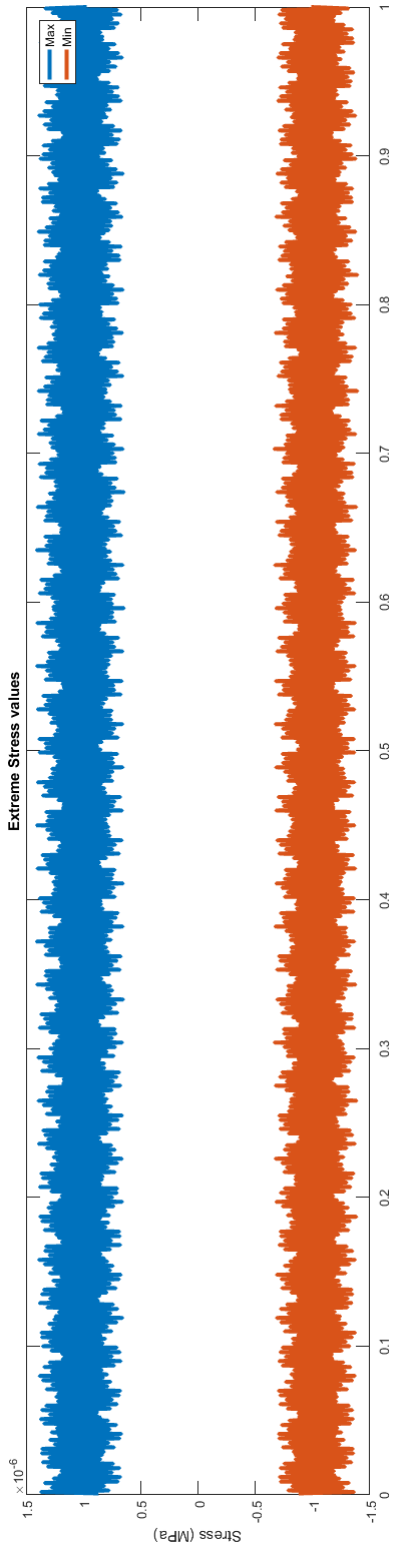

Figure 7.15: Maximum and minimum values of the stress component σ_{11} at the mid-section for all time-steps

made of an MH-104 airfoil for stall controlled wind turbines with a 1.9 m chord length as shown in Fig. 7.18. The blade is 55 m long. The properties of the materials used in the blade for this study are listed in Table 7.6. Also, the rotor blade is made of multiple layers and subjected to a clamped boundary condition at the root. At the tip, it is loaded in the direction of x_3 with a force of magnitude $1000\sin(4\pi t)$ for 1 sec. Table 7.7 contains the information about the distinct layers of various materials in each segment of the wind turbine blade. The information includes the thickness of the layer as well as the layup angle. Furthermore, there are three cases considered for the present analysis as written below:

- Case 1: The layup angle of material 1 in all appearances in segment 4 is 30°.
- Case 2: The layup angle of material 1 in all appearances in segment 4 is 0°.
- Case 3: The layup angle of material 1 in all appearances in segment 4 is -30°.

Each of these rotor blade cross sections are meshed with a combination of 85,945 2-D quadratic triangular and quadrilateral elements.

Table 7.6: Sectional details of the wind turbine blade [34]

ID	Material	E_{11}[1]	E_{22}, E_{22}[1]	G_{12}, G_{13}, G_{23}[1]	ν_{12}, ν_{13}, ν_{23}	ρ[2]
1	uni-direction FRP[3]	3.70E+10	9.00E+09	4.00E+09	0.28	1860
2	double-bias FRP[3]	1.03E+10	1.03E+10	8.00E+09	0.30	1830
3	Gelcoat	10.00	10.00	1.00	0.30	1830
4	Nexus	1.03E+10	1.03E+10	8.00E+09	0.30	1664
5	Balsa	1.00E+07	1.00E+07	2.00E+05	0.30	1280

[1]All numbers are in SI units: Pa
[2]Units of density: kg/m^3 [3]Fiber-Reinforced Plastics

When VABS is employed to evaluate sectional properties, we obtain the 6×6 Timoshenko stiffness matrices for case 1, case 2 and case 3 mentioned above in tables 7.8, 7.9 and 7.10 respectively. It can be seen that there is a significant effect of a change in layup angle in a small segment of the rotor blade. Further,ore, an eigenvalue analysis reveals that even the fundamental modes of the rotor blade have evidence of coupling between various dominant modes of deformation as shown in Fig. 7.16. So, different components of stresses

Table 7.7: Sectional details of the wind turbine blade taken from Ref. [34]

Component Name	Number of Plies	Layer Thickness (m)	Layup Angle	Material ID
Segments 1 & 2	1	0.000381	0°	3
	1	0.00051	0°	4
	18	0.00053	20°	2
Segment 3	1	0.000381	0°	3
	1	0.00051	0°	4
	33	0.00053	20°	2
Segment 4	1	0.000381	0°	3
	1	0.00051	0°	4
	17	0.00053	20°	2
	38	0.00053	30°	1
	1	0.003125	0°	5
	37	0.00053	30°	1
	16	0.00053	20°	2
Segment 5	1	0.000381	0°	3
	1	0.00051	0°	4
	17	0.00053	20°	2
	1	0.003125	0°	5
	16	0.00053	0°	2
Webs 1 & 2	38	0.00053	0°	1
	1	0.003125	0°	5
	38	0.00053	0°	1

become relevant for design studies in case of a transverse dynamic load (flapping) applied at the tip.

Finally, 3-D stress results are obtained and plotted for visualization in Figs. 7.19–7.33. In the first five sets of Figs. 7.19–7.23, variation of σ_{11} (i.e. the axial stress) with time is visualized. The subsequent two sets, Figs. 7.24–7.28 and Figs. 7.29–7.33, demonstrate the variation in the other two stress components, σ_{12} and σ_{13}, respectively. These visuals are eventually compiled in the form of a .gif file which can be viewed as a video. This analysis demonstrates how changes in layup angle and dynamic loads in a transient nonlinear analysis lead to a change in sectional 3-D stress values and can quickly shape an engineering judgment if such visual information is available at low computational cost, time and labor.

Table 7.8: Stiffness values for the wind turbine blade (Case 1)

2.417911E+09	−1.112242E+06	8.227612E+06	−3.447348E+07	6.855436E+07	$-5.501234E+08$
	4.394973E+08	−3.171674E+06	−1.794748E+07	1.549949E+07	−8.688117E+04
		2.881997E+07	8.672243E+05	2.477192E+05	−4.883738E+06
			2.251472E+07	−1.994482E+06	2.218328E+06
	symmetric			2.146413E+07	−9.386292E+06
					4.822139E+08

Table 7.9: Stiffness values for the wind turbine blade (Case 2)

3.528131E+09	−1.601881E+05	−3.308735E+06	1.868497E+07	1.038427E+08	−7.146835E+08
	4.047644E+08	−4.539963E+06	−1.664892E+07	−6.837039E+06	−8.606600E+05
		2.731048E+07	1.723904E+06	−1.125049E+05	−1.016677E+07
			1.819529E+07	7.233034E+05	−5.596187E+06
	symmetric			3.458891E+07	−1.401613E+07
					5.739008E+08

Table 7.10: Stiffness values for the wind turbine blade (Case 3)

2.399011E+09	−1.085819E+06	−1.609341E+07	7.357231E+07	6.765158E+07	−5.435317E+08
	4.168510E+08	−1.241847E+06	−1.698556E+07	−2.510880E+07	−4.151913E+06
		2.900384E+07	6.533691E+05	−6.856855E+05	−1.556683E+07
			2.308568E+07	3.278698E+06	−1.341666E+07
	symmetric			2.026303E+07	−8.788460E+06
					4.816898E+08

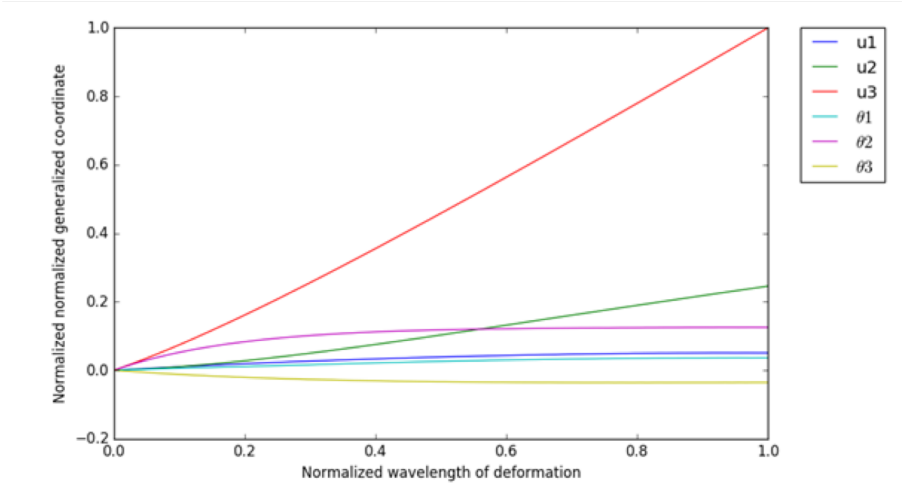

(a) First mode: coupled lead-lag with flapping mode

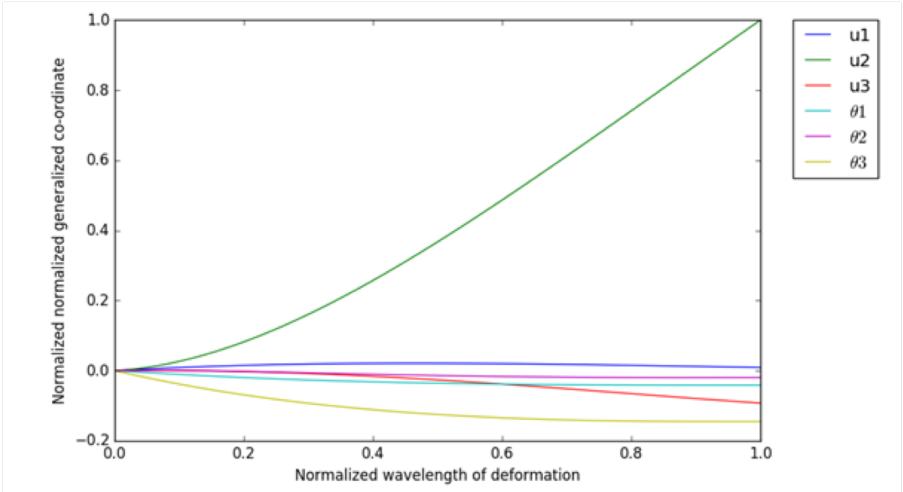

(b) Second mode: lead-lag mode

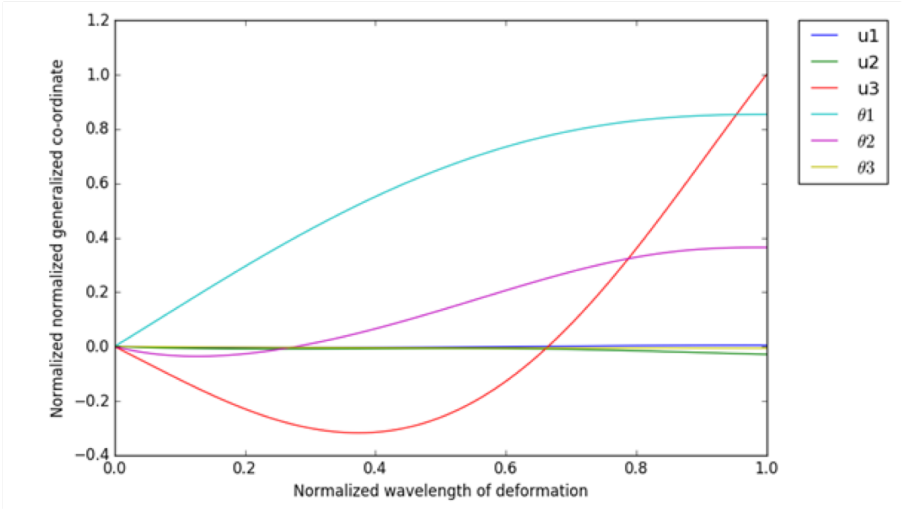

(c) Third mode: coupled flapping and twisting mode

Figure 7.16: Fundamental modes shapes of the wind turbine rotor blade

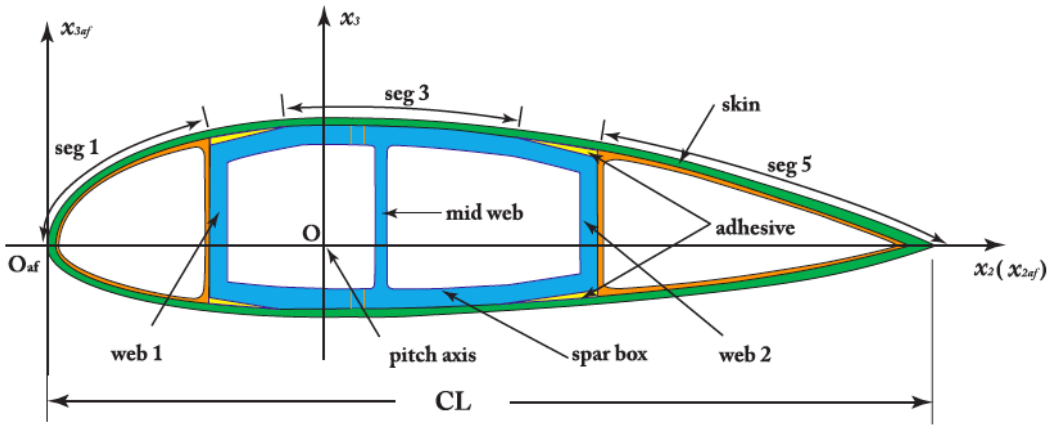

Figure 7.17: Cross-sectional sketch of a typical wind turbine blade [34]

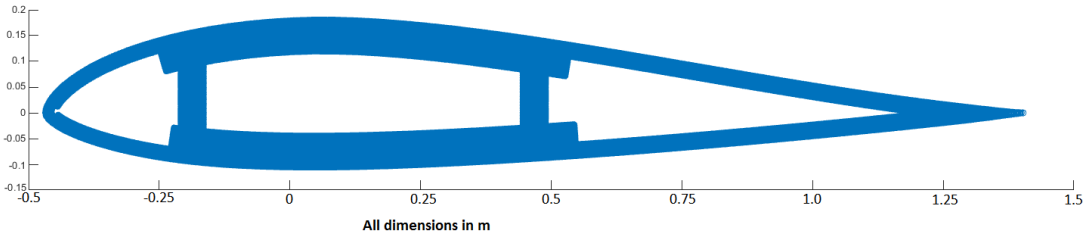

Figure 7.18: Cross section of a realistic wind turbine rotor blade

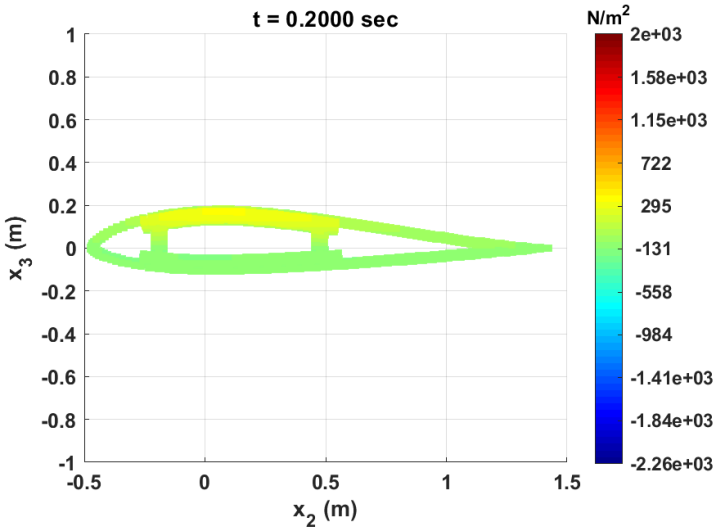

Segment 4, material 1, layup = 30°

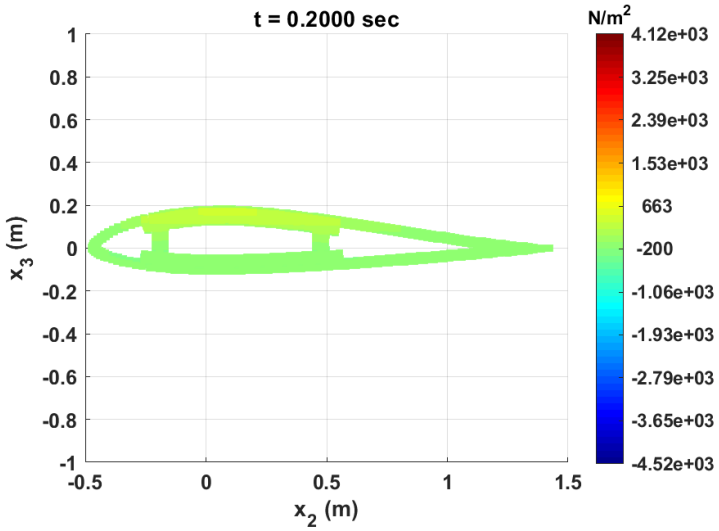

Segment 4, material 1, layup = 0°

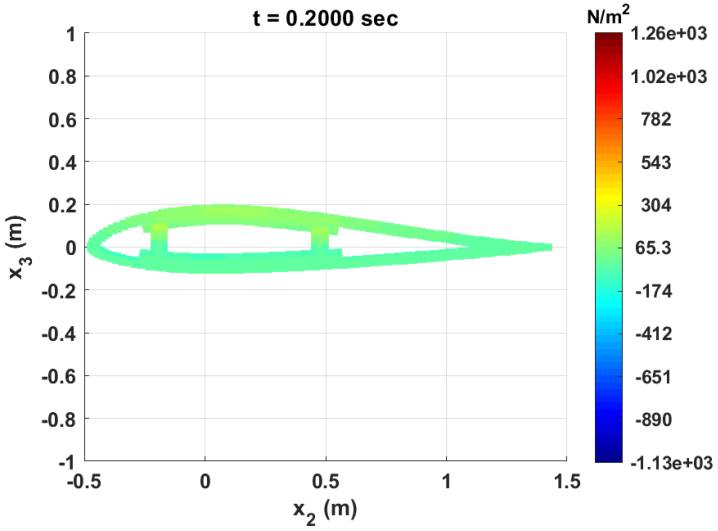

Segment 4, material 1, layup = −30°

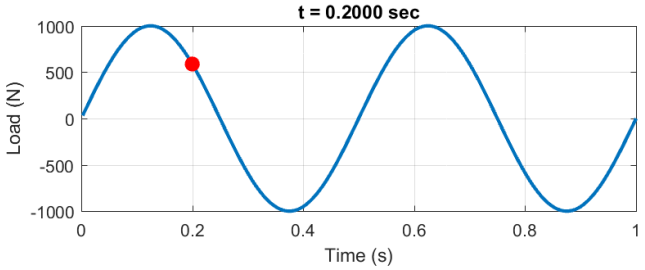

Loading information – transverse tip shear force

Figure 7.19: 3-D Stress (σ_{11}) field at the mid-section of wind turbine blade at $t = 0.2$ sec for different layups in Segment 4

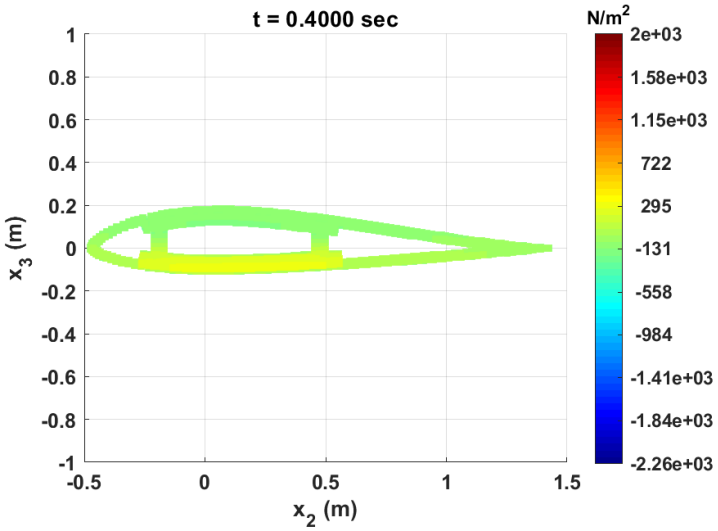

Segment 4, material 1, layup $= 30°$

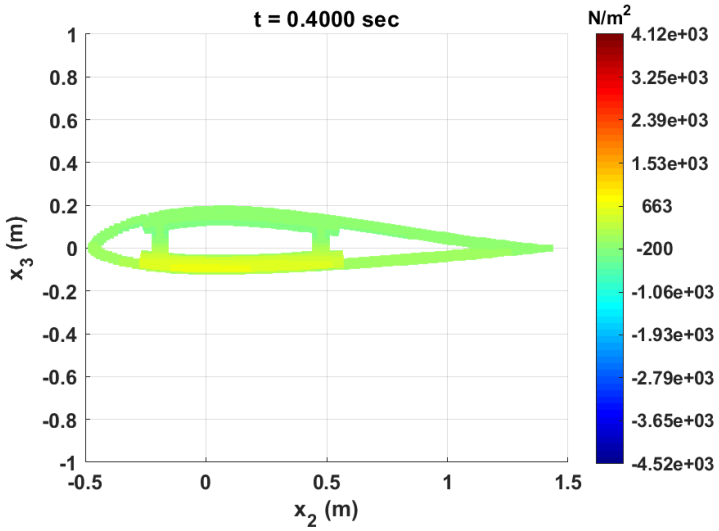

Segment 4, material 1, layup $= 0°$

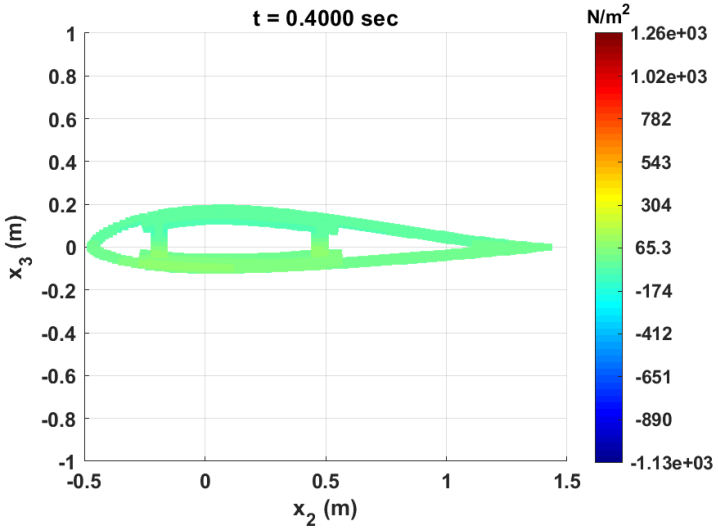

Segment 4, material 1, layup $= -30°$

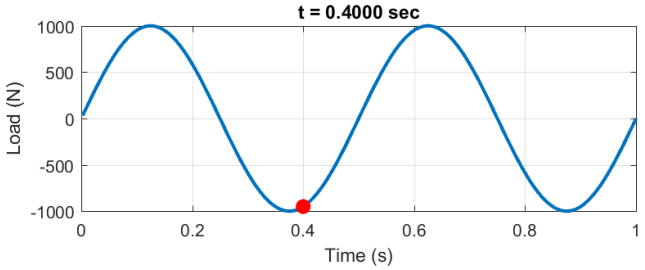

Loading information – transverse tip shear force

Figure 7.20: 3-D Stress (σ_{11}) field at the mid-section of wind turbine blade at $t = 0.4$ sec for different layups in Segment 4

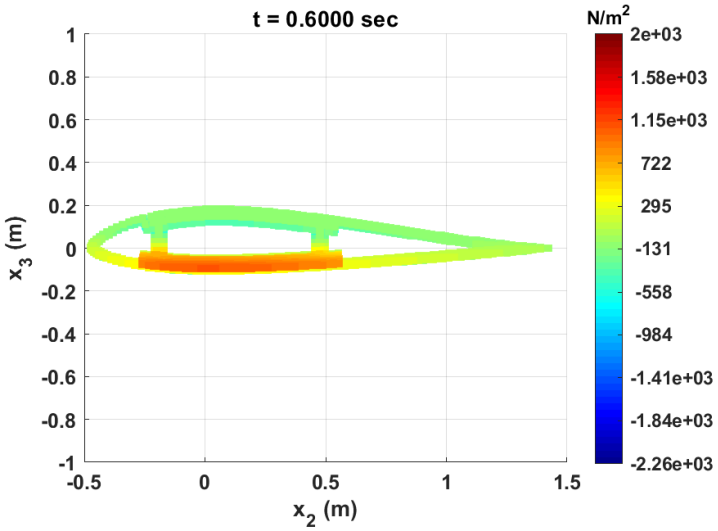

Segment 4, material 1, layup = 30°

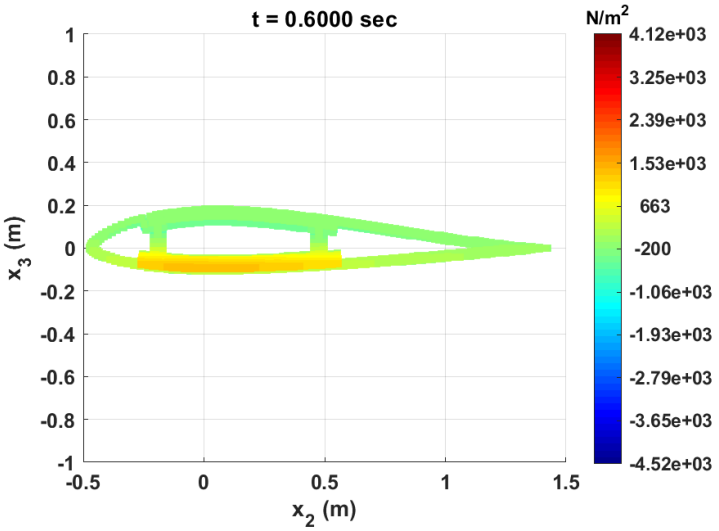

Segment 4, material 1, layup = 0°

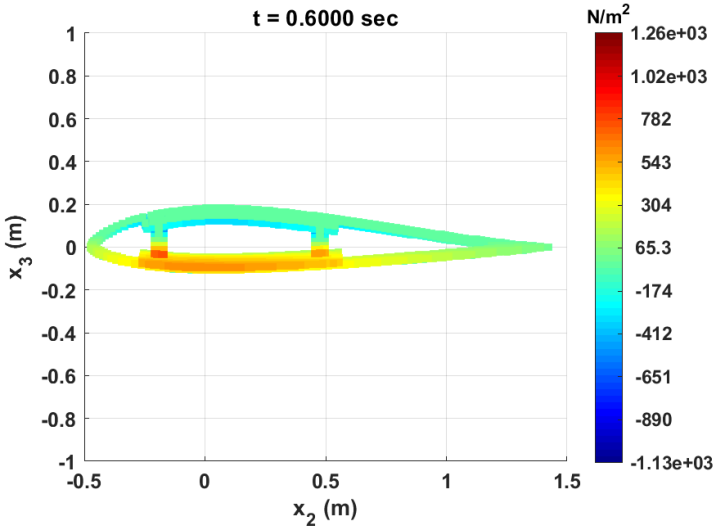

Segment 4, material 1, layup = −30°

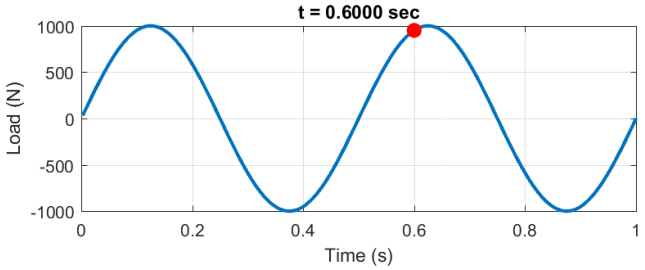

Loading information – transverse tip shear force

Figure 7.21: 3-D Stress (σ_{11}) field at the mid-section of wind turbine blade at $t = 0.6$ sec for different layups in Segment 4

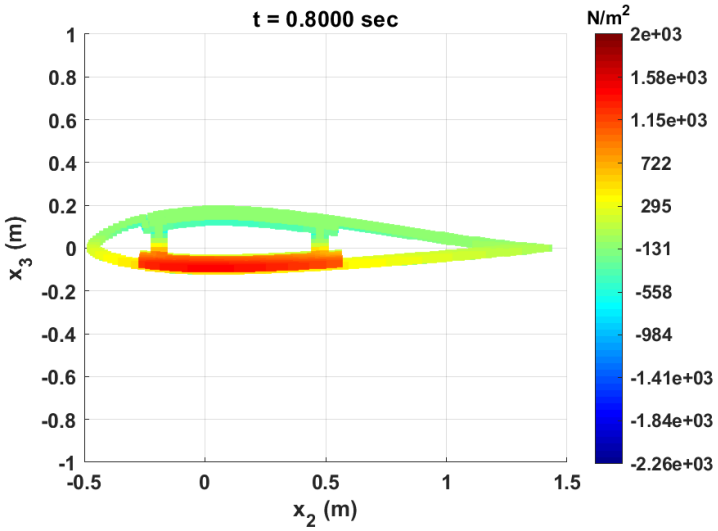

Segment 4, material 1, layup = 30°

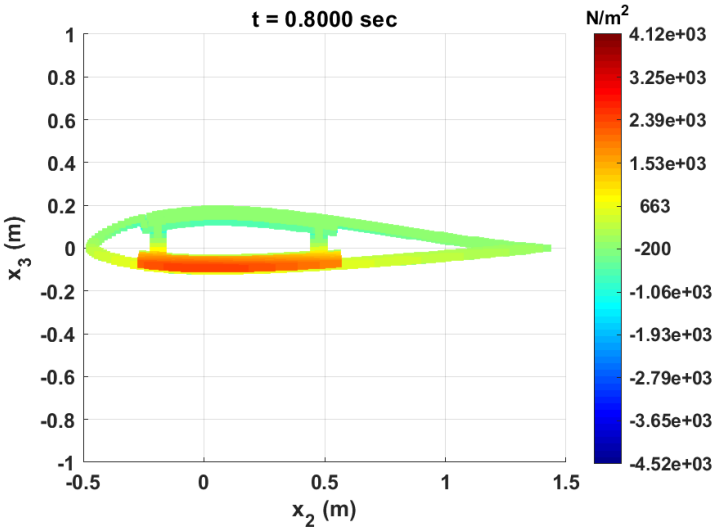

Segment 4, material 1, layup = 0°

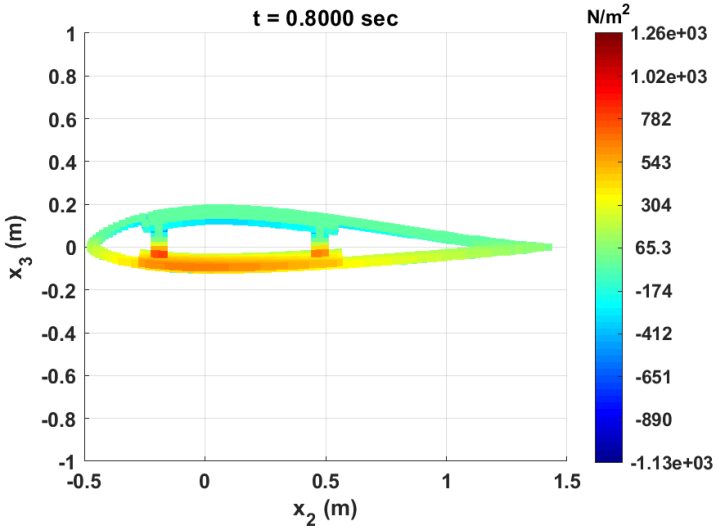

Segment 4, material 1, layup = −30°

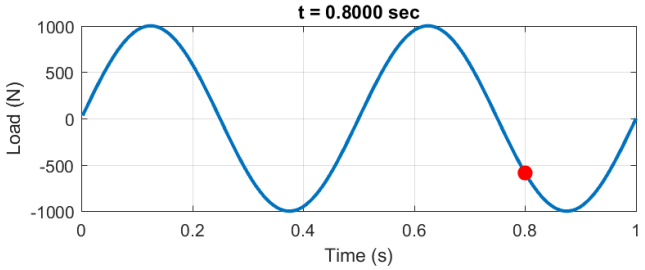

Loading information – transverse tip shear force

Figure 7.22: 3-D Stress (σ_{11}) field at the mid-section of wind turbine blade at $t = 0.8$ sec for different layups in Segment 4

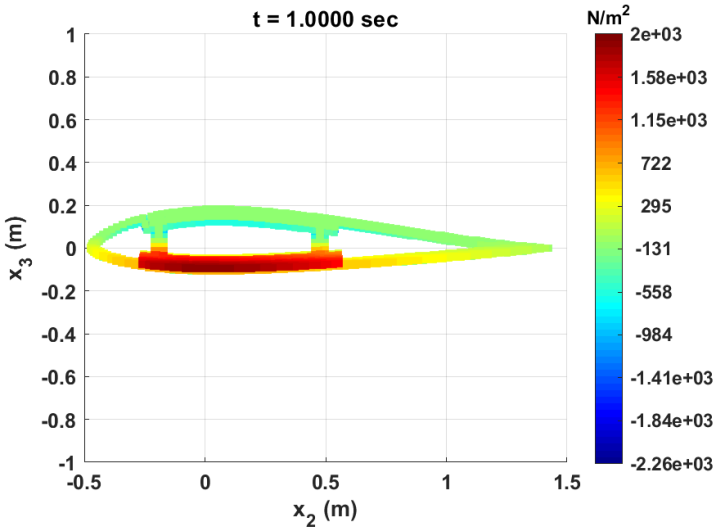

Segment 4, material 1, layup = 30°

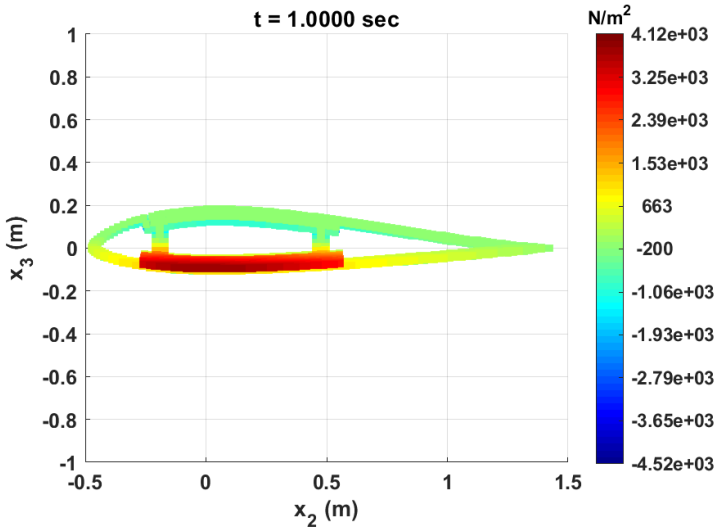

Segment 4, material 1, layup = 0°

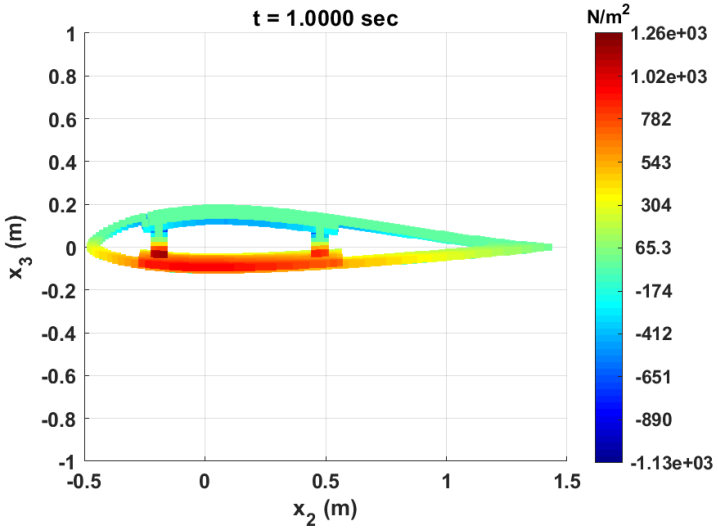

Segment 4, material 1, layup = −30°

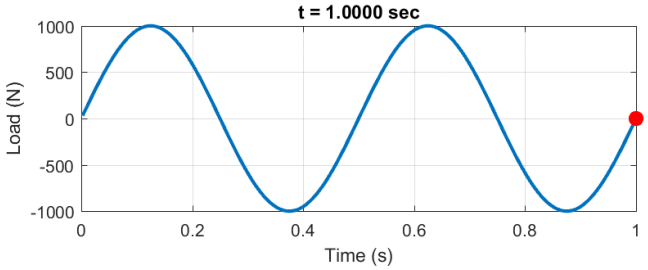

Loading information – transverse tip shear force

Figure 7.23: 3-D Stress (σ_{11}) field at the mid-section of wind turbine blade at $t = 1.0$ sec for different layups in Segment 4

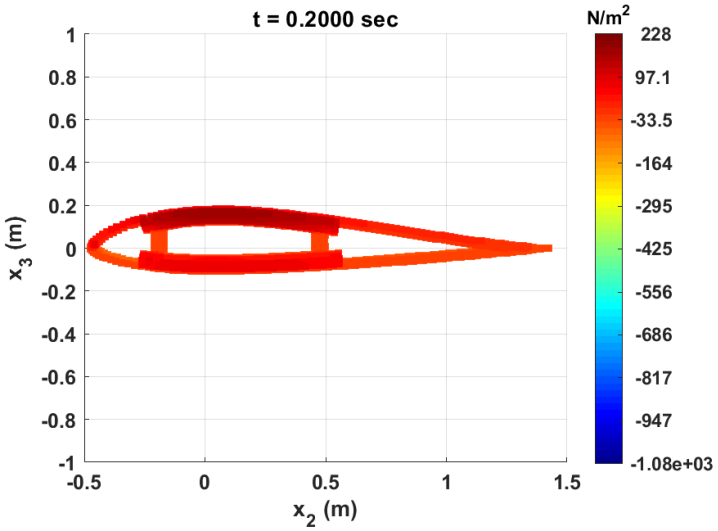

Segment 4, material 1, layup = 30°

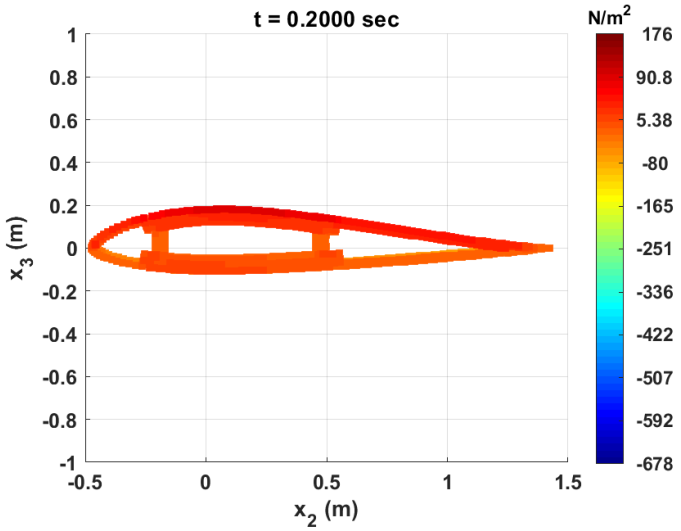

Segment 4, material 1, layup = 0°

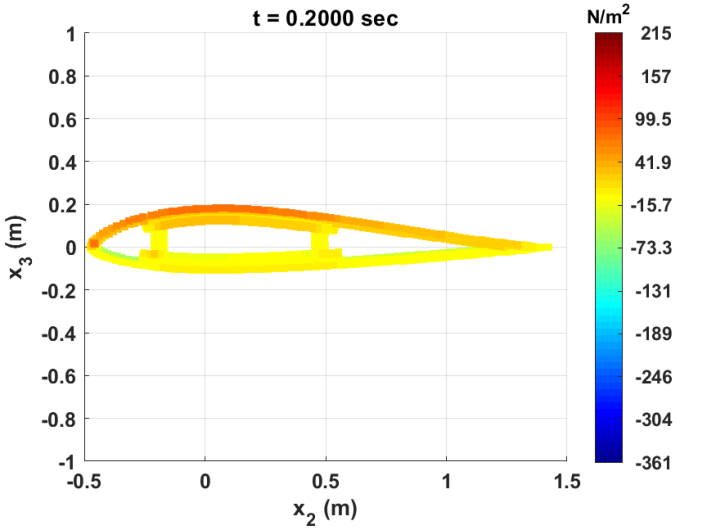

Segment 4, material 1, layup = −30°

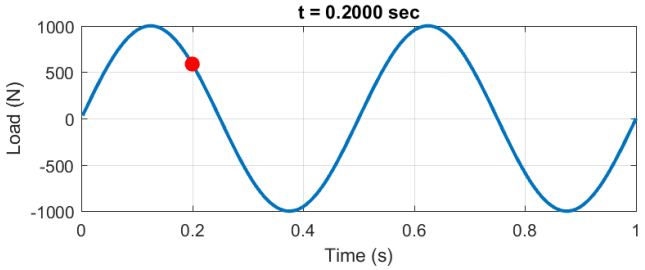

Loading information – transverse tip shear force

Figure 7.24: 3-D Stress (σ_{12}) field at the mid-section of wind turbine blade at $t = 0.2$ sec for different layups in Segment 4

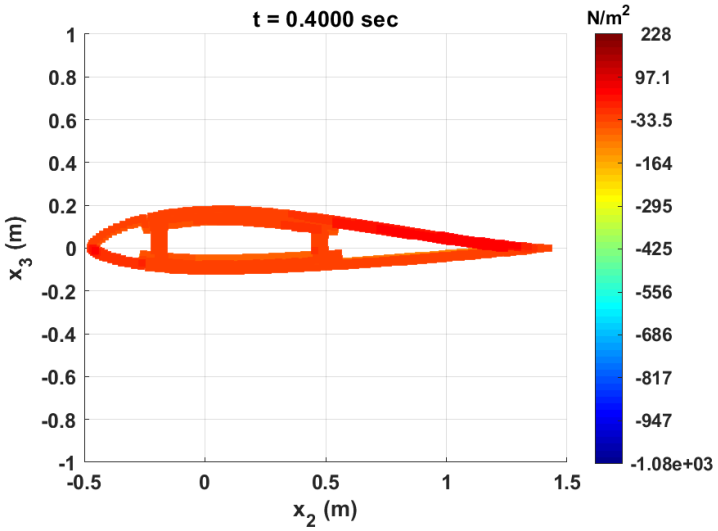

Segment 4, material 1, layup = 30°

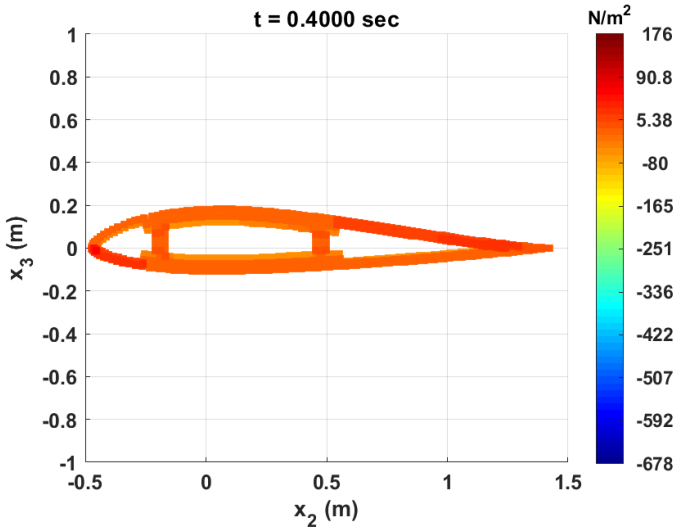

Segment 4, material 1, layup = 0°

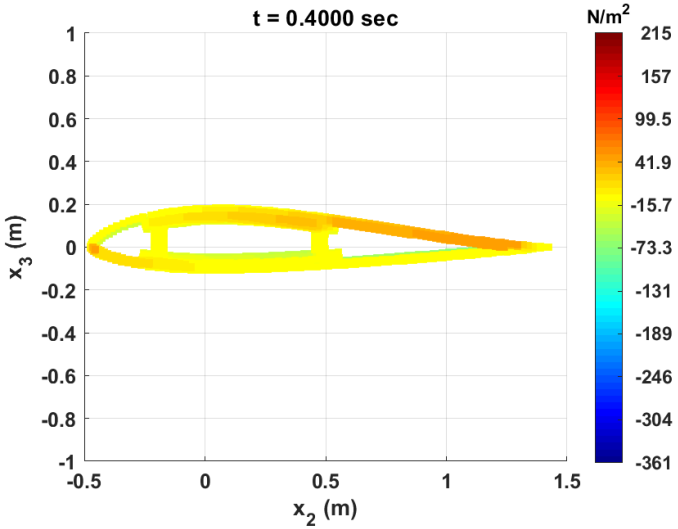

Segment 4, material 1, layup = −30°

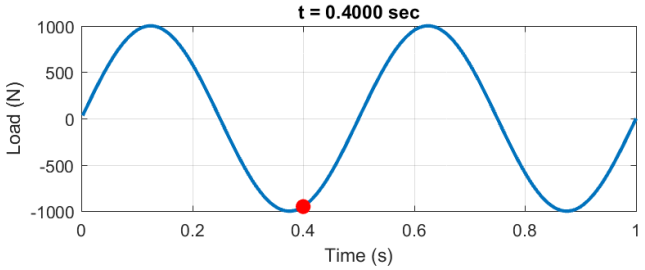

Loading information – transverse tip shear force

Figure 7.25: 3-D Stress (σ_{12}) field at the mid-section of wind turbine blade at $t = 0.4$ sec for different layups in Segment 4

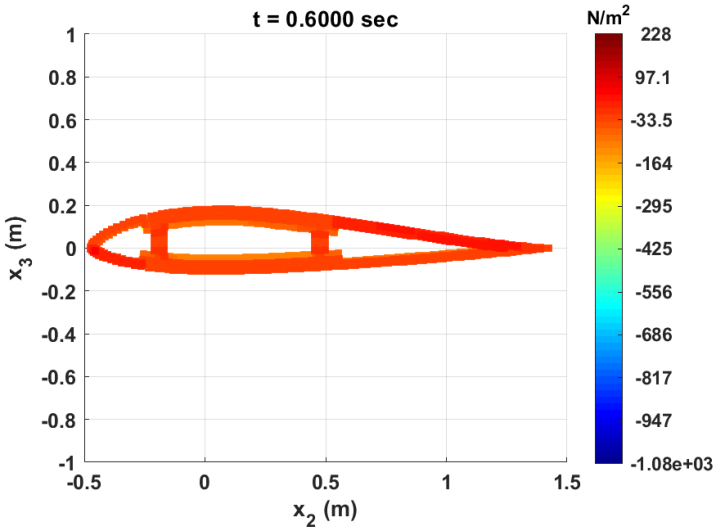

Segment 4, material 1, layup = 30°

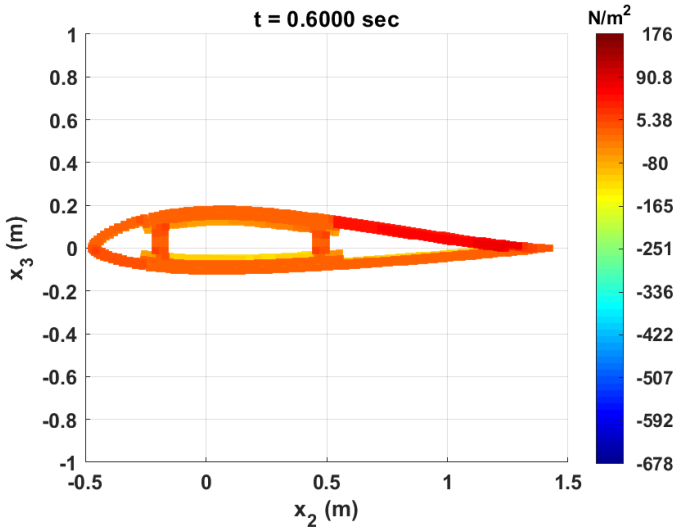

Segment 4, material 1, layup = 0°

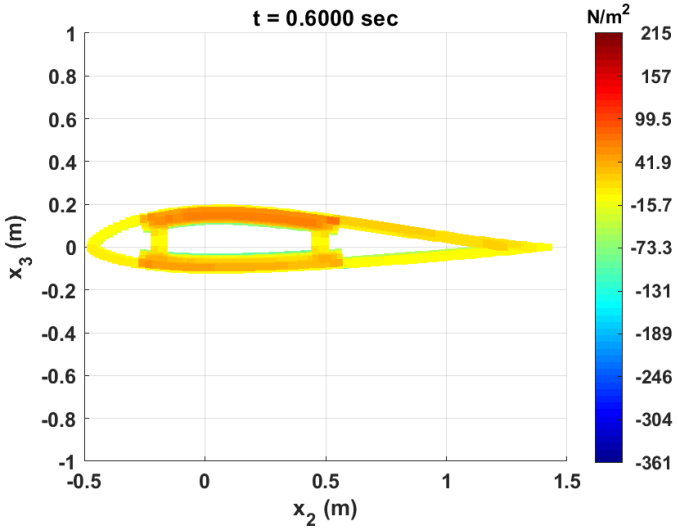

Segment 4, material 1, layup = −30°

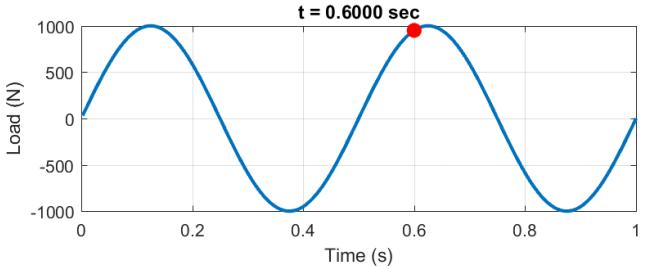

Loading information – transverse tip shear force

Figure 7.26: 3-D Stress (σ_{12}) field at the mid-section of wind turbine blade at $t = 0.6$ sec for different layups in Segment 4

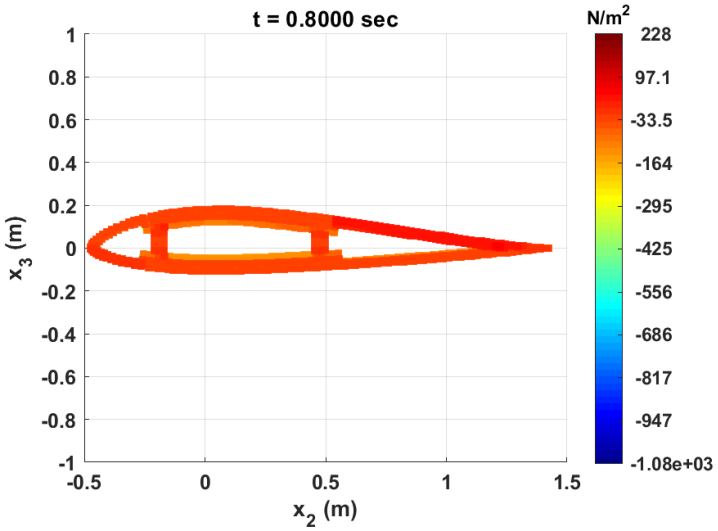

Segment 4, material 1, layup = 30°

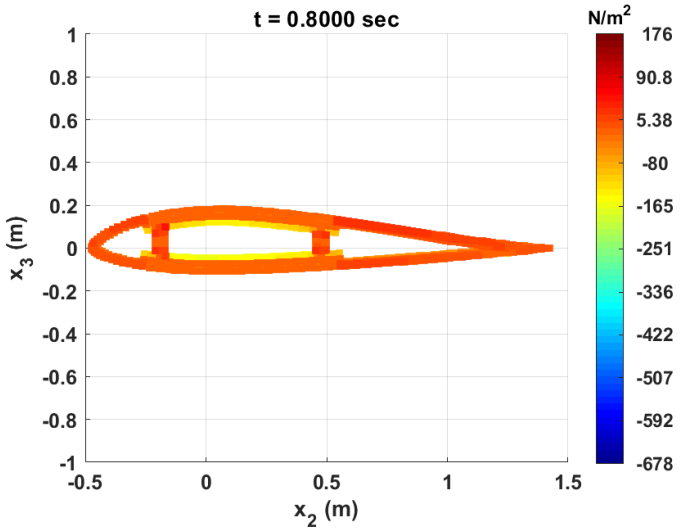

Segment 4, material 1, layup = 0°

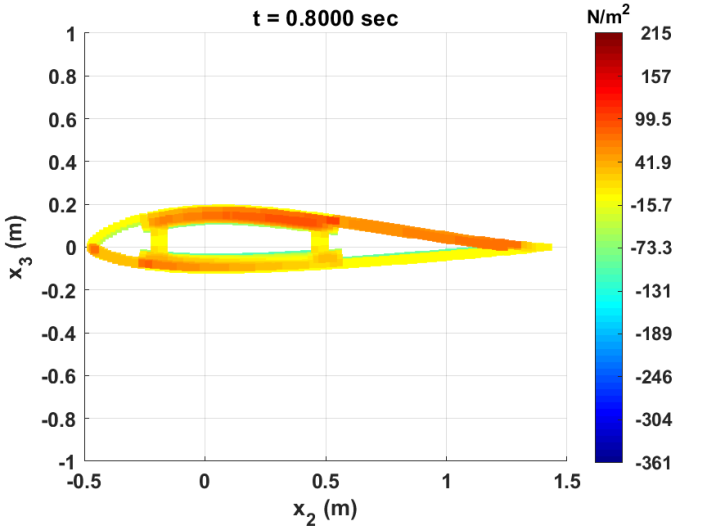

Segment 4, material 1, layup = −30°

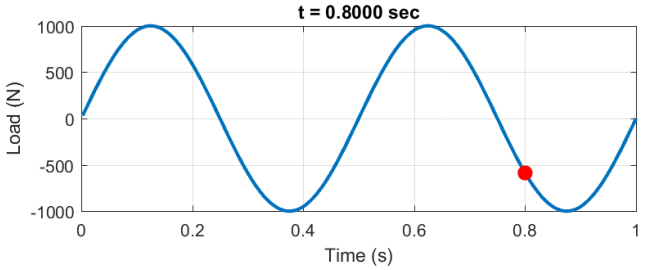

Loading information – transverse tip shear force

Figure 7.27: 3-D Stress (σ_{12}) field at the mid-section of wind turbine blade at $t = 0.8$ sec for different layups in Segment 4

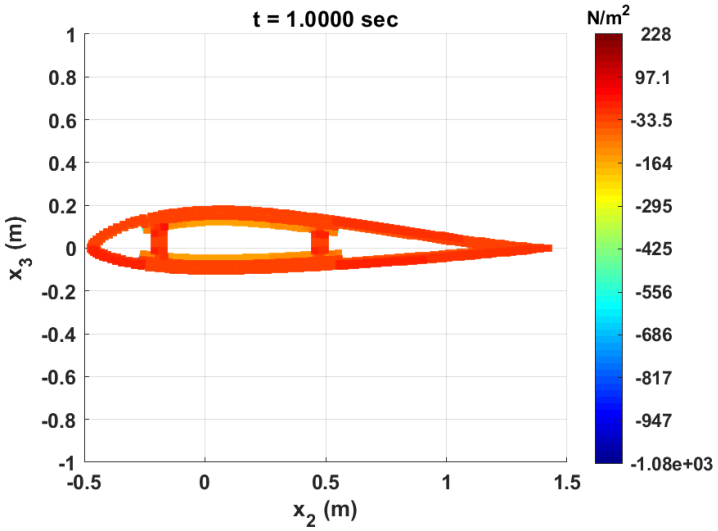

Segment 4, material 1, layup = 30°

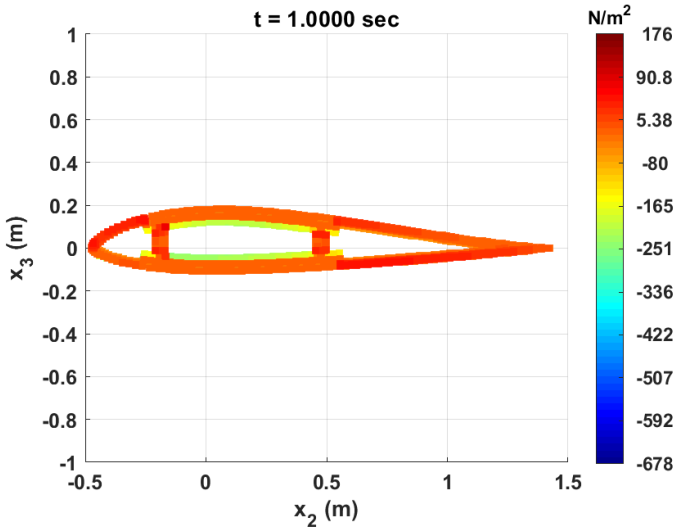

Segment 4, material 1, layup = 0°

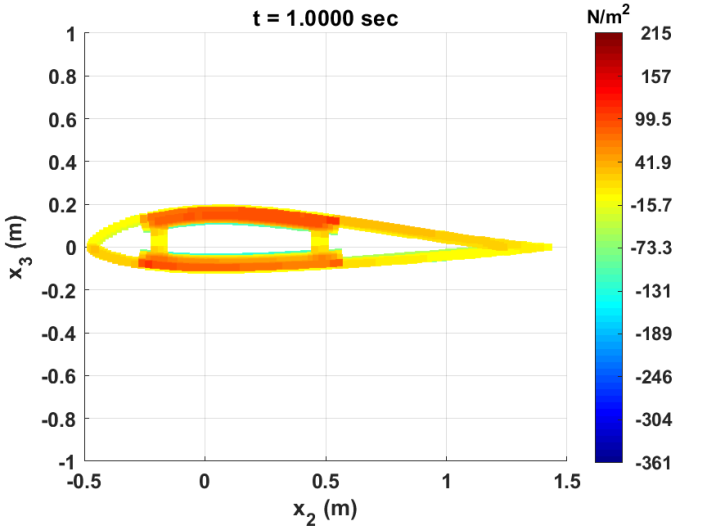

Segment 4, material 1, layup = −30°

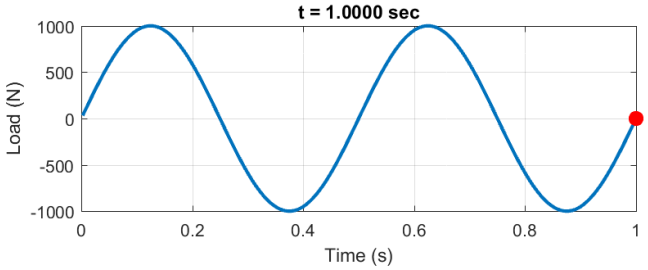

Loading information – transverse tip shear force

Figure 7.28: 3-D Stress (σ_{12}) field at the mid-section of wind turbine blade at $t = 1.0$ sec for different layups in Segment 4

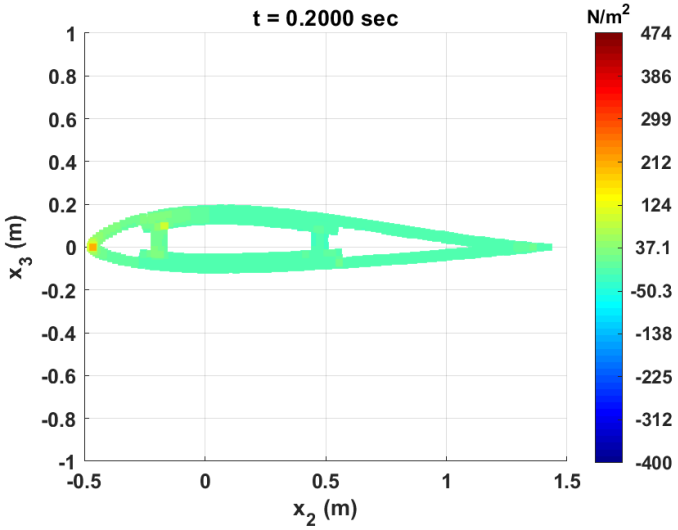

Segment 4, material 1, layup = 30°

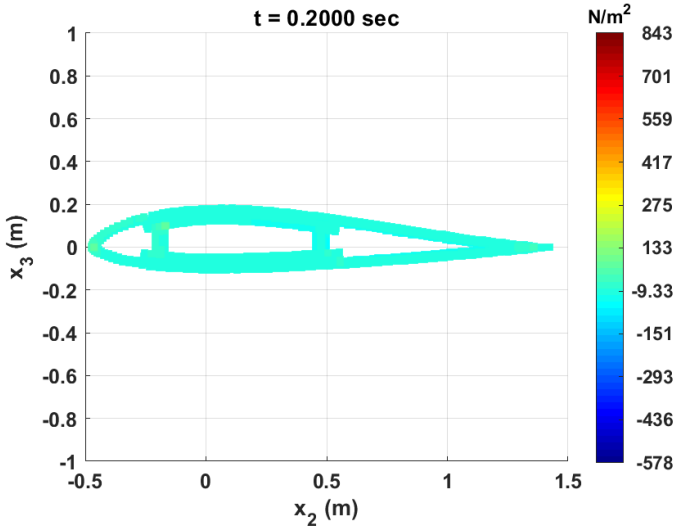

Segment 4, material 1, layup = 0°

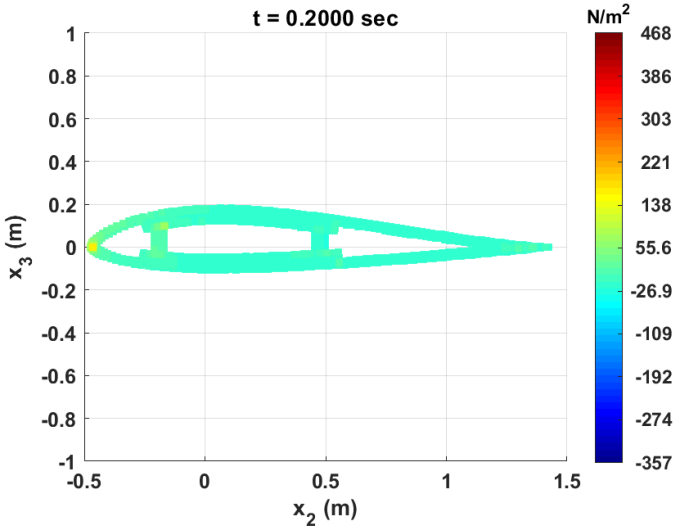

Segment 4, material 1, layup = −30°

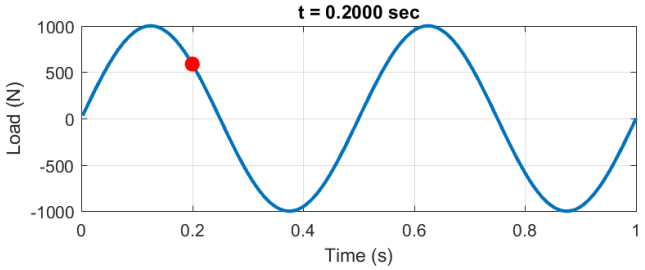

Loading information – transverse tip shear force

Figure 7.29: 3-D Stress (σ_{13}) field at the mid-section of wind turbine blade at $t = 0.2$ sec for different layups in Segment 4

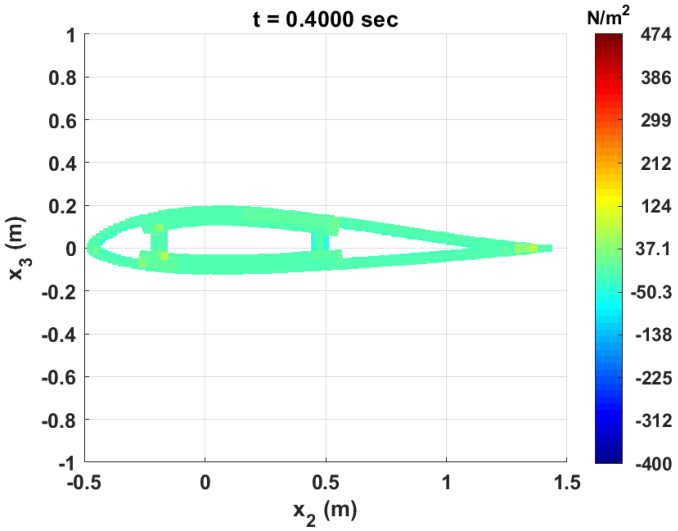

Segment 4, material 1, layup = 30°

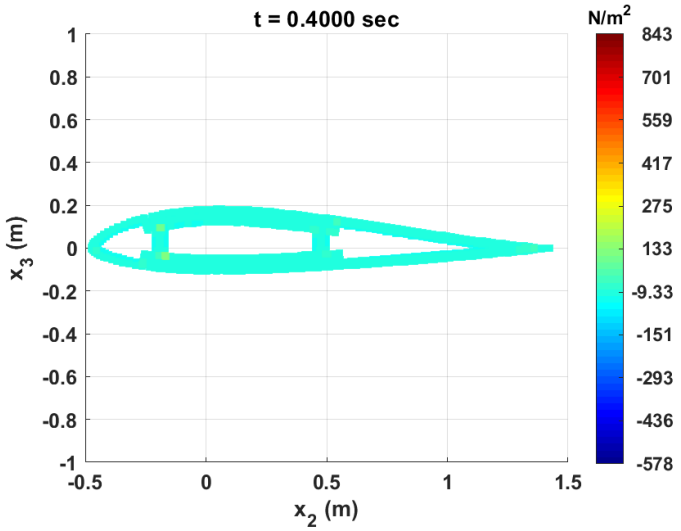

Segment 4, material 1, layup = 0°

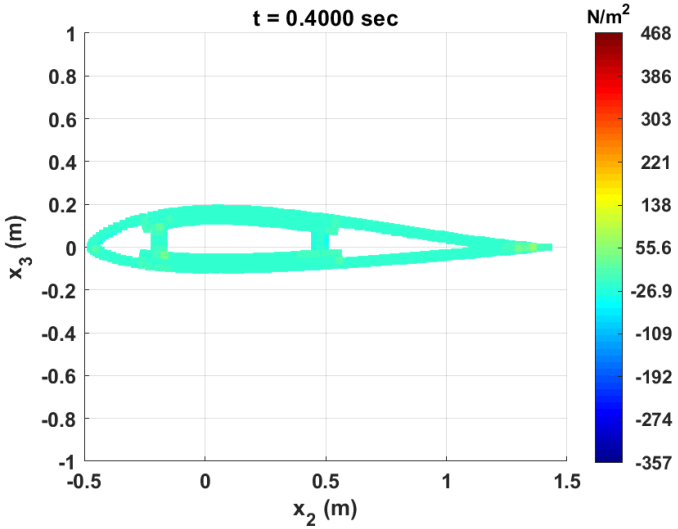

Segment 4, material 1, layup = −30°

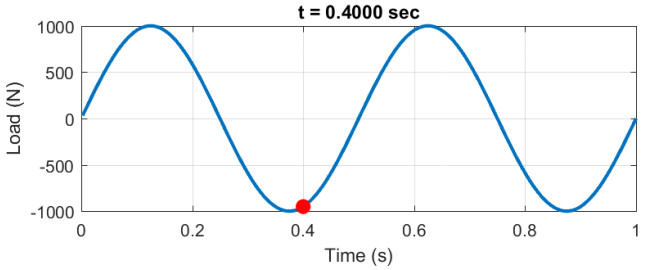

Loading information – transverse tip shear force

Figure 7.30: 3-D Stress (σ_{13}) field at the mid-section of wind turbine blade at $t = 0.4$ sec for different layups in Segment 4

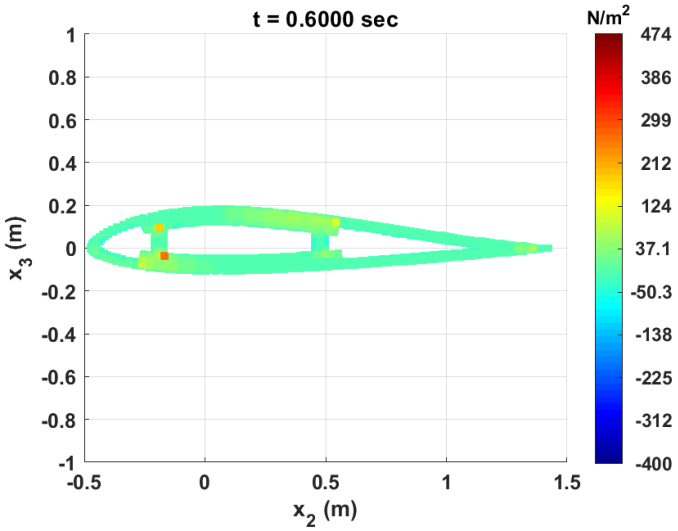

Segment 4, material 1, layup = 30°

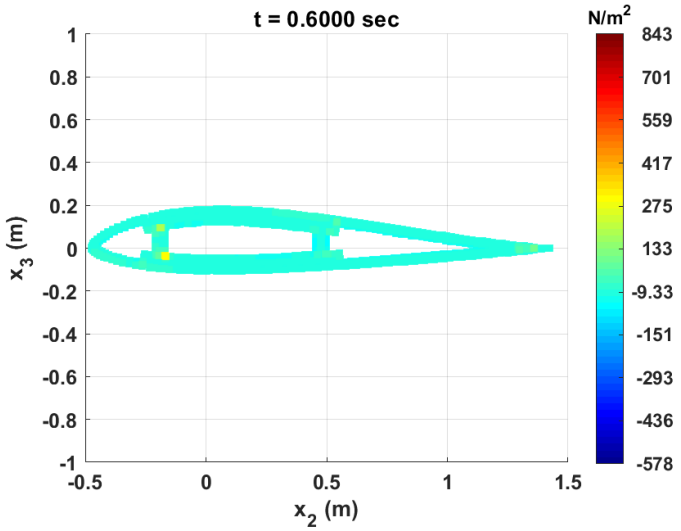

Segment 4, material 1, layup = 0°

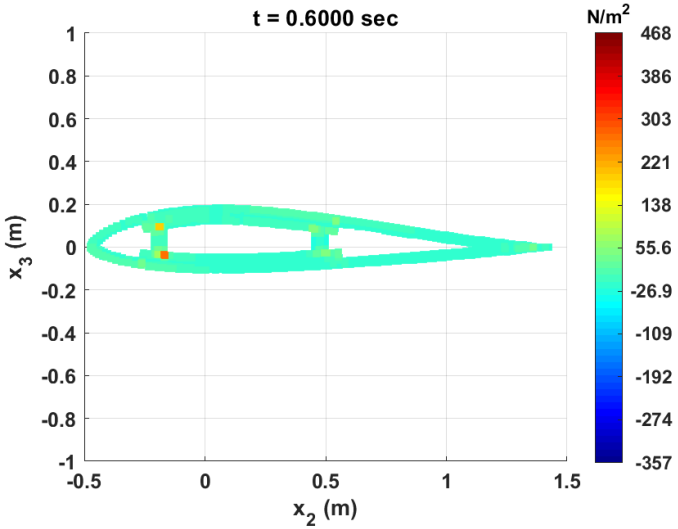

Segment 4, material 1, layup = −30°

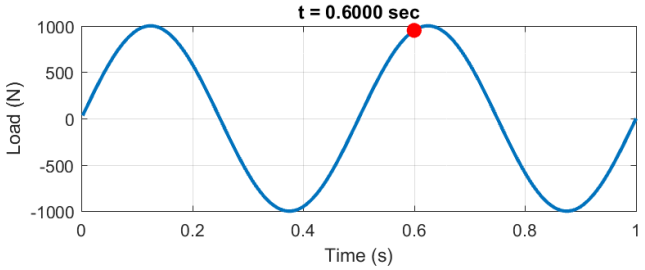

Loading information – transverse tip shear force

Figure 7.31: 3-D Stress (σ_{13}) field at the mid-section of wind turbine blade at $t = 0.6$ sec for different layups in Segment 4

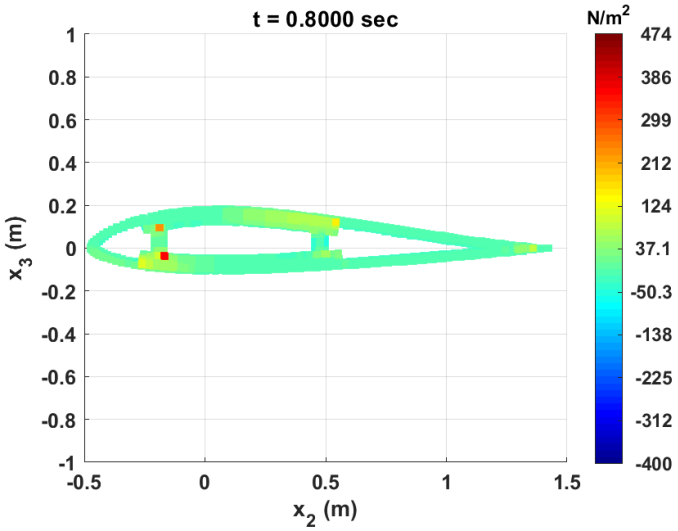

Segment 4, material 1, layup = 30°

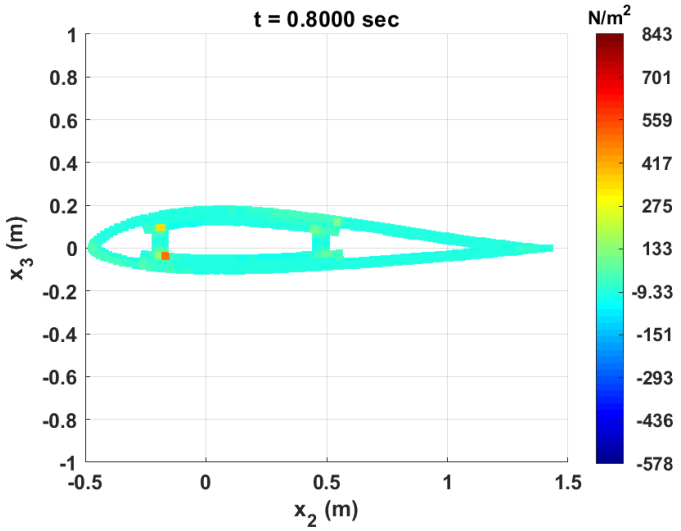

Segment 4, material 1, layup = 0°

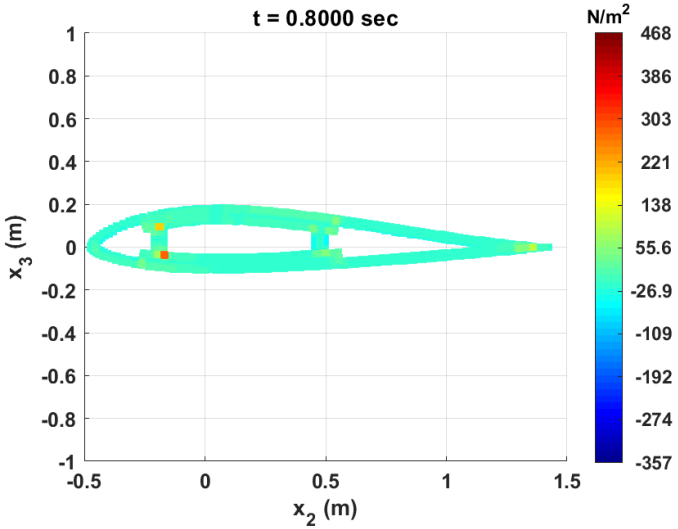

Segment 4, material 1, layup = −30°

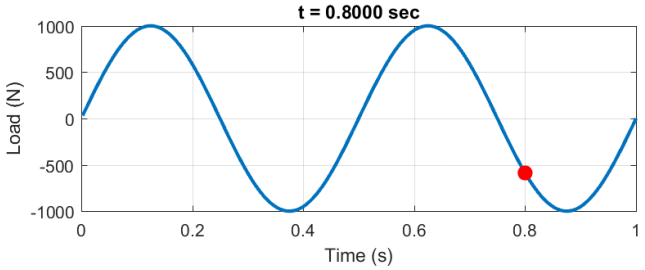

Loading information – transverse tip shear force

Figure 7.32: 3-D Stress (σ_{13}) field at the mid-section of wind turbine blade at $t = 0.8$ sec for different layups in Segment 4

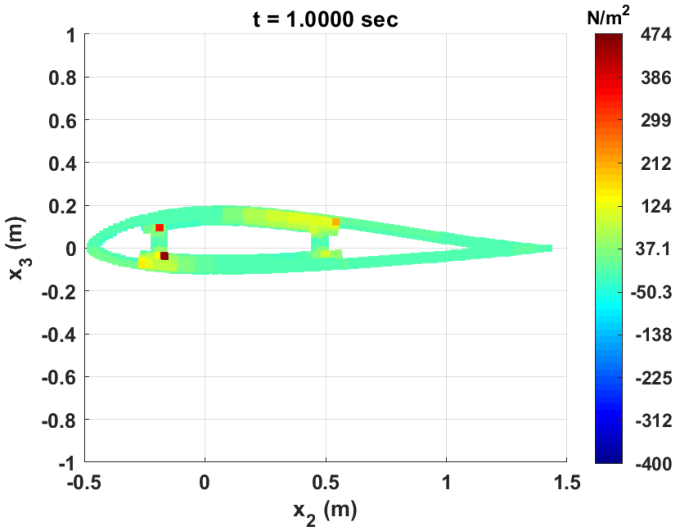

Segment 4, material 1, layup = 30°

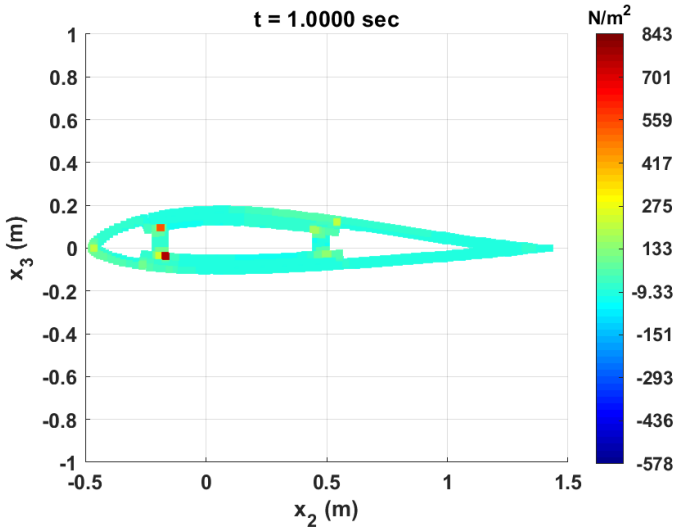

Segment 4, material 1, layup = 0°

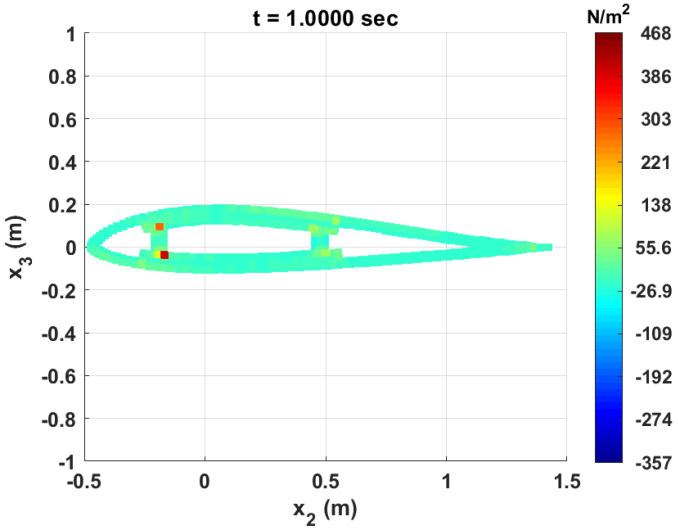

Segment 4, material 1, layup = −30°

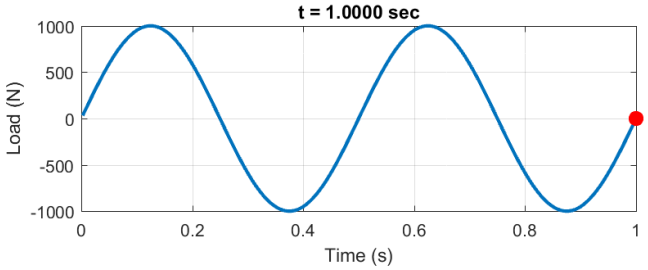

Loading information – transverse tip shear force

Figure 7.33: 3-D Stress (σ_{13}) field at the mid-section of wind turbine blade at $t = 1.0$ sec for different layups in Segment 4

Part 4

Applications

CHAPTER VIII

APERIODIC AND INHOMOGENEOUS STRUCTURES

Aircraft preliminary design and optimization relies on the dynamic response of complex structures such as wings. This analysis cannot leverage high-fidelity analysis which typically involves computationally expensive three-dimensional finite element models. Complex structures can be reduced to one-dimensional structures, known as *stick models* to decrease computational time. Instead, this work presents a methodology for reducing the three-dimensional model of a complex structure into an equivalent beam-like model to obtain a set of elastic constants for its distinct cross sections using the Variational Asymptotic Method. This is followed by the application of Geometrically Exact Beam Theory to obtain the 1-D displacements for the entire structure. A key step in creating the beam model presented in this work is the approximation of sectional stiffness properties for the equivalent beam cross section against the stiffness properties of its three-dimensional counterpart. A stiffness matching procedure is developed to obtain a 6×6 stiffness matrix by altering material properties in the derived geometric model. This procedure ensures that the intricate details of the complex 3-D structure are not lost. Validation of the proposed model is provided by comparing against three-dimensional finite element analysis. Such a formulation is well suited for the design of any aperiodic, inhomogeneous complex structure. This methodology enables designers to capture features in a conceptual design that are typically only considered in the detailed design. Thus, it reduces the need for computationally ex-

pensive tools. The approach presented in this chapter is well-suited for an optimization framework as such.

8.1 Introduction

Static and dynamic response prediction forms a critical component in the development of structural loads for which an aircraft must be sized. These responses focus on predicting the displacement field of the structure as a function of time under applied loading. For aircraft wings, this is a coupled aerodynamics, structural dynamics, and flight dynamics problem.

Aircraft wings are 3-D structures with intricate details, such as ribs, spars, and skin, as seen in Fig. 8.1a. The construction is usually semimonocoque, where the skin resists tension and shear while the stiffeners resist compression. The skin is stiffened by stringers that run along the span of the wing. The rib gives the wing its shape and has to sustain multiple loads such as structural weight, fuel weight and pressure loads from aerodynamic forces. It consists of structural elements, such as stiffeners, rib feet, panels, and holes, as shown in Fig. 8.1b. The primary function of the spar webs is to resist the shear and torsional loads.

There are several methods to capture the dynamic response of aircraft wings can be categorized under a few main categories such as detailed finite-element analysis (FEA), modal analysis, and stick models. Using 3-D FEA, a 3-D structure is discretized into many small finite elements, resulting in a large number of degrees of freedom. A detailed finite-element mesh is also generated in modal analysis. Here, the structural modes of the aircraft are obtained by solving an eigenvalue problem. These modes reduce the degrees of freedom, and are used to obtain the dynamic response [78]. However, the use of modal analysis linearizes the response and is not suitable for highly flexible aircraft wings. In any case, the simulation of dynamic maneuvers is a computationally expensive process. Hence, researchers in the industry have traditionally used models with low degrees of freedom.

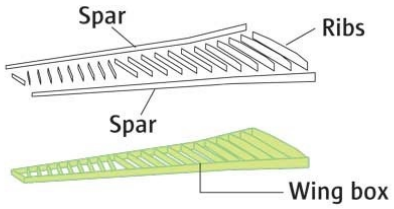

(a) Representation of a wing box made of complex beam-like sections (ribs) along the span

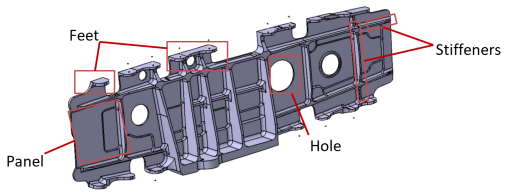

(b) Representation of complex structure of ribs present in the wings

Figure 8.1: Intricate 3-D geometries in an airframe

Hajela and Chen [57] have presented an equivalent beam model. This approach represents the span-wise distribution of sectional moments of inertia and the torsional constant for an equivalent beam model of a built-up wing. This kind of representation is referred to as a *stick model*. The section properties are scaled to account for shear lag effects. The use of a nominal "average material" concept to link geometrical data to cross-sectional stiffness properties has been explored. Gern et al. [49] used a hexagonal wing box, where the thickness of the six sides of a hexagon were varied to match the stiffness of the structure. Elsayed et al. [1] presented a methodology for extracting bending stiffness properties of an aircraft wing using its 3-D finite element model which can then be used in the stick model. Carrera et al. [25] used a component-wise model where each component (stringers, panels, ribs) has a unique 1-D formulation. Piperni et al. [132] presented another method for generating the stick model by using thin-walled, single-cell sections to represent the wing box. Each wing box section is modeled with a set of skin-stringer panels, front and rear spars and upper and lower spar caps. Other researchers simplify the wingbox to box beams. For example, Bindolino et al. [18] represents the wing box as a rectangular box beam and calculates the *stick model* properties. It is important to note that approximate equations are used for the skin and web panel shear stresses based on the beam load resultants.

Goron et al. [54] takes an approach where the critical loads on the airframe can be found by assuming the aircraft to be rigid and only considering the interactions between aerodynamics, propulsion and flight mechanics. The authors simulated the checked-pitch maneuver for a business jet through the entire flight for three weight configurations. Drela [46]

simplified the nonlinear beam equations derived by Rivello [142] to only account for wing up-down bending. The beam equations were coupled to a lifting line theory with roll rate, yaw, and yaw rate effects included. The coupled nonlinear system was solved simultaneously using a Newton system for the structural and aerodynamic states. Subsequently, the tool ASWING [47] was developed and it uses the nonlinear Timoshenko beam theory developed by Minguet [116], an unsteady lifting-line model, and a structural damping model.

In a series of papers by Nguyen and colleagues, the authors derived the equations for the flight dynamics of flexible aircraft. They use an Euler-Bernoulli beam theory formulation for structural dynamics. In an early paper, Nguyen [120] derived the equations for strain in a beam where the bending deflections are coupled to the torsional deflection via the derivative of the wing pre-twist angle. Subsequently, the flight dynamics equations for six degree-of-freedom motion of the aircraft were coupled to the elastic response of the structure [121]. In [122], the authors investigate the inertial force effect on aircraft elasticity with geometric nonlinearity due to rotational and tension stiffening. The axial, bending and torsion stiffness values are fully coupled in the stiffness matrix. The partial differential equations which describe the coupled bending and torsion motion of the wing due to aerodynamic, propulsive and inertial forces are derived.

The objective of these works is to accurately obtain the displacement response of aircraft due to maneuvers or gusts. The computation of stresses and strains has typically not being carried out. Researchers in some articles do compute the stress and strain by either simplifying the geometry, or by leaving out the nonlinear deformation characteristics and layup information in composites. Jasa et al. [74] developed an open-source aerostructural optimization named OpenAeroStruct. The structure in OpenAeroStruct is modeled as a beam with circular cross section using Euler-Bernoulli beam theory, and Euler-Bernoulli beam theory equations are used to obtain the displacement and stress response. Other researchers simplify the wingbox to box beams. For example, Bindolino et al. [18] represents the wing box as a rectangular box beam and calculates the *stick model* properties. It

is important to note that approximate equations are used for the skin and web panel shear stresses based on the beam load resultants.

With advances in wing design which uses parts such as ribs, booms, spars and stringers made of composite materials, it becomes cumbersome to find applications of state of the art tools and techniques mentioned above to reliably model these wing structures. Because of the complexity, the analysis of components in the interior region of aircraft structures is thought to be best carried out using 3-D Finite Element Method (FEM), given that the FEA tools provide high-fidelity modeling of complex geometries. However, there are some major drawbacks. First, invariably all FEA tools are computationally expensive compared to the alternative modeling approaches mentioned above, often by two to three orders of magnitude.

8.2 Proposed Methodology

Unlike existing models and techniques for analyzing complex aircraft geometries in the literature, use of the proposed theory in Section 2.3 allows for a beam-like formulation for an entire wing that is free of ad hoc assumptions. For this analysis, VAM is employed multiple times at different length scales for each of the aperiodic components obtained by deconstructing an aircraft wing such as skin, spars, stringers, ribs, booms, etc. An approach to solve problems with such complex sections has been developed by Liu and Yu [105] using Mechanics of Structural Genome (MSG) where a 3-D structural genome is identified and used to solve heterogeneous beams, but with periodic appearances of the identified structural genome. With all these advancements and features developed in VAM described in Section 2.1, there is still a drawback. The 2-D cross-sectional analysis carried out using the VAM is not sufficient yet, to deal with complex and intricate geometries of an aircraft wing. It is because in complicated 3-D geometries, sometimes a closed 2-D cross section cannot be defined. We cannot have a cross section with disconnected portions of geometry being analyzed in one cross section. So, it becomes important to deduce a way to

expand the use of beam theory-based tools (e.g., VABS) to solve such complex problems.

8.3 Dimensional Reduction

Aperiodic inhomogeneous structures such as complex aircraft wing geometries can be treated as beam-like structures because the wing span is significantly larger than cross-sectional dimensions (chord and thickness) of the wing. However, as mentioned in Section 8.1, the sporadic presence of complex and intricate geometries along the wingspan, renders the use of the sectional analysis based on VAM ineffective for analyzing such a structure. To overcome this challenge, the present work elaborates on the dimensional reduction technique being developed. Through this technique, a complete 3-D body such as an aircraft wing could be reduced to multiple beam segments of soft/stiff beam sections distributed along a beam reference line along with features like initial curvatures and twist, taper, dihedral, etc. The equivalent beam sections thus generated need not bear a certain material property, and thus could be composite sections.

The idea is best summarized in Fig. 8.2 for a generic beam-like structure. At first, information about the beam-like 3-D geometry/part is obtained from the user in the form of a CAD model or information about the dimensions. Further, information about the materials, layup information in case of composites, boundary conditions and loading information are also required at this step. The part is then analyzed for constructing an equivalent beam-like model suitable for a VAM-based analysis. The structure can be processed further using the Nonlinear Composite Beam Theory described in Sec. 2.3 and 5.2 with the help of VABS and GEBT if it can be dimensionally reduced to a set of 2-D cross sections distributed along a 1-D reference line to reproduce the complete 3-D part. The theory is sufficient to analyze such beam-like structures, even with initial curvatures and twist, taper, and discontinuities along the length of the beam. In case the 3-D part is complex, such that it consists of discontinuous beam/strip-like elements such as stiffeners, along the length, then the need for an equivalent model arises (e.g., consider the presence of stiffened ribs in a beam-like struc-

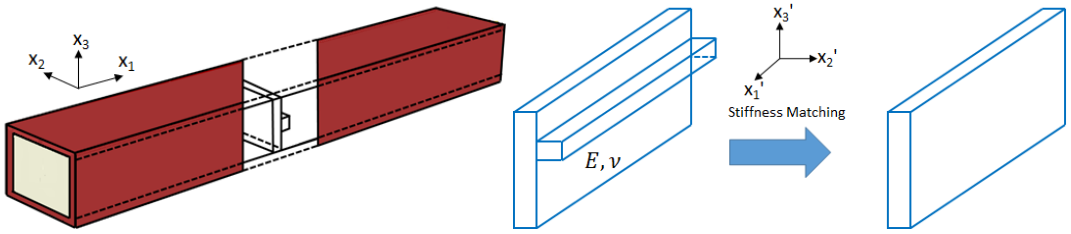

(a) 3-D geometry with aperiodicity along length

(b) Isolate regions containing aperiodicity. Aperiodic regions are themselves 3-D geometries.

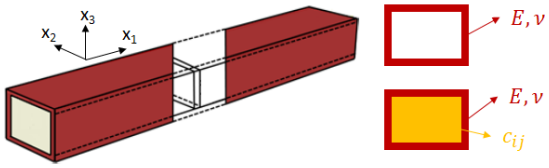

(c) 3-D geometry now has aperiodicity along span with each aperiodic region being a 2-D geometry. This structure can be treated with the VAM.

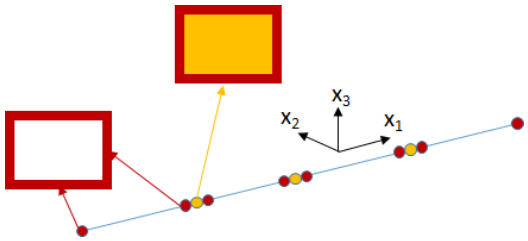

(d) 1-D geometry with segments having different stiffness properties along length of the beam.

Figure 8.2: Methodology for generating equivalence model for components of beam-like structure.

ture as shown in Fig. 8.2a). Once the parts are identified, the 3-D parts are dimensionally reduced to 2-D structures as shown in Fig. 8.2b, using a matrix matching process described in Section 8.4. Each 2-D section is now, theoretically, made of a composite material the properties of which depend on the choice of the matrix matching process from Section 8.4. This results in an overall structure that is beam-like with aperiodic structures as shown in Figs. 8.2c and 8.2d. In summary, a general 3-D structure having intricate structural details along the length of the beam-like structure can be dimensionally reduced to a composite beam structure with an appropriate stiffness matrix matching procedure. Here, the material constants for the derived equivalent beam-like structure are obtained as outputs from the stiffness matrix matching procedure.

8.4 Stiffness Matching Using an Inverse Approach

The response of a beam depends mainly on its length and cross-sectional properties. The cross-sectional properties are dependent on the properties of the constituent materials, their

geometry, and additional information such as layup orientation if the materials are composites. It is well known that a perturbation in the geometry or design may have a significantly larger effect on the overall sectional properties of the component, as opposed to a perturbation in material properties. Adding stiffeners to a structure is a deliberate attempt to leverage this physical phenomenon. It is indeed a modification in the design to make a structure stiffer in one or more modes, or to avoid stress concentration in a particular region. Such an application of stiffeners is very common in aerospace structures such as aircraft wings.

A specific case of that application is described in this section along with a novel approach to perform local smearing for the purpose of the structural analysis. Consider a box-beam as shown in Fig. 8.2a. It has a typical cross section (here and hereafter referred to as a *built-up section*) along the span of the beam as shown in Fig. 8.2b. This is representative of a rib with a stiffener on it. The response of this structure can be obtained by finding the response of an equivalent section without the rib such that its effective stiffness is the same as the section with the rib. This is shown in Fig. 8.3. Two approaches to generate the equivalent model are shown in the bottom of Fig. 8.3, used to accommodate the stiffener's properties by preparing equivalent rib geometry. This smearing approach is extensively used in plate theory [39]. Here, the properties of the stiffener are smeared entirely on the rib, thus having the rib of a uniform material. In the bi-material approach, a composite section is formed for the rib instead of a smeared section such that only a portion of the original rib structure is altered to model an equivalent structure. In both approaches, the effective section will have some or all of it as an anisotropic material, whose material properties are now represented as a general 6×6 matrix, c_{ij}. The approaches will be discussed in the following sub-sections.

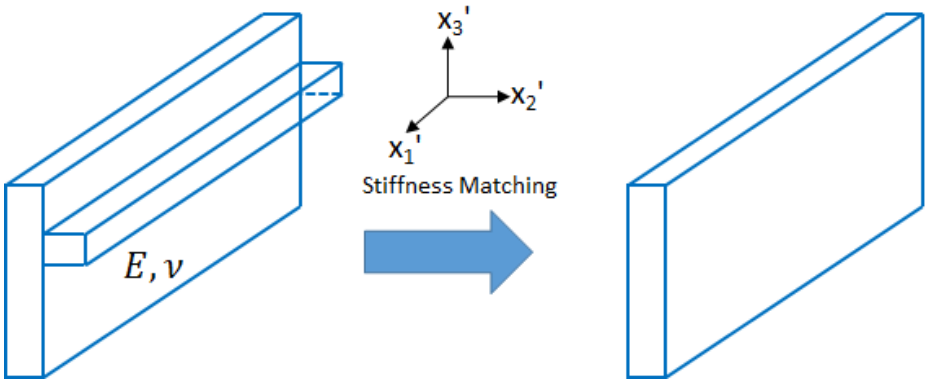

(a) Intent of matching stiffness properties of the built-up section and an equivalent section

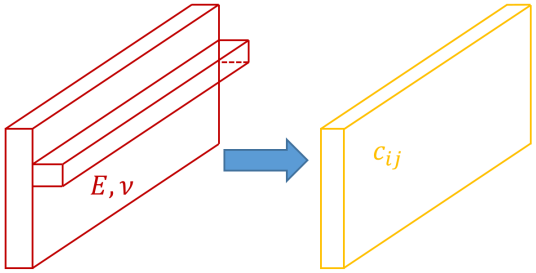

(b) Smearing properties on entire section

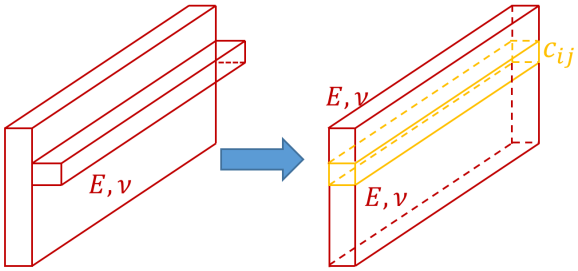

(c) Local smearing of properties

Figure 8.3: Methods to obtain equivalent section.

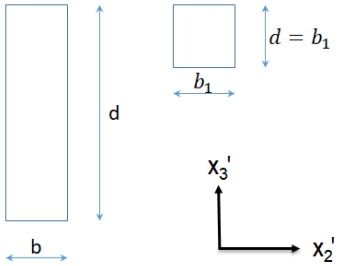

Figure 8.4: Rectangular and square cross section

8.4.1 Challenges in Stiffness Matching

The present work is extensively based on matching stiffness properties of two cross sections of different shapes to enable either partial smearing or smearing of the entire cross sections, as explained in later subsections. Thus, the present work is highly dependent on a technique that is able to match stiffness properties by altering material properties. But completely matching stiffness properties (i.e., matching all the elements of the 6×6

Table 8.1: Expressions for stiffness for the original rectangular vs. the equivalent square cross section

(a) Stiffness values for rectangular section

Stiffness	Axis	Formula
Axial	1	Ebd
Bending	2	$E\frac{bd^3}{12}$
Bending	3	$E\frac{db^3}{12}$

(b) Stiffness for square section

Stiffness	Axis	Formula
Axial	1	$E_{eq}b_1^2$
Bending	2	$E_{eq}\frac{b_1^4}{12}$
Bending	3	$E_{eq}\frac{b_1^4}{12}$

stiffness matrix for cross sections of different shapes) is often not easy and, at times, unfeasible. To clearly explain this challenge, consider a prismatic isotropic beam made of material with Young's modulus E and rectangular cross section, of width b and depth d as shown in Fig. 8.4. The analytical expressions for axial and bending stiffness properties of this section are given in Table 8.1a. Using the present approach, if a square section of side b_1 and homogeneous, isotropic material properties with Young's Modulus E_{eq} is chosen to be a section of equivalent stiffness, then the analytical expressions for corresponding stiffness properties are shown in Table 8.1b.

As seen, it is clearly impossible to vary the material property E_{eq} in such a way that the axial and the two different bending stiffness components are matched simultaneously. For a beam made of a rectangular cross section, the two flexural stiffness values would be different as opposed to a beam made of square cross section. Hence, for appropriate stiffness matching, the material properties in the equivalent section generated, would have to be different in different directions. Isotropic materials cannot have such behavior, but orthotropic or anisotropic materials do possess such characteristics and may help in getting the stiffness matrix of equivalent section to match the stiffness matrix of the original cross section. Since an anisotropic material matrix provides versatility in defining material properties with the largest number of independent parameters, we use the anisotropic material matrix's input format of a 6×6 matrix, for carrying out the matching process and, subsequently, the final analysis. However, to choose a starting point for the stiffness matching process, the material properties are chosen such that the 6×6 material matrix is not fully

populated. The non-zero elements of that matrix are found by identifying the anisotropic material matrix possessing properties of an orthotropic material is given by the inverse of matrix in the equation below

$$\begin{Bmatrix} \sigma_{11} \\ \sigma_{12} \\ \sigma_{13} \\ \sigma_{22} \\ \sigma_{23} \\ \sigma_{33} \end{Bmatrix} = \underbrace{\begin{bmatrix} \frac{1}{E_1} & 0 & 0 & -\frac{\nu_{12}}{E_1} & 0 & -\frac{\nu_{13}}{E_1} \\ 0 & \frac{1}{G_{12}} & 0 & 0 & 0 & 0 \\ 0 & 0 & \frac{1}{G_{13}} & 0 & 0 & 0 \\ -\frac{\nu_{12}}{E_1} & 0 & 0 & \frac{1}{E_2} & 0 & -\frac{\nu_{23}}{E_2} \\ 0 & 0 & 0 & 0 & \frac{1}{G_{23}} & 0 \\ -\frac{\nu_{13}}{E_1} & 0 & 0 & -\frac{\nu_{23}}{E_2} & 0 & \frac{1}{E_3} \end{bmatrix}}_{\text{c}} \begin{Bmatrix} \Gamma_{11} \\ 2\Gamma_{12} \\ 2\Gamma_{13} \\ \Gamma_{22} \\ \Gamma_{23} \\ \Gamma_{33} \end{Bmatrix} \tag{8.1}$$

Further, orthotropic materials properties can be chosen in a manner such that the moduli in different directions bear the same value, which matches the axial and at least one flexural stiffness. As the axial stiffness depends on cross-sectional area, the material properties of the equivalent cross sections are chosen such that

$$E_1 = E_2 = E_3 = AF * E \tag{8.2}$$

where E is the Young's modulus of the built-up section, E_1, E_2, E_3 for the orthotropic values are chosen to be equal for the starting point (i.e., baseline material matrix of the equivalent section), and the area factor AF is given by

$$AF = \frac{\text{Area of built-up section}}{\text{Area of equivalent section}} \tag{8.3}$$

The shear moduli are chosen to be

$$G_{12} = \frac{E_1}{2(1+\nu)}, \quad G_{13} = \frac{E_1}{2(1+\nu)}, \quad G_{23} = \frac{E_1}{2(1+\nu)} \tag{8.4}$$

where $\nu_{12} = \nu_{23} = \nu_{13} = \nu$, for simplicity. This process helps to choose a baseline material matrix that would help match the axial stiffness, transverse shear moduli and one of the two bending stiffness values (which was bound to happen) at the start of the stiffness matching process. During the matching process, this baseline matrix would be used and iterated upon to find a suitable material matrix that matches the two stiffness matrices in consideration. It is important to note that the two bending stiffness values vary differently, as pointed out earlier in this section because of the dimensions of the two cross sections under consideration. As is known from the beam kinematics and the 1-D strain measures, unless the shapes of the two cross sections are similar to each other, the two beam bending stiffness values of equivalent sections would never match the original section in event of a change in material properties, no matter how much anisotropy is introduced in the equivalent beam section. This challenge is navigated by considering various approaches where different equivalent sections are developed and their stiffness matrices are obtained and studied further in detail over the next three subsections.

8.4.2 Approach 1: Smearing Approach

The first approach "smears" the effect of the stiffener onto the entire original section of the rib. This entails modifying the material properties of the entire equivalent section to match the stiffness of the built-up section.

The built-up section and the effective section used in this study are shown in Fig. 8.5a and Fig. 8.5b respectively, with the coordinate frame as shown and origin is located at the intersection of the two axes of symmetry. For analysis purposes throughout this section, the built-up section is considered to be made of isotropic material of Young's modulus $E = 70 \times 10^9$ Pa and Poisson's ratio $\nu = 0.327$. Further, the dimensions are illustrated in Fig. 8.5. The stiffness matrix (S), represented in Eq. (2.52), for the built-up section

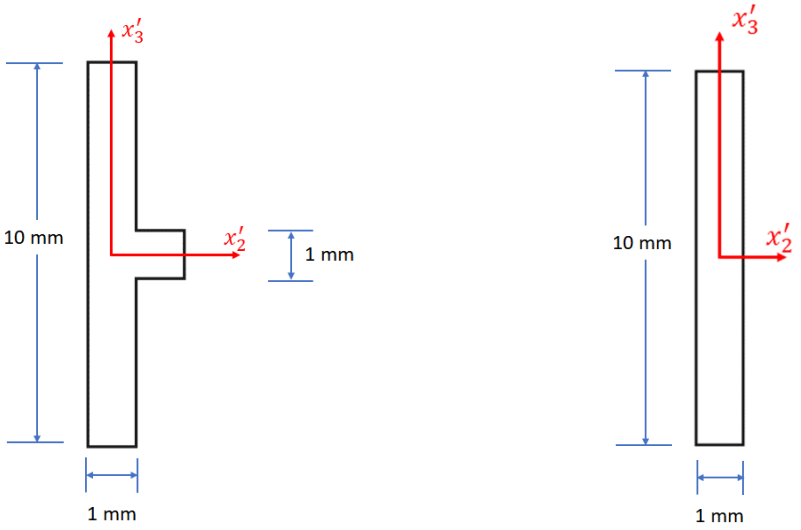

(a) Built-up section (b) Equivalent section

Figure 8.5: Cross sections used in the analysis for smearing approach

obtained from cross-sectional analysis performed in VABS is given by:

$$S = 1 \times 10^{12} \begin{bmatrix} 0.770000 & 0.000000 & 0.000000 & 0.000000 & 0.000000 & -0.070000 \\ & 0.054409 & 0.000001 & 0.000000 & 0.000000 & 0.000000 \\ & & 0.226740 & 0.008380 & 0.000000 & 0.000000 \\ & & & 0.096470 & 0.000000 & 0.000000 \\ & & & & 5.839230 & 0.000000 \\ & & & & & 0.134230 \end{bmatrix} \tag{8.5}$$

As usual, a consistent set of SI units is being followed where force measures are represented in N and moment measures are represented in Nm. The equivalent section shown in Fig. 8.5b is entirely made up of a baseline material matrix as described in Section 8.4.1, before any changes are made to the material properties. Defaulting to baseline values and using the inverse of the matrix shown in Eq. (8.1) the material matrix is generated. It is reasonable now to define the material matrix in the present work to be the product of the Young's

modulus of the isotropic built-up section, and a factor matrix (KF) as shown:

$$KF = \begin{bmatrix} 1.612360 & 0.000000 & 0.000000 & 0.783418 & 0.000000 & 0.783418 \\ & 0.414469 & 0.000000 & 0.000000 & 0.000000 & 0.000000 \\ & & 0.414469 & 0.000000 & 0.000000 & 0.000000 \\ & & & 1.612360 & 0.000000 & 0.783418 \\ & & & & 11/32 & 0.000000 \\ & & & & & 1.612360 \end{bmatrix} \tag{8.6}$$

A factor matrix is a matrix of the same size of the material matrix and is obtained by dividing every element of the material matrix by the value E. It is useful when the elements of the factor matrix are perturbed during the stiffness matching procedure. Cross-sectional analysis is performed on this section with the anisotropic material properties shown in Eq. (8.6). The resulting stiffness matrix is then

$$S = 1 \times 10^{12} \begin{bmatrix} 0.770000 & 0.000000 & 0.000000 & 0.000000 & 0.000000 & 0.000000 \\ & 0.046810 & 0.000000 & 0.000000 & 0.000000 & 0.000000 \\ & & 0.241770 & 0.000000 & 0.000000 & 0.000000 \\ & & & 0.090614 & 0.000000 & 0.000000 \\ & & & & 6.416690 & 0.000000 \\ & & & & & 0.064166 \end{bmatrix} \tag{8.7}$$

As seen, the axial stiffness, S_{11} has been matched to the axial stiffness of the original cross section as intended. The torsional stiffness S_{44} is almost the same, while the bending stiffness S_{55} is close to the same bending stiffness coefficient of the built-up section. The term S_{16} has a large value in the built-up section stiffness matrix, but it is zero in the equivalent section. To obtain the desired stiffness matrix for the built up section and account for the change in design, we alter the material properties of the equivalent section. However, it is required to know the material properties that affect a particular element of the stiffness

matrix under consideration.

In order to understand the effect of the components of the material matrix on the stiffness matrix, a Design of Experiments (DoE) is generated. A DOE is simply a technique which runs a solver multiple times with different values obtained by perturbing one or more input parameters from a set of the given inputs. Further, the output from DOE is a compilation of results from the solver, with each result mapped to the set of input parameters chosen for each instance of solver's execution. In this work, the values are perturbed about the material-matrix given in Eq. (8.6). A full factorial analysis with 6 factors and 7 levels is performed. Table 8.2 gives the factors chosen and the values for each. This results in 147,649 cases. The 6 factors chosen to be varied are the 6 rows in Table 8.2. The 7 levels are represented by the columns from L1 to L7. Each level is a value the corresponding factor can take-on.

Table 8.2: Factors and levels to generate full factorial DoE for smearing case

Factor (KF)	L1	L2	L3	L4	L5	L6	L7
(1,4)	0.533418	0.600118	0.666818	0.733418	0.833418	0.908418	0.983418
(1,6)	0.533418	0.600118	0.666818	0.733418	0.833418	0.908418	0.983418
(2,2)	0.164469	0.231169	0.297869	0.364469	0.464469	0.539469	0.614469
(3,3)	0.164469	0.231169	0.297869	0.364469	0.464469	0.539469	0.614469
(4,4)	1.362360	1.429060	1.495760	1.562360	1.662360	1.737360	1.812360
(6,6)	1.362360	1.429060	1.495760	1.562360	1.662360	1.737360	1.812360

The data generated from the DoE is analyzed using the statistical tool, JMP. A neural network , to study how the output changes with the change in the input, is generated using the data and a prediction profiler, as shown in Fig. 8.6. The prediction profiler allows us to vary various factors and see its effect on all the responses simultaneously. The factors are varied along the x-axis, and the responses (corresponding stiffness values mentioned on the left of the row) are varied along the y-axis. The numbers in black on the x-axis correspond to the ranges by which the factor was varied. The number in red is the current value for which the graph is shown. The values on the y-axis provide the same information for the responses. A large slope on the graph indicates the factor has a significant impact on

the response, and further gives insight into the nature of the response (linear or non-linear, increasing or decreasing). This information is important as it would help in determining what values of material properties in the modified cross section should be altered to obtain the desired stiffness matrix (original cross section) as output. The following inferences can

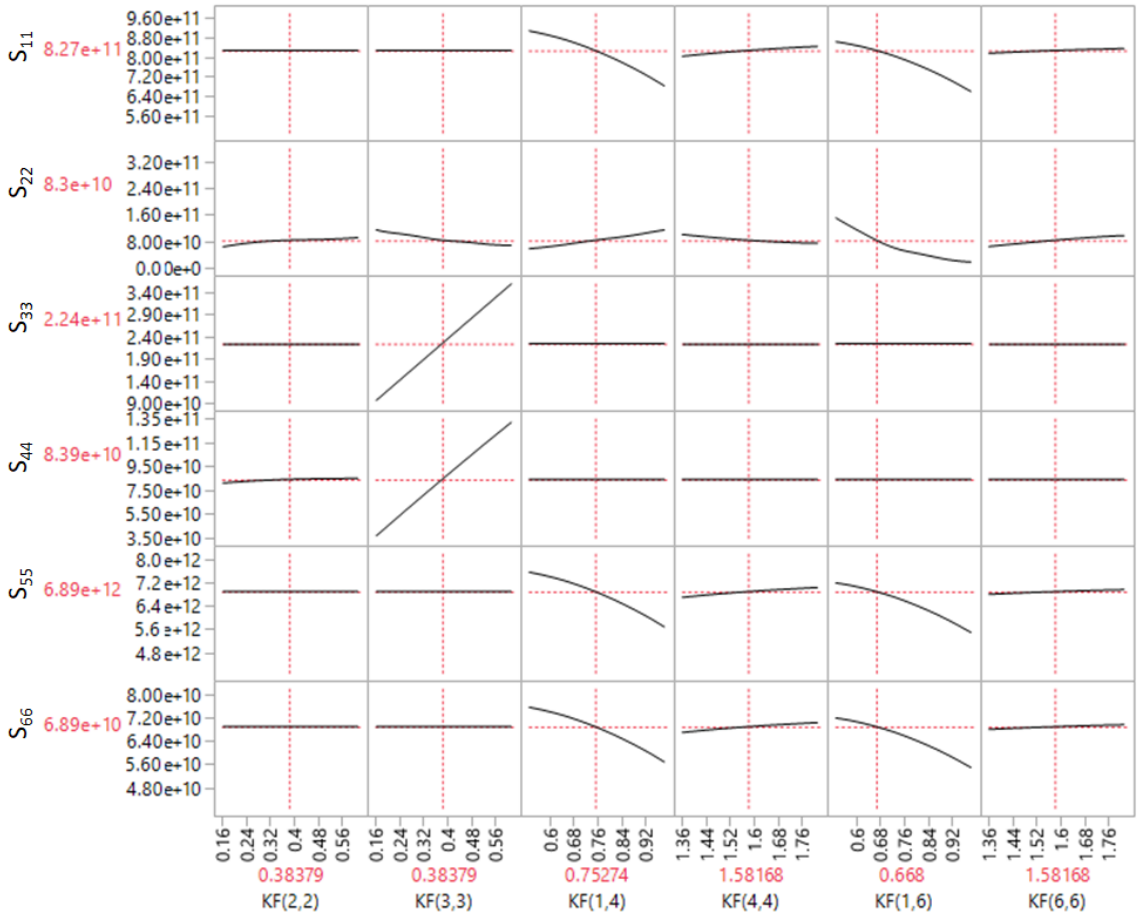

Figure 8.6: Prediction profiler for smearing approach

be drawn from the observations:

1. Attempting to match the bending stiffness values without changing the axial stiffness is not possible.

2. It is possible to match the torsional stiffness S_{44} and bending stiffness S_{55}, with a slight mismatch in axial stiffness S_{11}.

3. Matching torsional stiffness S_{44} and bending stiffness S_{66} results in a large mismatch

of axial stiffness S_{11}.

8.4.3 Approach 2: Stiffener's Properties Accounted in Adjacent Material

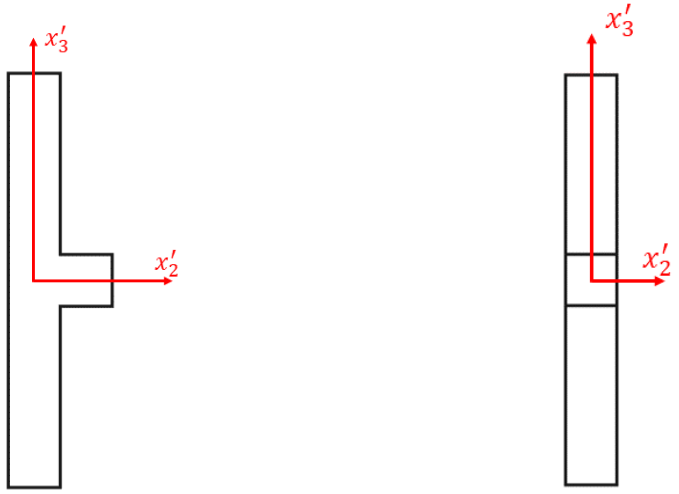

(a) Built-up section (b) Equivalent section

Figure 8.7: Cross sections used in the analysis in approach 2

In this approach, the stiffener is accounted for in the formulation when an equivalent section is generated by modifying the region where it is attached to the rib. Fig. 8.7a shows the original built-up section. The equivalent section is shown in Fig. 8.7b. There are three regions. The top and bottom region retain the isotropic material of the built-up section. The local region in the middle is proposed to have anisotropic material properties from where the stiffener has been removed. As mentioned in Section 8.4.2, we can start with a baseline material matrix. The baseline matrix, in every case, is created such that at least the axial stiffness elements of the original and the modified cross sections of the rib are in agreement with each other. Finally, the effects of factors on the responses are seen and varied using the prediction profiler shown in Fig. 8.8. From the analysis, the following observations are drawn before choosing appropriate factor matrix:

1. It is not possible to change the torsional stiffness S_{44} without affecting the shear moduli S_{22} and S_{33}.

2. Given a problem in which matching the torsional stiffness is necessary, and shear stiffness does not play a significant role, the torsional stiffness can be matched by varying $KF(2,2)$ and $KF(3,3)$.

3. It is possible to match axial stiffness S_{11}, torsional stiffness S_{44} and bending stiffness S_{55} simultaneously.

4. It is possible to match torsional stiffness S_{44} and bending stiffness S_{66}, but at the cost of a mismatch in axial stiffness S_{11}.

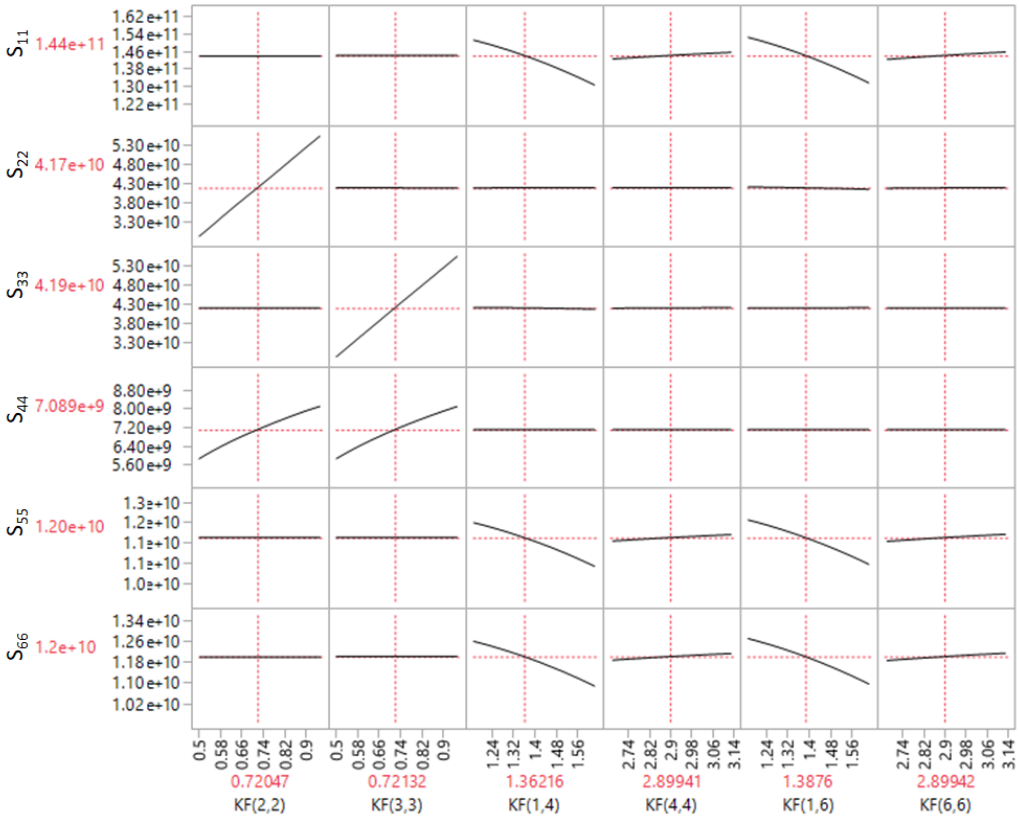

Figure 8.8: Prediction profiler for approach 2

8.4.4 Approach 3: Stiffener's Properties Accounted in Adjacent Material of Reduced Size

In this approach, the stiffener is scaled down, while preserving its aspect ratio, to a point where the width of the stiffener is equal to the width of the rib. The original section is

shown in Fig. 8.9a. The equivalent section shown in Fig. 8.9b has three portions: the scaled down middle portion that has anisotropic material while the top and bottom portions have isotropic properties of the original section. As in previous sections, we start with a

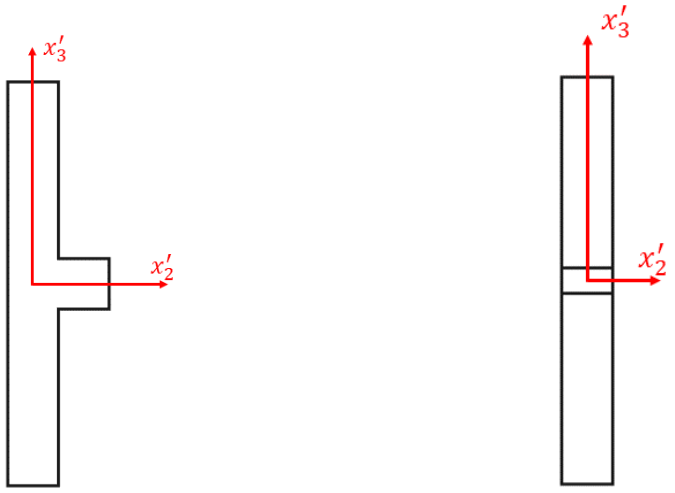

(a) Original section (b) Equivalent section

Figure 8.9: Cross sections used in the analysis for scaling approach

suitable baseline matrix and a DoE is generated. The effects of factors on the responses are seen and varied using the prediction profiler shown in Fig. 8.10. The trends in this approach are similar to those in approach 2. Some of the unique observations, influencing the choice of factor matrix, are:

1. KF(3,3) has a far larger influence on S_{44} than KF(2,2).
2. KF(1,4) has the largest influence on S_{55}, whereas in approach 2, KF(1,6) had the largest influence.
3. KF(1,6) has the largest influence on S_{66}, whereas in approach 2, KF(1,4) had the largest influence.

The above observations stem from scaling down the size of the stiffener such that the width of the stiffener is equal to the width of the rib, whereas in approach 2, the shape of the stiffener was changed.

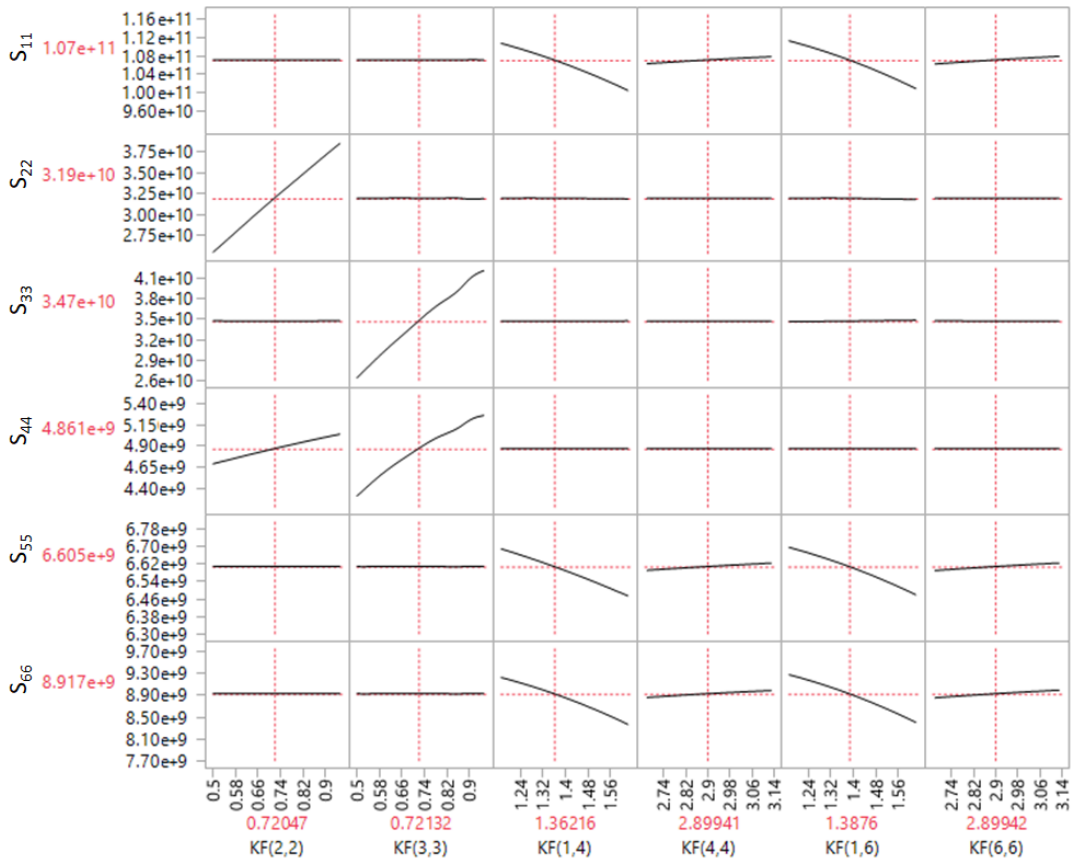

Figure 8.10: Prediction profiler for scaling approach

From the studies carried out in Section 8.4, we obtain factor matrices for various stiffness matching approaches where a specific set of elements from the stiffness matrix are matched. These factor matrices can be appropriately chosen based on the direction of loading on the equivalent section and the expectations from the aperiodic 3-D geometry under consideration. This process can be carried out in the background and the user does not need to get involved with the process of constructing an equivalent section and choosing an appropriate factor matrix to carry out the analysis.

8.5 Validation Study

As mentioned earlier, the present work splits the analysis in two parts: a 2-D cross-sectional analysis and a 1-D beam analysis. As the component being analyzed is complex such that discontinuities and multiple cross sections are present along the span of the beam, there

is a need to perform the cross-sectional analysis multiple times and finally obtain stiffness matrices/elastic constants associated with each of the cross sections identified in the beam geometry using VABS, whether modified using approach presented in section 8.4 or not. When elastic constants for all the required cross sections are obtained, this information is entered to the 1-D beam analysis, performed using GEBT [186]. Through this analysis, the displacement and rotations are obtained at points along the span of the beam. The number of points where these results are obtained depends on the number and types of beam elements defined for analysis through GEBT.

The present approach is verified against a commercially available finite element tool, namely ABAQUS CAE. The purpose of conducting FEA is to verify the equivalent model generated in Section 8.4 for the structure under consideration. Computer Aided Engineering through the means of FEM has proved to be an accurate and reliable numerical scheme in the field of aircraft design and optimization. The 3-D FEM models set up for verification are discussed in subsequent sub-sections. It is important to note that the problem considered in this work can be solved using VABS for 2-D and GEBT for 1-D without resorting to any of the approaches described in section 8.4. The stiffener considered in this problem spans the entire width in the cross section and hence can be modeled as a part of the entire cross section of its own in VABS and GEBT. Figure 8.11a represents a schematic of the 1-D beam formulation with seven members (two key points at each end), three different types of cross-sections, as shown in Fig. 8.11b, along the span based on the design of stiffeners in the original problem. If, on the other hand, the stiffener does not span the cross section,

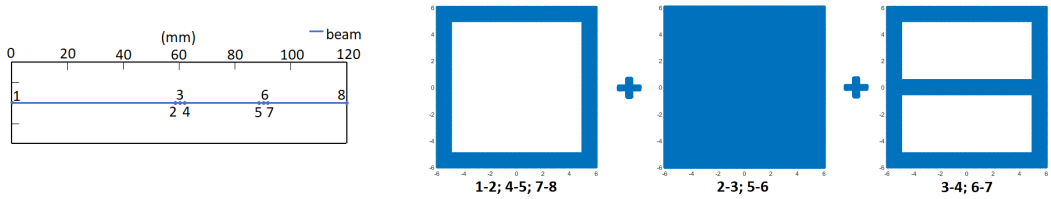

(a) 1-D beam analysis (b) Identified cross-sections for VAM based analysis

Figure 8.11: Schematics for analysis of the box-beam with ribs and stiffeners using VABS and GEBT

it would not be possible to model this directly in VABS. The approaches of section 8.4 are important to be studied so that a strong foundation is created for understanding the behavior of even more complex structures. Hence, all the approaches considered in the present work are compared against results obtained from FEM as well as from these powerful tools without using any of the smearing approaches mentioned above.

8.5.1 Geometry

For the purpose of verification and detailed studies, 3-D FEA was carried out on a simplistic model of the chosen box-beam as shown in Fig. 8.2a with 12 mm $\times$12 mm cross-sectional dimensions, equipped with two 1 mm thick ribs each of which is with a 1mm thick stiffener, along the 120 mm span at $0.5\times L$ and at $0.75\times L$, in order to understand the effects of stiffeners in the design as well as verify the accuracy of the present formulation to capture the presence of a stiffener under various types of loading. Once the CAD model was developed and coupled with ABAQUS, various features were set up in order to conduct the analyses appropriately. The material currently employed is aluminum having Young's Modulus of 70 GPa, Poisson's ratio of 0.327 and density of 2700 kg/m^3.

8.5.2 Mesh for 3-D FEA

Considering, the time required for computation, linear tetrahedron elements were considered. Furthermore, identification of critical elements was done to include mesh optimization and use parabolic tetrahedron elements to improve accuracy. These elements can be used without compromising the accuracy since the material range used is linearly elastic [143].

8.5.3 Boundary Conditions

The aim of this research topic has been to investigate a wing-like structure. Hence, the boundary conditions applied align with this aim. In the Finite Element (FE) formulation,

the box-beam was given a fixed (ENCASTRE) boundary condition on one end face in order to restrict all its displacements and rotations at the root. The other end was left free from any geometric boundary conditions. As far as the 1-D beam analysis using the present formulation is concerned, cantilever boundary conditions are used such that average displacements and rotations at the root of the beam are zero. This definition of cantilever boundary condition is different from the ENCASTRE condition used in ABAQUS, Hence, this may introduce slight differences between the two results.

8.5.4 Applications of Loads in FE Modal

In order to avoid stress concentrations in the FE model that are caused by application of concentrated loads, a rigid body tie constraint was used at the end where loads need to be applied. A reference point was created at the centroid of the free end. This reference point was then tied to the entire face using a rigid-body constraint as shown in Fig. 8.12b in order to apply the load appropriately on the free face. For the beam formulation using the approach discussed in this work, the load is applied at the free end of the beam. The concentrated load served as a transverse load on the beam. The magnitude used for the transverse load is 1000 kN. Representative results for a sample transverse loading case are shown in Fig. 8.12a.

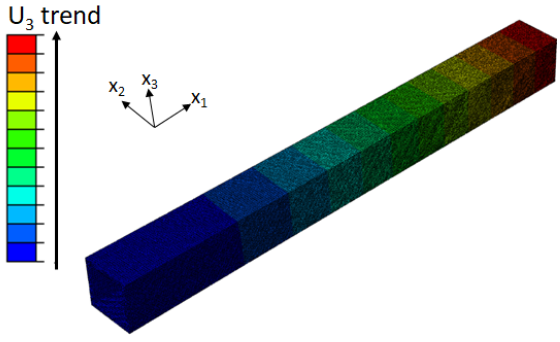

(a) Displacement (Y) contours under transverse loading

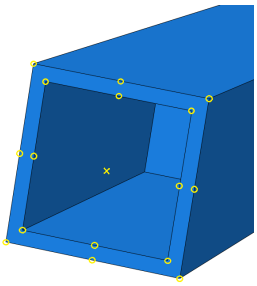

(b) Rigid body tie

Figure 8.12: Schematics from 3-D FEM using ABAQUS

8.6 Results

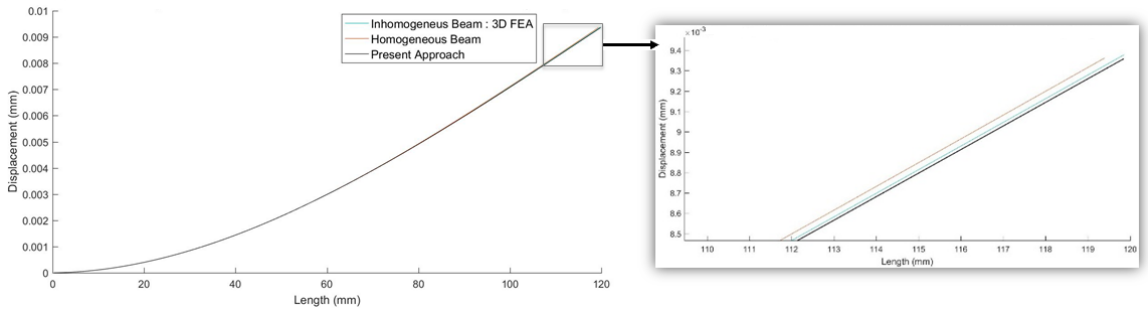

Figure 8.13: Transverse displacement along the span of the beam under shear force at the tip

According to the modeling details provided in Section 8.5, results for transverse displacement of a box-beam under various conditions are presented in Fig. 8.13 under a tip shear force (F_3). The 3D FEA results for the original beam are represented as Inhomogeneous Beam: 3D FEA, whereas the homogeneous beam represents results for the beam with stiffeners not considered. This is done to show that the stiffener significantly contributes to the bending stiffness. Finally, results from the present approach outlined in Section 8.4.3 matching S_{11}, S_{22}, S_{44} and S_{55} are plotted alongside. A zoomed view of the overlapping

Table 8.3: Transverse tip displacement under concentrated shear force at the free end

Approach	Matched Elements (S)	Tip Displacement ($\times 10^{-2}$ m)	% Difference (VABS+GEBT)	% Difference (3-D FEM)
VABS + GEBT	–	9.395110	–	0.334766
Approach 2	$S_{11}\ S_{22}\ S_{44}\ S_{55}$	9.395150	0.000466	0.335234
Approach 3	$S_{11}\ S_{22}\ S_{33}\ S_{66}$	9.395150	0.000490	0.335257
Approach 3	$S_{11}\ S_{22}\ S_{33}\ S_{55}$	9.395150	0.000490	0.335257
Approach 3	$S_{11}\ S_{22}\ S_{44}\ S_{55}$	9.395180	0.000781	0.335550
Approach 2	$S_{11}\ S_{22}\ S_{44}\ S_{66}$	9.395180	0.000782	0.335551
Approach 3	$S_{11}\ S_{22}\ S_{33}\ S_{55}$	9.395210	0.001077	0.335847
Approach 2	$S_{22}\ S_{44}\ S_{66}$	9.394930	0.001881	0.332879
Approach 1	$S_{11}\ S_{22}\ S_{44}\ S_{55}$	9.395370	0.002807	0.337582
Approach 1	$S_{11}\ S_{22}\ S_{33}\ S_{55}$	9.391800	0.035200	0.299448
Approach 1	$S_{11}\ S_{22}\ S_{44}\ S_{66}$	9.374040	0.224203	0.109813
3-D FEM	–	9.363760	0.403276	–

plots is shown on the right to show that the present approach is able to capture the effect coming due to the use of stiffeners. Values of the tip displacement (u_3) obtained using various approaches mentioned in Section 8.5, the tools VABS and GEBT and finally 3-D FEM are tabulated in Table 8.3. Along with the tip displacement values, percentage errors against the results obtained from VABS and GEBT and from 3-D FEM are presented. It can be seen that there are multiple approaches present in the table that are capable of closely matching the elements of the stiffness matrices. On pursuing a comparative study, a few inferences, listed below, can be drawn:

1. The approaches where the maximum number of intermediate stiffness elements are matched during the stiffness matching process, is actually the approach with displacement results having the least percentage error when compared against the values of VABS and GEBT as shown in Table 8.3.

2. The values obtained from VABS and GEBT possess an error of approximately 0.33% when compared with 3-D FEM. It is expected that the case solved with stiffness matching procedure would also yield results with a similar error. The error is not very high, but other approaches present displacement results that are much closer to those obtained from 3-D FEM with the percentage error as low as 0.1%.

3. It is necessary to know the best approach from the ones presented in this work. In the current example, approach 1 is a more accurate approach as far as comparison against 3-D FEM results is concerned. However, the error can be erratic for different designs or conditions. Also, the 3-D stress recovery where the stiffener would not offer useful information. Unlike approach 1, the other two approaches offer more useful information related to 3-D stress recovery as the change in material properties remain localized, so the stress recovery using current methodology would be correct except in the near vicinity of stiffener. In approach 1, the recovery would yield incorrect results for the entire cross section.

4. The section considered in this problem related to box-beams possesses symmetry about both cross-sectional axes. Hence, only the transverse displacement is considered under a tip shear force, as that would be the dominant mode of deformation. However, in more generic or complex cases where there is no axis of symmetry and the coupling terms offer modes of deformation comparable to the dominant modes under a given loading, all the other important loading conditions and displacement parameters can be considered at once to identify which approach is the best when multiple loading conditions are required to be considered.

To strengthen the claims for the use of approach 2 and 3 mentioned in Sections 8.4.3 and 8.4.4, respectively, there is another problem as shown in Fig. 8.14 with cross-sectional view shown in Fig. 8.15 such that the stiffeners are placed along the length. Here, a stiffened panel with stiffeners of the same size is considered, but where the stiffeners are not equally spaced. The entire panel is cantilevered such that the cross section at the root is fixed. The unequal spacing renders use of the smearing approach [39] used in plate theory ineffective. When the stiffened panel is treated with approach 2, the new cross section for the panel is

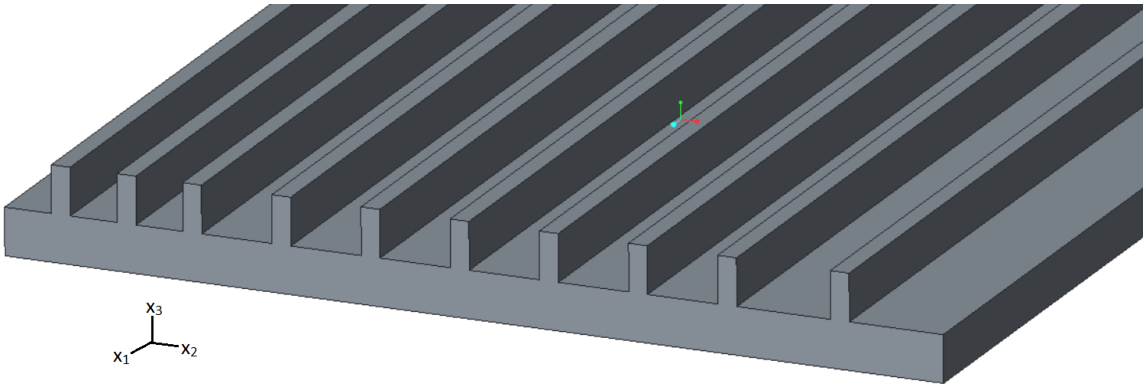

Figure 8.14: Stiffened Panel

shown in Fig. 8.16 and the factor matrices evaluated in section 8.4.3 can be used directly. However, the factor matrices developed in approach 1 explained in section 8.4.2 cannot be used directly, as the number of stiffeners, their position and dimension affect the cross-sectional properties of the entire panel. This is because approach 1 smears the properties of

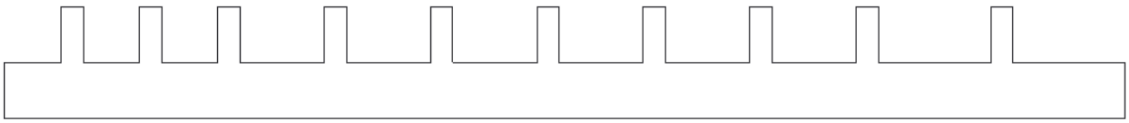

Figure 8.15: Stiffened Panel: Cross-Sectional View

Figure 8.16: Stiffened panel treated with approach 2

the stiffener uniformly on the entire panel, so a factor matrix developed using approach 1 is valid for a specific case. For example, we performed stiffness matching with the objective to minimize the error between the axial stiffness and in-plane bending stiffness about x_3 (i.e., S_{11} and S_{66}, respectively). For this purpose, we used predetermined factor matrices corresponding to approaches 1 and 2 for matching the desired stiffness values, and the values obtained are mentioned in Table 8.4. It is observed that use of the factor matrix from approach 1 leads to an error of approximately 16% as compared to the use of the factor matrix from approach 2, which leads to a maximum error of 0.001%. It is evident that approach 1 cannot be generalized to solve different problems, whereas a correct set of information can directly lead to excellent results using approach 2 without any computational expense. For approach 1, a fresh DoE analysis is required to be executed each time to evaluate a new factor matrix suitable for the analysis, but it would not be as efficient as approach 2, where it needs to be done only once. Through this work, a ribbed beam with stiffeners of the design as explained in the current example, can be analyzed using beam theories, which was not possible until now.

Table 8.4: Comparison of stiffness values using present work with the exact values

Stiffness	Stiffened Panel	Approach 1	Error	Approach 2	Error
S_{11}	$4.199992E+11$	$3.500606E+11$	16.65%	$4.199999E+11$	0.00016%
S_{66}	$3.432744E+12$	$2.917156E+12$	15%	$3.432712E+12$	0.001%

CHAPTER IX

CONCLUSIONS AND FUTURE WORK

Through the present work, significant advancements have been made to the overall framework of structural analysis laid out by Hodges [69]. The framework employs the Variational Asymptotic Method (VAM) and the geometrically exact beam theory. The tool for sectional analysis based on the VAM is named as VABS while the tool to perform the 1-D beam analysis is referred to as GEBT. In this work, the advancements are made to the cross-sectional analysis and the stress-strain recovery which are part of the sectional analysis done in VABS. Capabilities of the 1-D beam analysis done using GEBT are also enhanced. Further, this thesis aims to find applications of the developed framework to solve important problems in the field of aerospace engineering and beyond. The reason to pursue this development or extensive use of the developed framework is the saving in computational costs and time, while retaining the accuracy that the best commercially available tools based on 3-D FEM can provide.

Through this work, an important issue in VABS has been addressed, where analysis of thin-walled beams with reasonably large initial twist and curvatures resulted in negative diagonal elements of the stiffness matrix. A detailed investigation in which variables such as initial curvature, thickness-to-width ratio and ratio of Young's modulus in two different directions demonstrate that an interaction of all these variables/small parameters are a reason for the appearance of non-physical effects. Another key conclusion from the investigation

is that the perturbation solution is wrong. In an attempt to tackle the initial curvature or the thickness-to-width ratio, the methodologies obtained do not result in a solution which can treat arbitrary cross-sections. It is found that the best way to solve the problem of negative stiffness values is to perform a correct order of magnitude analysis considering the ratio of Young's modulus in different directions as a small parameter, a priori. The methodology results in correct set of results without any non-physical effects as demonstrated in Sec. 4.3.3. As part of the next steps, it would be important to obtain general expressions for the formulation of sectional analysis, Sec. 2.3, and implement in VABS. Besides, solving the nonlinear exact transformation equations using newton's method for a correct solution of the generalized Timoshenko stiffness matrix may have significant benefits over the perturbation solution that is currently being used.

9.1 2-D Sectional Analysis using VAM

Through this work, a broadened use and verification of the already existing tool Variational Asymptotic Beam Sectional analysis (VABS), is presented for thin-walled beams especially thin-walled structures with asymmetry and open sections. Note that, for thin-walled open section beams, there exists another capability in VABS to model using Generalized Vlasov (GV) theory which provides a 5×5 stiffness matrix as opposed to a 6×6 stiffness matrix obtained from the Generalized Timoshenko (GT) model. Efforts are underway to identify problems where both the shear deformation effects and Vlasov effects are sufficiently important to need both shear deformation and warping restraint effects in a single model. The cases presented did not involve torsional loads so a GT model was used to obtain shear stress variations in the cross section of the Z-section thin-walled beam.

Results in Section 3.2 show that the thin-walled beam theory is asymptotically correct, but it is limited to modeling beams with thin-walled sections as combinations of lines or curves, as opposed to areas in VABS. Obtaining asymptotically correct solutions with variations in the cross section along with a capability to model beams made up of composite

materials easily and efficiently as compared to 3-D FEM, and provides a reason to use VABS over any other simulation tool for engineering applications.

Through this work, an important issue in VABS has been addressed, where analysis of thin-walled beams with reasonably large initial twist and curvatures resulted in negative diagonal elements of the stiffness matrix. A detailed investigation in which variables such as initial curvature, thickness-to-width ratio and ratio of Young's modulus in two different directions demonstrate that an interaction of all these variables/small parameters are a reason for the appearance of non-physical effects. Another key conclusion from the investigation is that the perturbation solution is wrong. In an attempt to tackle the initial curvature or the thickness-to-width ratio, the methodologies obtained do not result in a solution which can treat arbitrary cross-sections. It is found that the best way to solve the problem of negative stiffness values is to perform a correct order of magnitude analysis considering the ratio of Young's modulus in different directions as a small parameter, a priori. The methodology results in correct set of results without any non-physical effects as demonstrated in Sec. 4.3.3. As part of the next steps, it would be important to obtain general expressions for the formulation of sectional analysis, Sec. 2.3, and implement in VABS.

9.2 Nonlinear 1-D Beam Analysis

9.2.1 Structural Damping

An implementation of a 3-D damping formulation by decomposing the rotation tensor to split the problem into 2-D and 1-D parts is presented. The resulting analysis requires modifications of both the 2-D cross-sectional analysis as well as 1-D geometrically exact beam theory. This work presents comprehensive details of the modified mathematical procedure behind the aforementioned analyses, and how the constitutive equations are modified to consider 3-D structural damping behavior of a beam. This work is a successful attempt to include a Kelvin-Voigt model in the constitutive law which enters the mixed formulation of the 1-D beam analysis to obtain damped frequencies and damped dynamic behavior. To

verify the accuracy of current implementation, the results are obtained from the developed methodology and compared against commercially available finite element tools. Moreover, to implement any damping model, coefficients associated with the damping are required. Most texts and prior research offer material damping constants and directly use them in a beam's governing differential equation in the form of either a viscous damping term or proportional damping terms. These values are then generally determined experimentally. The finite element tools are also designed to take a proportional damping coefficient. In reality, however, different modes of beam vibrations may have different damping coefficients which may not be proportional to stiffness or mass matrices.

Through this work, a methodology is provided to obtain these 3-D damping coefficients and modify the cross-sectional constitutive law instead of requiring the user to input these coefficients. Sometimes, these coefficients are very hard to obtain due to the associated experimental complexities. As part of the proposed future work, a suitable molecular dynamics approach can be applied to prove the need for a 3-D damping matrix as opposed to a proportionality damping coefficient and consider obtaining the material damping coefficient or the 3-D damping coefficients directly from the simulation.

9.2.2 Initially Curved and Twisted Smart Beams

This work analyzes smart beams, which have electroded surfaces parallel to the reference axis. It incorporates the modified constitutive equations into the intrinsic equations to formulate a set of linear solutions applicable for both the actuator and sensor application of piezo-composite cantilevered beams when subjected to different loading conditions. Displacements and rotations are obtained for prismatic smart beams as well as initially curved and twisted smart beams. Each of the cases is analyzed separately as an actuator and as a sensor. VABS software is used to obtain the cross-sectional constants which are used as inputs. Various examples are discussed, and the results obtained from modified linear equations are compared with earlier works [144, 149] and the 3-D FEM analysis done in

ABAQUS CAE. Excellent agreement has been found between the present theory and the 3-D FEM even for the smart beams with curvatures and coupled loads. These equations are capable of handling arbitrary cross-sectional geometry and material of smart piezoelectric beams under arbitrary actuation voltages and sensing loads to perform quick and efficient analysis.

9.3 Time Histories of Recovered 3-D Variables

This work demonstrates the capability of VABS and GEBT to obtain the 3-D stress-strain histories for composite beams undergoing dynamic loading in a nonlinear transient structural analysis. The macros and scripts have been developed to automate the process of recovery. In the present work, isotropic and composite cantilever beams have been used to demonstrate the results that eventually have been compared with results obtained from commercially available FEA tools such as ANSYS. It is observed that the use of VABS and GEBT for the transient structural analysis is significantly advantageous over 3-D FEM. The time required for such an analysis greatly reduces from the order of multiple hours to a few minutes just for an isotropic beam. Due to the extremely fast computations associated with VABS and GEBT, coupled with the higher fidelity of recovery relations and the ability with which complex cross-sections are handled, results obtained for the 3-D stress, strain and displacement variables are accurate, fast and require far less storage when compared to ANSYS. Because, the present work is currently in its infancy, the results for the complex composite geometry in this work need to be verified against the results from 3-D FEM. Further, this work needs to be tested on real-life components such as rotor blades. Also, more sophisticated macros and scripts need to be developed to associate the entire framework with the preprocessor PreVABS or bring under one user-friendly and practical package for industry use.

9.4 Aperiodic and Inhomogeneous Beam-Like Structures

Through this work, a unique dimensional reduction technique is presented to analyze aperiodic and inhomogeneous structures, especially those structures where there are abrupt changes in material properties or geometrical characteristics along the length. It is known that use of commercially available Finite Element codes to analyze structures is cumbersome and computationally expensive, while VABS and GEBT are proven to solve problems with even greater complexity involving composite materials in a very small fraction of the time taken by a 3-D FE solver. This competitive advantage brings in a lot of versatility in design methodology for structural members or components. Designers working on critical components with harmful failure modes, even now, resort to simple analyses based on crude approximations and inaccurate results during the preliminary design phase. Currently, to obtain accuracy, structural analysis through FE tools is performed only in the detailed design phase, which takes a large fraction of time from the overall product development time. The rotorcraft industry is slowly moving towards use of high fidelity and reliable tools such as VABS and GEBT, based on a rigorous beam theory formulation for analysis of critical components such as rotor blades. Because of complex structural designs along the span of other beam-like structures, tools based on beam theory previously could not fulfill that need.

To overcome the problem, local smearing is carried out only for those parts/components in the entire structure that cannot be modeled using a beam theory approach, including such structural members as stiffeners on the rib of an aircraft wing. The material properties of the rib have now been altered locally, where stiffeners were present. This technique allows simplification of complex beam-like problems in multiple steps, until the optimal level of complexity is achieved in which tools based on beam theory can be used to quickly solve problems. The benefit of this technique over standard smearing practices followed for analyzing complex structures is that during stress recovery, the present technique would

be able to obtain 3-D stress resultants far more accurately, because stress recovery using other smearing approaches might result in high stresses where there is actually a stiffener present in the structure. The design framework developed to automate the process of finding suitable material properties for appropriate local smearing is also fast, owing to the use of similar tools to compare material properties of the original section to the equivalent section generated. It is also important to note that unless the shape of the two cross sections is similar to each other, all the stiffness components of equivalent section will never match simultaneously to the stiffness components of the original section, no matter how much anisotropy is introduced in the equivalent beam section. We navigate through this challenge by generating multiple instances where different elastic constants of the equivalent stiffness matrix are in agreement with its original counterpart and then incorporate those cases in the formulation to obtain final desired result. The methodology behind the case which offers the best agreement in final results is suggested to be used for stiffness matching purposes for complex problems.

This technique can significantly improve the current preliminary design phase as well as can significantly reduce the time spent in detailed design phase while maintaining desired accuracy for the reasons mentioned above. As part of the future work, the authors plan to develop an automated working code based on the presented technique which would automatically choose a smearing technique based on the type of structure being analyzed using the design methodologies presented. Furthermore, there is a plan to implement this technique to solve a complex aircraft wing section under dynamic loading, compare results against commercially available FE tools and quantify benefits against those tools and current approximate smearing practices.

9.5 Unified GT-GV Model

The current Vlasov (GV) and Timoshenko (GT) models in VABS are separately done. While the GT model offers a 6×6 stiffness matrix for beam with arbitrary cross sections,

the GV theory yields a 5×5 stiffness matrix for thin-walled beams with open sections. It is already established that the GV theory is not valid for beams with closed-sections [69]. A single unified theory not only would be convenient but would also cater to the transverse shear deformation in thin-walled beams. Initial efforts to unify the GT and GV models were put forward by Volovoi et al. [167], who showed a decoupling only for the isotropic, prismatic case. An issue identified was the assignment of terms which contribute both to GT and GV theories. Further ambiguities which need to be addressed include the process of integration by parts before the GT transformation and definition of the Vlasov 1D variable. While integration by parts is used to remove the x_1 derivatives of warping, Ref. [184] discovered that integration by parts of the final second-order asymptotically correct strain energy results in negative shear stiffness. Such an ambiguity clearly does not exist for plates and shells [183].

An effort to study the boundary layer effects using the dispersion curves [166] did not prove to be helpful mainly because the development of characteristic equations for dispersion analysis do not consider boundary conditions. The dispersion curves assume that the beam is of infinite length.

Rajagopal [138] explains that Wempner [177] uses a warping variable $\alpha(x_1)$ not directly connected to torsion. The warping solution procedure in VABS is handicapped by the fact that it can only pick up the warping as cross-sectional variations of 1D variables that already exist in the problem. Therefore, the fundamental challenge is to revisit the beam kinematics and accommodate an α-like variable. Unlike Ref. [177], the VAM procedure never assumes warping to be of any specific form but rather solves for it using an asymptotic method. Studies in this direction are promising given the utility of such a theory. The final stiffness matrix will be an 8×8 array from which the GT and GV model can be obtained.

9.6 Modeling Triboelectric Effect using VAM for Triboelectric Nanogenerators

The last decade saw significant research efforts towards building low power electronics [81, 113, 131, 158, 160]. In addition to better power management strategies, there has been a recent push to make embedded devices thin and flexible [118, 179]. To achieve this overreaching vision of self–sustainable flexible electronics, materials science, structural mechanics and microelectronics communities have been working on new device designs for sensing [151, 127], computing [125], feedback [192], energy harvesting [135] and storage [80, 61] which leverage new materials, nano-structures, and printing technologies. The Ubiquitous Computing (UbiComp) research community has often sought ways to make these technological innovations more practical, reliable and easy to use for various applications [77, 79].

A new breed of self-powered sensors based on the triboelectric effect work exactly on this concept, and one recent example is the Triboelectric Nanogenerator (TENG) [172, 173, 175]. The design of these sensors is based on the principles of triboelectrification (or contact electrification) and electrostatic induction and convert any kind of mechanical energy to a highly correlated electrical response. With their lightweight, low-cost, and high efficiency even at low frequency, TENGs have been shown as passive or self-powered sensors for detecting mechanical motion such as pressure [104, 182], touch [62, 43], vibrations [35, 180], linear displacement [191, 106], speed [181], rotation [103], and acceleration [190].

Significant efforts have already been made towards the applications of mechanical devices based on triboelectric effect in building microphones. Microphones convert mechanical vibrations induced by speech into electrical signals. Because of reduced costs and increased availability, microphones are being used in variety of sensing applications. These include occupancy detection [56, 90], control [102, 129, 156], human behavior studies [38], structural maintenance [53], health monitoring [93, 176], hearing aids [40], activity recognition [92, 123, 164, 193] and sound source localization [134, 162]. For all these

applications and research being done, the objective always is to develop compact and self-powered devices.

However, commercially available passive (or self-powered) microphones either consume power, are bulky (e.g., a moving coil dynamic microphone [48]) or use Polyvinylidene Fluoride (PVDF) films. This results in either a low sensitivity contact microphone [117, 5] or complex to manufacture and costly to scale in size [82, 152]. The challenge lies in designing a microphone which is passive and has sound quality comparable to its active counterparts while still preserving a lightweight and versatile form factor [101]. Recent advances in materials science have demonstrated the possibility of such self-powered, easy-to-manufacture sensors that take advantage of the triboelectric effect to convert mechanical vibrations into electrical energy [10, 173, 175].

This section explains the design, fabrication and working of TENG based microphones that is made up of a thin and inexpensive PTFE/paper/copper layers and is derived from Ref. [10] as Self-powered Audio Triboelectric Ultra-thin Rollable Nanogenerator (SATURN) microphone, shown in Fig. 9.1. Finally, it establishes a need for the present formulation to incorporate triboelectric effect in the cross-sectional and the 1-D analysis. Based on the form factor of the sensor, a beam theory formulation or a plate theory formulation can be considered for modeling TENG using the variational asymptotic method. Recent work by Kovvali [86] to include the drilling degrees of freedom may come handy while analyzing TENG in a plate-like formulation depending on the working mechanism for a given application.

9.6.1 Theory of operation : Triboelectricity

The operation of the SATURN microphone is based on the principle of two, coupled phenomena–electrostatic induction and contact electrification. Electrostatic induction is the generation of opposite charges on two different materials, while contact electrification or triboelectrification, is charge transfer between two surfaces in contact. The fundamental

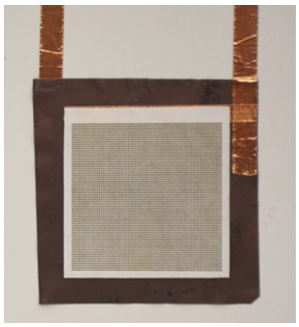

Figure 9.1: TENG based microphone: Close-up of the device

theory of triboelectrification lies in Maxwell's displacement current and change in surface polarization [174]. By introducing a thin conducting electrification layer, the charge difference between the two polarized surfaces generated due to triboelectricity can be measured. This combined structure is called the triboelectric nanogenerator (TENG). The polarity and strength of the charges produced are dependent on many material variables such as surface roughness, temperature, and dielectric constant.

9.6.2 Device Construction

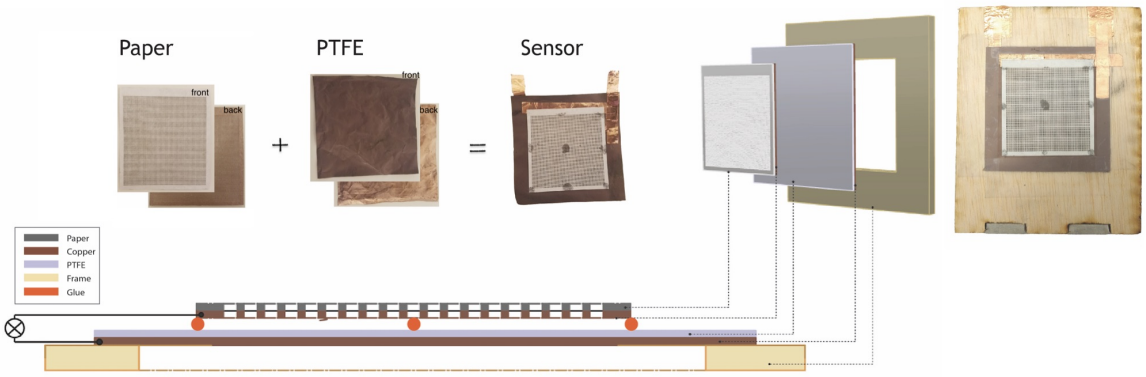

Figure 9.2: Structural design of SATURN Microphone consisting of copper coated paper and PTFE

The multi-layered device structure of the SATURN microphone is schematically depicted in Figure 9.2. It consists of a thin film of dielectric polytetrafluoroethylene (PTFE), which has a permanent negative charge stored on its surface, sandwiched between two

copper layers. These copper layers act as electrification layers that generate triboelectric charges upon coming in contact with PTFE. The first layer of the copper is laminated on the PTFE itself (bottom layer) while the other is deposited on paper (top layer). The paper in the SATURN microphone structure is neutral and used only for structural support for the copper electrification layer which comes in contact with PTFE due to vibration. To minimize the air friction which dampens the vibrations, holes have been introduced on the paper to act as a mini-resonant cavity for air when sound propagates, resulting in enhancement of the vibration effect. Paper is used because of its flexibility, lightweight structure, low cost, and ease of cutting holes.

9.6.3 Working Mechanism

The SATURN microphone works on the principle of vibration-induced contact and charge generation due to triboelectrification and electrostatic induction. This process is explained in detail in Fig. 9.3. Propagation of the sound through air causes compression and rarefaction corresponding to the frequencies present in it. When a compression is incident on the SATURN microphone it causes vibrations in its membrane-like structure, resulting in the copper layer on the paper coming in contact with the PTFE (Fig. 9.3a). Contact electrification generates charges on both surfaces. PTFE layer has a greater electron affinity, thus, it is able to gain electrons from the copper [22] and becomes negatively charged, whereas the copper layer on the paper becomes positively charged. When subsequent rarefaction separates the paper and the PTFE (Fig. 9.3b), it induces a potential difference across the two copper electrodes, causing current to flow from the paper towards the PTFE if the device is connected to an external load. This flow of current reverses the polarity (Fig. 9.3c) of charges on the two copper electrodes (i.e., now the copper on PTFE has more positive charge than the copper layer on the paper). The next compression results in the paper moving towards the PTFE again, resulting in a reversed direction of current flow (Fig. 9.3d), completing the cycle of electricity generation.

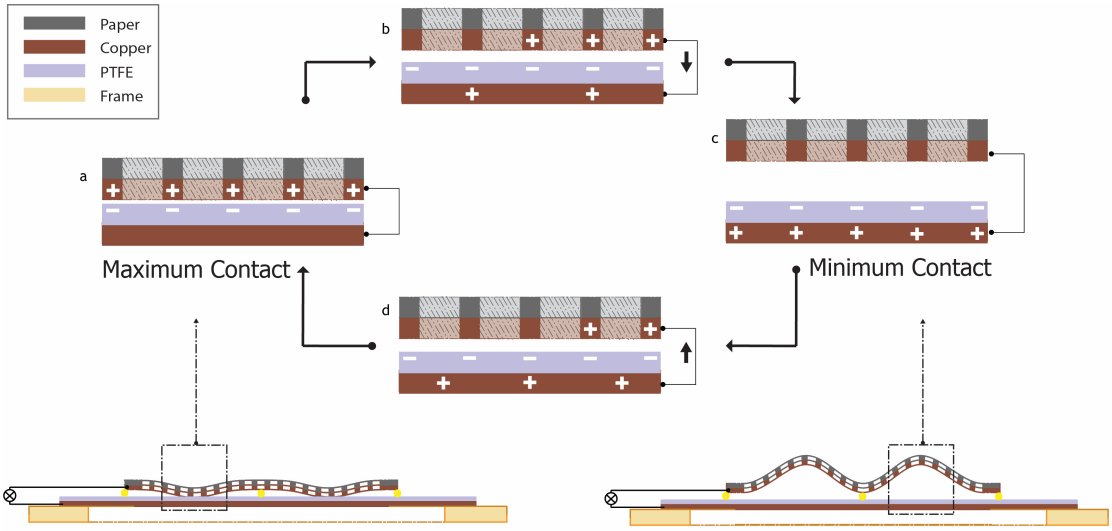

Figure 9.3: Cycle of electricity generation process under external acoustic excitation

9.6.4 Detailed Structural Analysis for Design and Optimization

Several design parameters impact the performance of the SATURN microphone, specifically the geometric characteristics of a SATURN patch, its initial curvature, the size and spacing of holes in the layer made of paper, and the method of attaching the various layers to each other (i.e., the boundary conditions of both PTFE and paper). The main aim of analyzing this structure is to reduce experimentation and optimize design of SATURN microphones so that electrical response across a wide range of frequencies can be increased in order to achieve a better acoustic sensitivity. Besides, in prior research related to TENGs [173, 174], the two layers are assumed to be rigid, which isn't realistic. In those cases, the open circuit potential difference generated by the device as a function of time(t) is given by the equation [124]

$$V_{oc} = \frac{\sigma x(t)}{\epsilon_0} \tag{9.1}$$

where, $x(t)$ is the physical separation distance between the PTFE and paper, σ is the charge density generated on the surface, and ϵ_0 is the relative permittivity of the dielectric. This mathematical model is overly simplified, and would not work for SATURN microphone

because neither the paper nor the PTFE layer are rigid. In practice, the PTFE layer will either be in a simply supported condition or would be completely attached to a surface so it can be considered as rigid. The paper layer, however, behaves more like a flexible membrane.

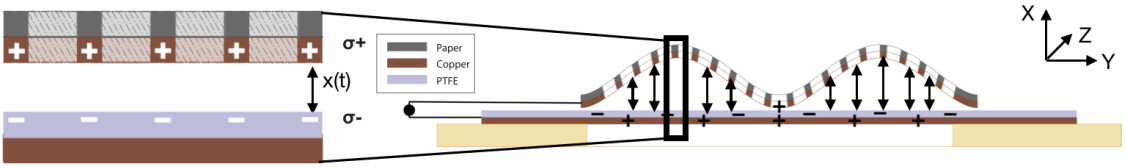

Figure 9.4: Factors effecting potential difference generation : $\sigma_{effective}$ surface charge density and $d_{effective}$ separation distance between the two plates

The separation distance between the paper and PTFE layers changes over time when we assume that the paper layer is vibrating, as shown in Fig. 9.4. When our membrane is placed in the Y-Z plane of a right-handed reference coordinate frame, if we take an infinitesimal element with area $dydz$ at a location $(0, y, z)$ with respect to the origin, then the potential difference across the infinitesimal element is a slight modification of Eq. (9.1) and is given by:

$$V_{oc} = \frac{\sigma_{eff}}{\epsilon_0} x(y, z, t), \tag{9.2}$$

where σ_{eff} is the effective surface charge density, and the separation distance x is a function of y, z and time, which varies along y and z for the flexible membrane. Hence, the open circuit potential difference for a flexible paper layer can be written as:

$$V_{oc} = \frac{\sigma_{eff}}{A\epsilon_0} \iint_A x(y, z, t)\, dy\, dz. \tag{9.3}$$

To increase V_{OC} for the SATURN microphone, one way is to maximize d_{eff} (the effective separation during flexural vibrations) is $1/A \iint_A x(y, z, t)\, dy\, dz$. To facilitate that, a comprehensive optimization tool can be developed where VAM is employed. The readers are informed that these structures appear to be simple plate-like structures and seem to be

analyzed quickly, using 3-D FEM tools. However, there are a lot of issues, viz., large number of holes, small wall-thickness, complex boundary conditions and mesh convergence which force a user to use a fine mesh, leading to long simulations and huge computational costs. Instead, application of VAM for Plates And Shells (VAPAS) can prove to be very efficient in designing and optimizing the TENGs. Besides, analytical closed-form solutions can also be developed for $x(t)$ using VAM which would be the best as far as computational efficiency and accuracy are concerned.

A challenge to perform structural analysis on TENGs is to characterize the physics behind the phenomenon. It is important to develop a physics-based model which relates the mechanical deformation in different layers to the open-circuit voltage developed across the electrodes. To do that, first we would need to relate the energy associated with the triboelectric effect to the mechanical degrees of freedom with the help of accurate material properties. This energy can subsequently be added to the strain energy expression for cross-sectional analysis. Furthermore, this energy can be minimized to obtain a constitutive relationship which has information about the mechanical, electrical as well as the coupled electro-mechanical behavior of the TENGs. A framework based on this approach would prove to be very fruitful in analyzing TENGs and triboelectric effect in a very fast and computationally efficient manner. Moreover, a range of origami structures leveraging TENGs can be developed for various applications as well as solve relevant problems using VAM.

Appendices

APPENDIX A

SOLUTION TO THE NON-PHYSICAL BEHAVIOR

This chapter contains solution to a specific case that was solved after modifying parts of VABS code to accommodate interaction of small parameters including the ratio of material properties in different directions (i.e., E_2/E_1). In Sec. 4.2, it has been demonstrated that the other ratios of material properties do not have any non-physical effect on the values in the stiffness matrix. This particular problem considers an orthotropic strip (1.2×0.06 in.) with out-of-plane initial curvature of 0.08 rad/in. The material properties of the strip are such that Young's Moduli $E_1 = 20.59 \times 10^6$ psi and $E_2 = E_3 = 1 \times 10^5$ psi, bulk modulus, $G_{12} = G_{13} = G_{23} = 8 \times 10^6$ psi, and Poisson's ratio, $\nu_{12} = \nu_{13} = 0.3$ and $\nu_{23} = 0.335$. The analytical procedure provided in this chapter is a demonstration of how the small parameters in both the expressions of 3-D strain and the material matrix need to be considered for an accurate order of magnitude analysis.

For the formulation, the Jaumann-Biot-Cauchy strain tensor can be expressed as

$$\Gamma_{ij} = \frac{1}{2}(\chi_{ij} + \chi_{ji}) - \delta_{ij} \tag{1.1}$$

where δ_{ij} is the Kronecker symbol, and χ_{ij} is the mixed-basis component of the deformation gradient tensor, such that

$$\chi_{ij} = \mathbf{B}_i \cdot \mathbf{G}_k \mathbf{g}^k \cdot \mathbf{b}_j \tag{1.2}$$

with $\mathbf{G}_k$ as the covariant base vectors of the deformed configuration and $\mathbf{g}^k$ as the contravariant base vectors of the undeformed configuration, which are tangent to the coordinate curves. The covariant base vectors of the undeformed configuration can be obtained from beam kinematics as

$$\begin{gathered}\mathbf{g}_1 = \mathbf{b}_1 + x_\alpha \mathbf{b}'_\alpha = (1 - x_2 k_3 + x_3 k_2)\mathbf{b}_1 - k_1 x_3 \mathbf{b}_2 + x_2 k_1 \mathbf{b}_3, \\ \mathbf{g}_\alpha = \mathbf{b}_\alpha\end{gathered} \tag{1.3}$$

where $\alpha = \{2, 3\}$. The contravariant base vectors of the undeformed configuration, which are normal to the coordinate curves are calculated as

$$\mathbf{g}^i = \frac{1}{2\sqrt{g}} e_{ijk}(\mathbf{g}_j \times \mathbf{g}_k) \tag{1.4}$$

where

$$g = \det \begin{bmatrix} \mathbf{g}_1 \cdot \mathbf{g}_1 & \mathbf{g}_1 \cdot \mathbf{g}_2 & \mathbf{g}_1 \cdot \mathbf{g}_3 \\ \mathbf{g}_2 \cdot \mathbf{g}_1 & \mathbf{g}_2 \cdot \mathbf{g}_2 & \mathbf{g}_2 \cdot \mathbf{g}_3 \\ \mathbf{g}_3 \cdot \mathbf{g}_1 & \mathbf{g}_3 \cdot \mathbf{g}_2 & \mathbf{g}_3 \cdot \mathbf{g}_3 \end{bmatrix} = \det(\mathbf{g}_i \cdot \mathbf{g}_j) \tag{1.5}$$

Further evaluation of the expression above yields

$$\sqrt{g} = 1 - x_2 k_3 + x_3 k_2 \tag{1.6}$$

The categorization of the terms in the equation above, is done based on the order of the terms involved. For example, $g_0 = \mathcal{O}(\epsilon^0)$, zeroth order in strain, subsequently, $g_i = \mathcal{O}(\epsilon^i)$, where i is a non-negative integer. The inverse of $\sqrt{g}$ can be expanded using Taylor series

$$\begin{aligned}\frac{1}{\sqrt{g}} =& \frac{1}{1 - x_2 k_3 + x_3 k_2} \\ =& \underbrace{1}_{g_0} + \underbrace{(x_2 k_3 - x_3 k_2)}_{g_1} + \underbrace{(x_2 k_3 - x_3 k_2)^2}_{g_2} + O(k_i^3) \\ =& g_0 + g_1 + g_2 + O(k_i^3)\end{aligned} \tag{1.7}$$

Now, the contravariant base vectors in the undeformed configuration, after substituting the values of intermediate expressions, are obtained as

$$\mathbf{g}^1 = \frac{1}{k_2 x_3 - k_3 x_2 + 1}\mathbf{b}_1 \tag{1.8a}$$

$$\mathbf{g}^2 = \frac{k_1 x_3}{k_2 x_3 - k_3 x_2 + 1}\mathbf{b}_1 + \mathbf{b}_2 \tag{1.8b}$$

$$\mathbf{g}^3 = \frac{-k_1 x_2}{k_2 x_3 - k_3 x_2 + 1}\mathbf{b}_1 + \mathbf{b}_3 \tag{1.8c}$$

Using these expressions and the , the contravariant base vectors in the deformed configuration are calculated as

$$\begin{aligned}\mathbf{G}^1 = &\Big(1 + x_3(\overline{\kappa_2}(x_1) + k_2) - x_2(\overline{\kappa_3}(x_1) + k_3) + \overline{\gamma_{11}}(x_1) + k_2 w_3(x_1, x_2, x_3) \\ &- k_3 w_2(x_1, x_2, x_3) + w_{1,1}(x_1, x_2, x_3)\Big)\mathbf{b}_1 \\ &+ \Big(- x_3(\overline{\kappa_1}(x_1) + k_1) - k_1 w_3(x_1, x_2, x_3) + k_3 w_1(x_1, x_2, x_3) + w_{2,1}(x_1, x_2, x_3)\Big)\mathbf{b}_2 \\ &+ \Big(x_2(\overline{\kappa_1}(x_1) + k_1) + k_1 w_2(x_1, x_2, x_3) - k_2 w_1(x_1, x_2, x_3) + w_{3,1}(x_1, x_2, x_3)\Big)\mathbf{b}_3\end{aligned} \tag{1.9a}$$

$$\mathbf{G}^2 = w_{1,2}(x_1, x_2, x_3)\mathbf{b}_1 + \Big(1 + w_{2,2}(x_1, x_2, x_3)\Big)\mathbf{b}_2 + w_{3,2}(x_1, x_2, x_3)\mathbf{b}_3 \tag{1.9b}$$

$$\mathbf{G}^3 = w_{1,3}(x_1, x_2, x_3)\mathbf{b}_1 + w_{2,3}(x_1, x_2, x_3)\mathbf{b}_2 + \Big(1 + w_{3,3}(x_1, x_2, x_3)\mathbf{b}_3\Big) \tag{1.9c}$$

Finally, substituting the value of $k_1 = 0$ and $k_3 = 0$ (initial out-of-plane curvature only) and using δ to represent the order of magnitudes of different terms such that $\delta = \mathcal{O}(\epsilon)$, then

the expression for 3-D strain is written as

$$\Gamma = \begin{bmatrix} \Gamma_{11} \\ 2\Gamma_{12} \\ 2\Gamma_{13} \\ \Gamma_{22} \\ \Gamma_{23} \\ \Gamma_{33} \end{bmatrix} \tag{1.10}$$

such that

$$\begin{aligned}
\Gamma_{11} &= (\delta^2 k_2^2 x_3^2 - \delta k_2 x_3 + 1)\Big(\overline{\gamma_{11}}(x_1) - x_2\overline{\kappa_3}(x_1) + x_3\overline{\kappa_2}(x_1) \\
&\quad + \delta k_2 w_3(x_1, x_2, x_3) + \delta w_{1,1}(x_1, x_2, x_3)\Big) && \text{(1.11a)} \\
2\Gamma_{12} &= (\delta^2 k_2^2 x_3^2 - \delta k_2 x_3 + 1)\Big(x_3\overline{\kappa_1}(x_1) + w_{1,2}(x_1, x_2, x_3) \\
&\quad + x_3\delta k_2 w_{1,2}(x_1, x_2, x_3) + \delta w_{2,1}(x_1, x_2, x_3)\Big) && \text{(1.11b)} \\
2\Gamma_{13} &= (\delta^2 k_2^2 x_3^2 - \delta k_2 x_3 + 1)\Big(x_2\overline{\kappa_1}(x_1) - k_2\delta w_1(x_1, x_2, x_3) \\
&\quad + (1 + \delta x_3 k_2) w_{1,3}(x_1, x_2, x_3) + \delta w_{3,1}(x_1, x_2, x_3)\Big) && \text{(1.11c)} \\
\Gamma_{22} &= w_{2,2}(x_1, x_2, x_3) && \text{(1.11d)} \\
\Gamma_{23} &= w_{2,3}(x_1, x_2, x_3) + w_{3,1}(x_1, x_2, x_3 && \text{(1.11e)} \\
\Gamma_{33} &= w_{3,3}(x_1, x_2, x_3) && \text{(1.11f)}
\end{aligned}$$

Also, the material matrix for a composite material case can be written as

$$\begin{pmatrix}
\frac{(\nu-1)E_1^2}{2E_2\nu^2+(\nu-1)E_1} & 0 & 0 & -\frac{\nu E_1E_2}{2E_2\nu^2+(\nu-1)E_1} & 0 & -\frac{\nu E_1E_2}{2E_2\nu^2+(\nu-1)E_1} \\
0 & \frac{E_1}{2\nu+2} & 0 & 0 & 0 & 0 \\
0 & 0 & \frac{E_1}{2\nu+2} & 0 & 0 & 0 \\
-\frac{\nu E_1E_2}{2E_2\nu^2+(\nu-1)E_1} & 0 & 0 & \frac{E_2\left(\nu^2E_2-E_1\right)}{2(\nu+1)E_2\nu^2+(\nu^2-1)E_1} & 0 & -\frac{\nu E_2(E_1+\nu E_2)}{2(\nu+1)E_2\nu^2+(\nu^2-1)E_1} \\
0 & 0 & 0 & 0 & \frac{E_1}{2\nu+2} & 0 \\
-\frac{\nu E_1E_2}{2E_2\nu^2+(\nu-1)E_1} & 0 & 0 & -\frac{\nu E_2(E_1+\nu E_2)}{2(\nu+1)E_2\nu^2+(\nu^2-1)E_1} & 0 & \frac{E_2\left(\nu^2E_2-E_1\right)}{2(\nu+1)E_2\nu^2+(\nu^2-1)E_1}
\end{pmatrix}$$

This material matrix considers that E_1 is larger than E_2 by at least 1–2 orders of magnitude, only $\nu_{12}, \nu 13$ and $\nu 23$ are determined by the user, rest all of the Poisson's ratios are internally determined. Besides, the values of Poisson's ratio input by the user are same. Also, $G = E_1/2(1+\nu)$. Clearly some terms in the material matrix do not have the same order of magnitude now as compared to the case when $E_1 = E_2$. So, the strain energy expression

$$\mathcal{U} = \int_0^L \langle\langle \Gamma^T \, D\Gamma \rangle\rangle dx_1 \tag{1.12}$$

can be evaluated by taking into account, the order of magnitude of each terms after the multiplication of measured number of 3-D strains with the elements of the 6×6 material matrix. Further, the variational asymptotic method is carried out as laid out in Sec. 2.3.

APPENDIX B

FORMULATION: ELECTRIC FIELD

By definition,

$$\mathbf{E} = -\nabla\phi \tag{2.1}$$

where the electric field ($\mathbf{E}$) is characterized by the electric potential $\phi(x_1, x_2, x_3)$. The distribution of electric potential is solved such that ϕ is considered to be unknown except for the points where the potential is applied externally, as in case of actuators. It can be represented in the component form as

$$E_i = -\frac{\partial\phi}{\partial x_i}(\mathbf{g}^i \cdot \mathbf{b}^i) \tag{2.2}$$

components of which in $\mathbf{b}_i$ system are

$$\begin{aligned} E_1 &= -\frac{1}{\sqrt{g}}\left[\phi' + \left(x_3\frac{\partial\phi}{\partial x_2} - x_2\frac{\partial\phi}{\partial x_3}\right)k_1\right] \\ E_2 &= -\frac{\partial\phi}{\partial x_2} \qquad E_3 = -\frac{\partial\phi}{\partial x_3} \end{aligned} \tag{2.3}$$

where k_1 is the initial twist of the structure. From [69], $\sqrt{g} = 1 - (x_2k_3 - x_3k_2)$. Use of the binomial expansion will then result in:

$$\frac{1}{\sqrt{g}} = 1 + (x_2k_3 - x_3k_2) + (x_2k_3 - x_3k_2)^2 + O\left(\frac{h^3}{R^3}\right) \tag{2.4}$$

In the present study, smart materials are coated with electrodes which are embedded or present on surfaces parallel to the beam reference line, thus forming equipotential regions with prescribed electric potential. Most applications of smart beams use this kind of electrode arrangement [147].

APPENDIX C

VABS ERRATA

Like any other tool developed in a research environment, VABS also suffers a limitation of restricted access to any user services or help in execution. CdmHub, an online portal for composites resources, information, and networking which hosts VABS and other apps and commercial tools that run in the cloud and are accessible through a web browser. At times, even the resources on cdmhub may not be enough to successfully prepare a VABS input file with or without the help of a preprocessor. There may not be any debugging support to correct the errors in the input file once it is prepared. This document lists down the errors that are commonly generated by VABS in the <inputfilename>.ech file along with a potential solution to the error.

Errors thrown by VABS

1. Error: Cannot open the file "Filename.dat.opt" for reading!:

   Solution: The Flag for recovery in the input file is 1 in the first iteration. It means that the Timoshenko Beam analysis or classical beam analysis hasn't been carried out before the 3-D recovery.

2. Error: Could not read the material properties

   Solution: It means while generating the input file for VABS, there is an element extra in the line after the flags. That has to be removed so that the nmaterial

flag is shifted to its proper position according to the new version.

3. Error: Memory Error

   Solution: The size of the input file is too large to be handled by the cdmHUB VABS version. Use VABS.exe to run the iteration on the system.

4. Error: Singular element in the coefficient matrix

   Solution: If one is using VABS piezo-electric, it means that the dielectric/piezo-electric coefficients for at least one of the materials used are zero. If a zero dielectric coefficient is used, the output stiffness matrices may have NaN as well.

5. Output stiffness matrix has NaN and diagonals as Infinity

   Solution: There could be a problem with the units used in the material properties or the curvature values could be unrealistic.

6. Error: Jacobian is less than 1

   Solution: Means the aspect ratio of the elements formed for the cross-sectional analysis is high. That has to be retained to limits before VABS is executed

7. Error: Using VABS-ANSYS Macro, the element stiffness connectivity may not appear according to the type of element taken, in the generated .dat file.

   Solution: Use SHELL281 for the element to make it 8-noded and follow steps for the quadrilateral element in the macro. Then un-comment the last 5 VGET lines for the zeros to show up as the node numbers.

8. Error: Last box and material data is not coming up in the input file after using VABS-ANSYS macro

   Solution: Not yet resolved but for an isotropic material, it is not difficult to formulate that using column operations of Notepad++ (alt + mouse drag)

9. Error: I/O error : Read material density

   Solution: The flag next to the first old/new flag should be 0 and there should be 3 to 4 blank lines after the syntax at the end of the VABS input file.

10. Error: I/O error: Read global beam displacements or could not open the filename.dat for reading!

    Solution: Could be because of many reasons but mainly because the terminal is looking for files elsewhere. This can be resolved by moving the current directory to the directory containing the files.

11. Error: Material number cannot be zero or negative: element

    Solution: The list of elements with the layup information has missing element rows causing it to be a reduced set as compared to the total number of elements in the mesh.

REFERENCES

[1] M. S. A. Elsayed, R. Sedaghati, and M. Abdo, "Accurate stick model development for static analysis of complex aircraft wing-box structures," *AIAA Journal*, vol. 47, no. 9, pp. 2063–2075, 2009.

[2] S Adhikari, *Structural Dynamic Analysis with Generalised Damping Models: Identification*. John Wiley & Sons, 2013.

[3] S. Adhikari, "Damping modelling using generalized proportional damping," *Journal of Sound and Vibration*, vol. 293, no. 1-2, pp. 156–170, 2006.

[4] S. Adhikari, *Structural dynamic analysis with generalized damping models: analysis*. John Wiley & Sons, 2013.

[5] R. Aimi, "Percussion instruments using realtime convolution: Physical controllers," in *Proceedings of the 7th international conference on New interfaces for musical expression*, ACM, 2007, pp. 154–159.

[6] J. Ajitsaria, S.-Y. Choe, D Shen, and D. Kim, "Modeling and analysis of a bimorph piezoelectric cantilever beam for voltage generation," *Smart Materials and Structures*, vol. 16, no. 2, p. 447, 2007.

[7] B. Akgoz and O. Civalek, "Strain gradient elasticity and modified couple stress models for buckling analysis of axially loaded micro-scaled beams," *International Journal of Engineering Science*, vol. 49, no. 11, pp. 1268 –1280, 2011.

[8] F. Alijani, M. Amabili, P. Balasubramanian, S. Carra, G. Ferrari, and R. Garziera, "Damping for large-amplitude vibrations of plates and curved panels, part 1: Modeling and experiments," *International Journal of Non-Linear Mechanics*, vol. 85, pp. 23–40, 2016.

[9] G. A. Altay and M. C. Dökmeci, "Some comments on the higher order theories of piezoelectric, piezothermoelastic and thermopiezoelectric rods and shells," *International journal of solids and structures*, vol. 40, no. 18, pp. 4699–4706, 2003.

[10] N. Arora, S. L. Zhang, F. Shahmiri, D. Osorio, Y.-C. Wang, M. Gupta, Z. Wang, T. Starner, Z. L. Wang, and G. D. Abowd, "Saturn: A thin and flexible self-powered microphone leveraging triboelectric nanogenerator," *Proc. ACM Interact. Mob. Wearable Ubiquitous Technol.*, vol. 2, no. 2, 60:1–60:28, Jul. 2018.

[11] H. T. Banks and D. J. Inman, "On damping mechanisms in beams," *Journal of Applied Mechanics*, vol. 58, no. 3, pp. 716–723, 1991.

[12] O. A. Bauchau, "Computational schemes for flexible, nonlinear multi-body systems," *Multibody System Dynamics*, vol. 2, no. 2, pp. 169–225, 1998.

[13] O. A. Bauchau and J. I. Craig, *Structural analysis: with applications to aerospace structures*. Springer Science & Business Media, 2009, vol. 163.

[14] O. A. Bauchau and S. Han, "Three-dimensional beam theory for flexible multibody dynamics," *Journal of Computational and Nonlinear Dynamics*, vol. 9, no. 4, p. 041 011, 2014.

[15] V. Berdichevskii, "Variational-asymptotic method of constructing a theory of shells: Pmm vol. 43, no. 4, 1979, pp. 664–687," *Journal of Applied Mathematics and Mechanics*, vol. 43, no. 4, pp. 711–736, 1979.

[16] J. Biggerstaff and J. Kosmatka, "Damping performance of cocured graphite/epoxy composite laminates with embedded damping materials," *Journal of Composite Materials*, vol. 33, no. 15, pp. 1457–1469, 1999.

[17] M Bilasse, L Azrar, and E. Daya, "Complex modes based numerical analysis of viscoelastic sandwich plates vibrations," *Computers & Structures*, vol. 89, no. 7-8, pp. 539–555, 2011.

[18] G Bindolino, G Ghiringhelli, S Ricci, and M Terraneo, "Multilevel structural optimization for preliminary wing-box weight estimation," *Journal of Aircraft*, vol. 47, no. 2, pp. 475–489, 2010.

[19] J. Blasques and B Lazarov, "Becas v2, a cross-section analysis tool for anisotropic and inhomogeneous beam sections of arbitrary geometry," *RisøTechnicalReportRisø-R 1785, TechnicalU-niversity of Denmark*, 2012.

[20] M. Borri, G. L. Ghiringhelli, and T. Merlini, "Linear analysis of naturally curved and twisted anisotropic beams," *Composites Engineering*, vol. 2, no. 5-7, pp. 433 –456, 1992.

[21] N. Buannic and P. Cartraud, "Higher-order effective modeling of periodic heterogeneous beams. I. Asymptotic expansion method," *International Journal of Solids and Structures*, vol. 38, pp. 7139–7161, 2001.

[22] T. A. Burgo, T. R. Ducati, K. R. Francisco, K. J. Clinckspoor, F. Galembeck, and S. E. Galembeck, "Triboelectricity: Macroscopic charge patterns formed by self-arraying ions on polymer surfaces," *Langmuir*, vol. 28, no. 19, pp. 7407–7416, 2012.

[23] E. Carrera, F. Miglioretti, and M. Petrolo, "Computations and evaluations of higher-order theories for free vibration analysis of beams," *Journal of Sound and Vibration*, vol. 331, pp. 4269 –4284, 2012.

[24] E. Carrera and G. Giunta, "Refined beam theories based on a unified formulation," *International Journal of Applied Mechanics*, vol. 2, no. 01, pp. 117–143, 2010.

[25] E. Carrera, A. Pagani, and M. Petrolo, "Classical, refined, and component-wise analysis of reinforced-shell wing structures," *AIAA Journal*, vol. 51, no. 5, pp. 1255–1268, 2013.

[26] E. Carrera and M. Petrolo, "On the effectiveness of higher-order terms in refined beam theories," *Journal of Applied Mechanics*, vol. 78, no. 2, 2010, article 021013.

[27] C. E. S. Cesnik and D. H. Hodges, "Stiffness constants for initially twisted and curved composite beams," *Applied Mechanics Reviews*, vol. 46, no. 11, Part 2, S211 –S220, 1993.

[28] C. E. S. Cesnik and D. H. Hodges, "Variational-asymptotical analysis of initially twisted and curved composite beams," *International Journal for Engineering Analysis and Design*, vol. 1, no. 2, pp. 177 –187, Apr. 1994.

[29] P. D. Cha and J. M. Rinker, "Enforcing nodes to suppress vibration along a harmonically forced damped Euler-Bernoulli beam," *Journal of Vibration and Acoustics*, vol. 134, no. 5, 051010, p. 051 010, 2012.

[30] C.-S. Chang, D. H. Hodges, and M. J. Patil, "Flight dynamics of highly flexible aircraft," *Journal of Aircraft*, vol. 45, no. 2, pp. 538–545, 2008.

[31] A. Chattopadhyay and C. E. Seeley, "A higher order theory for modeling composite laminates with induced strain actuators," *Composites Part B: Engineering*, vol. 28, no. 3, pp. 243–252, 1997.

[32] C. Y. Chee, L. Tong, and G. P. Steven, "A review on the modelling of piezoelectric sensors and actuators incorporated in intelligent structures," *Journal of Intelligent Material Systems and Structures*, vol. 9, no. 1, pp. 3–19, 1998.

[33] C. Y. Chee, L. Tong, and G. P. Steven, "A mixed model for composite beams with piezoelectric actuators and sensors," *Smart materials and Structures*, vol. 8, no. 3, p. 417, 1999.

[34] H. Chen, W. Yu, and M. Capellaro, "A critical assessment of computer tools for calculating composite wind turbine blade properties," *Wind Energy*, vol. 13, no. 6, pp. 497–516, 2010.

[35] J. Chen, G. Zhu, W. Yang, Q. Jing, P. Bai, Y. Yang, T.-C. Hou, and Z. L. Wang, "Harmonic-resonator-based triboelectric nanogenerator as a sustainable power source and a self-powered active vibration sensor," *Advanced materials*, vol. 25, no. 42, pp. 6094–6099, 2013.

[36] W. Chen, L. Li, and M. Xu, "A modified couple stress model for bending analysis of composite laminated beams with first order shear deformation," *Composite Structures*, vol. 56, pp. 2723 –2732, 2009.

[37] I. Chopra, "Review of state of art of smart structures and integrated systems," *AIAA Journal*, vol. 40, no. 11, pp. 2145–2187, 2002.

[38] T. Choudhury and A. Pentland, "Sensing and modeling human networks using the sociometer," in *Proceedings of the 7th International Symposium on Wearable Computers*, IEEE, 2003, p. 216.

[39] C. Collier, "Stiffness, thermal expansion, and thermal bending formulation of stiffened, fiber-reinforced composite panels," in *34th Structures, Structural Dynamics and Materials Conference*, 1993, p. 1569.

[40] M. T. Cord, R. K. Surr, B. E. Walden, and L. Olson, "Performance of directional microphone hearing aids in everyday life," *Journal of the American Academy of Audiology*, vol. 13, no. 6, pp. 295–307, 2002.

[41] E. F. Crawley and E. H. Anderson, "Detailed models of piezoceramic actuation of beams," *Journal of Intelligent Material Systems and Structures*, vol. 1, no. 1, pp. 4–25, 1990.

[42] D. A. Danielson and D. H. Hodges, "A beam theory for large global rotation, moderate local rotation, and small strain," *Journal of applied mechanics*, vol. 55, no. 1, pp. 179–184, 1988.

[43] K. Dong, J. Deng, Y. Zi, Y.-C. Wang, C. Xu, H. Zou, W. Ding, Y. Dai, B. Gu, B. Sun, *et al.*, "3d orthogonal woven triboelectric nanogenerator for effective biomechanical energy harvesting and as self-powered active motion sensors," *Advanced Materials*, vol. 29, no. 38, 2017.

[44] S. B. Dong, J. B. Kosmatka, and H. C. Lin, "On Saint-Venants problem for an inhomogeneous, anisotropic cylinder, part I: Generalized saint-venant solutions," *Journal of Applied Mechanics*, vol. 68, no. 3, pp. 376 –381, 2001.

[45] S. Dong, C. Alpdogan, and E. Taciroglu, "Much ado about shear correction factors in timoshenko beam theory," *International Journal of Solids and Structures*, vol. 47, no. 13, pp. 1651–1665, 2010.

[46] M. Drela, "Method for simultaneous wing aerodynamic and structural load prediction," *Journal of aircraft*, vol. 27, no. 8, pp. 692–699, 1990.

[47] M. Drela, "Integrated simulation model for preliminary aerodynamic, structural, and control-law design of aircraft," in *40th Structures, Structural Dynamics, and Materials Conference and Exhibit*, 1999, p. 1394.

[48] J. Eargle, *The Microphone Book: From mono to stereo to surround-a guide to microphone design and application*. CRC Press, 2012.

[49] F. H. Gern, A. H. Naghshineh-Pour, E. Sulaeman, R. K. Kapania, and R. T. Haftka, "Structural wing sizing for multidisciplinary design optimization of a strut-braced wing," *Journal of aircraft*, vol. 38, no. 1, pp. 154–163, 2001.

[50] G. L. Ghiringelli and P. Mategazza, "Linear, straight and untwisted anisotropic beam section properties from solid finite elements," *Composites Engineering*, vol. 4, no. 12, pp. 1225 –1239, 1994.

[51] V. Giavotto, M. Borri, P. Mantegazza, G. Ghiringhelli, V. Carmaschi, G. C. Maffioli, and F. Mussi, "Anisotropic beam theory and applications," *Computers and Structures*, vol. 16, no. 1-4, pp. 403 –413, 1983.

[52] V. Giurgiutiu, "Review of smart-materials actuation solutions for aeroelastic and vibration control," *Journal of Intelligent Material Systems and Structures*, vol. 11, no. 7, pp. 525–544, 2000.

[53] V. Giurgiutiu, *Structural health monitoring: with piezoelectric wafer active sensors*. Academic Press, 2007.

[54] G. Goron, R. Duca, D. Sarojini, S. Shah, I. Chakraborty, S. I. Briceno, and D. N. Mavris, "Simulation-driven approach for predicting flight loads during complex dynamic maneuvers," in *17th AIAA Aviation Technology, Integration, and Operations Conference*, 2017, p. 3767.

[55] M. Gupta and D. H. Hodges, "Modeling thin-walled beams using VAM," in *58th AIAA/ASCE/AHS/ASC Structures, Structural Dynamics, and Materials Conference*, 2017, p. 1832.

[56] E. Hailemariam, R. Goldstein, R. Attar, and A. Khan, "Real-time occupancy detection using decision trees with multiple sensor types," in *Proceedings of the 2011*

Symposium on Simulation for Architecture and Urban Design, Society for Computer Simulation International, 2011, pp. 141–148.

[57] P. Hajela and J. L. Chen, "Preliminary weight estimation of conventional and joined wings usingequivalent beam models," *Journal of Aircraft*, vol. 25, no. 6, pp. 574–576, 1988.

[58] D. Han, W. Yu, and S. Roy, "A geometrically exact active beam theory for multibody dynamics simulation," *Smart materials and structures*, vol. 16, no. 4, p. 1136, 2007.

[59] S. Han and O. A. Bauchau, "Nonlinear three-dimensional beam theory for flexible multibody dynamics," *Multibody System Dynamics*, vol. 34, no. 3, pp. 211–242, 2015.

[60] D. Harursampath, *Nonclassical nonlinear effects in thin-walled composite beams*. 1999.

[61] D. Harursampath, M. Gupta, S. A. Ponnusami, S. Agrawal, D. Veerasamy, and S. AP, "Blending modern multifunctional materials with traditional structures: An approach towards cleaner and greener future," in *72nd Annual Forum of American Helicopter Society (AHS)*, 2016.

[62] X. He, Y. Zi, H. Yu, S. L. Zhang, J. Wang, W. Ding, H. Zou, W. Zhang, C. Lu, and Z. L. Wang, "An ultrathin paper-based self-powered system for portable electronics and wireless human-machine interaction," *Nano Energy*, vol. 39, pp. 328–336, 2017.

[63] Hibbett, Karlsson, and Sorensen, *ABAQUS/standard: User's Manual*. Hibbitt, Karlsson & Sorensen, 1998, vol. 1.

[64] J. C. Ho, W. Yu, and D. H. Hodges, "Energy transformation to generalized timoshenko form by the variational asymptotic beam section analysis," in *Proceedings of the 51st Structures, Structural Dynamics and Materials Conference, Orlando, Florida*, Paper AIAA-2010-3017, Reston, Virginia: AIAA, 2010.

[65] J. C. Ho, W. Yu, and D. H. Hodges, "Energy transformation to generalized Timoshenko form for nonuniform beams," *AIAA Journal*, vol. 48, no. 8, pp. 1268 –1272, 2010.

[66] D. H. Hodges and E. H. Dowell, "Nonlinear equations of motion for the elastic bending and torsion of twisted nonuniform rotor blades," NASA, Technical Note TN D-7818, 1974.

[67] D. H. Hodges, "A mixed variational formulation based on exact intrinsic equations for dynamics of moving beams," *International journal of solids and structures*, vol. 26, no. 11, pp. 1253–1273, 1990.

[68] D. H. Hodges, "Geometrically exact, intrinsic theory for dynamics of curved and twisted anisotropic beams," *AIAA Journal*, vol. 41, no. 6, pp. 1131–1137, 2003.

[69] D. H. Hodges, *Nonlinear composite beam theory*. AIAA, 2006.

[70] D. H. Hodges, D. Harursampath, V. V. Volovoi, and C. E. Cesnik, "Non-classical effects in non-linear analysis of pretwisted anisotropic strips," *International Journal of Non-Linear Mechanics*, vol. 34, no. 2, pp. 259–277, 1999.

[71] J. C. Houbolt and G. W. Brooks, "Differential equations of motion for combined flapwise bending, chordwise bending and torsion of twisted nonuniform rotor blades," NACA, Report 1346, 1958, Supersedes NACA Technical Note 3905, 1957.

[72] W.-S. Hwang and H. C. Park, "Finite element modeling of piezoelectric sensors and actuators," *AIAA Journal*, vol. 31, no. 5, pp. 930–937, 1993.

[73] D. Iesan, "On Saint-Venant's problem," *Archive for Rational mechanics and Analysis*, vol. 91, pp. 363–373, 1986.

[74] J. P. Jasa, J. T. Hwang, and J. R. Martins, "Open-source coupled aerostructural optimization using python," *Structural and Multidisciplinary Optimization*, vol. 57, no. 4, pp. 1815–1827, 2018.

[75] C. D. Johnson and D. A. Kienholz, "Finite element prediction of damping in structures with constrained viscoelastic layers," *AIAA journal*, vol. 20, no. 9, pp. 1284–1290, 1982.

[76] S. N. Jung, V. T. Nagaraj, and I. Chopra, "Refined structural model for thin- and thick-walled composite rotor blades," *AIAA Journal*, vol. 40, no. 1, pp. 105 –116, 2002.

[77] M. E. Karagozler, I. Poupyrev, G. K. Fedder, and Y. Suzuki, "Paper generators: Harvesting energy from touching, rubbing and sliding," in *Proceedings of the 26th annual ACM symposium on User interface software and technology*, ACM, 2013, pp. 23–30.

[78] M. Karpel, "Reduced-order models for integrated aeroservoelastic optimization," *Journal of Aircraft*, vol. 36, no. 1, pp. 146–155, 1999.

[79] Y. Kawahara, S. Hodges, B. S. Cook, C. Zhang, and G. D. Abowd, "Instant inkjet circuits: Lab-based inkjet printing to support rapid prototyping of ubicomp de-

vices," in *Proceedings of the 2013 ACM international joint conference on Pervasive and ubiquitous computing*, ACM, 2013, pp. 363–372.

[80] S.-J. Kim and J.-S. Lee, "Flexible organic transistor memory devices," *Nano letters*, vol. 10, no. 8, pp. 2884–2890, 2010.

[81] S. Kim, H.-J. Kwon, S. Lee, H. Shim, Y. Chun, W. Choi, J. Kwack, D. Han, M. Song, S. Kim, *et al.*, "Low-power flexible organic light-emitting diode display device," *Advanced Materials*, vol. 23, no. 31, pp. 3511–3516, 2011.

[82] S. C. Ko, Y. C. Kim, S. S. Lee, S. H. Choi, and S. R. Kim, "Micromachined piezoelectric membrane acoustic device," *Sensors and Actuators A: Physical*, vol. 103, no. 1, pp. 130–134, 2003.

[83] J. B. Kosmatka, H. C. Lin, and S. B. Dong, "On Saint-Venants problem for an inhomogeneous, anisotropic cylinder, part II: Cross-sectional properties," *Journal of Applied Mechanics*, vol. 68, no. 3, pp. 382 –391, 2001.

[84] J. Kosmatka, "Damping behavior of initially-stressed beams," in *49th AIAA/ASME/ASCE/AHS/ASC Structures, Structural Dynamics, and Materials Conference, 16th AIAA/ASME/AHS Adaptive Structures Conference, 10th AIAA Non-Deterministic Approaches Conference, 9th AIAA Gossamer Spacecraft Forum, 4th AIAA Multidisciplinary Design Optimization Specialists Conference*, 2008, p. 2080.

[85] J. B. Kosmatka and G. Appuhn, "Design and fabrication of integrally damped composite fan blades," in *Smart Structures and Materials 1999: Passive Damping and Isolation*, International Society for Optics and Photonics, vol. 3672, 1999, pp. 358–368.

[86] R. K. Kovvali, "A nonlinear theory of cosserat elastic plates using the variational-asymptotic method," PhD thesis, Georgia Institute of Technology, 2015.

[87] R. K. Kovvali and D. H. Hodges, "Verification of the variational-asymptotic sectional analysis for initially curved and twisted beams," *Journal of Aircraft*, vol. 49, no. 3, pp. 861–869, 2012.

[88] J. Kristek and P. Moczo, "Seismic-wave propagation in viscoelastic media with material discontinuities: A 3d fourth-order staggered-grid finite-difference modeling," *Bulletin of the Seismological Society of America*, vol. 93, no. 5, pp. 2273–2280, 2003.

[89] U. Kushnir and O. Rabinovitch, "Nonlinear ferro-electro-elastic beam theory," *International Journal of Solids and Structures*, vol. 36, pp. 2397 –2406, 2009.

[90] T. Labeodan, W. Zeiler, G. Boxem, and Y. Zhao, "Occupancy measurement in commercial office buildings for demand-driven control applicationsa survey and detection system evaluation," *Energy and Buildings*, vol. 93, pp. 303–314, 2015.

[91] R. S. Lakes, "Viscoelastic measurement techniques," *Review of scientific instruments*, vol. 75, no. 4, pp. 797–810, 2004.

[92] O. D. Lara and M. A. Labrador, "A survey on human activity recognition using wearable sensors.," *IEEE Communications Surveys and Tutorials*, vol. 15, no. 3, pp. 1192–1209, 2013.

[93] E. C. Larson, M. Goel, G. Boriello, S. Heltshe, M. Rosenfeld, and S. N. Patel, "Spirosmart: Using a microphone to measure lung function on a mobile phone," in *Proceedings of the 2012 ACM Conference on Ubiquitous Computing*, ACM, 2012, pp. 280–289.

[94] B. J. Lazan, "Damping of materials and members in structural mechanics," *PERGAMON PRESS LTD, OXFORD, ENGLAND. 1968, 317*, 1968.

[95] K. Le, *Vibrations of Shells and Rods*. Springer, 1999.

[96] S. Leadenham and A. Erturk, "Unified nonlinear electroelastic dynamics of a bimorph piezoelectric cantilever for energy harvesting, sensing, and actuation," *Nonlinear Dynamics*, vol. 79, no. 3, pp. 1727–1743, 2015.

[97] S. Lee, J. Reddy, and F Rostam-Abadi, "Transient analysis of laminated composite plates with embedded smart-material layers," *Finite Elements in Analysis and Design*, vol. 40, no. 5, pp. 463–483, 2004.

[98] Y. Lei, M. I. Friswell, and S. Adhikari, "A galerkin method for distributed systems with non-local damping," *International Journal of Solids and Structures*, vol. 43, no. 11-12, pp. 3381–3400, 2006.

[99] G. A. Lesieutre, "How membrane loads influence the modal damping of flexural structures," *AIAA journal*, vol. 47, no. 7, pp. 1642–1646, 2009.

[100] G. A. Lesieutre, "Frequency-independent modal damping for flexural structures via a viscous" geometric" damping model," *Journal of guidance, control, and dynamics*, vol. 33, no. 6, pp. 1931–1935, 2010.

[101] J. Lewis, "Understanding microphone sensitivity," *Analog Dialogue*, vol. 46, no. 2, pp. 14–16, 2012.

[102] B. Li, T. Sainath, A. Narayanan, J. Caroselli, M. Bacchiani, A. Misra, I. Shafran, H. Sak, G. Pundak, K. Chin, *et al.*, "Acoustic modeling for google home," 2017.

[103] L. Lin, S. Wang, S. Niu, C. Liu, Y. Xie, and Z. L. Wang, "Noncontact free-rotating disk triboelectric nanogenerator as a sustainable energy harvester and self-powered mechanical sensor," *ACS applied materials & interfaces*, vol. 6, no. 4, pp. 3031–3038, 2014.

[104] L. Lin, Y. Xie, S. Wang, W. Wu, S. Niu, X. Wen, and Z. L. Wang, "Triboelectric active sensor array for self-powered static and dynamic pressure detection and tactile imaging," *ACS nano*, vol. 7, no. 9, pp. 8266–8274, 2013.

[105] N. Liu and W. Yu, "Evaluation of smeared properties approaches and mechanics of structure genome for analyzing composite beams," *Mechanics of Advanced Materials and Structures*, vol. 25, no. 14, pp. 1171–1185, 2018.

[106] R. Liu, X. Kuang, J. Deng, Y.-C. Wang, A. C. Wang, W. Ding, Y.-C. Lai, J. Chen, P. Wang, Z. Lin, *et al.*, "Shape memory polymers for body motion energy harvesting and self-powered mechanosensing," *Advanced Materials*, 2018.

[107] X. Liu and W. Yu, "A novel approach to analyze beam-like composite structures using mechanics of structure genome," *Advances in Engineering Software*, vol. 100, pp. 238–251, 2016.

[108] R. G. Loewy, "Recent developments in smart structures with aeronautical applications," *Smart Materials and Structures*, vol. 6, no. 5, R11, 1997.

[109] H. M. Ma, X. L. Gao, and J. N. Reddy, "A microstrcuture-dependent Timoshenko model based on a modified couple stress theory," *Journal of Mechanics and Physics of Solids*, vol. 56, pp. 3379 –3391, 2009.

[110] S. P. Machado and C. M. Saravia, "Shear-deformable thin-walled beams in tnternal and external resonance," *Composite Structures*, vol. 97, pp. 30 –39, 2013.

[111] J. Mackerle, "Smart materials and structures-a finite-element approach: A bibliography (1986–1997)," *Modelling and Simulation in Materials Science and Engineering*, vol. 6, no. 3, p. 293, 1998.

[112] J. Mackerle, "Smart materials and structures-a finite element approachan addendum: A bibliography (1997–2002)," *Modelling and Simulation in Materials Science and Engineering*, vol. 11, no. 5, p. 707, 2003.

[113] G. Mathur, P. Desnoyers, P. Chukiu, D. Ganesan, and P. Shenoy, "Ultra-low power data storage for sensor networks," *ACM Transactions on Sensor Networks (TOSN)*, vol. 5, no. 4, p. 33, 2009.

[114] J. Mendiguren, F. Cortés, and L. Galdos, "A generalised fractional derivative model to represent elastoplastic behaviour of metals," *International Journal of Mechanical Sciences*, vol. 65, no. 1, pp. 12–17, 2012.

[115] C. G. Merrett, "Time to flutter of a viscoelastic goland wing," in *56th AIAA/ASCE/AHS/ASC Structures, Structural Dynamics, and Materials Conference*, 2015, p. 0193.

[116] P. J. Minguet, "Static and dynamic behavior of composite helicopter rotor blades under large deflections," PhD thesis, Massachusetts Institute of Technology, 1989.

[117] K. Nakatsuma, R. Takedomi, T. Eguchi, Y. Oshima, and I. Torigoe, "Active bioacoustic measurement for human-to-human skin contact area detection," in *SENSORS, 2015 IEEE*, IEEE, 2015, pp. 1–4.

[118] A. Nathan, A. Ahnood, M. T. Cole, S. Lee, Y. Suzuki, P. Hiralal, F. Bonaccorso, T. Hasan, L. Garcia-Gancedo, A. Dyadyusha, *et al.*, "Flexible electronics: The next ubiquitous platform," *Proceedings of the IEEE*, vol. 100, no. Special Centennial Issue, pp. 1486–1517, 2012.

[119] M. A. Neto, W. Yu, and S. Roy, "Two finite elements for general composite beams with piezoelectric actuators and sensors," *Finite Elements in Analysis and Design*, vol. 45, no. 5, pp. 295–304, 2009.

[120] N. Nguyen, "Integrated flight dynamic modeling of flexible aircraft with inertial force-propulsion-aeroelastic coupling," in *46th AIAA Aerospace Sciences Meeting and Exhibit*, 2008, p. 194.

[121] N. Nguyen and I. Tuzcu, "Flight dynamics of flexible aircraft with aeroelastic and inertial force interactions," in *AIAA Atmospheric Flight Mechanics Conference*, 2009, p. 6045.

[122] N. T. Nguyen, E. Ting, and S. Lebofsky, "Inertial force coupling to nonlinear aeroelasticity of flexible wing aircraft," in *15th Dynamics Specialists Conference*, 2016, p. 1094.

[123] J. Nishimura and T. Kuroda, "Eating habits monitoring using wireless wearable in-ear microphone," in *Wireless Pervasive Computing, 2008. ISWPC 2008. 3rd International Symposium on*, IEEE, 2008, pp. 130–132.

[124] S. Niu, S. Wang, L. Lin, Y. Liu, Y. S. Zhou, Y. Hu, and Z. L. Wang, "Theoretical study of contact-mode triboelectric nanogenerators as an effective power source," *Energy & Environmental Science*, vol. 6, no. 12, pp. 3576–3583, 2013.

[125] K. Nomura, H. Ohta, K. Ueda, T. Kamiya, M. Hirano, and H. Hosono, "Thin-film transistor fabricated in single-crystalline transparent oxide semiconductor," *Science*, vol. 300, no. 5623, pp. 1269–1272, 2003.

[126] R. W. Ogden, *Non-linear elastic deformations*. Courier Corporation, 1997.

[127] C. Pang, C. Lee, and K.-Y. Suh, "Recent advances in flexible sensors for wearable and implantable devices," *Journal of Applied Polymer Science*, vol. 130, no. 3, pp. 1429–1441, 2013.

[128] C. Park, C. Walz, and I. Chopra, "Bending and torsion models of beams with induced-strain actuators," *Smart Materials and Structures*, vol. 5, no. 1, p. 98, 1996.

[129] S. N. Patel and G. D. Abowd, "Blui: Low-cost localized blowable user interfaces," in *Proceedings of the 20th annual ACM symposium on User interface software and technology*, ACM, 2007, pp. 217–220.

[130] M. J. Patil and D. H. Hodges, "Flight dynamics of highly flexible flying wings," *Journal of Aircraft*, vol. 43, no. 6, pp. 1790–1799, 2006.

[131] M. Pedram and J. M. Rabaey, *Power aware design methodologies*. Springer Science & Business Media, 2002.

[132] P. Piperni, M. Abdo, and F. Fafyeke, "The application of multi-disciplinary optimization technologies to the design of a business jet," in *10th AIAA/ISSMO Multidisciplinary Analysis and Optimization Conference*, 2004, p. 4370.

[133] B. Popescu and D. H. Hodges, "On asymptotically correct Timoshenko-like anisotropic beam theory," *International Journal of Solids and Structures*, vol. 37, no. 3, pp. 535–558, 2000.

[134] A. N. Popper, R. R. Fay, and A. N. Popper, *Sound source localization*. Springer, 2005.

[135] Y. Qi and M. C. McAlpine, "Nanotechnology-enabled flexible and biocompatible energy harvesting," *Energy & Environmental Science*, vol. 3, no. 9, pp. 1275–1285, 2010.

[136] S Raja, K Rohwer, and M Rose, "Piezothermoelastic modeling and active vibration control of laminated composite beams," *Journal of intelligent material systems and structures*, vol. 10, no. 11, pp. 890–899, 1999.

[137] K Rajabi and S. Hosseini-Hashemi, "Application of the generalized hooke's law for viscoelastic materials (ghvms) in nonlocal free damped vibration analysis of

viscoelastic orthotropic nanoplates," *International Journal of Mechanical Sciences*, vol. 124, pp. 158–165, 2017.

[138] A. Rajagopal, "Advancements in rotor blade cross-sectional analysis using the variational-asymptotic method," PhD thesis, Georgia Institute of Technology, Atlanta, GA, 2014.

[139] A. Rajagopal, D. H. Hodges, and W. Yu, "Asymptotic beam theory for planar deformation of initially curved isotropic strips," *Thin-Walled Structures*, vol. 50, no. 1, pp. 106–115, 2012.

[140] M. P. Rao, D. Harursampath, and K Renji, "Prediction of inter-laminar stresses in composite honeycomb sandwich panels under mechanical loading using variational asymptotic method," *Composite Structures*, vol. 94, no. 8, pp. 2523–2537, 2012.

[141] E. Reissner, "On one-dimensional large-displacement finite-strain beam theory," *Studies in Applied Mathematics*, vol. LII, no. 2, pp. 87 –95, 1973.

[142] R. M. Rivello, *Theory and analysis of flight structures*. McGraw-Hill College, 1969.

[143] A. Rizzi, J. Oppelstrup, M. Zhang, and M. Tomac, "Coupling parametric aircraft lofting to cfd & csm grid generation for conceptual design," in *49th AIAA Aerospace Sciences Meeting including the New Horizons Forum and Aerospace Exposition, Aerospace Sciences Meeting, Orlando, FL*, 2011, p. 160.

[144] D. Robbins and J. Reddy, "Analysis of piezoelectrically actuated beams using a layer-wise displacement theory," *Computers & structures*, vol. 41, no. 2, pp. 265–279, 1991.

[145] S. Roy and W. Yu, "A variational-asymptotic theory of smart slender structures," in *ASME 2005 International Mechanical Engineering Congress and Exposition*, American Society of Mechanical Engineers, 2005, pp. 65–72.

[146] S. Roy and W. Yu, "A coupled timoshenko model for smart slender structures," *International Journal of Solids and Structures*, vol. 46, no. 13, pp. 2547–2555, 2009.

[147] S. Roy, W. Yu, and D. Han, "An asymptotically correct classical model for smart beams," *International Journal of Solids and Structures*, vol. 44, no. 25-26, pp. 8424–8439, 2007.

[148] C. Sachdeva, M. Gupta, and D. H. Hodges, "Modeling of initially curved and twisted smart beams using intrinsic equations," *International Journal of Solids and Structures*, 2017.

[149] D. Saravanos and P. Heyliger, "Coupled electromechanical response of composite beams with embedded piezoelectric sensors and actuators," 1994.

[150] D. A. Saravanos and P. R. Heyliger, "Coupled layerwise analysis of composite beams with embedded piezoelectric sensors and actuators," *Journal of Intelligent Material Systems and Structures*, vol. 6, no. 3, pp. 350–363, 1995.

[151] M. Segev-Bar and H. Haick, "Flexible sensors based on nanoparticles," *ACS nano*, vol. 7, no. 10, pp. 8366–8378, 2013.

[152] W.-H. Seol, Y. M. Lee, and J.-K. Park, "Enhancement of the mechanical properties of pvdf membranes by non-solvent aided morphology control," *Journal of Power Sources*, vol. 170, no. 1, pp. 191–195, 2007.

[153] J Sieber, D. Wagg, and S Adhikari, "On the interaction of exponential non-viscous damping with symmetric nonlinearities," *Journal of Sound and Vibration*, vol. 314, no. 1-2, pp. 1–11, 2008.

[154] N. Silvestre and D. Camotim, "First-order generalised beam theory for arbitrary orthotropic materials," *Thin-Walled Structures*, vol. 40, pp. 755–789, 2002.

[155] N. Silvestre and D. Camotim, "Second-order generalised beam theory for arbitrary orthotropic materials," *Thin-Walled Structures*, vol. 40, pp. 791–820, 2002.

[156] R. C. Simpson and S. P. Levine, "Voice control of a powered wheelchair," *IEEE Transactions on Neural Systems and Rehabilitation Engineering*, vol. 10, no. 2, pp. 122–125, 2002.

[157] H. R. Sobuz, E. Ahmed, N. M. Sutan, N. M. S. Hasan, M. A. Uddin, and M. J. Uddin, "Bending and time-dependent responses of RC beams strengthened with bonded carbon fiber composite laminates," *Construction and Building Materials*, vol. 29, pp. 597 –611, 2012.

[158] T. Starner, "The challenges of wearable computing: Part 1," *Ieee Micro*, vol. 21, no. 4, pp. 44–52, 2001.

[159] C. T. Sun, *Vibration damping of structural elements*. Prentice Hall, 1995.

[160] V. Talla, B. Kellogg, S. Gollakota, and J. R. Smith, "Battery-free cellphone," *Proceedings of the ACM on Interactive, Mobile, Wearable and Ubiquitous Technologies*, vol. 1, no. 2, p. 25, 2017.

[161] H. Tzou and R Ye, "Analysis of piezoelastic structures with laminated piezoelectric triangle shell elements," *AIAA Journal*, vol. 34, no. 1, pp. 110–115, 1996.

[162] J.-M. Valin, F. Michaud, J. Rouat, and D. Létourneau, "Robust sound source localization using a microphone array on a mobile robot," in *Intelligent Robots and Systems, 2003.(IROS 2003). Proceedings. 2003 IEEE/RSJ International Conference on*, IEEE, vol. 2, 2003, pp. 1228–1233.

[163] V. Valliappan, D. Harursampath, S. Roy, and W. Yu, "Variational asymptotic modelling of an initially-curved and pre-twisted smart beam," 2014.

[164] T. Van Kasteren, A. Noulas, G. Englebienne, and B. Kröse, "Accurate activity recognition in a home setting," in *Proceedings of the 10th international conference on Ubiquitous computing*, ACM, 2008, pp. 1–9.

[165] V. Z. Vlasov, *Thin-Walled Elastic Beams*. National Science Foundation and Department of Commerce, 1961.

[166] V. V. Volovoi, "On end effects for prismatic beams.," 1998.

[167] V. V. Volovoi, W. Yu, and D. H. Hodges, "Asymptotic treatment of the Vlasov effect for composite beams," in *Proceedings of the 43rd Structures, Structural Dynamics and Materials Conference, Denver, Colorado*, Reston, Virginia: AIAA, 2002.

[168] B. Wang, J. Zhao, and S. Zhou, "A micro scale Timoshenko beam model based on strain gradient elasticity theory," *European Journal of Mechanics A/Solids*, vol. 29, pp. 1591 –1599, 2010.

[169] Q. Wang, "Asymptotic multiphysics modeling of composite beams," 2011.

[170] Q. Wang and W. Yu, "Geometrically nonlinear analysis of composite beams using wiener-milenković parameters," *Journal of Renewable and Sustainable Energy*, vol. 9, no. 3, p. 033 306, 2017.

[171] S. Wang, "A finite element model for the static and dynamic analysis of a piezoelectric bimorph," *International Journal of Solids and Structures*, vol. 41, no. 15, pp. 4075–4096, 2004.

[172] Z. L. Wang, "Triboelectric nanogenerators as new energy technology for self-powered systems and as active mechanical and chemical sensors," *ACS nano*, vol. 7, no. 11, pp. 9533–9557, 2013.

[173] Z. L. Wang, "Triboelectric nanogenerators as new energy technology and self-powered sensors–principles, problems and perspectives," *Faraday discussions*, vol. 176, pp. 447–458, 2015.

[174] Z. L. Wang, "On maxwell's displacement current for energy and sensors: The origin of nanogenerators," *Materials Today*, 2017.

[175] Z. L. Wang, J. Chen, and L. Lin, "Progress in triboelectric nanogenerators as a new energy technology and self-powered sensors," *Energy & Environmental Science*, vol. 8, no. 8, pp. 2250–2282, 2015.

[176] K. Watanabe, Y. Kurihara, T. Nakamura, and H. Tanaka, "Design of a low-frequency microphone for mobile phones and its application to ubiquitous medical and healthcare monitoring," *IEEE Sensors Journal*, vol. 10, no. 5, pp. 934–941, 2010.

[177] G. Wempner, *Mechanics of solids with applications to thin bodies*. Springer Science & Business Media, 1982, vol. 2.

[178] M. D. Williams, F. van Keulen, and M. Sheplak, "Modeling of initially curved beam structures for design of multistable MEMS," *Journal of Applied Mechanics*, vol. 79, no. 1, 011006, p. 011 006, 2012.

[179] W. S. Wong and A. Salleo, *Flexible electronics: materials and applications*. Springer Science & Business Media, 2009, vol. 11.

[180] M. Xu, P. Wang, Y.-C. Wang, S. L. Zhang, A. C. Wang, C. Zhang, Z. Wang, X. Pan, and Z. L. Wang, "A soft and robust spring based triboelectric nanogenerator for harvesting arbitrary directional vibration energy and self-powered vibration sensing," *Advanced Energy Materials*, 2017.

[181] M. Xu, Y.-C. Wang, S. L. Zhang, W. Ding, J. Cheng, X. He, P. Zhang, Z. Wang, X. Pan, and Z. L. Wang, "An aeroelastic flutter based triboelectric nanogenerator as a self-powered active wind speed sensor in harsh environment," *Extreme Mechanics Letters*, vol. 15, pp. 122–129, 2017.

[182] P.-K. Yang, Z.-H. Lin, K. C. Pradel, L. Lin, X. Li, X. Wen, J.-H. He, and Z. L. Wang, "Paper-based origami triboelectric nanogenerators and self-powered pressure sensors," *ACS nano*, vol. 9, no. 1, pp. 901–907, 2015.

[183] W. Yu, "Mathematical construction of a reissner-mindlin plate theory for composite laminates," *International Journal of Solids and Structures*, vol. 42, pp. 6680–6699, 2005.

[184] W. Yu and D. H. Hodges, "Elasticity solutions versus asymptotic sectional analysis of homogeneous, isotropic, prismatic beams," *Journal of Applied Mechanics*, vol. 71, no. 1, pp. 15 –23, 2004.

[185] W. Yu, *Variational asymptotic modeling of composite dimensionally reducible structures*. Georgia Institute of Technology, Atlanta GA, 2002.

[186] W. Yu and M. Blair, "Gebt: A general-purpose nonlinear analysis tool for composite beams," *Composite Structures*, vol. 94, no. 9, pp. 2677–2689, 2012.

[187] W. Yu, D. H. Hodges, and J. C. Ho, "Variational asymptotic beam sectional analysis–an updated version," *International Journal of Engineering Science*, vol. 59, pp. 40–64, 2012.

[188] W. Yu, D. H. Hodges, V. Volovoi, and C. E. Cesnik, "On Timoshenko-like modeling of initially curved and twisted composite beams," *International Journal of Solids and Structures*, vol. 39, no. 19, pp. 5101–5121, 2002.

[189] W. Yu, D. H. Hodges, V. V. Volovoi, and E. D. Fuchs, "A generalized Vlasov theory for composite beams," *Thin-Walled Structures*, vol. 43, no. 9, pp. 1493–1511, 2005.

[190] H. Zhang, Y. Yang, Y. Su, J. Chen, K. Adams, S. Lee, C. Hu, and Z. L. Wang, "Triboelectric nanogenerator for harvesting vibration energy in full space and as self-powered acceleration sensor," *Advanced Functional Materials*, vol. 24, no. 10, pp. 1401–1407, 2014.

[191] S. L. Zhang, Y.-C. Lai, X. He, R. Liu, Y. Zi, and Z. L. Wang, "Auxetic foam-based contact-mode triboelectric nanogenerator with highly sensitive self-powered strain sensing capabilities to monitor human body movement," *Advanced Functional Materials*, vol. 27, no. 25, 2017.

[192] L. Zhou, A. Wanga, S.-C. Wu, J. Sun, S. Park, and T. N. Jackson, "All-organic active matrix flexible display," *Applied Physics Letters*, vol. 88, no. 8, p. 083 502, 2006.

[193] Y. Zigel, D. Litvak, and I. Gannot, "A method for automatic fall detection of elderly people using floor vibrations and soundproof of concept on human mimicking doll falls," *IEEE Transactions on Biomedical Engineering*, vol. 56, no. 12, pp. 2858–2867, 2009.

VITA

Mohit Gupta was born on February 09, 1993 in Jind, Haryana, India which is one of the oldest towns in the state. He graduated with Bachelors in Engineering (B.E.) from Thapar University, India, in 2014 majoring in Mechanical Engineering. He began his graduate studies in Aerospace Engineering at Georgia Tech. in the same year of 2014 and became a Graduate Research Assistant working with Prof. Dewey H. Hodges. He earned his masters (MSc) degree in 2016. While working towards his Ph.D., Mohit obtained a Graduate Certificate in Engineering Entrepreneurship from Scheller College of Business as well.

Mohits research at Georgia Tech. was supported by the US Army through Vertical Lift Research Center of Excellence which is the largest rotorcraft center in the United States. He has been successful in tackling complex problems related to realistic composite rotor blade analysis and advance the application of variational asymptotic methods to the next level, by understanding the behavior of aircraft wings. The other way to solve such complex problems is using Finite Element Methods which require a lot of man-hours and huge computational power to run. Apart from that, Mohit also serves as a reviewer to highly reputed journals viz. Nonlinear Dynamics by Springer, Engineering Structures by Elsevier, Thin-Walled Structures by Elsevier, Journal of Renewable and Sustainable Energy by AIP and the Journal of American Helicopter Society (AHS).

He has also worked significantly outside his core research area as well, mainly on multifunctional energy harvesting and energy storing smart composites, which has been recognized by UNESCO, Airbus, and the collaborating institutions in UK, Netherlands, and

India. Owing to his contributions and significant accomplishments, he has been recognized with international awards by UNESCO-Airbus Fly Your Ideas, Airbus Innovation Showdown winning titles, multiple Vertical Flight Foundation Scholarships, Dutch Aerospace Society, GAMM and WTiN.

He is an active collaborator and a great mentor to his peers. To work on multifunctional composites, Mohit was part of a geographically diverse team led by Prof. Dineshkumar Harursampath, whose members were associated with TU Delft, Netherlands, Indian Institute of Science, Bangalore and City University London, thus spread over 3 different continents and 4 different time zones. Further, work related to these tasks on smart composites has been published in the prestigious International Journal of Solids and Structures, Elsevier and presented at various reputed conferences such as AHS Sustainability 2015 in Montral and AHS Forum 2016, West Palm Beach, FL. Recently, he collaborated with Prof. Gregory Abowd in Ubiquitous Computing Group, Human-Computer Interaction at Georgia Tech. towards the development of self-powered multifunctional microphones. He has been very active in guiding many undergraduate researchers in their research on interdisciplinary topics leading to significant advancements. Besides, Mohit has actively organized and hosted important events and talks in the school of AE, actively participated in important discussions with School of AE Advisory Council and he does it all with great zeal and enthusiasm.

Mohit wishes to continue his research towards numerous futuristic applications of multifunctional composites and computational mechanics towards further development of products and services that possess an immense potential of assisting the future generations.